



SAPIENZA
UNIVERSITÀ DI ROMA

**Corso di dottorato in AUTOMATICA, BIOINGEGNERIA E RICERCA
OPERATIVA - ABRO**

XXX ciclo

**Statistical causality in the EEG for the study of
cognitive functions in healthy and pathological
brains**

**Dipartimento di Ingegneria Informatica, Automatica e Gestionale 'Antonio
Ruberti'**

Candidato
Alessandra Anzolin

Relatore
Laura Astolfi

Co-Relatore
Jlenia Toppi

“Vedere come ognuno di noi ha una sua ragione di esserci e rintracciare che cosa ci ha portato qui è un bellissimo esercizio d’umiltà e d’ammirazione per quell’Intelligenza che tiene assieme il mondo.”

*Tiziano Terzani
Un’idea di destino*

Summary

Preface	I
Chapter 1	1
Preliminary Concepts	1
1. Electrophysiology of the Central Nervous System (CNS).....	1
1.1 Cerebral cortex.....	2
1.2 Brodmann areas	3
2. Neurons.....	5
2.1 Anatomy of the neuron	5
2.2 Electrophysiology of the neuron.....	7
3. Electroencephalography (EEG).....	11
3.1 EEG generation and recording.....	11
3.2 EEG artifacts.....	16
3.3 EEG frequency rhythms.....	18
3.4 Event-Related Potential (ERP)	20
Chapter 2	23
Generation of simulated EEG data	23
1. Introduction.....	23
2. Methods	26
2.1 Multivariate Autoregressive Modeling (MVAR)	26
2.2 Partial Directed Coherence (PDC).....	27
2.3 Simulated EEG Data Generation.....	28
2.4 Features of the simulated data and the connectivity patterns.....	30
3. Toolbox Testing.....	33
3.1 Simulated data generation	33
3.2 Performance parameters	33
3.3 Results	35

4.	An example of application of the toolbox: investigating the effect of inter-trial variability on connectivity estimates	37
4.1	Study 1: effects on connectivity estimate of alterations in connections value	39
4.2	Study 2: effect on connectivity estimation of variable density	43
5.	Discussion	47
5.1	SEED-G toolbox capability	47
5.2	Application on PDC stability evaluation	49
6.	Conclusion	50
Chapter 3		51
Investigating performances of time-varying connectivity algorithms		51
1.	Introduction	52
2.	Methods	55
2.1	Time-varying MVAR and PDC	55
2.2	The Recursive Least Squares (RLS)	56
2.3	The General Linear Kalman Filter	57
3.	Simulation Study 1	57
3.1	Datasets Generation	59
3.2	Evaluation of performances	59
3.3	Statistical Analysis	63
4.	Simulation Study 2	64
4.1	Evaluation of performances	65
4.2	Statistical Analysis	65
5.	Results	66
5.1	Simulation Study 1: RLS vs GLKF	66
5.2	Simulation Study 2: Initial conditions in GLKF	77
6.	Conclusion and Discussion	79
Chapter 4		83

Effect of head volume conduction on directed connectivity estimated between reconstructed EEG sources 83

- 1. Introduction 84
- 2. Methods 87
 - 2.1 Forward Problem 87
 - 2.2 Inverse Problem 88
 - 2.3 Multivariate Directed Connectivity Estimation 91
 - 2.4 Statistical assessment of significant connections 95
 - 2.5 Simulation Framework 95
 - 2.6 Simulated time series generation 97
 - 2.7 Simulated time series location 97
 - 2.8 Pseudo-EEG signal generation 99
 - 2.9 Source reconstruction and directed connectivity estimation 99
 - 2.10 Performance parameters 100
 - 2.11 Statistical Analysis 101
 - 2.12 Topographical visualization of the results 102
- 3. Results 102
 - 3.1 Statistical analysis 102
 - 3.2 Brain maps 111
- 4. Discussion and Conclusion 119
- 7. Supplementary material 122
- Code and data availability 126

Chapter 5 127

Connectivity in attention processes 127

- 1. Introduction 128
- 2. Materials and methods 129
 - 2.1 Experimental Design 129
 - 2.2 Behavioral data 131
 - 2.3 EEG data pre-processing 131
 - 2.4 Study 1: Source data analysis 132

2.5	Study 2: Scalp data analysis	136
3.	Results	138
3.1	Behavioral analysis.....	138
3.2	Study 1: Source level analysis	141
3.3	Study 2: Sensors level analysis	149
4.	Discussion and Conclusion	154
4.1	Study 1: Source level analysis	154
4.2	Study 2: Sensor level analysis	155
Chapter 6	159
Connectivity in memory functions	159
1.	Introduction	159
2.	Materials and methods	162
2.1	Experimental group	162
2.2	Experimental Design.....	162
2.3	Behavioral data	164
2.4	EEG data pre-processing.....	164
2.5	Time-varying Connectivity estimation.....	164
2.6	Graph indices	165
2.7	Statistical Analysis	166
2.8	Preliminary study on stroke patients	167
3.	Results	168
3.1	Behavioral analysis.....	168
3.2	Healthy subjects.....	170
3.3	Stroke patients	177
4.	Conclusion and discussion.....	182
General conclusion		191
References		193
Acknowledgement		213
RESEARCH PRODUCTS		215

Preface

In the last years there has been a growing interest in studying the functional relationship (in statistical sense) between the activity in different parts of the brain [1]–[5], as a tool to improve the understanding of which brain areas are mainly involved in the execution of tasks (e.g. motor, cognitive, visual, auditory, social) and how they communicate to create the circuits underlying a specific cerebral function. Several estimators with different peculiarities have been developed to assess the existence, the intensity and the direction of the functional connections linking two or more signals. Some of them are characterized by a high versatility since they can be applied to signals acquired through different techniques, fMRI, EEG or MEG, on the basis of the specific applicative aims [6], [7]. EEG is one of the few techniques allowing to non-invasively study brain activity with a timing that matches the one of the processes under investigation. Lots of the available methods have been developed to estimate functional connectivity networks starting from this kind of signals recorded in the most varied contexts: during the execution of a cognitive or motor task, in clinical and operational contexts. The aim of this thesis was to employ such methodologies for investigating cognitive function like attention and memory in healthy subjects and in post stroke patients, in order to better understand the brain activity associated with such functions and with their recovery after an injury. Several studies investigated the properties of all the available methods providing different solutions for different application fields and highlighting the best approaches able to reproduce the brain circuits related to non-invasive EEG measurements. Among all the approaches used for connectivity estimation, worth of note is the class of estimators based on the theory of causality developed by developed by Wiener in 1965 and translated in a mathematical object by Granger in 1969 [8]–[10]. Such estimators are able to determine the direction of the influence between any given pair of signals. Notwithstanding the advancements provided in this respect during the last twenty years, the main problem still unsolved regards the stability and reliability of the connectivity patterns obtained from Granger

causality-based approaches. Such issue still needs to be solved in order to provide an instrument really able to fulfil clinical and applicative purposes, where the reliability of the results and their consistence within classes of pathologies are mandatory. In the present thesis, the term “causal” will be referred always to the concept of dynamic influence based on a predictive model (in the Granger sense). More generally, the framework of connectivity estimators is a manifold scenario where the selection of the appropriate algorithm on the basis of the research objectives is often difficult. For this reason, several studies tried to compare the performances of already existing algorithms under different experimental conditions with the aim to provide some guidelines to help researchers in orienting themselves in such intricate world. Moreover, every time a new algorithm is defined and implemented, an initial testing phase where it is compared to already existing approaches is required. In both cases, the comparison is always made on the basis of data reproducing a well-known connectivity pattern, which can be used as test bench for the algorithms. Unfortunately, a realistic benchmark is not easily available so that is often necessary to resort to simulated data. As for the EEG case, simulated data should reproduce the spectral properties of signals really acquired on human scalp otherwise the test might provide results on algorithms performances which could be contradicted on real data. After an introductory *Chapter 1* in which some preliminary notions will be briefly exposed, in *Chapter 2* we introduce a new toolbox, SEED-G, that allow to generate realistic simulated data with the same spectral properties of EEG (or ECoG) signals and with the possibility to set a whole series of parameters which make the dataset as close as possible to the user’s necessities. In particular, the user can choose the features of the signals to be generated (number of samples, number of trials composing the dataset, signal to noise ratio, inclusion or not of non-ideality or artifacts) and the features of the imposed connectivity pattern (number of nodes, density of the pattern and behaviour along time) in order to obtain a ground-truth in so many different interesting and not yet investigated experimental conditions.

One of the main issues related with the accuracy of the brain connectivity estimates regards the fact that all the MVAR based methodologies for the causal

connectivity require the hypothesis of stationary signals (in wide-sense), thus, they are not able to capture the variability in the dynamical statistical properties of the signals. To overcome this limitation, different algorithms for the estimation of MVAR with time dependent coefficients were recently developed [11]. In the work proposed in *Chapter 3*, we considered two of the most used time-varying algorithm: a method based on a General Linear Kalman Filter (GLKF) [10] and the Recursive Least Squares [8]. We propose on one side a simulation study that provides the performance of such different approaches and allows to select the best practice in different real context, on the other side an adaptation of the GLKF algorithm with a significant improvement of the estimation accuracy. Another important open issue related to the connectivity estimation in real context will be treated in *Chapter 4* and regards the effect of volume conduction. The input coming from brain areas at different depths and the electrical properties of the tissues located between the cortex and the scalp have the effect to distort the electrical field generated by neural activity and therefore impede an attribution of scalp signals to the underlying brain sources. Thus, despite the large use of such approaches, it has been debated for a long time if the results obtained by applying causal connectivity estimates based on the scalp time series provided by EEG allows a clear interpretation in terms of interacting cerebral areas [12]. Although this is a well-known and described theme, it is still studied and discussed in the context of connectivity analysis because of the strong effect that the volume conduction has on the scalp measures and could lead to a misinterpretation of the results [13], as making inferences from the EEG signal is still not straightforward [12], [14]. In order to overcome or attenuate the volume conduction problem, several strategies and algorithms have been proposed to estimate source activities from multi-channel EEG recordings [15]. A combination of linear inverse approaches for extracting cortical and sub-cortical waveforms [16] and Granger-based estimators for functional connectivity estimation [17] can be used to extract and investigate the human brain circuits. Here we will try to provide a complete evaluation of the volume conduction effect in different simulated and controlled experimental conditions for two different algorithms for the source reconstruction: the linearly constrained minimum variance (LCMV) [18] and the

exact low-resolution tomography (eLORETA) [19]. This part of my thesis was developed in collaboration with the University of Ghent (Department of Data Analysis - Faculty of Psychological and Educational Sciences), where I spent a period of my PhD. After the described methodological part, the approaches emerged as the most performing were applied on real datasets with the aim to investigate the brain networks underlying fundamental human cognitive functions as attention and memory. In *Chapter 5*, the attention functions (alerting, orienting and executive control following the Posner's theoretical model [20]) were analyzed on a group of healthy subjects in two main steps. The first part of the study was performed at source level with the aim to provide a neuro-computation model including connectivity maps, spectral, spatial and causal information at the same time. After the description of the main properties of the information flows exchanged between brain areas we moved at sensors level in order to understand if some properties are preserved also in the EEG-scalp networks and if some of them vary at single subject level according to the behavioral performance of an attention task. The implications of synthetic neurophysiological indices could cover several aspects; they could be employed in future clinical applications to support the behavioral assessment or to evaluate the influence of specific attention deficits on Brain Computer Interface (BCI) performance and/or the effects of BCI training in cognitive rehabilitation. *Chapter 6* will report the last application, regarding a group of post-stroke patients and conducted in the framework of the EU FP7 Project CONTRAST (Cognitive Enhancement Training for Successful Rehabilitation After Stroke). Recent studies have shown that cognitive recovery is linked to neuronal plasticity phenomena, therefore research has focused on the study of changes in brain networks following rehabilitation interventions. In this context, we employed connectivity estimation algorithms combined with the extraction of EEG-based brain indices that can capture the main properties of brain networks to evaluate the effectiveness of a rehabilitation treatment.

Finally, *the last section* reports the general conclusion of the Thesis and outlines the possible future research directions.

Chapter 1

Preliminary Concepts

1. Electrophysiology of the Central Nervous System (CNS)

The nervous system is the coordination and control network that receives all the information coming both from the external and internal environment, processes them and responds in different and specific ways. It can be divided in two components called Central Nervous System (CNS) and Peripheral Nervous System (PNS) and including further subdivisions. The CNS consists of the brain and spinal cord (*fig. 1.1*).

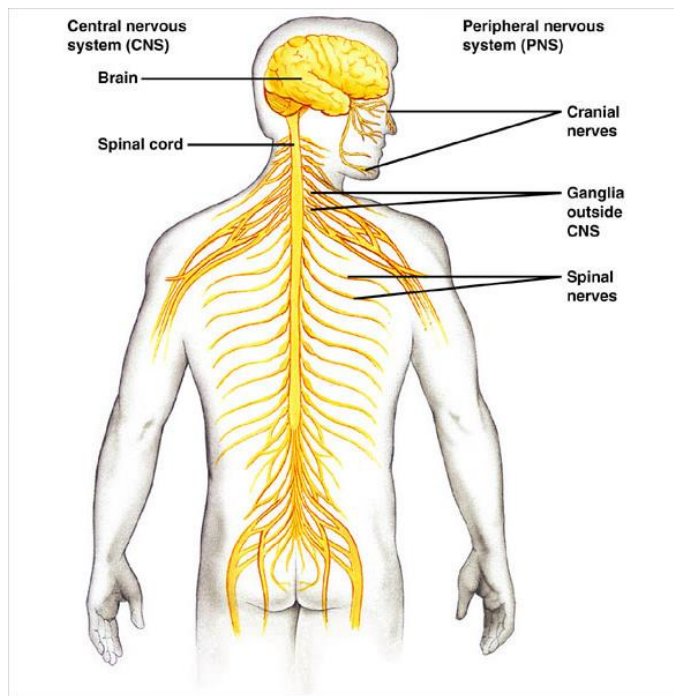


Figure 1.1- Schematic diagram showing the Central Nervous System (CNS) composed by the brain and the spinal cord and the Peripheral Nervous System (PNS) composed by cranial nerve, spinal nerves and ganglia outside the CNS.

Protected within the skull, the brain is composed of three parts closely related to each other: the cerebrum, cerebellum, and brainstem. In turn, as showed in *fig 1.2*, the cerebrum is divided into medulla oblongata, bridge, midbrain, diencephalon and telencephalon. The brain is responsible for the control and regulation of all the activities and functions of our body and is the center of the higher mental functions (such as memory, attention, language, executive functions). The stimuli (sensations and perceptions) come to the brain from the peripheral districts of the organism and its motor responses are transmitted to the skeletal musculature. The spinal cord, contained in the vertebral column, connects the CNS to the PNS. The PNS consists of the nerves and ganglia outside the brain and spinal cord, is responsible for transmission to the CNS of motor, sensory and proprioceptive activities. One of the main part of the PNS is the autonomic nervous system, whose task is to control and regulate vegetative functions, or functions that are independent of our will.

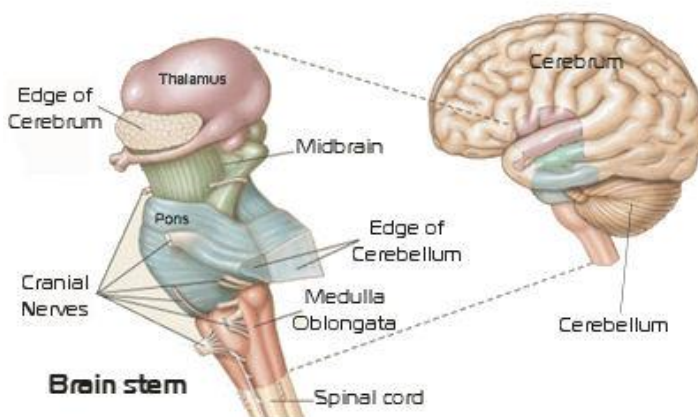


Figure 1.2-CNS main parts.

1.1 Cerebral cortex

The most developed and complex part of the human brain, that carry out high functions such as language, voluntary movements, learning and problem solving, is the telencephalon. The telencephalon is divided by a deep sulcus in two brain hemispheres (right and left) whose most external layer of neural tissue (grey

substance) takes the name of cerebral cortex. The cerebral cortex is greatly folded in order to contain a large surface area (half a square metre). Such irregular structure is the result of the particular evolution of primates, during which the volume of the brain increased faster than the volume of the skull, leading to the generation of a large number of grooves, called sulci, and convolutions, whose crests are called gyri. Gyri and sulci create the folded appearance of the brain in humans and other mammals but their shape and position varies from individual to individual. However, the presence of four sulci common to all individuals, two lateral and two central, allowed to divide the cerebral cortex of each hemisphere into four lobes: frontal, parietal, temporal and occipital (*fig. 1.3*).

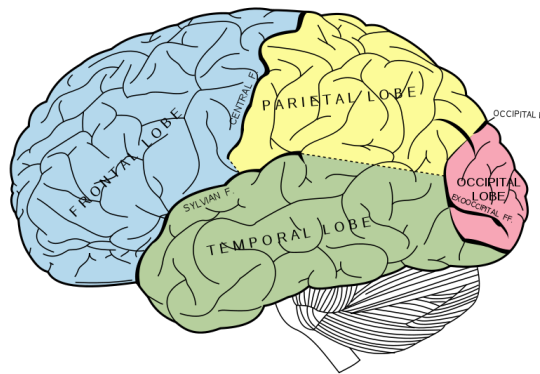


Figure 1.3-Macro-subdivision of the cerebral cortex (left hemisphere) into four lobes: frontal, parietal, temporal and occipital.

1.2 Brodmann areas

Each lobe is responsible to localized functions that can be identified in specific parts of the brain surface, called cortical areas. When these areas are damaged, it is possible to observe the degradation or disappearance of the corresponding functions. The most common classification of these cortical areas is the Brodmann's that divides the whole surface into 52 homogeneous areas on the basis of their histological structure. After a first identification of such areas, most of them have been associated with mental functions. For example, areas 1, 2 and 3 of the parietal lobe are related to somatosensory processes, areas 41 and 42 of the temporal lobe are related to auditory functions, areas 17 and 18 of the

occipital lobe are related to the visual system and area 4 is the primary motor area. A representation of some of the Brodmann areas is shown in *fig 1.4*.

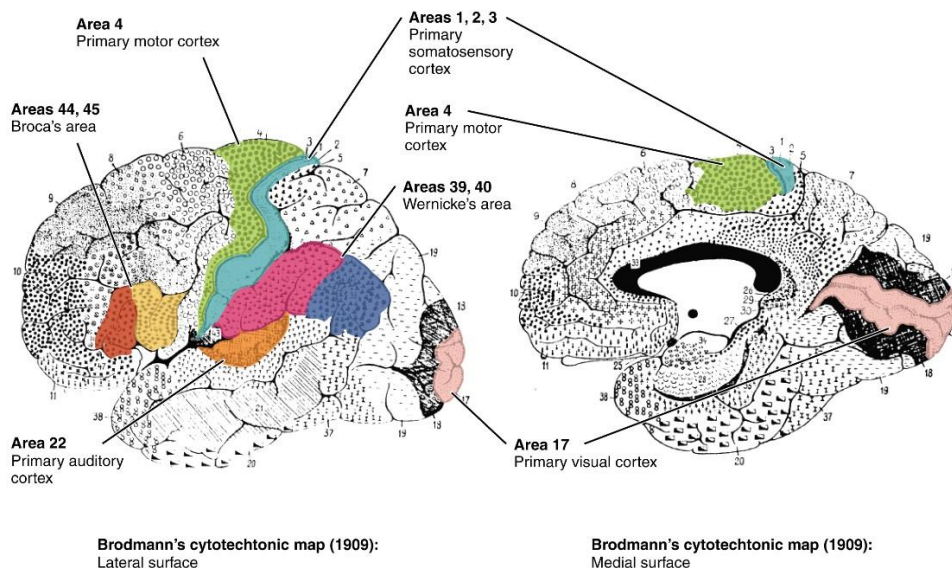


Figure 1.4 - Some of the most famous Brodmann areas.

Moreover, Dr. Wilder Penfield and his co-investigators Edwin Boldrey and Theodore Rasmussen introduced another important portrayal of the motor and cognitive functions associated to each cortex area: sensory and motor homunculi. In fact, they were the first to differentiate between sensory and motor function and to map the two across the brain separately, resulting in two different homunculi (see *fig. 1.5*). Their studies proved that areas of the nearby body are contiguous also on the cortex even if the various parts of the body are represented upside down vertically. The surface of the brain cortex attributable to the various parts of the body is not proportional to the size but rather to the possibilities of movement; for example hands, lips and tongue cover a much wider area of the thigh or trunk. When performing a voluntary movement, in a particular region of the cerebral cortex, a nervous impulse is generated which propagates through the CNS until it reaches the peripheral nerves responsible for the movement: the motor homunculus makes it possible to identify, for each movement, the cortical area in which the impulse was generated. About the sensory homunculus, recent

studies have improved the understanding of the somatosensory arrangement using techniques such as functional magnetic resonance imaging (fMRI).

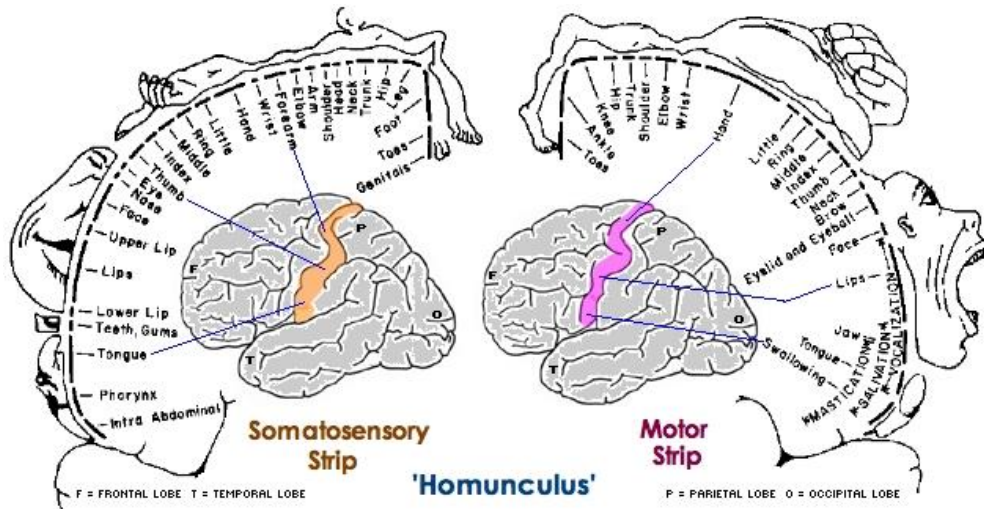


Figure 1.5 - 2D representation of the sensory (on the left) and motor (on the right) homunculi.

2. Neurons

2.1 Anatomy of the neuron

In the CNS there are two categories of cells: nerve cells called neurons and support cells or neuroglia usually called glial cells. The glial cells are supporting elements that provide shape and consistency to the nervous tissue. The neurons, on the other hand, are the primary components of the CNS. They are the basis of all the functional properties of the nervous system being excitable cells able to receive and transmit electrical impulses without attenuation and to process the received stimuli in specialized form. These signals between neurons occur via specialized connections called synapses. The neurons exist in a multitude of forms, all referable to a basic structure (*fig. 1.6*) consisting of a cellular body (soma), where the nucleus is located and from which the dendrites and axon depart. The dendrites are extensions, often short, numerous and ramified, responsible for

receiving the signal coming from other nerve endings. The axon, instead, is an isolated extension used for carrying the electrical signal that can be short or very long depending on the distance it has to reach. Several endings allow it to transmit the electrical impulse to more cells at the same time. All the characteristics of sensory experience and execution of movements, as well as thought processing, learning, language and any other mental activity, are possible thanks to the organization of neurons in complex networks.

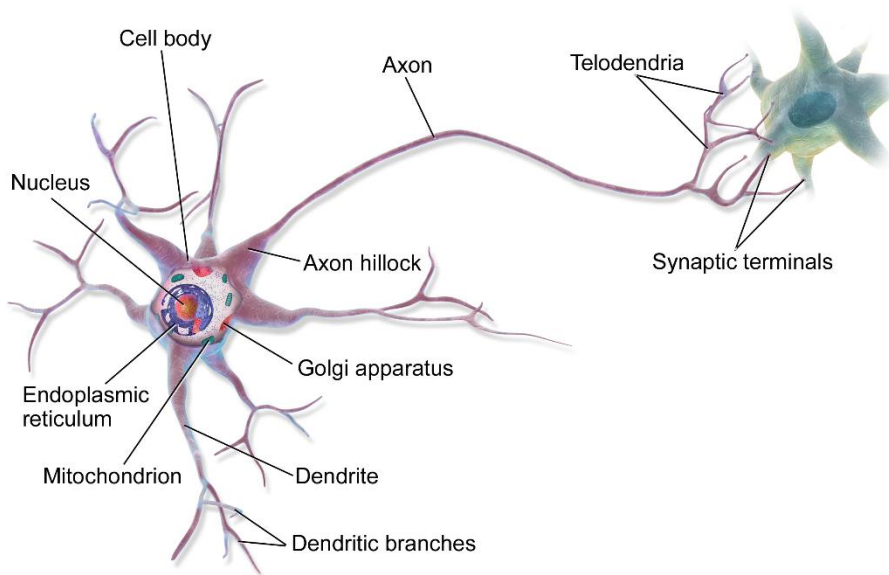


Figure 1.6 – Anatomy of a neuron.

At the cerebral cortex level, the two most important types of neurons are pyramidal cells and non-pyramidal cells. The first ones presents a large pyramidal bodies and apical dendrites crossing different cortical layers. They are always oriented perpendicular to the surface of the cortex. The electric fields generated by pyramidal cells are "open" fields that, if synchronous, can be added together and recorded by means of electrodes placed on the scalp (electroencephalography, EEG). In a similar way, the magnetic fields generated by the different pyramidal neurons are summed up and can be recorded by means of magnetoencephalography (MEG). Non-pyramidal cells are small, star-shaped and are often arranged radially or with random orientations with respect to the cortex

surface. The "closed" fields generated by them cannot add up and, therefore, the intra- and extra-cellular currents do not produce electric and magnetic fields outside. The possible contributions of such kind of cells cannot be unequivocally recognized.

2.2 Electrophysiology of the neuron

Every neuron is said to have "in small-scale, the integrative capacity of the entire nervous system". In fact, neurons can transform information and transmit it to other neurons. In most, the dendrite-cell body unit is specialized as a receptor and integrator of synaptic input from other neurons, and the axon is specialized to convey coded information from the dendrite-cell body unit to the synaptic junctions, where transformation functions take place with other neurons or effectors (muscles and glands). To serve these tasks, the neuron is thus organized into a receptive segment (dendrites and cell body), a conductive segment (axon), and an effector segment (synapse) (*fig. 1.7*). Neurons are specialized to generate electrical signals, which are then used to encode and convey information: these signals are expressed by alterations in the resting membrane potential. Voltage changes that are restricted to the sites where neurons are stimulated – or that are close to them - are called *graded potentials*. These ones can lead to the production of *action potentials (nerve impulses or spikes)*, which transmit information for substantial distances along an axon. Two forms of graded potential are *generator (receptor potentials)* and *synaptic potentials*. Generator potentials are evoked by sensory stimuli from the environment (both inside and outside the body). Information that passes from one neuron to another at synapses produces *synaptic potentials* in the postsynaptic neuron. The activity of either generator or synaptic potentials can elicit action potentials, which, in turn, produce synaptic potentials in the next neuron. Synaptic potentials elicited in effectors (skeletal muscle and glands) at synapses can result in the contraction of the muscle or emission of secretory product from a gland.

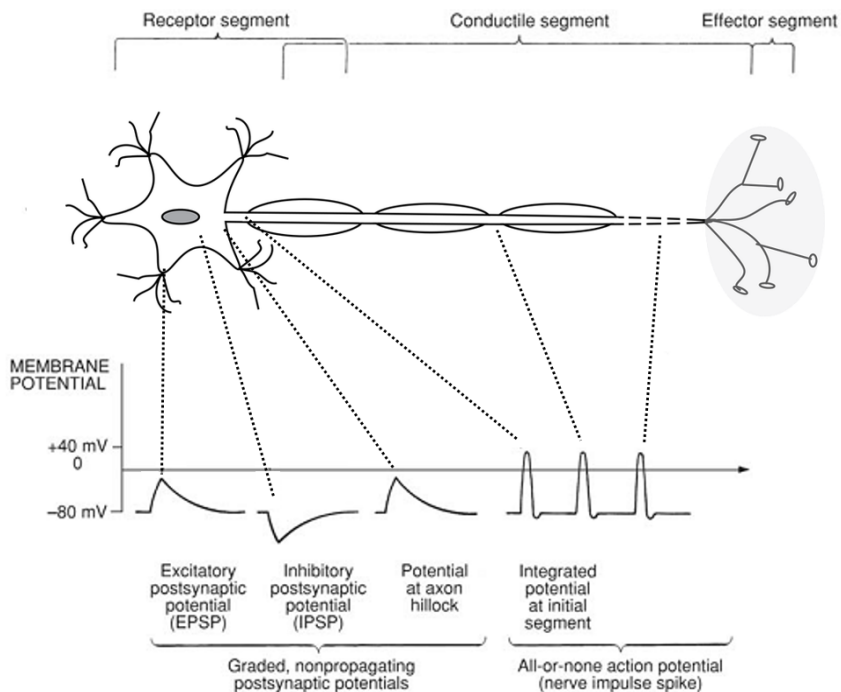


Figure 1.7 - On the surface of the dendrites and cell body are excitatory and inhibitory synapses, which, when stimulated, produce local, graded, non-propagating potentials. These are exhibited as an excitatory or depolarizing postsynaptic potential (EPSP) and as an inhibitory or hyperpolarizing postsynaptic potential (IPSP). These local potentials are summed at the axon hillock and, if adequate, could trigger an integrated potential at the initial segment and an “all-or-none” action potential, which is conducted along the axon to the motor end plate.

Resting Potential of the Neuron

The resting neuron is a charged cell that is not conducting a nerve impulse. The plasma membrane, which acts as a thin boundary between the extracellular (interstitial) fluid that is located outside the neuron and the intracellular fluid (neuroplasm) that is instead inside the neuron, is critical for maintaining this charged state or resting potential. The electric charge across the plasma membrane results from a thin film of positive and negative ions, unequally distributed across the membrane. These are sodium (Na^+) and chloride (Cl^-) ions (which are in higher concentration in the interstitial fluid), and potassium (K^+) and protein (organic) ions that are in higher concentration in the neuroplasm. A

tendency exists for the Na⁺, K⁺, and Cl⁻ ions to diffuse across the membrane from regions of high to low concentration (along concentration gradients), through Na⁺, K⁺, and Cl⁻ channels, respectively. The passage of ions across the membrane is known as *conductance*. Thus, the semipermeable plasma membrane is selectively permeable through non-gated open channels to Na⁺, K⁺, and Cl⁻ ions and impermeable to large protein ions. These channels, which are always open, are important in determining the resting potential. The ionic concentrations on either side of the membrane are produced and maintained by a system of membrane pumps called “the *sodium-potassium pump*”, which requires metabolic energy released by adenosine triphosphate (ATP). The sodium-potassium exchange pump is an integral membrane protein that utilizes ATP as an energy source for its role in *active transport*. This transport is an energy-dependent process in which the movement of Na⁺ and K⁺ ions is “uphill” against a concentration gradient. The activity of the pump results in the passage of three Na⁺ ions out of and two K⁺ ions into the neuron. This causes the restoration of a concentration of K⁺, 30 or more times higher within the neuroplasm than in the interstitial fluid, and in a concentration of Na⁺ that is 10 times and Cl⁻ that is 14 times higher in the interstitial fluid than in the neuroplasm. Most neurons do not have a Cl⁻ pump; hence, Cl⁻ ions diffuse passively across the membrane. These are the ionic concentrations responsible for establishing an electric potential across the membrane. The transmembrane potential, known as the *resting potential*, is about -70 to -80 (mV) (millivolts) inside the neuron. The resting potential is in a steady state (*dynamic equilibrium*) requiring metabolic energy to maintain the ionic gradients across the membrane. When the neuron is “at rest,” its membrane potential is the result of a balance (involving Na⁺ and K⁺ ions) between the active fluxes (movements) of ions metabolically driven by *pumps* and the passive fluxes caused by *diffusion*. The active fluxes result from the pump extruding three Na⁺ ions for every two K⁺ ions it brings into the neuron. The passive fluxes of ions take place through non-gated channels. The outward flux of positive charges by the pump tends to hyperpolarize the membrane. The greater the hyperpolarization, the greater the inward electrochemical force driving Na⁺ into the neuron, and the smaller the force driving K⁺ out. The steady state for the neuron is attained when

the resting potential is reached at the point when the net passive inward current (movement of electrical charge) through the ion channels exactly counterbalances the active outward current driven by the pump. The steady state is not basically the result of *passive diffusion*, which is the diffusion of a solute down a concentration gradient without the expenditure of energy.

Excitability of the Neuron

Excitability is a property that enables a neuron to respond to a stimulus and to transmit information in the form of electrical signals. The flow of information within a neuron and between neurons is conveyed by both electrical and chemical signals. The electrical signals, called *graded potentials* and *action potentials*, are all produced by temporary changes in the current flow into and out of the neuron - changes that are actually deviations from the normal value of the resting membrane potential. Ion channels within the plasma membrane control instead the inward and outward current flow. The channels have three features: (1) they conduct ions across the plasma membrane at rapid rates up to 100,000,000 ions per second; (2) they can recognize specific ions and be selective as to which can pass through; (3) they can selectively open and close, in response to specific electrical, chemical, and mechanical stimuli. Each neuron is presumed to have over 20 different types of channel with thousands of copies of each channel. The flux (movement of ions) through the ion channels is passive, requiring no expenditure of metabolic energy. The flux direction is determined by the electrochemical driving force across the plasma membrane, and the primary role of the ion channels in the neurons is to mediate rapid signalling. These channels, called *gated channels*, have a molecular "cap" or *gate*, which briefly opens to permit anion species to pass. Gated channels open when a neurotransmitter binds to them; *voltage-gated channels* open and close in response to changes in membrane potential; *modality-gated channels* are activated by specific modalities (e.g., touch, pressure, or stretch). Gating is the process by which a channel is opened or closed during activity. Each channel consists of several plasma membrane-spanning polypeptide subunits (proteins) arranged around a central pore. Each of these classes of channel belongs to a different gene family. Each member of a family shares common structural and biochemical features, which

presumably have evolved from a common ancestral gene of that family. The channels of the voltage-gated gene family are selective for Na⁺, K⁺, and Ca²⁺ ions. The channels for the transmitter-gated channels respond to acetylcholine, gamma amino butyric acid (GABA), and glycine. Most gated-channels are closed with the membrane at rest: they open when activated, following the binding of a ligand (ligand gating), a change in the membrane potential (voltage gating), or the stretch of the membrane (modality gating). In the transmitter-gated channel, the transmitter binds to a specific site on the external face of a channel that activates it to open briefly. The energy to open the channels is derived from three sources: (1) from the binding of the transmitter to the receptor protein in the ligand-gated channels; (2) from the changes in the membrane voltage within the voltage-gated channels; (3) presumably, from the mechanical forces resulting from cytoskeletal interaction at the modality-gated channels. There are two types of membranes response: (1) *hyperpolarization* or (2) *depolarization*. During the *first phase*, the membrane becomes more negative on the inside with respect to its outside (i.e., could go from -70 (mV) to -80 (mV)). During *depolarization*, the membrane becomes less negative inside with respect to its outside and it might even reverse polarity with its inside - becoming positive with respect to the outside. This is still called *depolarization* because the membrane potential becomes less negative than the resting potential (e.g., from -70 (mV) to 0 to +40 (mV)).

3. Electroencephalography (EEG)

3.1 EEG generation and recording

The *electroencephalogram* (EEG) comes from the summation of synchronously postsynaptic potentials. The contribution to the electric field of neurons acting synchronously is approximately proportional to their number, and, for those firing non-synchronously, as a square root of their number (Blinowska and Durka, 2006). The problem of the origins of EEG rhythmical activity has been approached by electrophysiological studies on brain nerve cells and by the modeling of electrical activity of the neural populations (Lopez da Silva, 1996; Freeman, 1991).

The question emerges whether the rhythms are caused by single cells with pacemaker properties or by the oscillating neural networks. It has been shown that some thalamic neurons display oscillatory behaviour, even in the absence of synaptic input (Jahnsen and Linas, 1984). Evidence exists that the intrinsic oscillatory properties of some neurons contribute to the shaping of the rhythmic behaviour of networks to which they belong. However, these properties may not be sufficient to account for the network rhythmic behaviour. It is generally accepted that cooperative properties of networks consisting of excitatory and inhibitory neurons connected by feedback loops play the crucial role in establishing EEG rhythms. The frequency of oscillation depends on the intrinsic membrane properties, on the membrane potential of the individual neurons, and on the strength of the synaptic interactions. Bursts of oscillatory activity may constitute a mechanism by which the brain can regulate changes of state in selected neuronal networks and change the route of information (Lopez da Silva, 1996). EEG is usually registered by means of electrodes placed on the brain scalp. They can be secured by an adhesive (like *collodion*) or embedded in a special snug cap. The resistance of the connection should be less than 10 (k Ω), so the recording site is first cleaned with diluted alcohol, and conductive electrode paste applied to the electrode cup. Knowledge of exact positions of electrodes is very important for both interpretation of a single recording as well as comparison of results, hence the need for standardization. The traditional *10–20 electrode system* (EEG montage showed in *fig. 1.8*) states positions of 19 EEG electrodes (and two electrodes placed on earlobes A1/A2) related to specific anatomic landmarks, such that 10 – 20% of the distance between them is used as the electrode interval. The first part of derivation's name indexes the array's row—from the front of head: Fp (Fronto-parietal), F (Frontal), C (Central), P (Parietal), and O (Occipital). The second part is formed from numbers even on the left and odd on the right side, and from “z” in the centre. Progress in topographic representation of EEG recordings brought demand for a larger amount of derivations. Electrode sites halfway between those defined by the standard 10 – 20 system were introduced in the extended 10 – 20 system [21]. EEG is a measure of potential difference; in

the referential (or unipolar) setup, it is measured relative to the same electrode for all derivations. This reference electrode is usually placed on the earlobe, nose, mastoid, chin, neck, or scalp centre.

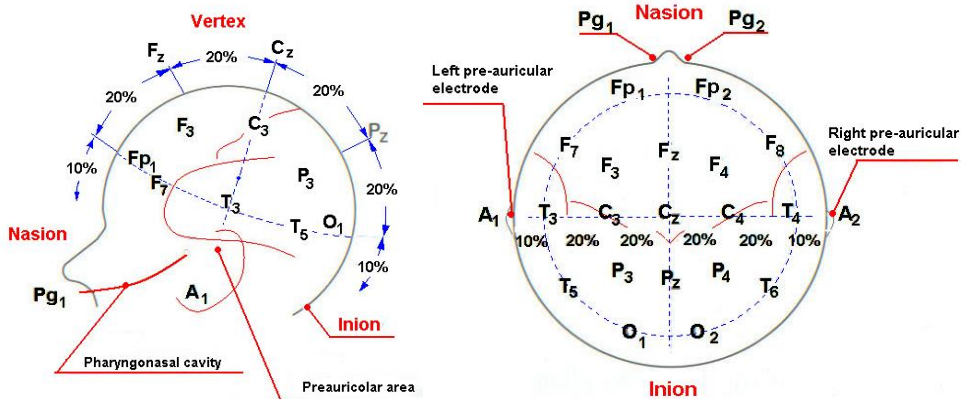


Figure 1.8 - 10-20 electrode system.

The first part of derivation's name indexes the array's row—from the front of head: Fp (Fronto-parietal), F (Frontal), C (Central), P (Parietal), and O (Occipital). The second part is formed from numbers even on the left and odd on the right side, and from "z" in the centre. Progress in topographic representation of EEG recordings brought demand for a larger amount of derivations. Electrode sites halfway between those defined by the standard 10 – 20 system were introduced in the extended 10 – 20 system[21]. EEG is a measure of potential difference; in the referential (or unipolar) setup, it is measured relative to the same electrode for all derivations. This reference electrode is usually placed on the earlobe, nose, mastoid, chin, neck, or scalp centre. No universal consent exists regarding the best position of the reference electrode, because currents coming from bioelectric activity of muscles, heart, or brain propagate all over the human body. In the bipolar setup (montage), each channel registers the potential difference between two particular scalp electrodes. Data recorded in a referential setup can be transformed into any bipolar montage. The common "average reference" montage can be obtained by subtracting from each channel the average activity from all the remaining derivations. The *Hjorth* transform references each electrode to the four closest neighbours, which is an approximation of the *Laplace transform* (LT). LT

is calculated as a second spatial derivative of a signal, offering information about vertical current density. For best performance, it needs an adequate spatial sampling-inter electrode distance around 20 (mm) (e.g., 128 electrodes on the scalp). The estimates obtained by means of LT for the electrodes lying at the scalp periphery are biased and have to be excluded. Therefore, the study of the cortical activity through the analysis of EEG potentials presents the limit to depend from the quality of the recorded data, from the selected electrodes montage and from the reference used. Any variations in the electrical potential adopted as reference for the recording of potentials on the scalp, in fact, can attenuate or obscure some cortical generators, acting, therefore, as a factor of spatial-temporal disturbance. Moreover, the potentials recorded on the scalp are not only attenuated, but also distorted and diffused due to the different electrical conductivity that tissues (liquors, meninges, skull and scalp) present when currents pass through. As result of the phenomena of spatial distortion induced by the anatomical structures of the head, the distribution of potential on the scalp presents a low spatial resolution, which does not allow a reliable localization of cortical generators of potentials. Such problem, well-known as “volume conduction effect”, the EEG signal is generally a potential that results from the sum of signals from different cortical and subcortical regions. The potential recorded by a certain electrode site, therefore, is not generated only by the underlying cortical source. It has been quantified, by simulations, that sources distributed in a radius of 3 cm below the electrode position contribute only 50% to the power measured by the electrode itself, while 90% can be reached by considering sources up to 6 cm distant. The explained distortion phenomena produces an increase in the low spatial frequencies of the potentials measured on the scalp (spatial blurring). For all the reasons, conventional analysis of spontaneous EEG activity or potential event-related events, performed by means of recordings from 20÷30 sensors, generally offers a spatial resolution in the order of 6÷7 cm, which is at least of an order of magnitude worse than the spatial resolution of other commonly available techniques, such as PET or fMRI. Increased spatial resolution in the study of EEG potentials cannot be achieved by simply increasing the number of sensors on the scalp. In fact, adequate electrode sampling of the potential on the scalp solve the

problem of the spatial aliasing phenomena during data acquisition but does not solve the problem of distortion and attenuation of potential distributions caused by low conductivity anatomical structures. A significant increase in spatial resolution of the EEG potentials recorded on the scalp can be obtained by using the technology indicated by the name of high density electroencephalography (hd-EEG) that include from 64 to 128 sensors placed on the scalp (see *fig. 1.9*). The recorded data are then processed by specific algorithms able to reduce the attenuation effects induced by low conductivity structures on the head. This last processing step, called *spatial deblurring* or *source reconstruction*, greatly improves performance when realistic head volume models obtained from the processing of magnetic resonance imaging (including scalp, skull, dura-mother and cerebral cortex models) are employed. This theme will be treated in a more exhaustive way in *Chapter 4*.

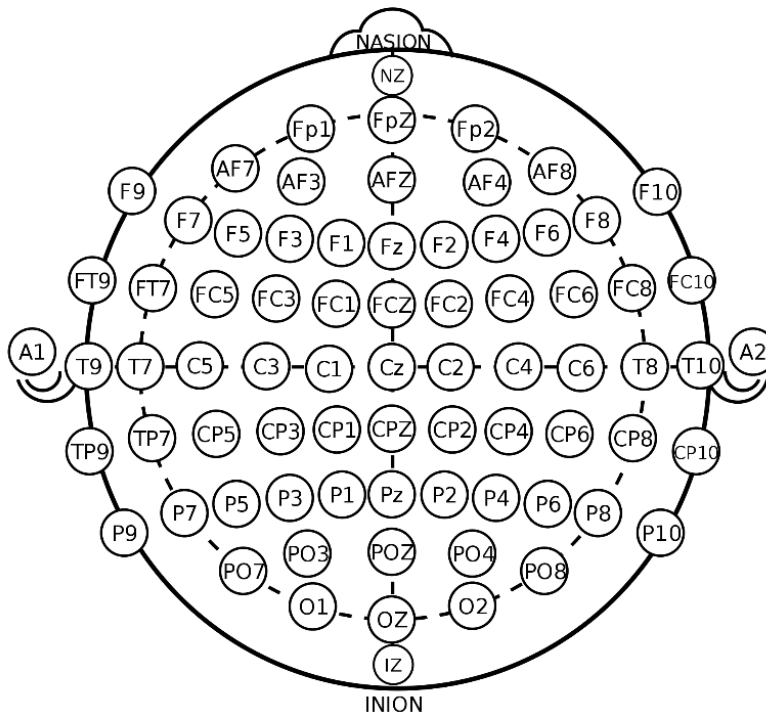


Figure 1.9 – 60-channels EEG montage

3.2 EEG artifacts

Artifacts are recorded signals that are non-cerebral in origin. Contrary to the open question of the reference, the necessity of artifact rejections is universally acknowledged. They may be divided into one of two categories depending on their origin: *physiological artifacts* or *non-physiological artifacts*. Physiological artifacts can stem from muscle or heart activity (EMG, ECG), eye movement (EOG), external electromagnetic field, poor electrode contact, subject's movement. Corresponding signals (EMG, EOG, ECG, and body movements) registered simultaneously with EEG could be helpful in the visual rejection of artifact-contaminated epochs. Non-physiological artifacts arise from two main sources: external electrical interference (power lines or electrical equipment), and internal electrical malfunctioning of the recording system (electrodes, cables, amplifier). The most problematic artifact for the EEG analysis is certainly the EOG. The EOG measures the electrical activity produced by eye movement, whose amplitude is usually high enough to be detected with EEG. The intensity of the signal recorded by EEG electrodes depends directly on the distance between the eyes and the electrodes. For that reason, movements are primarily picked up by the frontal electrodes, although they also extend further. The strength of the interference depends also on the direction in which the eye is moving. The eye movements, called saccades have a particular waveform which can be easily recognized even by visual inspection. Blinking also contaminates the EEG recording, usually with a change more rapid than that produced by eye movement, which is associated with higher frequency interference. Moreover, the amplitude of the blinking artifact is generally much larger than that of the background EEG activity [22]. The first techniques which artifacts were eliminate with, were for sure the regression algorithms, which were adopted up to the mid-1990s, especially for ocular interferences, thanks to their simplicity and reduced computational demands. Artifacts may be corrected by subtracting a regressed portion of each "interference" channel from the contaminated EEG. Regression may be done either in the time or frequency domain, by estimating the influence of the reference waveforms on the signal of interest. One hypothesis required by linear regression is that each EEG channel is the sum of the non-noisy source signal and

a fraction of the source artifact that is available through a reference channel. At this point, the regression tries to estimate the fraction of how much each EEG channel is contaminated by the reference channel, that is like a propagation fraction. Correction is then performed by subtracting the regressed portion(s) of the EOG reference waveform(s) from each EEG channel, resulting in an estimation of artifact-free measurements in the scalp. The problem is that many techniques which are based on the linear regression doesn't take into account the bidirectional interference between EEG signal and EOG signal. Therefore, when correction is performed, a useful part of the signal could be removed. In order to overcome this issue authors referred that a possible solution could be to low pass the EOG. This is supported by some studies that argue that most high frequency content in the EOG is of neural origin [23]. However, others argue that in fact all frequency bands (alpha, beta, delta and theta) are contaminated. Regression methods have been replaced by more sophisticated algorithms primarily because the former need one or more reference channels. Since other potentially more efficient algorithms (e.g. those based on blind source separation) emerged, like Principal Components Analysis (PCA) and Independent Component Analysis (ICA) that have become commonplace in most recent publications, regression has no longer been the default choice for EOG or ECG removal of artifacts from an EEG. Blind source separation (BSS) estimates the sources from the recorded EEG signal without the need for a reference waveform for either the desired signal or the unwanted artifacts, using only the information contained in all the electrodes. The effectiveness of BSS techniques is subjected to various assumptions, thus there are some hypothesis to be respected: uncorrelatedness, independence, non-Gaussianity, instantaneous propagation, linearity, etc. One of the most widely used BSS algorithm is the so called independent component analysis (ICA). Independent component analysis comprises several related methods for unmixing linearly mixed signals using only recorded time information, by imposing statistical independence of the sources. The frequently used ICA algorithms are based on exploiting high order statistics (HOS). HOS-ICA approaches find a linear transformation for the estimated sources to be as independent as possible. ICA

accuracy critically depends both on source independence and on the amount of available data.

3.3 EEG frequency rhythms

In the EEG, the following frequency rhythms are considered characteristic for its analysis (see their topology in *fig. 1.10*): delta (0.5 – 4 (Hz)), theta (4 – 8 (Hz)), alpha (8 – 12 (Hz)), beta (12 – 30 (Hz)), and gamma (above 30 (Hz)).

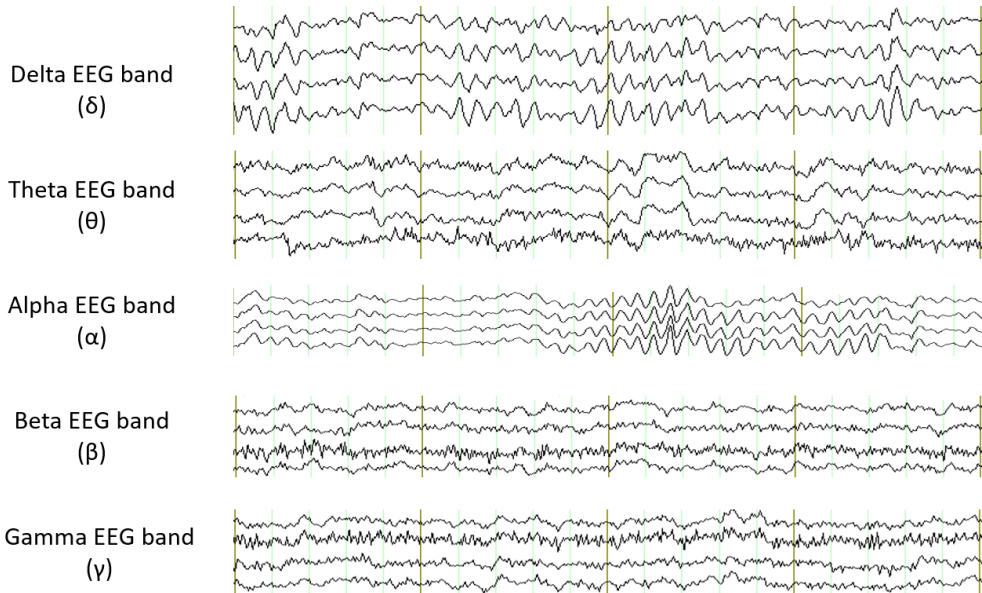


Figure 1.10 - Characteristic EEG rhythms, from the top: δ (0.5 – 4 (Hz)), θ (4 – 8 (Hz)), α (8 – 12 (Hz)), β (12 – 30 (Hz)). The gamma band could reach 100 (Hz).

Delta activity is characterized by high amplitude and low frequency. It is usually associated with the slow-wave in psychophysiology of sleep. It is suggested that it represents the onset of deep sleep phases in healthy adults. Theta rhythm is generally linked to the hippocampus activity as well as neocortex [24], [25]. It is thought to be linked to deep relaxation or meditation [26], and it has been observed during the transition between wake and sleep [27]. Moreover, theta rhythms are suggested to be important for learning and memory functions which involve high concentration [27], [28]. It has also been suggested that theta

oscillations are associated with the attentional control mechanism in the anterior cingulate cortex [26], [29], and it is often shown to increase with a higher cognitive task demand [30]. Alpha activity has been found in the visual cortex (occipital lobe) during periods of relaxation or idling (eyes closed but awake). In the continuous EEG, alpha band is characterized by high amplitude and regular oscillations, in particular over parietal and occipital areas. High alpha power has been assumed to reflect a state of relaxation or cortical idling; however, when the operator assigns more effort to the task, different regions of the cortex may be recruited in the transient function network leading to passive oscillation of the local alpha generators, in synchrony with a reduction in alpha power [29]. Recent results have suggested that alpha is involved in auditory attention processes and the inhibition of task irrelevant areas to enhance signal-to-noise ratio [31], [32]. Additionally, alpha activity may be further divided into sub-bands by means of the frequency corresponding to the alpha peak of the user, called *Individual Alpha Frequency* (IAF) [33]. For instance, *alpha 3* ($IAF \div IAF + 2$ (Hz)) reflects semantic memory performance, while *alpha 1* and *alpha 2* (respectively, $IAF - 4 \div IAF - 2$ and $IAF - 2 \div IAF$ (Hz)) reflect general task demands and attentional processes. Beta activity is predominant in wakefulness state, especially in frontal and central areas of the brain. High power in beta band is associated with the increased mental arousal and activity. Dooley, in 2009 pointed out that beta wave represents cognitive consciousness and active, busy, or anxious thinking. Furthermore, it has been revealed to reflect visual concentration and the orienting of attention [34]. This band can be further divided into *low beta wave* (12.5-15 (Hz)), *middle beta wave* (15-18 (Hz)), *high beta wave* (> 18 Hz). Low waves seem to be associated with inhibition of phasic movements during sleep, and high waves with dopaminergic system (Hagemann, 2008). Finally, Gamma is the fastest activity in EEG and it is thought to be infrequent during waking states of consciousness [34]. Recent studies reveal that it is linked with many cognitive functions, such as attention, learning, and memory [35]. Gamma components are difficult to record by scalp electrodes, because of their low amplitude, but with *Electrocorticography* (ECoG) components up to 100 (Hz), or even higher, may be registered. The contribution of different rhythms to the EEG depends on the age, psycho-cognitive

state of the subject, and level of alertness. Considerable inter - subject differences in EEG characteristics also exist, since EEG pattern is influenced by neuropathological conditions, metabolic disorders, and drug action. As showed in *fig. 1.11*, alpha and beta pics are really easy to identify in a typical EEG trace.

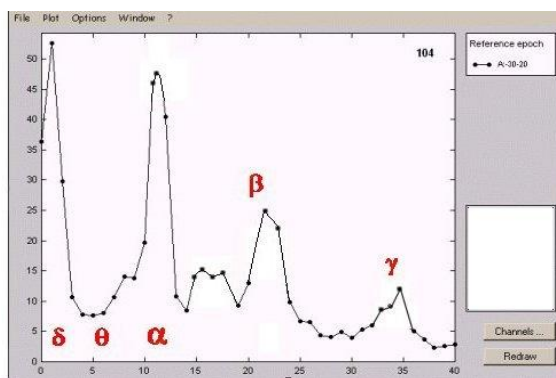


Figure 1.11- EEG power spectrum

3.4 Event-Related Potential (ERP)

Accepted that there is a basic brain activity and that variations in some parameters such as amplitude and fundamental frequency can be correlated with different mental states, it is possible to study EEG responses related to external (e.g. sensory stimuli) or internal (e.g. execution of movements) events. Such events can be detected because they induce two types of variations:

- a realignment of the phase (re-phase) of the signal with respect to the event.
- variations in signal amplitude at different frequencies.

As mentioned above, the EEG variations are dynamic and have a limited duration. The two processes can therefore take place simultaneously and represent only two aspects of the same physiological phenomenon, or they can take place in different moments. The Evoked Potential (EP) or more properly the Event-Related Potential (ERP) consists of a specific change in EEG resulting from stimulation of a sensory pathway or motor event. One of the main characteristics of ERPs is certainly the close temporal relationship between stimulation and response to the

stimulus itself. The variations produced by the external event (whether a visual, acoustic or movement stimulus) always occur at a fixed distance in time (latency) with respect to the event of interest. The temporal relationship between stimulus (or movement) and oscillatory activity is very stable and extremely repeatable if multiple stimulations are performed. Both processes (re-phasing and power increase) can affect only a few frequency bands, but generally, in ERPs, the entire spectrum from 4-6 Hz to 60-70 Hz is affected. Generally, the fastest oscillations (higher frequencies) occur in the instant just after the stimulus, and the ERP signal slows down and returns to background levels further away from the event. Several ERP components are showed in *fig. 1.12*.

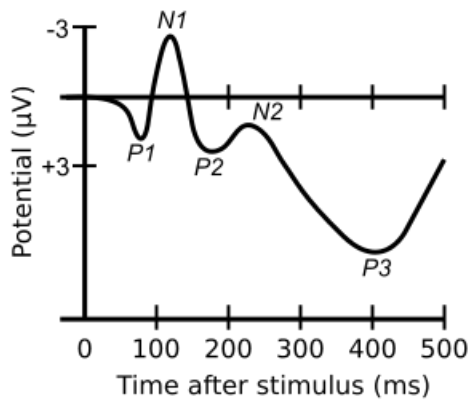


Figure 1.12 – Representation of several ERP components, including the most famous N100 and P300.

Chapter 2

Generation of simulated EEG data

1. Introduction

In the last years, the interest in connectivity estimation has been growing, especially in the world of neuroscience [1]–[5]. Its potentiality is given by the opportunity to understand which brain areas are mainly involved in the execution of motor or cognitive tasks and, mostly, how they communicate to create the networks underlying a specific cerebral function. Several connectivity estimators with different peculiarities have been developed to assess the existence, the intensity and the direction of the statistical connections linking two or more time series. Some of them are characterized by a high versatility since they can be applied to signals acquired through different techniques, fMRI, EEG or MEG, on the basis of the specific applicative aims [6], [7]. Among all the approaches used for connectivity estimation, worth of note is the class of estimators based on the theory of causality developed by Wiener in 1965 and translated in a mathematical object by Granger in 1969, according to which an observed time series $x(n)$ cause, with a statistical meaning, another series $y(n)$ if the knowledge of $x(n)$'s past significantly improves prediction of $y(n)$ [8]. This kind of relationship could be biunivocal but not reciprocal (i.e., $x(n)$ may cause $y(n)$ without $y(n)$ causing $x(n)$); for this reason, such estimators are able to determine the direction of the influence between any given pair of signals. The framework of connectivity estimators is a manifold scenario where the selection of the appropriate algorithm on the basis of the research objectives is often a really hard job. For this reason, several studies tried to compare the performances of already existing algorithms under different experimental conditions with the aim to provide some guidelines to help researchers in orienting themselves in such intricate world. Moreover, every time a new algorithm is defined and implemented, an initial testing phase where it is compared to already existing approaches is required. In both cases, the

comparison is always made on the basis of simulated data reproducing a pre-defined connectivity pattern, which can be used as test bench for the algorithms. The generation of such simulated data represents the weak point of such testing approach since the results of the comparisons between algorithms could be strongly influenced by the data used as reference. In particular, critical aspects of data generation concerned i) the way in which the ground-truth network is defined since a lot of parameters have to be chosen (number of nodes, network density, structural properties, presence of clusters) and ii) the approach used for reconstructing signals since it has to provide data reproducing the main properties of real ones. As for the EEG case, simulated data should reproduce the spectral and topological properties of signals really acquired on the scalp otherwise the test might provide results on algorithms performances which could be contradicted on real data.

The simulated EEG data generation is an issue which recently is gaining more and more importance since it really might impact on the quality of connectivity estimates made on real data. The first attempts in such field referred to the employment of time series i) generated from known linear toy models whose equations are designed so that the first signal behaves as an oscillator driving the other structures [17], [36] or ii) obtained by means of MVAR generator filters where white noise is given as input and the coefficients are manually imposed [37], [38]. The signals generated through these two approaches do not present any properties of realistic data. In order to generate more realistic time series, a cascade approach has been proposed where a real EEG signal is selected as source and all the other signals are iteratively obtained from it according to a ground-truth connectivity scheme also imposing a predefined signal-to-noise ratio [2], [5]. Such approach, even if reproducing the spectral properties of EEG signals, cannot be employ to generate datasets with high number of signals since the cascade, if repeated many times, let to an incontrollable increase of the signals amplitude. More recently, the advancements in the field led to the development of ready-to-use and free toolboxes devoted to the connectivity estimation that also provide functions for the simulated data generation for the validation phase. This is the case of Barnett and Seth who developed in 2014 a toolbox, called Multi Variate

Granger Causality (MVGC) toolbox, returning simulated multi-trial data from normally distributed residuals, for given VAR parameters, as test dataset for the proposed causal connectivity estimators [39]. Moreover, few months ago Haufe and Ewald proposed a toolbox for the generation of pseudo-EEG data (with an imposed directed interaction) in which the time courses of two distinct sources at cortical level are modeled using bivariate linear autoregressive models [40]. Both toolboxes, even if promising, present, as already stated by the proposers in the discussion of the related papers, some limitations. The MVGC toolbox is easy-to-use and allows to generate datasets potentially including high number of signals but the simulated signals have not the spectral properties of EEG signals. Moreover, it is not possible to modulate the SNR of the simulated data. The Haufe and Ewald's toolbox allows to simulate pseudo-EEG data including EEG-like spectral properties and spurious effects due to volume conduction, but the model is too simple since it includes only two signals. The relationship between the two signals is not bidirectional and no ground-truth network is available for data at scalp level. The reason for which we would like to give a contribution in this field is that currently the possibility to generate simulated data reproducing more realistic experimental conditions is still lacking. In particular, simulated data should reproduce datasets derived from high density EEG recordings characterized by at least 60 channels, all having the same spectral properties of real EEG signals. Data should be organized as a long single-trial recording or a multi-trial recording, main artifacts such as eye-blinks should be included. Moreover, the ground-truth applied should have a dependence on time since connectivity patterns are not static events to be investigate as a single frame.

In this work we introduce a new toolbox, SEED-G, that allows to generate realistic simulated data with the same spectral properties of EEG (or ECoG) signals and with the possibility to set a whole series of parameters which make the dataset as close as possible to the user's necessities. In particular, the user can choose the features of the signals to be generated such as the number of samples, the number of trials composing the dataset, the signal to noise ratio, the inclusion or not of non-idealities (inter-trials variability) or artifacts (ocular blink). Moreover, the toolbox allows to set the features of the imposed connectivity pattern (number of

nodes, density of the pattern and behavior along time) in order to obtain a ground-truth in so many different interesting and not yet investigated experimental conditions. The SEED-G toolbox was developed in MATLAB environment. All codes and materials necessary for the pseudo-EEG data generation will be made available to the community.

2. Methods

2.1 Multivariate Autoregressive Modeling (MVAR)

MVAR models are linear, discrete-time and time-invariant mathematical models able to predict the future instant of N inputs, with $N > 2$ (*multivariate, MV*), using a linear regression (*autoregressive, AR*). Let y be a set of m time series with N samples and

$$\mathbf{y}(n) = [y_1(n), y_2(n), \dots, y_m(n)]^T \quad (2.1)$$

is the vector containing the n -th sample of the m signals belonging to the dataset. The MVAR model with order p is defined as:

$$\mathbf{y}(n) = - \sum_{k=1}^p \mathbf{A}(k) \mathbf{y}(n-k) + \mathbf{u}(n) \quad (2.2)$$

Where $\mathbf{A}(k)$ is the coefficient matrix at delay k , and p is the number of temporal instants preceding the sample n , involved in the prediction, what is called optimal MVAR order. The order of the model is usually chosen by means of the *Akaike Information Criteria* (AIC) for MVAR processes. $\mathbf{u}(n)$ is a vector of multivariate zero-mean uncorrelated white noise processes; it is very important because if $\mathbf{u}(n)$ was zero all the time, then the MVAR process $\mathbf{y}(n)$ would also be zero. For this reason, $\mathbf{u}(n)$ is also called the *innovation process*. MVAR models describe (estimate) the value of each temporal series at instant n as linear combination of the p preceding values of all the others inputs with weights given by the model

coefficients \mathbf{a}_{ij} . Equation 2.2 can be transformed to the frequency domain in the following matrix form:

$$\mathbf{A}(f)\mathbf{Y}(f) = \mathbf{U}(f) \quad (2.3)$$

where $\mathbf{A}(f)$ represents the frequency transform of the vector of parameters $\mathbf{A}(k)$ along the considered p lags, and the element A_{ij} is the transfer function between the i -th input and the j -th output of the MVAR linear predictor defined as:

$$A_{ij}(f) = \sum_{k=0}^p \mathbf{a}_{ij}(k) e^{-j2\pi f T k} \quad (2.4)$$

Equation 2.3 can be even written as:

$$\mathbf{Y}(f) = \mathbf{A}^{-1}(f)\mathbf{U}(f) = \mathbf{H}(f)\mathbf{U}(f) \quad (2.5)$$

The new obtained equation can be seen as a model of how the observed values $\mathbf{Y}(f)$ have been generated. $\mathbf{H}(f)$ is the transfer matrix of the MVAR generator filter.

2.2 Partial Directed Coherence (PDC)

Partial Directed Coherence (PDC) [41] is a spectral measure to assess the dynamical influence between signals within a multivariate dataset. It is basically a frequency version of the concept of Granger causality [42]. PDC is defined squared and normalized as follows:

$$\pi_{ij}(f) = \frac{|\mathbf{A}(f)_{ij}|^2}{\sum_{k=1}^N |\mathbf{A}_{ik}(f)|} \quad (2.6)$$

PDC values fall in the range $[0, 1]$, where $\pi_{ij}(f)=0$ stands for the absence of a direct influence from x_i to x_j at the considered frequency f . PDC only estimates the direct influence between two signals, thus discounting for indirect effects of other channels in a similar way as pairwise-conditional GC. The definition has been

subsequently refined with the introduction first of a row-wise normalization [43]:

$$\pi_{ij}^{row}(f) = \frac{A_{ij}}{\sqrt{\sum_{k=1}^N A_{ik}(f)A_{ik}^*(f)}}, \quad (2.7)$$

then of a quadratic version, so that the new squared and normalized PDC can be interpreted as the portion of the i^{th} signal power density due to the j^{th} one:

$$sPDC_{ij}^{row}(f) = \frac{|A_{ij}(f)|^2}{\sum_{k=1}^N |A_{ik}(f)|^2}. \quad (2.8)$$

2.3 Simulated EEG Data Generation

In SEED-G toolbox, the generation of pseudo-EEG data with a well-known ground-truth network is performed using MVAR models as generator filters providing a benchmark for testing new and existing connectivity methodologies. Figure 2.1 reports a block diagram that synthesizes the simulated EEG data generation process, including the following steps:

1. *Ground-truth model generation.* If not provided by the user, the toolbox firstly generates weighted directed connectivity matrices to be used as ground-truth for simulated data. In particular, such matrices are built by assigning values randomly selected within an imposed range to some specific connections. All the other links are set to zero. In order to obtain simulated signals with the same spectral properties of EEG data, real sources are included in the model. In particular, on the basis of users' preferences, the toolbox randomly includes in the main diagonal of the model some AR components randomly extracted from real signals (scalp or cortical level) acquired during resting condition in healthy subjects. In this first phase, the parameters to be set are: the number of signals to be generated (NODES), the amount of connections imposed in the ground-truth network (DENSITY), the number and type (scalp or cortex signals)

of real sources included in the model (EEG-SOURCES). Moreover, the user can choose to introduce an additive real source in correspondence of isolated nodes in the network.

2. *Time series generation.* After ground-truth network generation, the toolbox employs the MVAR as generator filter to provide the corresponding simulated dataset. As input, the MVAR receives uncorrelated, zero mean innovation noise simulated through number series extracted from the normally distributed pseudorandom generator. The covariance of the innovation process is set equal to the identity matrix. In order to obtain signals as realistic as possible, the toolbox allows then to sum an additive noise whose amplitude is set so that the ratio between squared amplitudes of signal and noise processes satisfied a desired SNR value, and the ocular component (EOG signal) simulating the blink effect. In this second phase, the user can set the following parameters: number of data samples for each realization (SAMP), number of realizations to be generated (TRIALS) and SNR values (SNR). For each generated realization, an amplitude check is performed taking into account that EEG signals are usually lower than 80 (μV). Every time the amplitude of generated signals overcomes such threshold, the realization is deleted and its generation repeated. After an imposed number of unsuccessful attempts, the starting model is replaced.

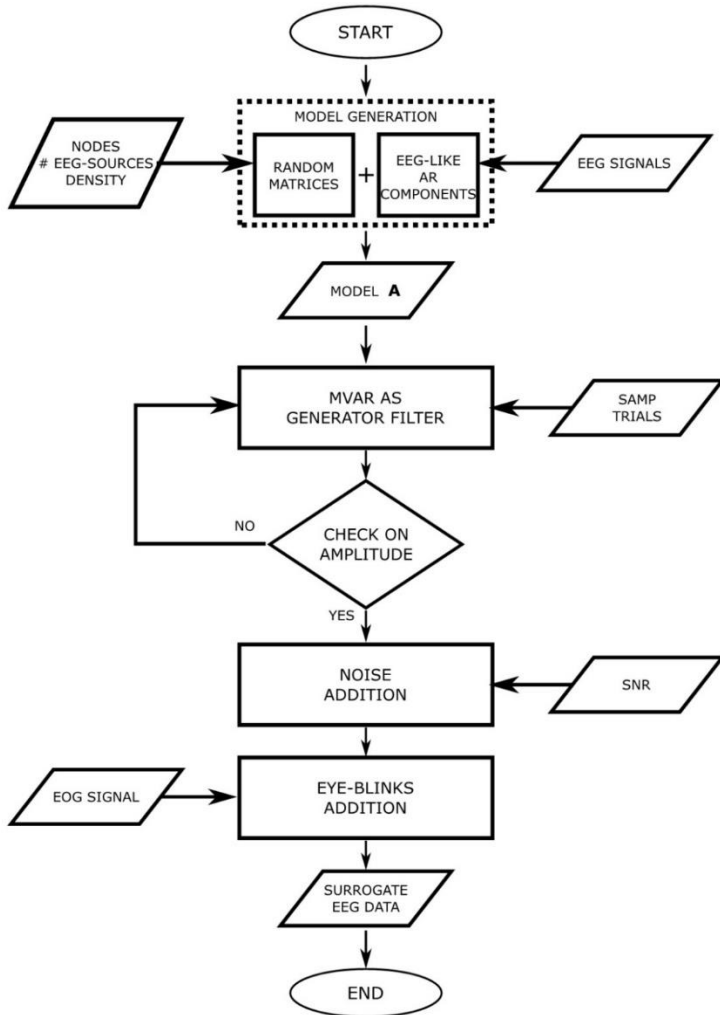


Figure 2.1: Block diagram describing the main methodological structure at the basis of the SEED-G generator

2.4 Features of the simulated data and the connectivity patterns

Inter-trial variability. If the user decides to generate a multi-trial dataset, he/she can decide to add an inter-trial variability to the ground-truth model in order to include an important realistic feature to the dataset. In fact, in every experiment including several realizations of a task, the networks involved are never perfectly the same at each realization. In the SEED-G toolbox, we modeled two kinds of alterations along trials to be applied to a specific model: i) inter-trial variability in

the value of an existing connection, and ii) variation of model density along trials. In the first approach, the parameters to be set are the percentage of altered trials, the number of connections to be modified, the entity and the direction of the variation (how much the connections value increase or decrease with respect to the initial value). In the second one, the user has to choose the number of altered trials and the number of spurious links to add to the original model.

Ocular component. Real EEG data always show ocular blinks, especially at the level of frontal electrodes. The developed toolbox allows to simulate such artifact adding a real ocular component on the generated signals with a specific amplitude depending on the position of the electrodes. Such component was extracted from a real ocular signal in which everything but blinks is set to zero. Amplitude distribution was calculated from a correlation mask obtained on a common 60-channel montage. Such correlation mask and a schematization of the sum between an EEG and an EOG signals are represented in *fig. 2.2*. The user can simulate different experimental conditions choosing the total number of blink to be add.

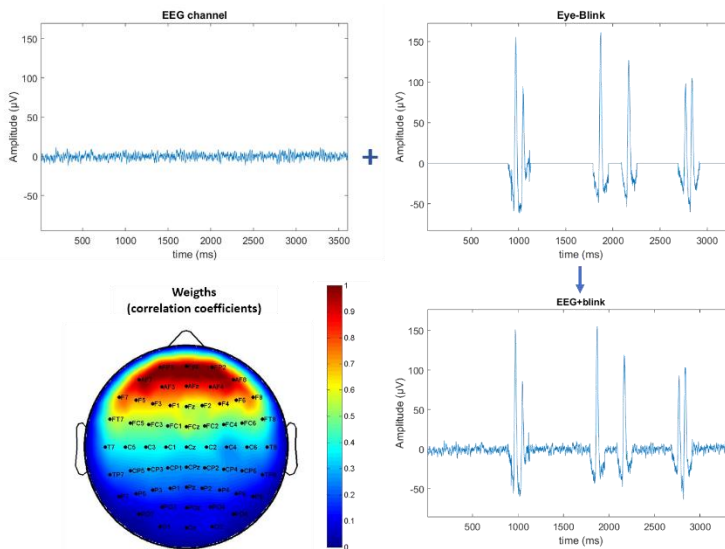


Figure 2.2 – Correlation mask (down-left) obtained from real EEG and EOG data in order to perform a weighted sum between simulated signals.

Time-varying networks. SEED-G toolbox allows to impose stationary or time-varying connectivity patterns. The generation process is the same but in the time-varying case, a specific model is applied for each sample of the innovation process. It is possible to set the following parameters: percentage of time-varying connections, instant in which the transition starts, magnitude and kind of variation: currently the user can choose between a step change and a variation following a ramp function.

Signal generation at source level. Depending on the type of real sources used for the signal generation the toolbox can provide simulated data with the same characteristics of the real ones at scalp or cortical level. Default, toolbox take the necessary real sources from ECoG (electrocorticography) data available at <http://math.bu.edu/people/kolaczyk/datasets.html>. In order to take into account the effect of the volume conduction can be interesting to generate data with an imposed pattern at source level and to project them at scalp level. SEED-G toolbox allows mapping the activity to EEG sensors using a realistic model of electrical current propagation in the head. In particular, the user can choose between the most commonly used individual head model Colin27 [44] and the Average Brain Stereotaxic Registration Model (average of 152 T1-weighted MRI scans, called AVG-21) made available from the Montreal Neurological Institute. The Least-Squares criterion was implemented for solving the direct and inverse problem [45] using a lead-field matrix with 4097 dipoles. If interested in considering the effect of volume conduction, the user can choose the following parameters:

- Brodmann areas in which generate the cortical signals (52 areas);
- the head model (Colin27 or AVG-21);
- the type of current distribution on the source: all the dipoles of the selected areas have the maximum value of the generated signal, only the centroid, the centroid has the maximum value and all the others have an amplitude that decrease with the distance.

Since the Least-Squares criterion only allows to reconstruct the activity on the cortical sources (not in the 3D space), a future update of the toolbox should give the possibility to choose a method able to consider deeper brain areas.

3. Toolbox Testing

In this section we report the results of a simulation study with the double aim to demonstrate the potentiality and versatility of SEED-G toolbox in generating simulated EEG-like datasets according to the users' preferences, and to provide guidelines for the practical use of the toolbox SEED-G in different conditions. The study involves two main steps: i) use of the toolbox for the generation of simulated datasets for different values of model dimension, network density and number of real EEG signals to be included as sources in the process; ii) testing of toolbox performances in the different situations. The results reported here refer to simulated datasets obtained imposing real sources in the model for each isolated node, under ideal conditions in terms of stationarity in time and no variability along trials.

3.1 Simulated data generation

To cover a wide set of cases reproducing typical EEG datasets encountered in real experiments, we repeated the generation process for the following parameters:

- Model size: 5 – 10 – 19 – 32 – 60 nodes (in order to simulate the most typical EEG montages);
- Network density: 5 – 10 – 20 – 30 % with respect to all possible connections (higher densities were not applicable for all the selected model sizes);
- Number of real brain signals included as sources in the model (% Real Sources): 20 – 30 – 50 % of the total number of signals to be generated.

3.2 Performance parameters

The time required for generating a complete dataset with the desired characteristics, the number of necessary iterations and the spectral properties of the signals were evaluated by means of the following performance parameters:

- **Extra Required Iterations (*ERIt*):** number of iterations carried out to achieve the number of trials required by the user. Recalling the concept

for which every time the amplitude of simulated signals exceeds the 80 μV threshold, the generated ground-truth is discarded and a new iteration is required, $ERIt$ can be defined as follows:

$$ERIt = \frac{n^{\circ}Iterations}{n^{\circ}Iterations_{Max}} \quad (2.9)$$

A null value of the parameter means that the dataset was generated without extra iterations; on the contrary $ERIt = 1$ means that the dataset cannot be generated with the imposed maximum number of iterations which is set to 1000 ($n^{\circ}Iterations_{Max}$)

- **Computational Time:** seconds required for the generation of a complete dataset (Intel Core i5 3.2GHz CPU, 16GB RAM).
- **EEG-like Signals (EEG1_S%):** percentage of simulated signals showing EEG-like spectral properties. Real sources were excluded from the computation of this index. The similarity with EEG signals was quantified by performing a Pearson's correlation between the Power Spectral Density (PSD) of each simulated data and the PSD of a real EEG data used for the generation. The signal was considered an "EEG-like signal" if such correlation is higher than 0.6. The investigated parameter is defined as follows:

$$EEG1_S\% = \frac{n_x - n_{AR}}{N - n_{AR}} * 100 \quad (2.10)$$

where n_x is the number of EEG-like signals, n_{AR} is the number of the MVAR real sources (with an AR component different from zero), and N is total number of generated signals.

To increase the robustness of the subsequent results, the entire procedure of data generation and performances evaluation was repeated 300 times.

3.3 Results

We report below the results showing the mean value of the three performance parameters computed over the 300 iterations. Figure 2.3 reports results relative to *ERIt* parameter (panel a) and computational time (panel b) when the number of pure real sources included in the model is set to 30%. Reported diagrams showed how, when the density of the desired network is 5% or 10%, the toolbox is able to generate simulated EEG dataset with up to 60 nodes, without extra iterations, in less than 5 seconds. Furthermore, it is possible to generate 32 time series fitting an MVAR model with a density equal to 30% even if the 25% of extra iterations is required. The most complicated case is represented by EEG dataset with 60 signals and density higher than or equal to 20% that cannot be currently generate. Similar results were obtained even when the percentage of real source in the model is equal to 20% or 50%.

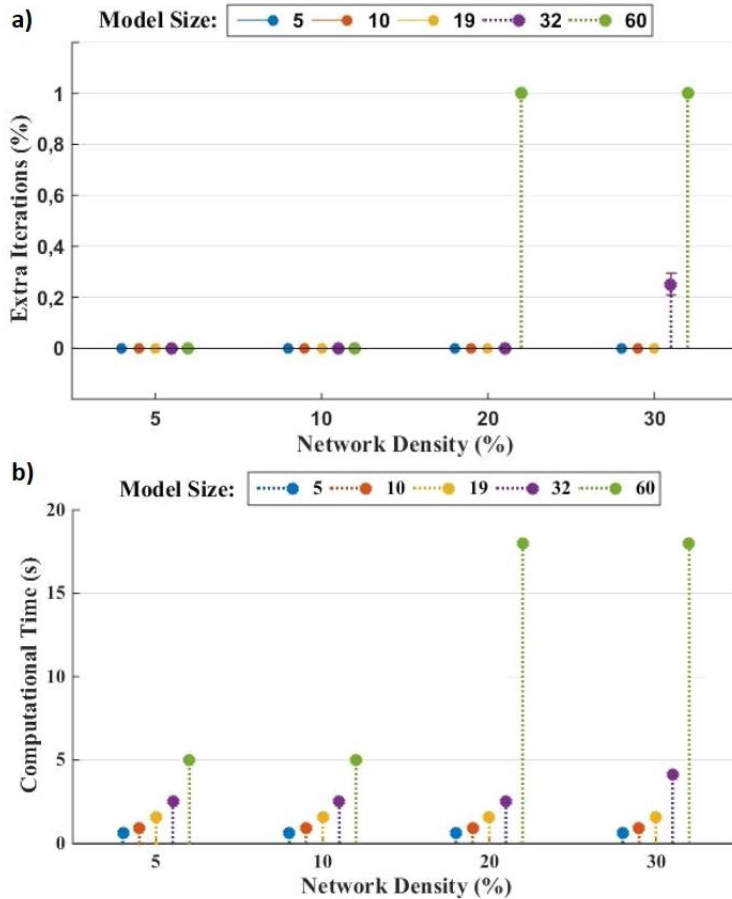


Figure 2.3. Plot of means of Extra Required Iterations, ERIt (panel a) and Computational Time (panel b) relative to the generation of a single simulated EEG dataset. The diagrams show the mean value over 300 iterations of the two indices for different values of Model Size and Network Density. Standard deviation is reported but in most cases it is lower than 10^{-1} , therefore not appreciable in the figure. The value of the factor % Real Source is fixed to 30%.

In figure 2.4 a bar diagram shows the values of the parameter EEGI-S% for different model size and percentages of real sources. Results refers to a network density fixed to 10% in order to include all the levels of the factor Model Size. In fact, in the case of 60 nodes densities of 20 and 30% cannot be applied, as seen in figure 2.2. The bar diagram demonstrates that, independently from the number of real sources included in the model, more than 85% of the simulated signals shows

real EEG spectral properties. As expected such parameter is higher when the percentage of real sources included in the model increase.

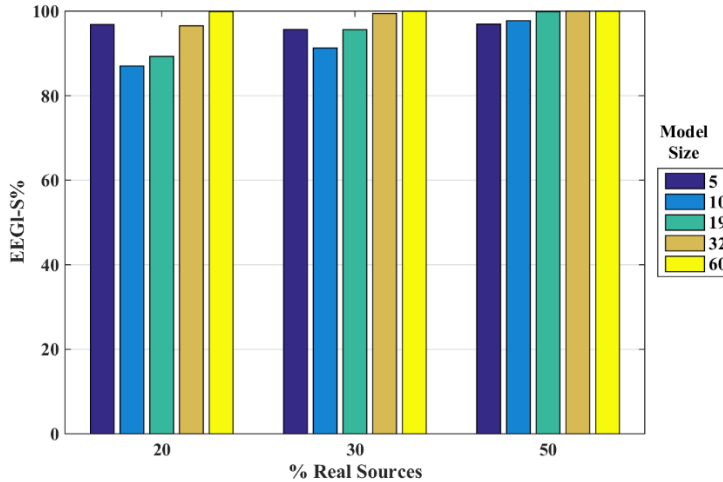


Figure 2.4. Plot of means of the parameter %EEG-like Signals relative to the generation of a single simulated EEG dataset under different conditions. The diagram shows the mean value of the index over 300 iterations for different levels of the factors % Real Sources and Model Size. The network density is fixed to 10%.

4. An example of application of the toolbox: investigating the effect of inter-trial variability on connectivity estimates

Neuro-electrical brain circuits elicited during several repetitions of a cognitive or motor task are often characterized by a high variability across the different task realizations because of many possible reasons, some related to methodological issues (degradation of the signal quality) and some others to subjects' contribution (subjects' fatigue, loss of concentration, oscillations in the task performance). Multivariate connectivity estimators, if applied to multi-trials data, do not provide a connectivity pattern for each realization but an average connectivity pattern including all the aspects in common to the different trials. This happens since for accurately applying a multivariate approach to multi-trial datasets all the data samples belonging to the different realizations are used for producing the connectivity estimates. How much the network inter-trial

variability affects the connectivity estimate is still unknown. What impedes its study is the availability of multi-trial simulated datasets fitting a ground-truth network slightly varying across the different process realizations. SEED-G toolbox was born with the main aim to provide an instrument that enables to test methodologies in the field of brain connectivity estimation under non-ideal experimental conditions, not rigorously tested until now, such as this one related to the inter-trial variability of brain networks. For this reason, the use case application proposed here aims to demonstrate the benefits earned from the employment of SEED-G toolbox in the study of the effect of inter-trial variability on the stability and accuracy of connectivity estimate. Among the available connectivity estimators, in this application we focused on PDC just to give an example of the potentialities of the toolbox. A first study in this direction was proposed relatively to 10 node models [46] but many more experimental conditions can be simulated and investigated with the developed toolbox SEED-G. Figure 2.5 reports a block diagram describing the principal steps of the simulation framework. In brief, the toolbox was employed for simulating several non-ideal multi-trial EEG datasets including signals related according to pre-defined ground-truth network characterized by an inter-trial variability. Such variability was imposed in two-way, as allowed by the toolbox: i) increasing/decreasing the value of some existing connections in the ground-truth network (study 1); ii) increasing ground-truth network density through the addition of some spurious connections to the existing ones (study 2). The simulated datasets were then subjected to a process combining connectivity estimation through PDC and the consequent statistical validation through the asymptotic statistic algorithm [47], [48],[49]. The obtained connectivity pattern was then compared with the one used for fitting the data in terms of false positives, false negatives and relative error.

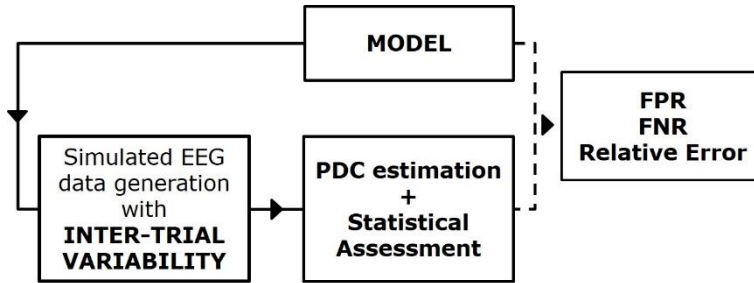


Figure 2.5: Block diagram describing the simulation framework.

Analysis of variance (ANOVA) was carried out to evaluate the performances showed by the estimator in the different simulated conditions. Since we modeled the inter-trial variability with a modified density or variability in the values of existing connections, we can divide the analysis in the study of the two distinct effects on the PDC accuracy and stability. In both of them the correction of Greenhouse-Geisser for the violation of the spherical hypothesis was used in all the analyses. Tukey's post-hoc test was used for testing differences between sublevels of ANOVA's factors and Bonferroni-Holm correction was applied for multiple ANOVAs. In order to increase the robustness of the subsequent statistical analysis, the entire procedure was executed 100 times with a different ground truth at each repetition of the simulation process.

4.1 Study 1: effects on connectivity estimate of alterations in connections value

Simulated EEG data

Several pseudo-EEG datasets were generated by means of the SEED-G toolbox. Set parameters are the following:

- Model size: 5 – 10 – 20 nodes
- Network Density: 20% of the possible connections
- Connections weights: selected in the range [-0.5÷ 0.5].
- Percentage of modified trials: 1 – 10 – 30 – 50 % of the total number of trials generated
- Percentage of modified links: 10 – 20 – 50 % of existing connections

- Amplitude of the variation: 20 – 50 – 70 % of the original value of the connection
- Type of variation: positive (increase) /negative (decrease)

Performance parameter

The quality of the estimation was assessed computing the *Relative Error*. It is defined as the Frobenius norm of the prediction error (difference between the estimate averaged across frequencies and the imposed connection value) evaluated for each existing arc and normalized for the value of the same link contained in the model:

$$R_Err = \sum_{i=1}^{Nc} \left| \frac{PDC_i - |Model_i|}{|Model_i|} \right| \quad (2.11)$$

Statistical Analysis

In order to quantify the effect of alterations in connections value on the estimation a four-way ANOVA was performed. The main within factors were the percentage of modified connections (%MOD_CON), the entity of variation (%VAR), the direction of the variation (VAR_DIR) and the percentage of modified trials (%TRIALS). The dependent variable was the Relative Error.

Results

The results of the four-way ANOVA for the Relative Error parameter are reported in table 2.1 for three different model size: 5, 10 and 20 nodes. We found a significant effect of the main factors VAR_DIR, %VAR, %MOD_CON, %TRIALS and of the interaction factors on the investigated dependent variable for all the model size levels.

<i>RELATIVE ERROR</i>			
<i>Factors DOF</i>	<i>5 nodes</i>	<i>10 nodes</i>	<i>20 nodes</i>
VAR_DIR (1, 99)	98.3 p=1*10 ⁻⁵	162 p=1*10 ⁻⁵	14.8 p=0.0002
%VAR (2, 198)	994.79 p=1*10 ⁻⁵	2991.9 p=1*10 ⁻⁵	7274.8 p=1*10 ⁻⁵
%MOD_CON (2, 198)	1236.7 p=1*10 ⁻⁵	4290.1 p=1*10 ⁻⁵	10176 p=1*10 ⁻⁵
%TRIALS (3, 297)	1414.7 p=1*10 ⁻⁵	2860 p=1*10 ⁻⁵	6189.5 p=1*10 ⁻⁵
%VAR x VAR_DIR (2, 198)	5.37 p=0.0056	33.05 p=1*10 ⁻⁵	903.69 p=1*10 ⁻⁵
%MOD_CON x VAR_DIR (2, 198)	2.91 p=0.056	21.59 p=1*10 ⁻⁵	558.33 p=0,084
%MOD_CON x %VAR (4, 396)	339.62 p=1*10 ⁻⁵	1806.2 p=1*10 ⁻⁵	5204.5 p=1*10 ⁻⁵
%TRIALS x VAR_DIR (3, 297)	37.4 p=1*10 ⁻⁵	86.76 p=1*10 ⁻⁵	45.29 p=1*10 ⁻⁵
%TRIALS x %VAR (6, 594)	755.63 p=1*10 ⁻⁵	1675.8 p=1*10 ⁻⁵	4061.2 p=1*10 ⁻⁵
%MOD_CON x %MOD_CON (6, 594)	689.6 p=1*10 ⁻⁵	1994 p=1*10 ⁻⁵	6458 p=1*10 ⁻⁵
%MOD_CON x %VAR x VAR_DIR (4, 396)	13.06 p=1*10 ⁻⁵	167.07 p=1*10 ⁻⁵	1361.1 p=1*10 ⁻⁵
%TRIALS x %VAR x VAR_DIR (6, 594)	7.81 p=1*10 ⁻⁵	28.2 p=1*10 ⁻⁵	538.72 p=1*10 ⁻⁵
%TRIALS x %MOD_CON x VAR_DIR (6, 594)	4.14 p=0.0004	24.39 p=1*10 ⁻⁵	376.1 p=1*10 ⁻⁵
%MOD_CON x %VAR x %TRIALS (12, 1188)	132.38 p=1*10 ⁻⁵	404.73 p=1*10 ⁻⁵	1345.4 p=1*10 ⁻⁵
%MOD_CON x %VAR x %TRIALS x VAR_DIR (12, 1188)	4.3 p=1*10 ⁻⁵	38.75 p=1*10 ⁻⁵	321.6 p=1*10 ⁻⁵

Table 2.1 - Results of four-way repeated measures ANOVA on Relative Error. In the second column we reported the Degrees Of Freedom (DOF) followed by the values of the coefficient *F* and of the *p*-value of the test obtained for 5, 10 and 20 nodes.

In figure 2.6 we reported the plot of the means for the four-way interaction factor (%MOD_CON x %VAR x %TRIALS x VAR_DIR) for the Relative Error in the case of 10 nodes model size. As expected, such parameter is significantly higher when increase the number of modified trials and the amount of modified connections in both positive (panel a) and negative (panel b) magnitude variations. However, the error remains below 10% in all the cases except for percentage of modified connections above 50%, variations in connections weight above 50% in half of the repetition or above 70% in more than 30% of the trials. In the worst case, error reached values around 20%.

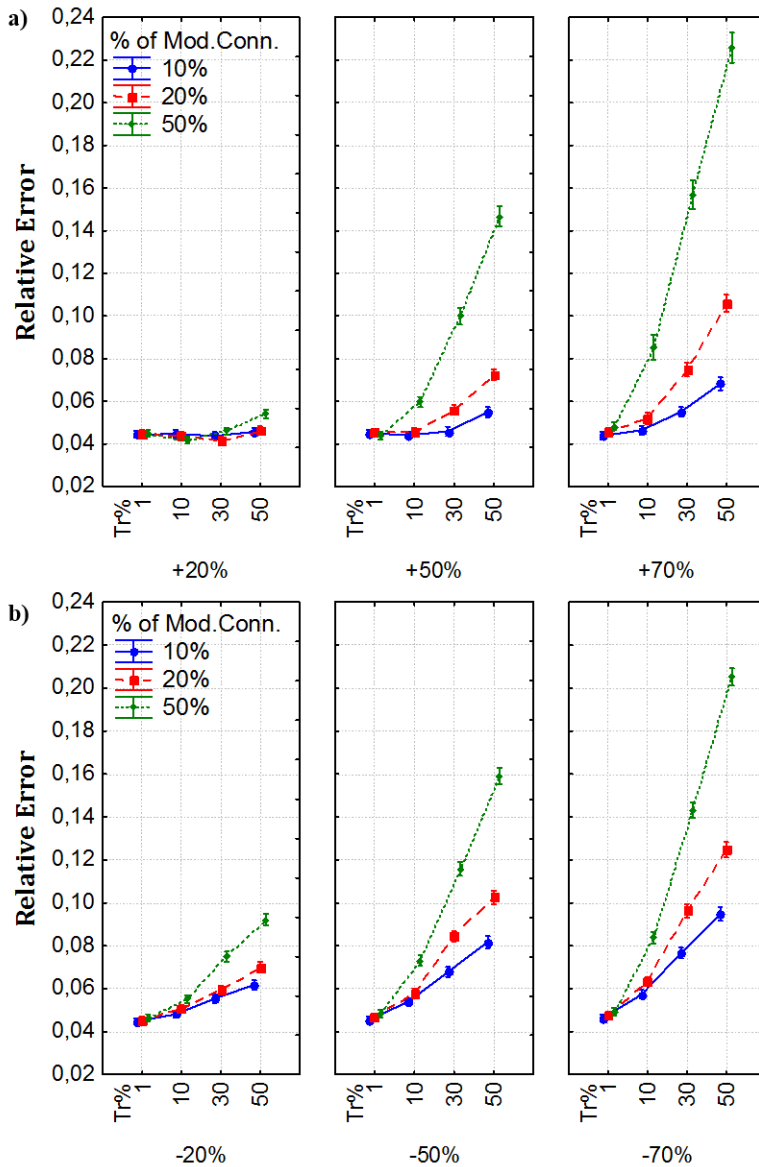


Figure 2.6. Plot of means associated to the four-way ANOVA performed on the Relative Error with respect to the interaction factor %MOD_CON (number of connections on which to apply a value variation) x %VAR (percentage of variation in the value of existing connections) x %TRIALS (percentage of modified trials) x VAR_DIR (direction of the variation). In particular the mean values obtained for positives (panel a) and negatives (panel b) variations are represented. The bars represent 95% confidence interval.

4.2 Study 2: effect on connectivity estimation of variable density

Simulated EEG data

Pseudo-EEG datasets were generated setting the following parameters:

- Model size: 5 – 10 – 20 nodes
- Network Density: 20% of the possible connections
- Connections weights: selected in the range $[-0.5 \div 0.5]$.
- Percentage of modified trials: 1 – 10 – 30 – 50 % of the total number of trials generated
- Percentage of added spurious links: 10 – 20 – 30 % of all existing connections.

Performance parameter

Connectivity estimation assessment was carried out by means of the following dependent variables:

- False Positive Rate (FPR). The percentage of false positives was obtained by comparing the connectivity estimation after the statistical validation and the average across frequencies (1-45Hz) with the imposed ground-truth. In other words, FPR was defined from the connections resulted as significant in the PDC estimation but their value in the model was set to zero. The amount of these links was than normalized on the number of all the possible false positive. We computed the FPR as follow:

$$FPR = \frac{1}{n_{null}} \sum_{n \in N_{null}} K^+[n] \quad (2.12)$$

Where N_{null} is the set of null arcs, n_{null} is the total number of null connections and $K^+[n]$ is 1 only if PDC value is above threshold, thus significant, for null arcs and 0 otherwise.

- False Negative Rate (FNR). The percentage of false negatives was obtained by comparing the connectivity estimation, after the statistical validation

and the average across frequencies (1-45Hz), with the imposed ground-truth. FNR was defined from the connections resulted as not significant in the PDC estimation while their value in the model was different from zero. The amount of these links was than normalized on the number of all the possible false negatives, thus on all the existing links. We computed the FNR as follow:

$$FNR = \frac{1}{n_{non-null}} \sum_{n \in N_{non-null}} K^{-}[n] \quad (2.13)$$

Where $N_{non-null}$ is the set of non-null arcs, $n_{non-null}$ is the total number of existing connections and $K^{-}[n]$ is 1 only when the PDC value is below threshold for non-null arcs and 0 otherwise.

Statistical Analysis

For studying the effect of altered connections values, we performed a three-way ANOVA. The main within factors were the percentage of added connections (%SPURIOUS) and the percentage of modified trials (%TRIALS). The model size (MOD_SIZE) was the between factor. FPR and FNR were the independent variables.

Results

The results of the three-way ANOVA computed on FPR and FNR are reported in Table 2. We found a significant effect of the main factors %SPURIOUS, %TRIALS, of the between factor MOD_SIZE and of all the interaction factors on the investigated dependent variables.

<i>Factors</i>	<i>DOF</i>	<i>FPR</i>	<i>FNR</i>
MOD_SIZE	(2, 297)	740,66 $p=1*10^{-5}$	251,08 $p=1*10^{-5}$
%SPURIOUS	(2, 594)	237,28 $p=1*10^{-5}$	118,65 $p=0,0003$
%TRIALS	(3, 891)	77,329 $p=1*10^{-5}$	189,44 $p=1*10^{-5}$
%SPURIOUS x MOD_SIZE	(4, 594)	186,79 $p=1*10^{-5}$	88,047 $p=1*10^{-5}$
%TRIALS x MOD_SIZE	(6, 891)	39,567 $p=1*10^{-5}$	149,26 $p=1*10^{-5}$
%SPURIOUS x %TRIALS	(6, 1782)	4,225 $p=0.0003$	50,675 $p=1*10^{-5}$
%SPURIOUS x %TRIALS x MOD_SIZE	(12, 1782)	6,7594 $p=1*10^{-5}$	33,639 $p=1*10^{-5}$

Table 2.2 - Results of the two-way repeated measures ANOVA on False Positive Rate (FPR) and False Negative Rate (FNR). In the second column are reported the Degrees Of Freedom (DOF) followed by the values of the coefficient F and of the p-value of the test obtained for the FPR and FNR parameters.

In figure 2.7 we reported the plot of means for the three-way interaction factor (%SPURIOUS x %TRIALS x MOD_SIZE) of FPR (panel a) and FNR (panel b). In the investigated ranges of the factors, FPR remains below 10% and FNR below 1% for 5 and 10 nodes models. In the case of models with 20 signals, both FPR and FNR show a significant increase and the percentage of spurious links and modified trials significantly influence the performance parameters. FPR is less than 10% if there is the 10% of spurious connections, just over 15% for the 20% of spurious connections and over 20% if 20% of spurious links is added. The percentage of false negatives is less than 1 for 10% of spurious links, just over 2% for 20% of spurious connections and less than 5% for 30% of added links. About the influence of the number of modified trials, it is more evident in terms of FNR that is significantly higher when the factor %TRIAL increases. The same trend is showed by the FPR.

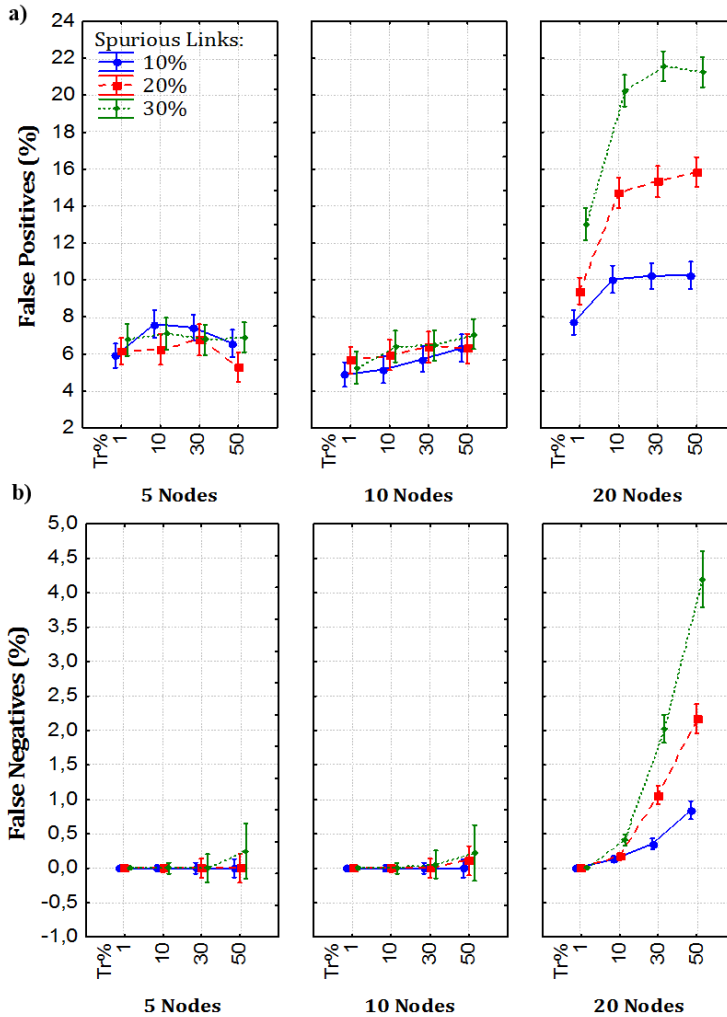


Figure 2.7 –Plot of means associated to the three-way ANOVA performed on False Positives Rate (panel a) and False Negatives Rate (panel b) with respect to the interaction factor %SPURIOUS (percentage of added links) x %TRIALS (percentage of modified trials) x MOD_SIZE (number of nodes composing the dataset). The bars represent 95% confidence interval.

5. Discussion

5.1 SEED-G toolbox capability

The potential of brain connectivity in neuroscience studies and clinical applications is more and more recognized thanks to the numerous developments in this research area. Several connectivity estimators were defined in order to meet the wide range of case studies and possible employments. A recently emerged aspect regards the importance to test connectivity estimation algorithms before their application in a real context. Starting from the necessity to validate such algorithms with a stable and reliable process, we developed our toolbox, SEED-G. Results presented in the current study demonstrated the possibility to employ the toolbox for generating a “personalized” simulated EEG dataset, with a well-known connectivity pattern, as benchmark for testing different connectivity procedures under different conditions. In other words, the strength of this instrument resides in the freedom of choice the properties of the pseudo-EEG signals and of the connectivity pattern by the user, on the basis of the estimator performance that he/she want to investigate. The user can choose to reproduce scalp or cortical signals on the basis of his research interests. In order to perform a reliable testing procedure whose conclusions can be effectively extended to real cases, SEED-G toolbox simulates data with the spectral and topological properties of signals really acquired. With the same objective to simulate dataset as similar as possible to real signals, some non-idealities, as the connectivity pattern variability across the different realizations, can be taken into account during the generation and testing procedures. In this chapter, for example, we use the toolbox to investigate the effect of the inter-trial variability on the accuracy of the connectivity estimation under experimental conditions that we were not able to generate up to now. Also the SNR of the simulated data can be modulated extending the opportunity to analyze and quantify its influence on estimators performances. Similar studies have already been proposed on small models (<10) but their findings [50], [5], [36] could now be extended to datasets reproducing high-density EEG recordings. In fact, our simulation study, conducted on a multi-trial simulated dataset with stationary connectivity, showed that we are able to

generate up to 60 pseudo-EEG signals in few seconds. Besides all the MVAR based methodologies for the estimation of brain connectivity under stationary hypothesis, we were interested in their adaptation for time-varying estimates that allow to recover the physiological temporal dynamic of the influences between cerebral areas. For this reason, we included in the toolbox the possibility to select the generation of pseudo-EEG data with time-varying connectivity patterns. The imposed ground-truth in this case is not static but the user can choose its dependence on time setting different parameters. Such toolbox functionality could open the way for testing and comparing time-varying algorithms currently used for connectivity estimation and could have an important impact in their optimization. Another open issue in the field of brain connectivity regards the effect of specific signals pre-processing phases on the following estimate. SEED-G could allow to produce advancements in this direction filling the existing gap between the use of algorithms for the signals elaboration (fundamental for EEG data) and the possible artifacts introduced in the evaluation of causal relationships between the same signals. An important and interesting application could be the study of the effect of algorithms for ocular artifact removal, as the Independent Component Analysis (ICA), , thanks to the ability of the toolbox to generate pseudo-EEG signals with ocular artifacts (blink). Another important point is that the employment of the toolbox could give a contribution in the study of the volume conduction effect thanks to the possibility to generate pseudo-EEG data as projections of simulated cortical signals. Among the limitation of the developed toolbox there is the possibility to generate (or reconstruct) brain signals only at scalp or cortical level and not in all the brain sources. An advancement in such direction is desirable in order to add another real characteristic to the generated dataset and to increase the knowledge about the effect of the signals propagation in the brain on the connectivity estimates [51] [52]. Another weakness of the toolbox is represented by the limited possibility to increase the network density values in large models because of the too high amplification of the signals occurring during the generation process. In fact, in several instances the model generates time series of too large amplitude which need to be discarded. This is very likely a consequence of the fact that the diagonal

elements of the MVAR matrices are assigned through individual AR estimation and the off-diagonal elements are then randomly set to simulate connectivity. This may lead to unstable MVAR models, which are not realistic to be set even if a single realization does not diverge. A test for MVAR stability (all the poles of the transfer functions must lie inside the unit circle) could be introduced in the toolbox, or at least suggested as a future development acknowledging the limitation of the current formulation. A potential extension of the toolbox could also include the possibility to impose non-linear relationship between the signals composing the simulated dataset.

5.2 Application on PDC stability evaluation

The simulation studies were presented with the aim to provide an example of how to use the toolbox SEED-G. Thanks to the advancements proposed in the toolbox, we were able to investigate the effect of a very important factor like the inter-trial variability on the connectivity estimates in a wide range of possible real cases. It allow to define more specific range of applicability of the estimator PDC, overcoming the limitations of the previous study on the topic [46]. Results obtained through the generation of a realistic dataset (patterns with inter-trial variability) and PDC estimation with asymptotic statistic demonstrated that the estimator can be consider stable in terms of accuracy, but always we need to take into account a certain number of false positive and false negative, and a certain relative error. Such errors in the estimates due to inter-trial variability are actually due to variations imposed in the generative model rather than true errors arising from the estimator or from factors like the data length. When the ground-truth network size is not too high, both investigated effects (variable connections value and variable network density) showed a restrained effect on the estimates that are reliable and repeatable. On the other side, the number of altered trials provided an important effect on PDC performances, especially when the model includes more than 20 nodes. For a high number of altered trials, the performance parameters reached not negligible percentage. Similar results can be extended to all the PDC normalization because of the statistical equivalence of asymptotic statistics for all different PDC formulations, demonstrated in [53] and confirmed

in [49]. These results indicate the importance of the stationarity of the data along trials, showing that when half of the trials contains artifacts and incorrect links, the real network is not clear and not easily identifiable. At the same time, they show that PDC validated by asymptotic statistic is robust with respect to a certain degree of non-ideality in this respect.

6. Conclusion

SEED-G toolbox was developed with the aim to provide a useful validation instrument addressed to researchers that conduct their activity in the field of connectivity estimation. We can finally test the ability of different estimators in increasingly less ideal conditions: low number of available samples and trials, high inter-trial variability (a condition that can be easily met when dealing with patients' data) or, again, time varying connectivity patterns to be estimated (where stationary hypothesis failed). The simulation study proposed as application of the toolbox regards the analysis of the performance of PDC when connectivity estimation involve EEG data with different levels of inter trial variability. Obtained results demonstrate the robustness and the accuracy of the PDC under a large range of conditions usually encountered in practice. Many other experimental conditions may be simulated by means of the toolbox SEED-G thus, with the hope to give a contribution to neuroscience research, all the MATLAB codes will be released and available for download.

Chapter 3

Investigating performances of time-varying connectivity algorithms

Recent advancements in functional connectivity field allowed finding a solution to two important open issues limiting the application of the existent procedures to high density EEG non-stationary signals. In particular, the existent methodologies for time varying connectivity are based on two different approaches. The first one employs the classical algorithms for connectivity estimation in short windows where the hypothesis of stationarity is verified [54]. Alternatively, it is possible to employ a recursive approach with forgetting factor weighting the influence of the past estimation [55], [56]. The two approaches do not allow at the same time to i) follow with high accuracy the temporal evolutions of connectivity patterns and ii) include the highest number of cerebral sources in the estimation process due to limitations in model's dimension. In 2010, a new approach for time-varying connectivity estimation based on Kalman filter was proposed as solution to the limitations of the existent procedures [57]. In this study we i) presented a characterization of the two most promising algorithms, Recursive Least Squares (RLS) and General Linear Kalman Filter (GLKF) under different conditions of data quality providing some guidelines for their use and ii) compared the performance of a new adaptation of the GLKF developed during the PhD course. The adaptation regards the setting of KF initial conditions in the first phase of the estimation where the algorithm has to move from a null starting point to the real value of the connection to be estimated. We proposed an approach that allows starting from a value close to the connection strength in the initial part of observed temporal window obtained by a preliminary stationary PDC estimation. The introduced adaptation of the algorithm led to a strong improvement of the performances in terms of accuracy of the estimates and initial adaptation time. The results achieved in both the simulation studies revealed high performances of the GLKF approach in time-varying connectivity estimates, opening the way of its application in different neuroscientific fields.

1. Introduction

All the Granger causality based connectivity estimators are able to accurately detect connectivity patterns by including all the relevant sources of the problem in the multivariate autoregressive model (MVAR) used for the estimation [1-3]. The existence of hidden sources, can cause the occurrence of false positives during the estimation process and, thus, misleading results (“hidden source dilemma”). Such spurious links are due to a common effect on two sources of a third one not included in the estimate. According to these considerations, not only a multivariate approach is preferable, in terms of accuracy of the pattern reconstruction, to a pairwise one, as demonstrated in [58], but it is also crucial to insert all relevant sources in the multivariate modeling. The issue of the model dimension becomes then essential to reach a full description of brain networks. Moreover, all the MVAR based methodologies for the causal connectivity estimation require the hypothesis of stationary in wide sense for the signals included in the estimate. Thus, the temporal dynamics of the influences between cerebral areas are completely lost. To overcome this limitation, different algorithms for the estimation of MVAR with time dependent coefficients were recently developed [11]. In particular, these methodologies are based on short-time window approaches, assuming the stationary of signals in short time intervals [54] or on an adaptive estimation of the MVAR model by means of a recursive algorithm involving a weighted influence of the past of the signal, as in the multi-trial Recursive Least Squares (RLS) method with Forgetting Factor [59], [60]. However, even if the RLS overcomes the problem of non-stationary data, it presents a limitation, due to computational complexity, in the number of signals to be considered at the same time in the estimation [57], [61]. The problem of the model dimension can be solved by reducing the number of electrodes time series to be included in the model [61]–[63] or by using cortical waveforms of some regions of interest derived through linear inverse procedures from high resolution EEG data [60]. However, the need to reduce the model dimension introduces a significant error due to the “hidden source dilemma”. Since each time a relevant source of information of the problem is removed from the autoregressive modeling this introduces spurious connectivity links and degrades

the reconstruction of the connectivity network. In 2010, a new method based on a General Linear Kalman Filter (GLKF), was provided as a solution to the limitation in the number of signals to be considered simultaneously in estimation process [57]. Even if the RLS method for time varying functional connectivity estimation has been proposed in literature from 2001, its performances under different conditions of available amount of data (different number of trials) and imposed adaptation constant were studied only on datasets composed by a small number of signals [60]. The GLKF method has been introduced and compared with the RLS by means of a simulated time varying MVAR of dimension 20 [62]. A rigorous demonstration of RLS limitation in the number of signals to be considered simultaneously in the estimation hasn't still been performed. Moreover, a comparison between the two methods in terms of accuracy and adaptation speed of estimates under different condition of number of trials and signals included in the estimation process it is necessary to understand in which cases one method show better performances than the other. An important aspect to be taken in consideration in the algorithms for time varying connectivity consists in the definition of initial conditions to be employed for the estimate. Being based on iterative approaches, the performances of the two algorithms, especially for the GLKF, are strongly influenced by such initial conditions. Thus, an exhaustive comparison of the performances between the two algorithms cannot be performed without including also this aspect.

In the present work, we proposed a simulation study performed for comparing the two approaches in terms of accuracy in the estimation process and of speed in the adaptation to the temporal evolution of the estimated patterns, under different conditions of number of nodes included in the network (factor SIG_NUM), amount of trials to be used in the analysis (factor TRIAL) and adaptations constants set for applying the methods (factor CONST). In the second part of the study we tested our adaptation of the algorithm in which we use the stationary Partial Directed Coherence to provide non-null initial conditions and improve the performance of the algorithm also in the initial phase of the estimation. This adaptation of the algorithm could be used in the future to employ the GLKF also in lots of real applications in which a long initial time for the

adaptation before the part of interest of the trial is not available. In particular, the simulation study allowed addressing the following specific questions:

- Does the RLS procedure show a real limitation in estimating time-varying information flows in networks characterized by a high number of nodes ($N=60$)?
- Can the GLKF approach substitute it in the estimation of temporal evolution of connectivity patterns characterized by a high number of nodes?
- What is the influence of the adaptation constants (c for the RLS algorithm; $c1$ and $c2$ for the GLKF approach) on the performances of the two algorithms, and which can be a criterion for the choice of their optimum values?
- How are the performances of the two methods influenced by different factors affecting the recordings, like the amount of trials at disposal for the analysis (factor TRIAL)?
- Are the performances of the two algorithms significantly improved by the settings of specific initial conditions derived by stationary PDC applied in a window preceding the one of interest?

In order to perform such simulation study and to answer these questions, several datasets with imposed and controlled connectivity pattern were generated for each investigated experimental condition by means of the SEED-G toolbox described in *Chapter 2*. Time-varying causal connectivity were estimated and the results compared with the imposed models in order to extract some performance parameters related with the accuracy of the estimate and the adaptation time. Analysis of variance (ANOVA) and Tukey's pairwise comparisons were applied in order to compare the two methods and evaluate the effect of the different considered factors and the settings of initial conditions.

2. Methods

2.1 Time-varying MVAR and PDC

MVAR models are widely explained in paragraph 2.1 of the *Chapter 2*. Supposing that the following multivariate autoregressive (MVAR) model is an adequate description of the dataset Y :

$$\mathbf{y}(n) = - \sum_{k=1}^p \mathbf{A}(k)\mathbf{y}(n-k) + \mathbf{u}(n) \quad (3.1)$$

where $\mathbf{y}(n)$ is the data vector in time, $\mathbf{u}(n)$ is a vector of multivariate zero-mean uncorrelated white noise processes, $\mathbf{A}(k)$ is the matrix of model coefficients at lag k and p is the model order [64]. In order to investigate the spectral properties of the examined process, eq. 3.1 is transformed to the frequency domain:

$$\mathbf{A}(f)\mathbf{Y}(f) = \mathbf{U}(f), \quad A_{ij}(f) = \sum_{k=0}^p \mathbf{a}_{ij}(k)e^{-j2\pi fTk} \quad (3.2)$$

where T is the temporal interval between two samples. In the present study an adaptive formulation for MVAR model (AMVAR) will be employed [65]; where the time dependent parameter matrices were estimated by means of RLS and GLKF methods, both described in detail in the following paragraphs.

Once estimated the coefficients of the time-varying auto-regressive model, it is possible to define also a time-varying version of the PDC estimator. The estimated parameters will be function of the time:

$$\pi_{ij}(f, n) = \frac{|\mathbf{A}_{ij}(f, n)|^2}{\sum_{k=1}^N |\mathbf{A}_{ik}(f, n)|} \quad (3.3)$$

$$A_{ij}(f, n) = \sum_{r=0}^p a_{ij}(r, n) e^{-j2\pi frT}$$

2.2 The Recursive Least Squares (RLS)

The Recursive Least Squares with forgetting factor is a method based on the minimization of the squared prediction error, introduced for the analysis of event related EEG data. An extended version to the multi-trials case was provided by [59]. A set of EEG trials, recorded according to a certain stimulus, can be seen as several realizations of the same stochastic process. Consider a stochastic process Y composed by T repetitions (trials) of M trajectories (signals). At the time point n , the process observation can be defined as follows

$$Y_n = \begin{bmatrix} y_1^{(1)}(n) & \cdots & y_1^{(T)}(n) \\ y_2^{(1)}(n) & \cdots & y_2^{(T)}(n) \\ \vdots & \ddots & \vdots \\ y_M^{(1)}(n) & \cdots & y_M^{(T)}(n) \end{bmatrix} \quad (3.4)$$

where $y_m^{(t)}(n)$ is the t -th component ($t=1, \dots, T$) of the m -th trajectory ($m=1, \dots, M$) at time n ($n=1, \dots, N$). The trajectories Y_n will be fitted by the MVAR model, defined in eq. 3.1. In order to infer the adaptive estimation $\tilde{\Lambda}_n$ of parameters Λ_n , the instantaneous prediction error should be minimized:

$$E_n = \sum_{i=1}^n (1-c)^{n-i} \|Z_i\|^2 \quad (3.5)$$

where

$$Z_n = Y_n - W_n \tilde{\Lambda}_{n-1}^T \quad (3.6)$$

Z_n is the instantaneous prediction error and describes the difference between the desired response Y_n and the estimation $W_n \tilde{\Lambda}_{n-1}^T$, the matrix $W_n = (Y_{n-1}, \dots, Y_{n-p})$ includes the last p observations of the time series. The introduction of the exponential $(1-c)^{n-i}$, with $0 \leq c < 1$, allows to forget the distant past of the

signals in order to follow their non-stationary environment [65]. The constant c controls the compromise between adaptation speed and the estimation accuracy. In fact, values of c close to zero led to slower adaptation but higher stability in the estimation and vice versa. The details about the algorithm can be found in [59].

2.3 The General Linear Kalman Filter

In the GLKF an adaptation of the Kalman Filter to the case of multi-trial time series is provided. In particular:

$$\begin{aligned} Q_n &= G_{n-1}Q_{n-1} + V_n \\ O_n &= H_n Q_n + W_n \end{aligned} \quad (3.7)$$

where O_n represents the observation, Q_n is the state process, H_n and G_n are the transition matrices and V_n and W_n are the additive noises. To obtain the connection with the time-varying MVAR it is necessary to make the following associations:

$$Q_n = \begin{bmatrix} \Lambda_1(n)^T \\ \vdots \\ \Lambda_p(n)^T \end{bmatrix}, \quad O_n = \begin{pmatrix} y_1^{(1)}(n) & \cdots & y_M^{(1)}(n) \\ \vdots & \ddots & \vdots \\ y_1^{(T)}(n) & \cdots & y_M^{(T)}(n) \end{pmatrix} = Y_n \quad (3.8)$$

$$G_{n-1} = I_{dp}, \quad H_n = (O_{n-1}, \dots, O_{n-p}) \quad (3.9)$$

where T denotes the number of trials, whereas M is the dimension of the measured process. The details of the algorithm are provided in [62]. The quality of estimation is related to the definition of two parameters, c_1 and c_2 , which regulate the compromise between the quality of estimation and the speed of adaptation to transitions.

3. Simulation Study 1

A first simulation study was designed in order to compare the accuracy of the two methods and their adaptation speed in the information flows transitions, under

different conditions of number of signals included in the model and amount of trials at disposal for the estimation. The simulation study involved the following steps:

- 1) Generation of different simulated datasets fitting a predefined time-varying connectivity model using the SEED-G toolbox introduced in the *Chapter 2*. The optimal order chosen for the MVAR model used as generator filter is equal to 16. We simulated 50 datasets for each condition of interest. More in detail, we generated datasets with 5, 10, 20, 30, 60 nodes (factor SIG_NUM) imposing different levels of trials number (factor TRIAL: 30, 50, 100, each of 516 samples). The levels chosen for both SIG_NUM and TRIAL factors cover the typical ranges encountered in EEG recordings. The number of nodes included in the study was the one typical of standard EEG montages.
- 2) Evaluation, for each dataset, of AMVAR coefficients by means of RLS and GLKF methods and estimation of related time varying PDC. The AMVAR coefficients estimation was repeated for different values of adaptation constants c for RLS and $c1$ and $c2$ for GLKF, required for the application of the two methods. In both cases we selected $c=c1=c2= [0.01, 0.03, 0.05]$. The levels for the factor CONST were chosen on the basis of previous studies aiming at describing the properties of both time varying estimation methods. In particular, Astolfi et al. identified an interval of values from 0.02 to 0.05 as a valid range for high quality time varying functional connectivity estimates by means of RLS algorithm for different values of SNR and number of trials used in the estimation process [60]. On the other side, Milde et al. suggested to set, for the GLKF method, the two adaptation constants with the same value and around 0.03 [62].
- 3) Evaluation of performance indices, which allowed comparing the two methods in terms of estimation accuracy and speed of adaptation to transitions. In particular we evaluated the error in the estimated value in the samples before and after the transition, and the time needed for the algorithm to stably reach the true value of the connection.

All the procedures in steps 1-3 were repeated 50 times, each one under different conditions of signals number (SIG_NUM = 5, 10, 20, 30, 60) and trial number (TRIAL = [30; 50; 100]) with the aim to enforce the following statistical analysis. In particular, Analysis Of Variance (ANOVA) for repeated measures of the performance indexes, in order to evaluate the effects of the factors TRIAL, SIG_NUM and CONST on the performances of the analysed methods.

3.1 Datasets Generation

The first step of datasets generation consisted in the creation of a predefined time varying model. Due to the necessity to test the performances of the two methods in the estimation of time varying connectivity on datasets composed by different number of signals, the process of model generation was completely automated. SEEG-G toolbox employed for generating all the pseudo-EEG signals allowed to set the following parameters:

- The percentage of time-varying connections was fixed to 50%;
- The instant in which the transition starts was imposed at the sample 266 (at half of the trial) corresponding to 1.3 seconds;
- The magnitude and kind of variation. For this study we imposed step change with amplitude such that the final value of the connection is double or half with respect to the initial value unless the addition of a random value included in the range [-0.1;0.1].

3.2 Evaluation of performances

In order to compare from different point of views the two methods used for the estimation of time-varying connectivity patterns, we identified four parameters able to consider the accuracy achieved in the estimation process and the speed of adaptation to the transitions imposed in the time evolution of the investigated networks. The following figure (*fig. 3.1*) will help us in the definition of such parameters.

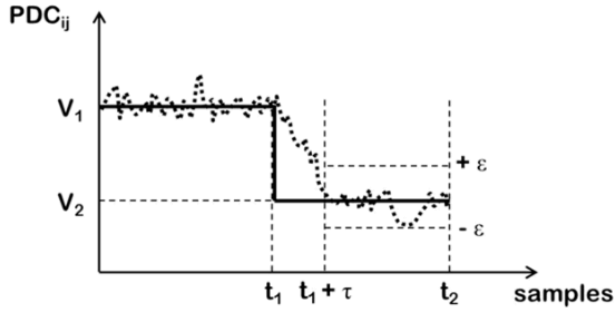


Figure 3.1 – Plot containing the over imposition of the imposed (solid line) and estimated (dotted line) trends for one generic connection ij . The imposed connection after 250 samples has a transition in the value moving from V_1 value to V_2 . In the representation the first 16 samples are not reported, since 16 is the order of the MVAR model and the estimate is performed starting from sample 17th.

For the evaluation of the accuracy achieved during the estimation process, we defined two errors whose formulation is reported in the follows:

- 1) Error_PRE: error committed in the estimation of the imposed values, before the transition (computed for all the connections different from zero). Consider $E_{ij,f}$ the difference between the estimated value ($PDC_{ij,f}$) of a connection and the imposed one ($Model_{ij,f} = V_1$ in the figure) for each sample and each frequency (f):

$$E_{ij,f} = PDC_{ij,f} - Model_{ij} \quad (3.10)$$

Error_PRE defined for one connection is:

$$Error_PRE_{ij} = \frac{1}{(t_1 - 1) - (popt + 1)} \frac{1}{f_{end}} \sum_{t=popt+1}^{t_1-1} \sum_{f=1}^{f_{end}} \frac{E_{ij,f}}{Model_{ij,f}} \quad (3.11)$$

where f_{end} is the last frequency considered in the range in which the PDC estimator was computed and t_1 is the sample in which the model was subjected to the transition as reported in *fig.3.1*. In other words, this

parameter is the mean value of E_{ij_f} on the interval from the optimal order of the model ($popt$) to the beginning of the transition and on all the frequencies considered in the estimate. In order to obtain the final $Error_PRE$ we averaged the errors obtained for all the non-null connections:

$$Error_PRE = \frac{1}{N_{no_null}} \sum_{i,j=1}^N Error_PRE_{ij} \quad (3.12)$$

where N_{no_null} is the number of connections different from zero.

- 2) $Error_POST$: error committed in the estimation of the specific imposed values, after the transition (only computed for the connections who showed a transition). It is mathematically defined in the same way of the $Error_PRE$. Given E_{ij_f} according to eq. 3.10, we can define the $Error_POST$ for one connection as follows:

$$Error_POST_{ij} = \frac{1}{(t_2) - (t_1 + \tau)} \frac{1}{f_{end}} \sum_{t=t_1+\tau}^{t_2} \sum_{f=1}^{f_{end}} \frac{E_{ij_f}}{Model_{ij_f}} \quad (3.13)$$

where f_{end} is the last frequency considered in the range in which the PDC estimation was computed, t_2 is the last sample of the trial and τ the samples at settling. $Error_POST_{ij}$ is the average on all the samples after the transition and after the stabilization of the algorithm and on all the frequencies considered in the estimate. The global $Error_POST$ was obtained mediating all the values computed for the considered connections:

$$Error_POST = \frac{1}{N_T} \sum_{i,j=1}^{N_T} Error_POST_{ij} \quad (3.14)$$

where N_T is the number of connections whose value undergoes the transition.

- 3) In order to evaluate the speed in adaptation to transitions we defined the samples at settling parameter (ST) as the first instant τ (following the transition) after which the error keeps definitely below the 20% of the transition amplitude. In particular, the condition for each connection was:

$$|E_{ij_f}| < \varepsilon \cdot (V_2 - V_1) / 100 \quad (3.15)$$

where E_{ij_f} is defined as in eq. 3.10 and is the difference between the imposed connection ij and its estimated value at time t and frequency f , ε was set to 20 and V_1 and V_2 are the values of PDC related to the arc directed from j to i before and after the transition applied at time t_1 (see fig. 3.1). Once calculated τ for each node in which the transition was applied and for each frequency sample, it is possible to define the samples at settling parameter as follows:

$$ST = \frac{1}{N_T} \frac{1}{f_{end}} \sum_{i,j=1}^{N_T} \sum_{f=1}^{f_{end}} \tau_{ijf} \quad (3.16)$$

where N_T is the number of nodes in which at time t_1 a transition was applied, f_{end} is the last frequency considered in the range used for PDC estimation and $\tau_{ij}(f)$ is the settling time for the specific connection directed from j to i at frequency f .

- 4) A similar parameter was defined in order to evaluate the speed of the algorithm to move from the initial conditions (set to zero) to the value of the connection independently of the transition. It was computed for all the links different from zero in all the samples before the possible transition (first 266 samples). We evaluated the first instant τ' after which the error keeps definitely below the 20% of the amplitude V_1 . In particular, the condition for each connection was:

$$|E_{ij_f}| < \varepsilon \cdot V_1 / 100 \quad (3.17)$$

where E_{ij_f} is defined as in eq. 3.10 and is the difference between the imposed connection ij and its estimated value at time t and frequency f , ε was set to 20 and V_1 is the values of PDC related to the arc directed from j to i before the transition (see fig.3.1). Once calculated τ' for each connection different from zero and for each frequency sample, it is possible to define the initial adaptation parameter as follows:

$$TAU = \frac{1}{N} \frac{1}{f_{end}} \sum_{i,j=1}^N \sum_{f=1}^{f_{end}} \tau'_{ijf} \quad (3.18)$$

where N is the number of non-null links, f_{end} is the last frequency considered in the range used for PDC estimation and $\tau_{ij}(f)$ is the settling time for the specific connection directed from j to i at frequency f .

3.3 Statistical Analysis

The parameters defined for comparing the two methodologies in terms of accuracy in the estimation process and of the speed of adaptation were subjected to separate ANOVAs. We performed a repeated measures three-way ANOVA aiming at studying the effect of different adaptation parameters (CONST) set during the estimation process on the performance indices defined above, taking into account several factors such as the number of trials (TRIAL) available for the analysis and the connectivity model size (SIG_NUM). This analysis was executed separately for RLS and GLKF algorithms. The within main factors of the ANOVA were:

- CONST with three levels: C=0.01, C=0.03, C=0.05, where C=c=c1=c2;
- TRIALS with three levels: 30, 50, 100.

The between factor of the ANOVA is the number of signals included in the estimate (SIG_NUM) and has five levels: 5, 10, 20, 30, 60. The dependent variables were the samples at settling (ST), the initial adaptation time of the algorithm (TAU) and the

errors before and after the transition (Error_PRE and Error_POST respectively). The correction of Greenhouse-Gasser for the violation of the spherical hypothesis was used. Tukey's pairwise comparisons were then performed in order to better understand the significance between different levels of the same factor or between the same levels of different factors.

4. Simulation Study 2

The main limitation we found in the algorithm based on the Kalman filter was the long time required to reach the true value of the connection starting from null conditions. This is true and amplified especially in the experimental case in which the constants ($c1$, $c2$) are equal to 0.01 even if all the other performance parameters related with the transition phase are set on their best values. The idea proposed in this study is to employ the first samples of the trials to compute a stationary estimation of the causal connectivity and to use the obtained values as initial conditions for the time-varying algorithm. The hypothesis was that such mathematical alteration could significantly improve the performance of the GLKF algorithm in term of adaptation time and error committed before the transition. In order to demonstrate our hypothesis, we performed a second simple simulation study involving the following steps:

- 1) Evaluation, for each dataset generated for the first simulation study, of AMVAR coefficients by means of GLKF method with constants $c1$ and $c2$ equal to 0.01 and estimation of related time varying PDC. The estimation was performed two times for each dataset changing the initial conditions from null to non-null, defining the factor IC_TYPE.
- 2) Evaluation of the performance parameters that allowed to compare the two version of the algorithm in terms of estimation accuracy and speed of initial adaptation.

The steps 1-2 were repeated 50 times in order to enforce the following statistical analysis. In particular, ANOVA for repeated measures of the performance indices, in order to evaluate the effects of the factors TRIAL, SIG_NUM and IC_TYPE.

4.1 Evaluation of performances

In order to evaluate the performance of the GLKF in two different conditions of initial condition we evaluated the error before the transition and the time needed for the algorithm to stably reach the true value of the connection to be estimate. The performance parameters TAU and Error_PRE have been already mathematically described in the previous paragraph (eq. 28 and eq. 24 respectively).

4.2 Statistical Analysis

The parameters defined in the time interval before the transition to demonstrate the improvement of the performances of the GLKF algorithm in the case of non-null initial conditions were subjected to ANOVA test. A repeated measures three-way ANOVA was performed in order to study the effect this factor (IC_TYPE) taking into account also the number of trials (TRIALS) available for the analysis and the connectivity model size (SIG_NUM). The within main factors of the ANOVA were:

- IC_TYPE with two levels: Null, Non-Null;
- TRIALS with three levels: 30, 50, 100.

The between factor of the ANOVA is the number of signals included in the estimate (SIG_NUM) and has five levels: 5, 10, 20, 30, 60. The dependent variables were the initial adaptation time of the algorithm (TAU) and the errors before the transition (Error_PRE). Tukey's pairwise comparisons were then performed in order to better understand the significance between different levels of the same factor or between the same levels of different factors. The analysis was conducted only for GLKF algorithm.

5. Results

5.1 Simulation Study 1: RLS vs GLKF

Results presented in figures 3.2-3.5 refer to the three-way ANOVA applied to the performance indices defined in previous section and computed separately for GLKF and RLS algorithms. In particular, the within main factors were the adaptation parameters set in the estimation process (CONST) and the number of trials (TRIALS) available for the analysis. The between factor was the number of signals composing the model (SIG_NUM). In *Table 3.1 and Table 3.2* we reported the results of the ANOVA performed for the four dependent variables: ST, TAU, Error_PRE and Error_POST. They revealed that most of the considered factors have a significant influence on the performances of the two algorithms. The interaction factors SIG_NUM x TRIALS and SIG_NUM x CONST x TRIALS do not show a significant influence on the variable ST when the RSL algorithm is employed. In the same kind of estimation, the interaction factor CONST x TRIALS does not show a significant influence on the variable TAU.

	Factors	Error_POST	Error_PRE
GLKF	SIG_NUM (4,245)	17.487 $p=1*10^{-5}$	105.78 $p=1*10^{-5}$
	CONST (2,490)	8219.5 $p=1*10^{-5}$	1224,7 $p=1*10^{-5}$
	TRIALS (2,490)	2831.8 $p=1*10^{-5}$	13317 $p=1*10^{-5}$
	SIG_NUM x CONST (8,490)	184.72 $p=1*10^{-5}$	654.12 $p=1*10^{-5}$
	SIG_NUM x TRIALS (8,490)	33.946 $p=1*10^{-5}$	116.39 $p=1*10^{-5}$
	CONST x TRIALS (4,980)	2222.4 $p=1*10^{-5}$	1831 $p=1*10^{-5}$
	SIG_NUM x CONST x TRIALS (16,980)	118.14 $p=1*10^{-5}$	408.86 $p=1*10^{-5}$
RLS	SIG_NUM (4,245)	33.219 $p=1*10^{-5}$	26.241 $p=1*10^{-5}$
	CONST (2,490)	350.06 $p=1*10^{-5}$	5166.5 $p=1*10^{-5}$
	TRIALS (2,490)	1767 $p=1*10^{-5}$	5130.2 $p=1*10^{-5}$
	SIG_NUM x CONST (8,490)	21.28 $p=1*10^{-5}$	27.461 $p=1*10^{-5}$
	SIG_NUM x TRIALS (8,490)	10.088 $p=1*10^{-5}$	42.153 $p=1*10^{-5}$
	CONST x TRIALS (4,980)	1789.7 $p=1*10^{-5}$	1717.9 $p=1*10^{-5}$
	SIG_NUM x CONST x TRIALS (16,980)	16.654 $p=1*10^{-5}$	17.427 $p=1*10^{-5}$

Table 3.1 - Results of the repeated measures three-way ANOVA (*F* values) computed considering as dependent variables *Error_POST* and *Error_PRE*.; the amount of trials (*TRIALS*) and adaptation constants (*CONST*) are the main within factors; the number of signals included in the estimates is the between factor (*SIG_NUM*). In the column “Factors” are also reported the degree of freedom.

	Factors	ST	TAU
GLKF	SIG_NUM (4,245)	6.99 $p=2*10^{-4}$	1165 $p=1*10^{-5}$
	CONST (2,490)	8219.5 $p=1*10^{-5}$	12077 $p=1*10^{-5}$
	TRIALS (2,490)	1197.4 $p=1*10^{-5}$	13936 $p=1*10^{-5}$
	SIG_NUM x CONST (8,490)	13.389 $p=1*10^{-5}$	554.94 $p=1*10^{-5}$
	SIG_NUM x TRIALS (8,490)	4.159 $p=8*10^{-4}$	538.16 $p=1*10^{-5}$
	CONST x TRIALS (4,980)	14.258 $p=1*10^{-5}$	3196.1 $p=1*10^{-5}$
	SIG_NUM x CONST x TRIALS (16,980)	5.05 $p=1*10^{-5}$	304.69 $p=1*10^{-5}$
RLS	SIG_NUM (4,245)	17.54 $p=1*10^{-5}$	234.74 $p=1*10^{-5}$
	CONST (2,490)	1376.2 $p=1*10^{-5}$	61.17 $p=1*10^{-5}$
	TRIALS (2,490)	888.75 $p=1*10^{-5}$	1101.1 $p=1*10^{-5}$
	SIG_NUM x CONST (8,490)	28.414 $p=0.004$	5.2 $p=1*10^{-5}$
	SIG_NUM x TRIALS (8,490)	1.39 $p=0.19$	181.45 $p=1*10^{-5}$
	CONST x TRIALS (4,980)	532.03 $p=1*10^{-5}$	2.59 $p=0.035$
	SIG_NUM x CONST x TRIALS (16,980)	1.62 $p=0.057$	1.92 $p=0.015$

Table 3.2 - Results of the repeated measures three-way ANOVA (*F* values) computed considering as dependent variables TAU and ST; the amount of trials (TRIALS) and adaptation constants (CONST) are the main within factors; the number of signals included in the estimates is the between factor (SIG_NUM). In the column "Factors" are also reported the degree of freedom.

Diagrams reported in the figures 3.2 and 3.3 allow to demonstrate how the two different time-varying connectivity estimators are differently sensitive, in terms of adaptation time and accuracy in following the transition (Error_POST), to the number of trials and signals composing the dataset and to the adaptation parameters c , $c1$ and $c2$.

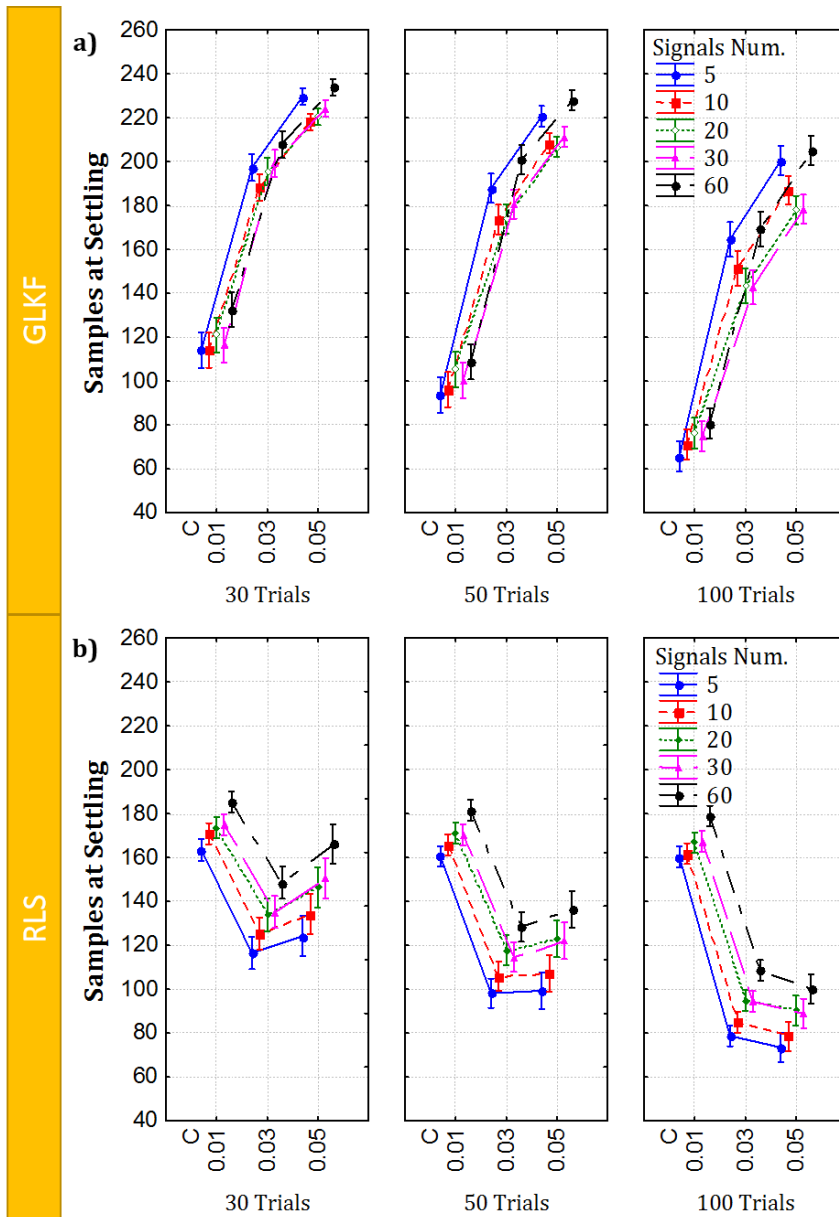


Figure 3.2 - Plot of means associated to the three-way interaction factor ($SIG_NUM \times TRIALS \times CONST$) of the ANOVA performed on the Samples at Settling (ST) parameter. Each panel is related with a specific algorithm for the AMVAR coefficients estimation: GLKF (panel a) and RLS (panel b). For each panel, we reported three graphs associated to the different available amount of trials: 30, 50 and 100 from left to right. X-axes always report the levels of the factor $CONST$ and the colours code for different model size. The bars represent their relative 95% confidence interval.

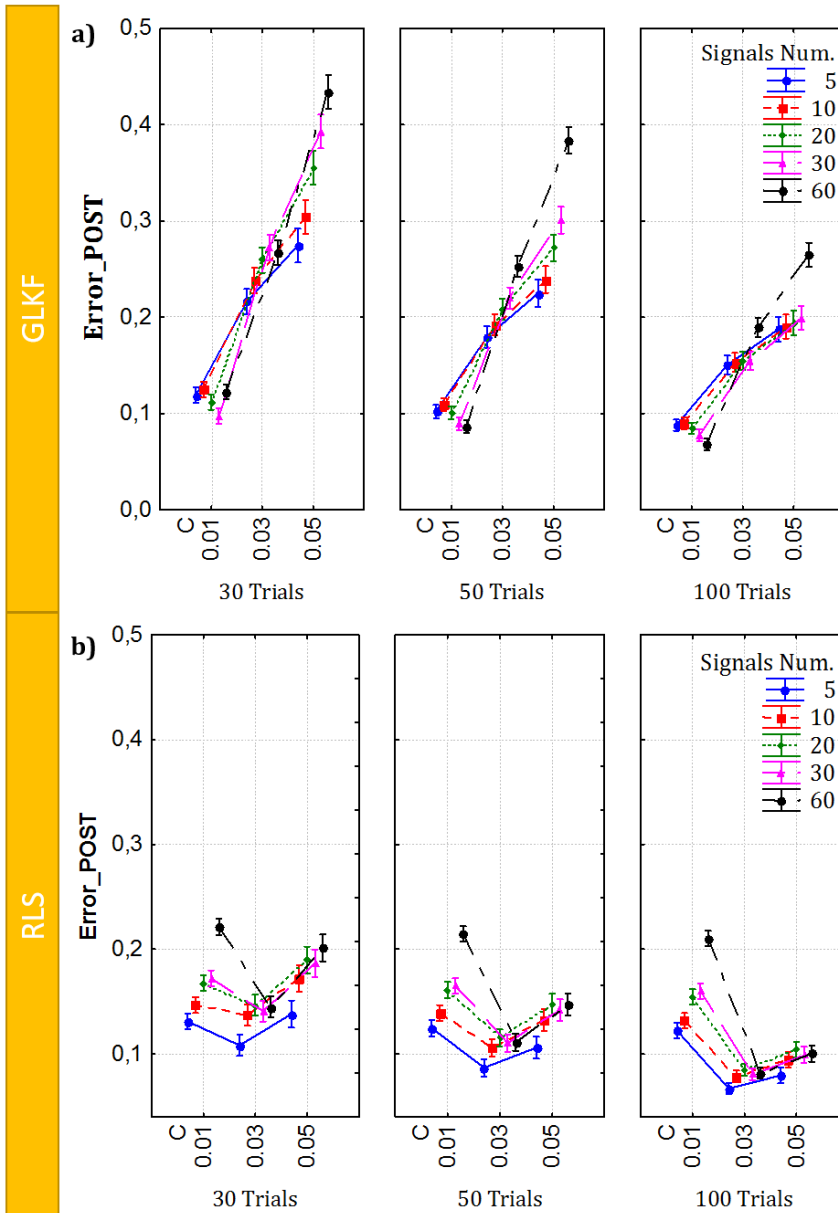


Figure 3.3 - Plot of means associated to the three-way interaction factor ($SIG_NUM \times TRIALS \times CONST$) of the ANOVA performed on the $Error_POST$ computed in the time interval after the transition. Each panel is related with a specific algorithm for the AMVAR coefficients estimation: GLKF (panel a) and RLS (panel b). For each panel, we reported three graphs associated to the different available amount of trials: 30, 50 and 100 from left to right. X-axes always report the levels of the factor $CONST$ and the colours code for different model size. The bars represent their relative 95% confidence interval.

Trials number: As expected, results showed a significant decrease of the samples at settling and of the Error_POST when the amount of trials increase for both the algorithms. It is true regardless of the adaptation constants and of the model size. For high number of signals involved in the estimate such phenomenon applied to the Error_POST results amplified.

Adaptation constants: The influence of such factor on the time-varying connectivity estimates is different for the GLKF and the RLS algorithm because of the different meaning that C assumes in the mathematical implementation of the two methods. Results related with the Kalman's filter based approach highlighted that it is possible to obtain the best performances when the adaptation parameters are both equal to 0.01. In such condition, the samples at settling are less than 80 when 100 trials are available and less than 130 for the lowest TRIALS level. Also in term of Error_POST we found good performance. In fact, the value of this parameter moves from a minimum of 7% to a maximum of 12% (*fig. 3.3a*) dependently of the amount of trials and signals. More in general we found a performance degradation of the GLKF algorithm when the adaptation parameter increases from 0.01 to 0.05. Regarding the RLS approach, the best adaptation constant emerged from the showed diagrams is 0.03, so that the trend of the performance parameters on the CONST levels has a "V" shape. There are some exceptions, like the ST when the amount of trials is 100. In this case the value of the index decreases for c equal to 0.05 but the difference is not consistent (only few samples). When c is equal to 0.03 the samples at settling are less than 120 when 100 trials are available (80 for small models) and less than 130 for the lowest TRIALS level. As showed in *fig. 3.3b*, the Error_POST value moves from a minimum of 5% (100 trials and small models) to a maximum of 15% (30 trials and large models).

Model size: The results obtained for the ST index and Error_POST revealed, on mean, a degradation of the performances when the number of signals included in the connectivity estimate increases. The time-varying algorithm based on the RLS has a clear growing trend for both the performance parameters (*fig. 3.2b* and *fig. 3.3b*). For the Kalman based algorithm such behaviour is mitigated. In terms of samples at settling (*fig. 3.2a*), only the level 60 of the factor SIG_NUM is

significantly different from all the others in all the trials number and constants value conditions. Moreover, the Error_POST diagram (fig. 3.3a) highlights an opposite trend in the relation between the parameter and the model size, particularly clear in the subplots related with the levels 50 and 100 of the factor TRIALS. What we found was a slightly improvement of the estimates accuracy for larger models. Such result is probably an effect of the number of signals on the adaptation constants of the GLKF algorithm. In figure 3.4, we reported the same transition estimated with the GLKF, with c_1 and c_2 equal to 0.01 and 30 trials. The only difference between the two panels is the size of the model to whom the connection comes from. It is evident how in the case of 60 nodes (panel b) the typical oscillations of the estimated value are smoother than in the case of 5 nodes (panel a) as if the adaptation constant were lower. Because the Error_POST is only computer after the adaptation phase, it is clear that in the second case the deviations from the true connection value are lower.

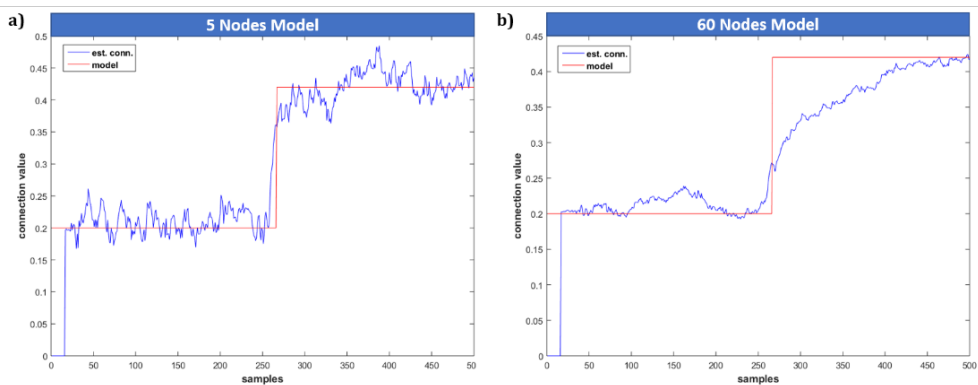


Figure 3.4 – Plot of one of the imposed connection that after 250 samples has a transition in the value. The connection represented in panel a) comes from a 5-nodes model. The connection in panel b) comes from a 60-channels model. In both cases the red line is the value of the connection imposed in the model, the blue line is the estimate sample by sample by GLKF algorithm with adaptation constants equal to 0.01 and 30 trials.

In summary, the performance of the two algorithms used with the correct adaptation constants (0.01 for GLKF and 0.03 for RLS) are comparable but, as expected, RLS related Error_POST is more sensitive to the factor SIG_NUM. When a number of trials lower than 100 is available, the Kalman filter has better and

more stable performance. In the field of neuro-physiological studies, it is really common to analyse datasets recorded by 60 channels and, at the same time the quality of such data could be not too high. If patients are included in the experiment could be difficult to collect a high number of trials (with low inter-trial variability). Thus, for the real application, the GLKF algorithm represents the best choice in terms of accuracy of the estimate and rapidity in following the link transitions.

In the next figures, we reported the ANOVA results for the others two performance indices: the initial adaptation time of the algorithms (TAU, *fig. 3.5*) and the Error_PRE committed independently of the presence of the transition (*fig. 3.6*). We investigated these variables in order to clarify the behaviour of the two methods in the time interval in which the algorithm move from the null initial conditions to the link strength value.

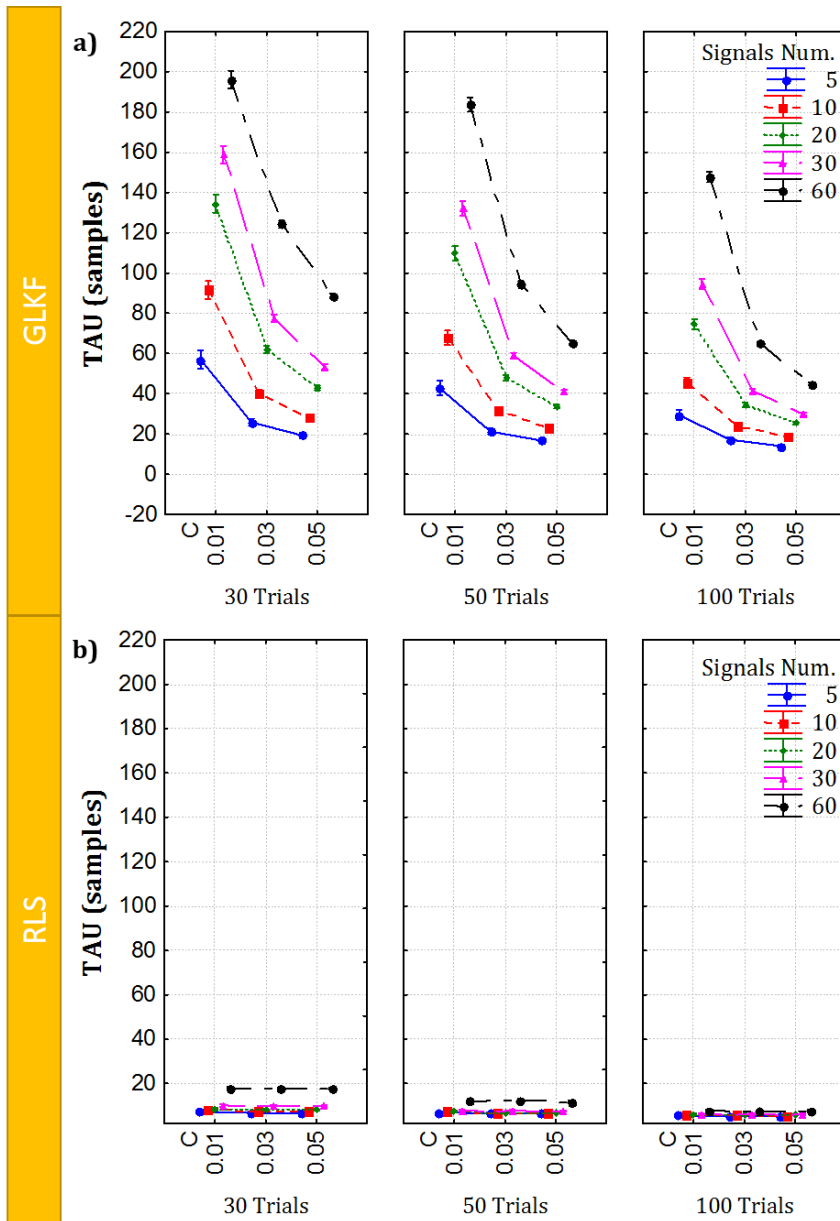


Figure 3.5 - Plot of means associated to the three-way interaction factor ($SIG_NUM \times TRIALS \times CONST$) of the ANOVA performed on the initial adaptation time of the estimator (TAU). Each panel is related with a specific algorithm for the AMVAR coefficients estimation: GLKF (panel a) and RLS (panel b). For each panel, we reported three graphs associated to the different available amount of trials: 30, 50 and 100 from left to right. X-axes always report the levels of the factor $CONST$ and the colours code for different model size. The bars represent their relative 95% confidence interval.

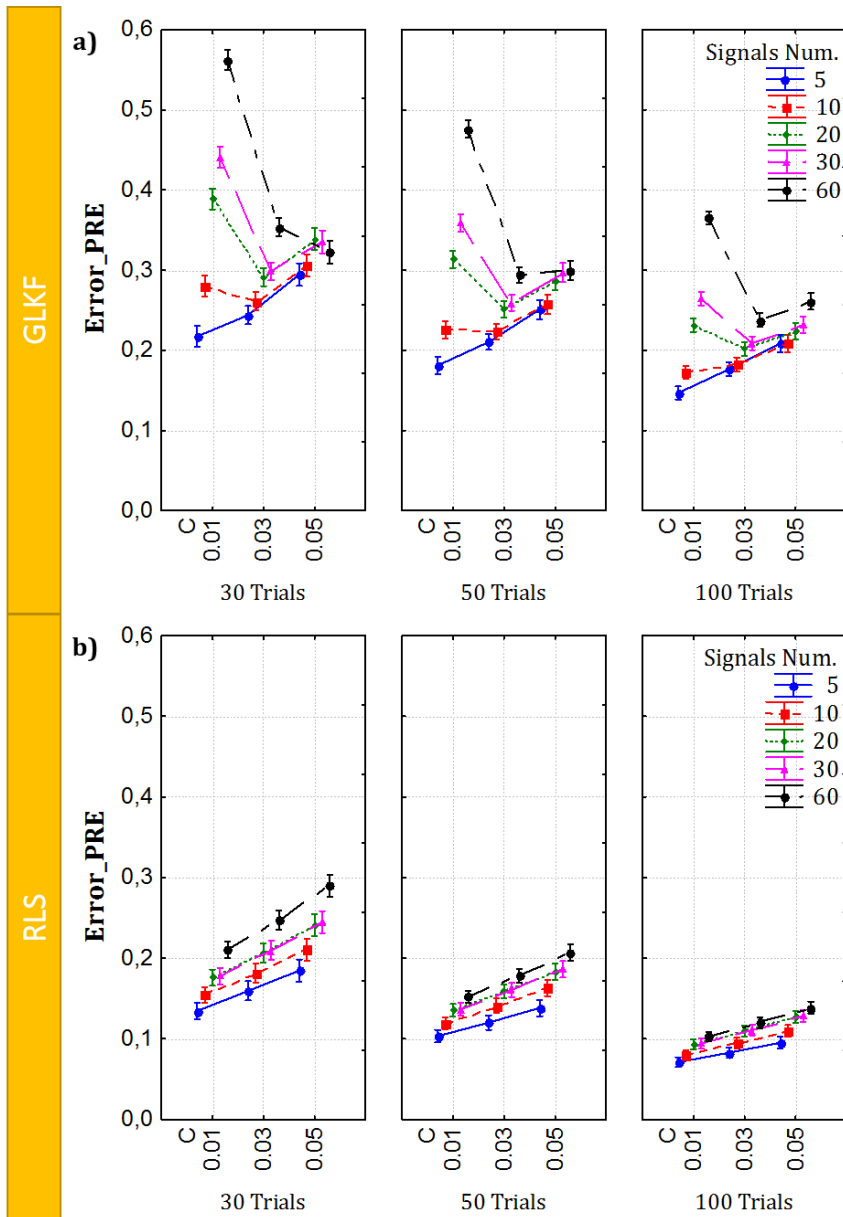


Figure 3.6 - Plot of means associated to the three-way interaction factor ($SIG_NUM \times TRIALS \times CONST$) of the ANOVA performed on the $Error_PRE$ computed in the time interval before the eventual transition. Each panel is related with a specific algorithm for the AMVAR coefficients estimation: GLKF (panel a) and RLS (panel b). For each panel, we reported three graphs associated to the different available amount of trials: 30, 50 and 100 from left to right. X-axes always report the levels of the factor $CONST$ and the colours code for different model size. The bars represent their relative 95% confidence interval.

The first evident result is that the algorithm based on the RLS showed better performance both in terms of accuracy of the estimation and initial adaptation time. TAU index is significantly lower in RLS with respect to the GLKF regardless of all the other parameters and conditions. In particular, figure 3.4b highlighted how the RLS algorithm take always less than 20 samples to reach stably the true value of the connection. On the contrary, the Kalman filter based method showed some limitation in this initial phase. TAU significantly increases when the adaptation constant decreases so that if we select $c1$ and $c2$ equal to 0.01, as concluded according to the results in *fig. 3.2* and *fig. 3.3* (low ST and Error_POST), TAU assumes very high values (*fig. 3.4a*). For this level of the adaptation constants, 30 trials condition and 60 nodes models the algorithm fails because it is not able to conclude the adaptation phase. Consequently, similar observation can be done for the parameter Error_PRE. On the other side, when the RLS algorithm is employed, Error_PRE maintains a value lower than 30% independently of the adaptation constant, the amount of available trials and the model size (*fig. 3.6b*). For the condition in which the adaptation constant is equal to 0.03 (that we identify as the best compromise in the results regarding the transition phase) and TRIALS is equal to 100, Error_PRE never overcome 10%. The GLKF algorithm showed higher value of this index and a significant increase whit the number of signals included in the estimation. Such effect appears amplified for adaptation constants equal to 0.01, when it moves from the 20% for 5-nodes models to 55% for 60-nodes models. In summary: i) RLS algorithm showed the best performance for c equal to 0.03 both, in the initial and transition phases; ii) GLKF results highlighted an important issue due to the difference in terms of accuracy and adaptation time between the two phases. In order to use the method in its best condition for catching the transition ($c1=c2=0.01$ as shown in previous figures) it is necessary to improve its performances in the initial phase of the estimation acting, for example, on the initial conditions. Results related with the initial phase of the GLKF estimates are reported in the following paragraph.

5.2 Simulation Study 2: Initial conditions in GLKF

Results presented in figures 3.7 and 3.8 are related with the three-way ANOVA applied separately to the performance indices defined to evaluate the accuracy and the adaptation time in the phase preceding the transition: Error_PRE and TAU, respectively. Such indices were evaluated on the connectivity patterns estimated by means of GLKF for adaptation constants equal to 0.01 and different levels of the within factors TRIALS and IC_TYPE and the between factor SIG_NUM. The IC_TYPE factor, as better explained in the previous paragraphs, is related with the initial conditions imposed in the algorithm that can assume null values (classical implementation) or values obtained by a stationary estimation of the PDC in the first $popt \times 2$ samples. In Table 3.2 we reported the results of the ANOVA. All the considered factors have a significant influence on the performance of the two algorithms.

Factors	Error_PRE	TAU
SIG_NUM (4,245)	153.02 $p=1*10^{-5}$	866.16 $p=1*10^{-5}$
IC_TYPE (1,245)	14491 $p=1*10^{-5}$	16544 $p=1*10^{-5}$
TRIALS (2,490)	11881 $p=1*10^{-5}$	8910.2 $p=1*10^{-5}$
SIG_NUM x IC_TYPE (4,245)	1008 $p=1*10^{-5}$	835.46 $p=1*10^{-5}$
SIG_NUM x TRIALS (8,490)	194.91 $p=8*10^{-4}$	180.17 $p=1*10^{-5}$
IC_TYPE x TRIALS (2,490)	6804 $p=1*10^{-5}$	6298.1 $p=1*10^{-5}$
SIG_NUM x IC_TYPE x TRIALS (8,490)	329.98 $p=1*10^{-5}$	127.92 $p=1*10^{-5}$

Table 3.2 - Results of the repeated measures three-way ANOVA (*F* values) computed considering as dependent variables Error_PRE and TAU, as within main factors the type of initial imposed conditions (IC_TYPE) and the amount of trials (TRIALS) and as between factor the number of signals included in the estimate (SIG_NUM). The adaptation constants are fixed and equal to 0.01. In the column "Factors" are also reported the degree of freedom.

In the following figures, we reported the box-plots of the three-way interaction factor (IC_TYPE x TRIALS x SIG_NUM) obtained for TAU (fig. 3.7) and Error_PRE (fig. 3.8) parameters, respectively. Diagrams in fig. 3.7 and fig. 3.8, immediately allow noticing the improvement in the considered performance indices when non-null initial conditions (panels b) are computed and imposed in the GLKF algorithm.

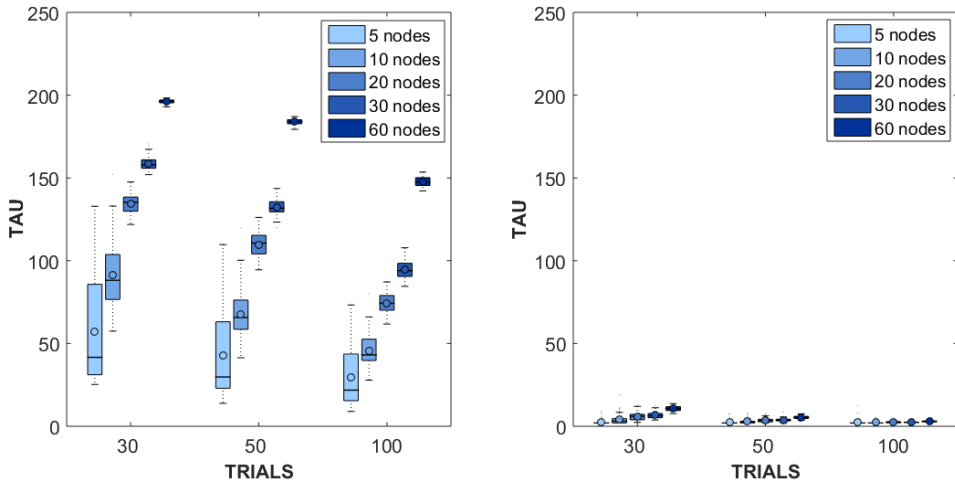


Figure 3.7 – Box-plot associated to the three-way interaction factor ($SIG_NUM \times TRIALS \times IC_TYPE$) of the ANOVA performed on the Samples at Settling (ST) parameter computed for the GLKF algorithm. Panel a) is related with the classical method in which the initial conditions are equal to zero. Panel b) refers to the proposed adaptation of the algorithm (Non-Null initial condition).

In both cases, with null and non-null initial conditions, TAU maintains the same trend with respect to the factors TRIALS and SIG_NUM. In particular, results revealed a significant increase with the increase of the number of signals when the number of trials is low. The most important results regard the difference between the two levels of the factor IC_TYPE. Comparing panels a) and b) emerges a significant and relevant decrease of the initial adaptation time. When the stationary PDC is used as starting point for the algorithm, the number of samples needed to stably reach the true value of the connection to be estimated is always lower than 20 (lower than 10 if the number of trials is 100).

Also the results related with the Error_PRE confirm the improvement in the performance when non-null initial conditions are employed. In panel b) the box plots revealed a significantly higher accuracy considering an error lower than 15% independently of the other factors. An inversion of the trend with respect of the SIG_NUM factor (Error_PRE slightly decrease for big models) can be explained by means of the effect that the amount of data have on the adaptation constants after the adaptation phase (see *fig. 3.4*). In conclusion, the limitations highlighted in the first simulation study for the GLKF algorithm can be overcome using non-

null initial condition exploiting all the advantages of the Kalman filter in the following transition phase.

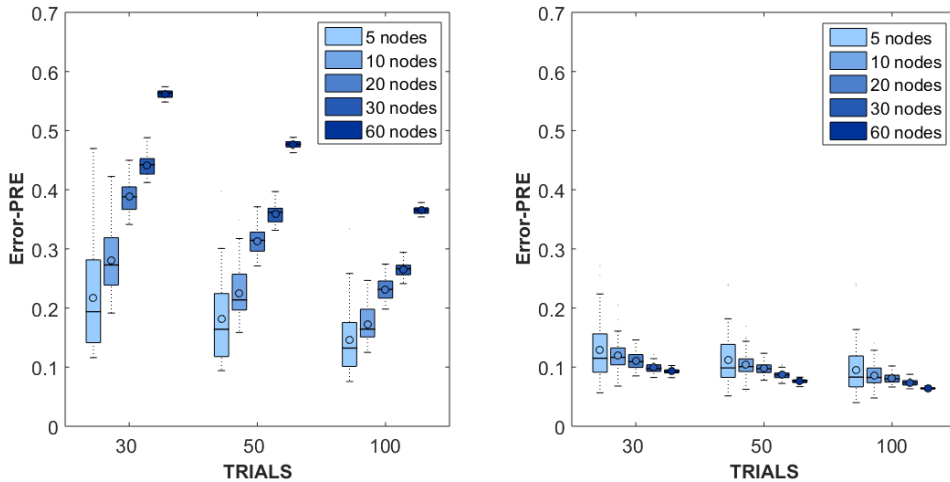


Figure 3.8 – Box-plot associated to the three-way interaction factor ($SIG_NUM \times TRIALS \times IC_TYPE$) of the ANOVA performed on the $Error_PRE$ computed for the GLKF algorithm in the time interval before the eventual transition with the adaptation constants equal to 0,01. Panel a) is related with the classical method in which the initial conditions are equal to zero. Panel b) refers to the proposed adaptation of the algorithm (Non-Null initial condition).

6. Conclusion and Discussion

The simulation studies described above were conducted with the aims to:

- characterize two of the most used techniques for estimating time-varying causal connectivity patterns: GLKF and RLS;
- describe their performances in relation to the adaptation constants to be set during their application in different conditions of amount of data and model size;
- identify their main limitations and try to overcome them.

In order to reach such aims we performed statistical analysis (ANOVAs and Tukey’s pairwise comparisons) on many simulated datasets with imposed connectivity models composed by different number of nodes (from 5 to 60), under different conditions of number of trials included in the estimate whose variability

range is similar to those found during real EEG recordings (30, 50, 100). In particular, we evaluated the performances of these two methods in terms of accuracy in the estimation process and in terms of speed of adaptation to transitions applied on the temporal evolution of connectivity patterns, also putting them in relation to the model dimension. Thus, the performance parameters were evaluated for the two time-varying approaches in relation to the amount of trials included in the estimate, to the adaptation constants set during the estimation process and to the number of nodes characterizing the investigated networks. The performed simulations provided the following answers:

- According to the previous literature we found that the best adaptation constants are 0.03 for the RLS algorithm and ($c_1=c_2$) 0.01 for the GLKF based estimator [57].
- Both the algorithms showed a slight but significant performance improvement when the amount of trial is higher. For datasets with 100 trials we found an increase from 5% to 10% in RLS estimate and from 7% to 9% for Kalman filter based algorithm.
- The most sensitive algorithm to the number of signals included in the estimate is the RSL. Its performance revealed a consistent degradation for big connectivity models. The GLKF, on the other side, once selected the good adaptation constants, showed more stable estimates independently of the quality and the amount of data. In the case of real datasets, especially for the application whom this thesis point at, could be important to record high density EEG (60 channels). At the same time, could be difficult to collect a high number of trials (with low inter-trial variability). Thus, for the real application, the GLKF algorithm represent the best choice in terms of accuracy of the estimate and rapidity in following the link transitions.
- The results obtained for the ST parameter lead to a preference for the GLKF method too. In fact, the comparison between the two algorithms performed in this study demonstrated that GLKF method can substitute the RLS approach in the time-varying estimation of connectivity patterns due to its higher performances in following the temporal dynamics of investigated networks. Time required for settling was below 550 ms for

all the numbers of trials and nodes considered in the study. Such time drastically reduced (around 350 ms) if the trials included in the estimate were 100.

In conclusion, the ANOVA results (integrated with the Tukey's test performed at $p < 0.05$) confirmed what has been qualitatively introduced in previous studies about the issues of time-varying connectivity and its limitation in the dimension of connectivity patterns. The results are in agreement with previous simulation studies performed on the effect of factors such as SNR level and number of trials on the samples at settling and accuracy parameters [60]. The showed simulations allowed to study of the algorithms behaviour only for step changes in the model parameters. In the next steps however, could be interesting to characterize their performances also for slowly varying parameters.

After the discussion of these first results, we tried to understand if the accuracy and the good adaptation times found in the transition phase showed the same range of values also in the initial phase when the algorithms have to start from null conditions. What we discovered was that the GLKF has strong limitations in this time interval. Even for the optimal choice in terms of adaptation constants, the error in the estimation is high (around 20% in the best conditions of number of trials and small model, more than 50% for big models). When the number of signals included in the model is 60, in most cases it is impossible to reach stably the true value of the connection in 1 second. The idea to overcome such limitation was to act on the initial conditions to be set in the algorithm. We modified the algorithm including a preliminary stationary estimation performed on few initial samples of the trials (the first $popt \times 2$, where $popt$ is the optimal order of the model). The estimated connections values where then used as initial condition from the time-varying algorithm. The improvement in the GLKF performances were significant and consistent. In less than 20 ms we are now able to stably reach the value of the link to be estimate and the mean error committed in this phase is always lower than 15%. In conclusion, the new adaptation of the GLKF algorithm for the estimation of time-varying connectivity is a valid tool able to overcome the limits of existent procedures. In fact, the method is able to provide good time-varying estimates characterized by a high accuracy and elevate speed of

adaptation both in the initial and transition phase, also for networks composed by a high number of nodes.

Chapter 4

Effect of head volume conduction on directed connectivity estimated between reconstructed EEG sources

Electrical activity recorded on the scalp using electroencephalography (EEG) results from the mixing of signals originating from different regions of the brain as well as from artefactual sources. In order to investigate the role of distinct brain areas in a given experiment, the signal recorded on the sensors is typically projected back into the brain (source reconstruction) using algorithms that address the so-called EEG “inverse problem”. Once that the activity of sources located inside of the brain has been reconstructed, it is often desirable to study the statistical dependencies among them, in particular to quantify directional dynamical interactions between brain areas. Unfortunately, even when performing source reconstruction, the superposition of signals that is due to the propagation of activity from sources to sensors cannot be completely undone, resulting in potentially biased estimates of directional functional connectivity. Here we perform a set of simulations involving interacting sources, and quantify source connectivity estimation performance as a function of the location of the sources, their distance to each other, the noise level, the source reconstruction algorithm, and the connectivity estimator. The generated source activity was projected onto the scalp and projected back to the cortical level using two source reconstruction algorithms, Linearly Constrained Minimum Variance (LCMV) beamforming and ‘Exact’ Low-resolution Tomography (eLORETA). In source space, directed connectivity was estimated using Multi-Variate Granger Causality (MVG), Time-Reversed Granger Causality (TRGC) and Partial Directed Coherence (PDC), and the estimated connectivity was compared with the imposed ground truth. Our results demonstrate that all considered factors significantly affect the connectivity estimation performance.

¹The study presented in this chapter was conducted in collaboration with the research group of the prof. Daniele Marinazzo at the University of Ghent (Department of Data Analysis, Faculty of Psychological and Educational Sciences) and has been submitted as journal paper.

1. Introduction

Understanding how the joint dynamics of separate brain regions gives rise to function is a fascinating and challenging issue. Several techniques are constantly being developed to investigate these dynamics. EEG signals, due to their high temporal resolution and non-invasiveness, are often employed to investigate how brain activity is modulated in different tasks or conditions [16], [50], [66]–[68]. One of the main issues associated with the EEG signals is the low spatial resolution due to the head volume conduction [13], [69]. It is well known that the electrical activity measured at sensors level is a mixture of the source activity coming from all the sources in the brain (in addition to contributions coming from outside of it). In other words, the spherical geometry of the head and the presence of several tissues with different electrical properties between the cortex and the scalp distort the electric field generated by active neurons so that it is not possible to associate a single brain area to each electrode. The high correlation between signals recorded from neighbouring electrodes at scalp level leads connectivity algorithms to estimate inaccurate patterns including spurious links and to taint results with poor interpretability. Making inferences on connectivity from the EEG signal is still not straightforward [70], [14]. In order to overcome or attenuate the volume conduction problem, several strategies and algorithms have been proposed to estimate source activities from multi-channel EEG recordings [15]. For example, simple spatial filters as the Laplacian can reduce the correlations among scalp-recorded channels induced by the source mixing [69]. Another possibility is given by the Blind Source Separation (BSS) techniques that allow to separate the data into underlying components representing the activity potentially extended networks at the source level. Two algorithms specifically developed for Granger-causal interactions assume that these components follow a multivariate autoregressive (MVAR) model with independent innovation noise [71], [72]. While such approaches allow one to reduce the volume conduction effect, the problem of the interpretability of the results is not completely addressed since directed dynamical influences are estimated between components and not on the cortical brain activity.

Another important choice concerns the connectivity estimator. There are different kind of algorithms and some of them were developed specifically to be less sensitive to artifacts of head volume conduction. Promising results have been obtained using the Phase-Slope Index (PSI) [73] and the Imaginary Coherence (ICoh) [74] but these methods, despite being less sensitive to volume conduction, do not solve the inverse problem and don't allow precise localisation. Furthermore, their bivariate nature leads in some conditions, to spurious links due to hidden sources. In fact, it is well known how pairwise approaches can lead to false positive detections of connections due to their inability to distinguish a direct interaction between two signals from the influence of a common driver acting on both signals. [75]. Among the directed connectivity estimators, worth of note is the class of multivariate estimators based on the concept of the Wiener-Granger Causality (GC) [76]. These data-driven approaches are computationally simple and require no a priori assumption on the presence or absence of interactions between specific pairs of variables. For this reason we decided to focus on three of them: the classical time-domain measure Multi-Variate Granger Causality (MVGC) [39], its adaptation called Time-Reversed Granger Causality (TRGC) that uses time-reversed data as surrogates for statistical testing [14], [77], and the frequency-domain measure Partial Directed Coherence (PDC) [78]. To achieve interpretable results, the reconstruction of brain sources prior to conducting connectivity estimation is required. To solve the ill-posed (as the number of sources higher than the number of sensors) EEG inverse problem, several algorithms are available. Two of the most commonly used algorithms are the 'exact' Low Resolution Tomography (eLORETA) [19], and the Linearly Constrained Minimum Variance (LCMV) Beamformer [18]. Previous studies on real EEG data have already highlighted differences associated with these inverse solutions [79] but additional simulations studies are necessary in order to provide reliable and more specific findings. In other words, different algorithms for the inverse problem solution and for the connectivity estimation could be more or less sensitive to the volume conduction problem, but the evaluation of their performances on real datasets is not possible since an objective ground truth is typically not available. Inverse approaches for extracting cortical waveforms and

Granger-based estimators for connectivity measures can be combined to extract and investigate the human brain circuits but a complete evaluation of the volume conduction effect, in terms of demixing quality, in different experimental conditions is still necessary. It is also important to consider the presence of a localization error associated to the forward model used to describe the relationship between activations in the brain and scalp potentials. A suitable forward model for such validations is the 'New York Head', which is a highly accurate finite element model (FEM) of the electrical current flow of the average adult human head that is based on the segmentation of a highly detailed magnetic resonance image (MRI) into six different tissue types [80]. The goal of the present study is to identify data analysis pipelines combining source localization approaches and methods for brain connectivity estimation that are able to provide accurate and reliable estimates insensitive to the spurious effects induced by the volume conduction, and thereby allow one to interpret the obtained results in neurophysiological terms. In particular, the present study:

- Demonstrates the possibility to significantly reduce the effect of the volume conduction on the connectivity estimates employing appropriate algorithms as the TRGC;
- Provides guidelines for the employment of the best methods with different spatial distributions of the sources (different depth and relative position);
- Evaluates, which source reconstruction approach, among eLORETA and LCMV, leads to a better performance in this context.

In order to reach these aims, a simulation study was performed starting from the generation of simulated data, which mimic brain source signals with an imposed connectivity pattern. The influence of volume conduction on connectivity estimates was investigated by assigning simulated source signals to different anatomical location in the brain. The results of these simulations allow us to identify the best-performing combination of algorithms for the estimation of the brain activity and connectivity in several realistic conditions.

2. Methods

Over the past few decades, different techniques of source localization applied to EEG data were developed to provide a non-invasive estimate of brain activity [81]. Such techniques employ voltage measurements at various locations on the scalp to estimate the current sources inside the brain which best fit these data. Source localization techniques are based on the follow generative model of EEG data:

$$\Phi(t) = \mathbf{L}J(t) + \varepsilon(t) \quad (4.1)$$

where $\Phi(t) \in R^M$ is the EEG signal measured from M scalp locations at time t , $J(t) \in R^{3N}$ is the activity of N sources with a 3D orientation in the space, $\mathbf{L} \in R^{M \times 3N}$ is the leadfield matrix summarizing the propagation of the N electrical sources j to the EEG sensors and $\varepsilon(t) \in R^M$ is the noise associated to the measures. The lead-field matrix \mathbf{L} contains information about the geometry and the conductivity of all the tissues in the head (between the sensors and the sources) and its computation is well-known as *forward modeling*. The estimation of the sources $j(t)$ from the measures $\Phi(t)$ contributes to the source reconstruction purpose and it is well-known as *inverse modeling*. The two modeling approaches will be described in detail below.

2.1 Forward Problem

The forward problem is solved starting from the electrical activity at source level and calculating the potentials at the sensors (electrodes) level. The result is the scalp activity as a function of the current density (produced by neuronal generators) and describes how the electrical field spreads through the different layers of the head. It depends on the geometry and on the electrical properties of the tissues. The New York Head is an accurate finite element electrical model of the average adult human head [80]. It is based on a highly detailed nonlinear average of T1-weighted structural MR image of 152 adults provided by the International Consortium for Brain Mapping (ICBM) [82]. A detailed segmentation of this average image into six tissue types (scalp, skull, CSF, grey matter, white matter, air cavities) was performed at the native MRI resolution of 0.5 mm^3 . The suitability of this volume conductor model to serve as an approximation for

individual heads was tested by comparison with additional BEMs and FEMs constructed for four subjects.

2.2 Inverse Problem

The inverse problem concerns the reconstruction of the brain sources that underlie the measured potentials in electrode space. Because of the difference between the number of sensors and the much higher number of active dipoles in the cortex, the inverse problem solution is not unique. Furthermore, it is very sensitive to small changes in the noisy data and also depends on the choice of the reference electrode. The accuracy of the source reconstruction is affected by a high number of factors including the head model errors, the source-modelling errors and EEG noise (instrumental or biological) [83]. Several algorithms were developed to solve the inverse problem. In the present study, we focused on two methods: i) the Linearly Constrained Minimum Variance Beamformer (LCMV) and ii) the 'Exact' Low Resolution Tomography (eLORETA).

Linearly Constrained Minimum Variance (LCMV)

Linearly constrained minimum variance filtering (LCMV) [83] is a spatial filtering method that lets brain activity coming from a specific location pass, while attenuating activity originating at other locations. The output of the filter is an estimate of the power of the electrical field generated by the neurons within a restricted area of the brain. The spatial pass-band of the filter depends on the dimension of that area, thus the higher the desired resolution the smaller required pass-band. A map of neural power as a function of location is obtained by designing multiple spatial filters, each with a different pass-band, and depicting output power as a function of pass-band location. This spatial filtering approach falls within the general category of beamforming. It is known that the signal at each location in the brain consists of the three dipole moments, so that three spatial filters for each location are required. The $N \times 3$ matrix $\mathbf{W}(q_0)$ represents the transfer function of the filter for the narrowband volume element Q_0 centered in q_0 . The output of the filter, J , is the inner product between $\mathbf{W}(q_0)$ and Φ .

$$J = \mathbf{W}^T(q_0)\Phi \tag{4.2}$$

Under ideal conditions, the transfer function of the filter has to satisfy two conditions:

$$\mathbf{W}^T(q_0)\mathbf{L}(q_0) = I \quad (4.3)$$

$$\mathbf{W}^T(q_0)\mathbf{L}(q_s) = 0 \quad (4.4)$$

As this cannot be achieved under general conditions, eq. 4.4 is replaced by the condition that the variance of the filter output (eq. 4.5) is minimal.

$$\widehat{\text{var}}(q_0) = \text{tr} \{[\mathbf{W}^T(q_0)\mathbf{C}^{-1}(x)\mathbf{W}(q_0)]\} \quad (4.5)$$

The optimal filter is given by:

$$\mathbf{W}(q_0) = [\mathbf{L}^T(q_0)\mathbf{C}_\phi^{-1}\mathbf{L}(q_0)]^{-1}\mathbf{L}^T(q_0)\mathbf{C}^{-1}(x) \quad (4.6)$$

The variance of the filter output can then be simplified as

$$\widehat{\text{var}}(q_0) = \text{tr} \{[\mathbf{L}^T(q_0)\mathbf{C}_\phi^{-1}\mathbf{L}(q_0)]^{-1}\} \quad (4.7)$$

where the sensor-space covariance is:

$$\mathbf{C}_\phi = E[\Phi\Phi^T]. \quad (4.8)$$

The optimal filter $\mathbf{W}(q_s)$ has a large output in q_s only if there is a significant energy originating from there. To localize the electrical activity of the brain sources, the variance of the LCMV filter output is evaluated as a function of location within the volume of the brain, normalized by the LCMV filter output on a reference (noise) data segment. Regions of large relative variance are presumably active, while regions with small relative variance can be considered inactive. Nevertheless, in the present study, the goodness in terms of localization is not of main interest. We only considered the estimated source time series (filter output) to assess connectivity patterns between them. Factors that may influence the accuracy of the LCMV are:

- The pass-band of the filter, indicating the spatial resolution. The spatial extent of the pass-band depends on the transfer matrices $\mathbf{L}(q)$, which in turn depend on the number of electrodes, their distribution, and source location.

- The SNR, because of the variance minimization procedure used to determine the spatial filters. In this context SNR has to be thought of not as ratio of the signal power to the noise power, but rather as the variance of the source divided by the variance of the noise.

'Exact' Low Resolution Tomography (eLORETA)

'Exact' Low Resolution Electromagnetic Tomography (eLORETA) [84] is a linear inverse method characterized by spatially smooth current density. In the most general case, linear solutions to the EEG inverse problem are of the following form:

$$\tilde{J}(\lambda) = \|LJ - \Phi\|^2 + \lambda J^T W J \quad (4.9)$$

where λ represents the Tikhonov regularization parameter which can be estimated through the general cross validation approach [85], and where W is a symmetric positive definite weight matrix. The idea of eLORETA is to find an appropriate W matrix in eq. 4.9 such that the solution has zero localization error for all single point sources in the brain [84]. These weights are obtained from the following expression:

$$w_i = [L_i^T (LW^{-1}L^T + \lambda I_M)^+ L_i]^1/2, \quad (4.10)$$

where w_i for $i = 1, \dots, N$ (number of voxels) are the diagonal elements of the weight matrix W , $L_i \in R^{M \times 1}$ represents the i -th column of lead field matrix L and the symbol $+$ refers to Moore-Penrose pseudoinverse. The solution to (eq. 4.10) can be found by iterating four steps. First, we have to initialize the diagonal matrix W with $w_i = 1$, for $i = 1, \dots, N$ and then compute:

$$C = (LW^{-1}L^T + \lambda I_M)^+. \quad (4.11)$$

Holding C fixed, we compute new weights for all the dipoles $i = 1, \dots, N$:

$$w_i = [L_i^T C L_i]^1/2 \quad (4.12)$$

and then we return to eq. 4.11 until convergence. Once the w_i have been estimated, the eLORETA solution is given by the following expression:

$$[J]_i = w_i^{-1} L_i^T (LW^{-1}L^T + \lambda I_M)^+ \Phi. \quad (4.13)$$

It has been suggested that eLORETA solution achieves exact localization to single test point sources under ideal (no-noise) conditions, outperforming all other linear solutions on both simulated and real EEG data in this respect [86]. However, in the presence of two or more sources (thus, in any setting involving source interaction), this property does not hold anymore.

2.3 Multivariate Directed Connectivity Estimation

Multivariate Granger Causality (MVGC)

The concept of Granger causality [76], [87] is based on the predictability of time series. Namely, if a time series $X_2(t)$ contains information that improves the predictability of future values of another time series $X_1(t)$ above and beyond what can be predicted on the basis of $X_1(t)$ alone, then $X_2(t)$ is said to Granger-cause $X_1(t)$. In other words, if the prediction error decreases by adding the past values of $X_2(t)$ to a regression model for predicting $X_1(t)$, we can assume that $X_2(t)$ Granger-causes $X_1(t)$. In the BIVAR (bi-variate vector-autoregressive) formulation, this notion is described as follows:

$$\begin{pmatrix} x_1(n) \\ x_2(n) \end{pmatrix} = \sum_{k=1}^p \begin{pmatrix} A_{11,k} & A_{12,k} \\ A_{21,k} & A_{22,k} \end{pmatrix} \begin{pmatrix} x_{1,n-k} \\ x_{2,n-k} \end{pmatrix} + \begin{pmatrix} e_{1,n} \\ e_{2,n} \end{pmatrix} \quad (4.14)$$

$$\Sigma \equiv \text{cov} \begin{pmatrix} e_{1,n} \\ e_{2,n} \end{pmatrix} = \begin{pmatrix} \Sigma_{11} & \Sigma_{12} \\ \Sigma_{21} & \Sigma_{22} \end{pmatrix} \quad (4.15)$$

At this point, one can perform a *full regression* (eq. 4.16), using both time series, and a *reduced regression* (eq. 4.17), using only the target time series:

$$x_1(n) = \sum_{k=1}^p A_{11,k} x_{1,n-k} + \sum_{k=1}^p A_{12,k} x_{2,n-k} + e_{1,n} \quad (4.16)$$

$$x_1(n) = \sum_{k=1}^p \mathbf{A}'_{11,k} x_{1,n-k} + e'_{1,n} \quad (4.17)$$

In the full regression, the dependence of X_1 on the past of X_2 , in addition to its own past, is encapsulated in the coefficients $\mathbf{A}_{12,k}$. There is no dependence between X_1 and X_2 if the coefficients are null for all lags k , $\mathbf{A}_{12,1} = \mathbf{A}_{12,2} = \dots = \mathbf{A}_{12,p} = 0$. Prediction error estimation is based on full and reduced regression residuals. In particular $\boldsymbol{\Sigma}'_{11} \equiv \text{var}(e'_{1,n})$ is the residual variance in the case of reduced regression and $\boldsymbol{\Sigma}_{11} \equiv \text{var}(e_{1,n})$ is the residual variance in the case of full regression. Pairwise time-domain Granger causality is defined as

$$f_{X_2 \rightarrow X_1} = \log \frac{|\boldsymbol{\Sigma}'_{11}|}{|\boldsymbol{\Sigma}_{11}|} \quad (4.18)$$

The value of $f_{X_2 \rightarrow X_1}$ is equal to 0 if there is no GC between the time series and their variance ratio is 1. If a dynamical influence from X_2 to X_1 exist, the value of $f_{X_2 \rightarrow X_1}$ is greater than zero. Let us suppose to have joint dependencies between X_1 and X_2 and a third set of variables, e.g. X_3 , then spurious influences may be reported. Spurious connections can be detected even when there is no direct influence $X_2 \rightarrow X_1$ but there are (possibly lagged) dependencies of X_1 and X_2 on X_3 . To overcome this problem, Barnett and Seth propose a different way to compute GC, introducing the so called *Pairwise Conditional Granger Causality (PWCGC)*, which conditions out common dependencies between variables before estimating pairwise GC scores, provided such dependencies are present in the data [88]. The MVAR model is again expressed in the form of full regression (eq. 4.19) and in the form of reduced regression (eq. 4.20), as:

$$x_1(n) = \sum_{k=1}^p \mathbf{A}_{11,k} x_{1,n-k} + \sum_{k=1}^p \mathbf{A}_{12,k} x_{2,n-k} + \sum_{k=1}^p \mathbf{A}_{13,k} x_{3,n-k} + e_{1,n} \quad (4.19)$$

$$x_1(n) = \sum_{k=1}^p \mathbf{A}'_{11,k} x_{1,n-k} + \sum_{k=1}^p \mathbf{A}'_{13,k} x_{3,n-k} + e'_{1,n} \quad (4.20)$$

$$f_{X_2 \rightarrow X_1 | X_3} = \log \frac{|\boldsymbol{\Sigma}'_{11}|}{|\boldsymbol{\Sigma}_{11}|} \quad (4.21)$$

Here, $F_{X_2 \rightarrow X_1 | X_3}$ may be read as “the degree to which the past of X_2 helps to predict X_1 , over and above the degree to which X_1 is already predicted by its own past and the past of X_3 ”. In our simulation study, we are going to use this approach. Additionally it is worth noting that we use the state-space formulation of Granger causality, which eliminates the bias due to the fact that the reduced model is VARMA (Vector Auto Regressive Moving Average) and not VAR [89].

Time reversed Granger causality

Granger-causal estimators are prone to detect spurious influences not only in the presence of hidden common drivers but also in the presence of additive correlated noise [14], [73], [77], [90], [91]. Correlated noise is a ubiquitous property of EEG data, which are by their very nature linear mixtures of contributions from different sources. Since this mixing process cannot be fully undone using source imaging techniques, it poses a serious problem for EEG-based brain connectivity analysis using GC. To overcome the problem of spurious connectivity for mixed data, Haufe et al. proposed time-reversal [14], [34]. The intuitive idea behind this approach is that, if connectivity is defined based on temporal delays, directed influence should be reduced (if not reversed) if the temporal order is reversed. This is in contrast to the observation that two signals that are correlated but Non-Interacting often appear spuriously connected no matter whether GC is applied on the original or time-reversed data. If, however, GC estimates obtained on original and time-reversed data are contrasted with each other, the instantaneous influence of volume conduction can be removed, and the false detection of connectivity can be avoided. GC is defined based on the *Granger-scores* defined in eq. 4.18, where $F_{x_1 \rightarrow x_2}$ is the direct influence from x_1 to x_2 , and it requires that the residual variance of the restricted model should be smaller than the one in the case of full model [73]. When time-reversing the data, we denote the residual covariance matrix of the time-reversed process (full model) by:

$$\tilde{\Sigma} = \begin{bmatrix} \tilde{\Sigma}_{11} & \tilde{\Sigma}_{12} \\ \tilde{\Sigma}_{21} & \tilde{\Sigma}_{22} \end{bmatrix} \quad (4.22)$$

As for the original GC, we define the dynamical influence as

$$F_{\tilde{x}_2 \rightarrow \tilde{x}_1} = \log \left(\frac{\tilde{\Sigma}'_{11}}{\tilde{\Sigma}_{11}} \right) \quad (4.23)$$

Finally, Time-reversed GC is given by the difference between the net GC scores obtained on the original and time-reversed GC:

$$\tilde{D}_{\tilde{x}_1 \rightarrow \tilde{x}_2} = F_{\tilde{x}_1 \rightarrow \tilde{x}_2} - \tilde{F}_{\tilde{x}_1 \rightarrow \tilde{x}_2} \quad (4.24)$$

Using the above definitions, the validation of a Granger causal influence that cannot be explained by a mixture of independent sources can be performed according to the following criterion, named Conjunction-based time-reversed GC:

- the directionality of GC is required to flip for time-reversed signals. The connection is regarded as significant if both GC values (with original and reversed data), are significant: $F_{\tilde{x}_1 \rightarrow \tilde{x}_2} > 0 \wedge \tilde{F}_{\tilde{x}_1 \rightarrow \tilde{x}_2} < 0$. This is the definition adopted in the present paper.

Other criteria, less stringent than this one, are discussed in [77]. Simulations have shown that TRGC leads to a reduced number of false connections, compared to original GC and its variants [14], [77], [90]–[92].

Theoretical work presented in [77] has moreover shown that :

- The application of time reversal to any connectivity measures that is based on second order statistics - which, besides GC and pairwise-conditional GC also includes its direct extension to frequency domain (spectral GC) and the popular frequency-domain measures partial directed coherence (PDC) and directed transfer function (DTF), among others - prevents the spurious detection of connectivity on mixtures of independent sources that would otherwise be highly likely.
- The application of time reversal to Granger causality (that is, the use of TRGC) is guaranteed to always yield the correct direction of interaction for systems that do not contain causal loops, and are noise-free.

Partial directed coherence (PDC)

Partial Directed Coherence (PDC) [41] is a spectral measure to assess the dynamical influence between signals within a multivariate dataset. It is basically

a frequency version of the concept of Granger causality [42]. Its mathematical definition has been introduced in the Methods section of the Chapter 2.

2.4 Statistical assessment of significant connections

The standard way to assess the statistical significance of Granger scores is a likelihood ratio test, which can be derived from large-sample theory [93]. If $\dim(X_1) = n_{x1}$, $\dim(X_2) = n_{x2}$ and $\dim(X_3) = n_{x3}$ (with $n_{x1} + n_{x2} + n_{x3} = n$) then the difference in the number of parameters between the full model and the nested reduced model (see eq. 4.20) is just $d \equiv p_{n_{x1} n_{x2}}$. Thus, under the null hypothesis of zero Granger-causal influence, the GC estimator scaled by sample size, $(m - p) F_{X_2 \rightarrow X_1 | X_3}(u)$, has an asymptotic χ^2 distribution. Under the alternative hypothesis, the scaled estimator has an asymptotic noncentral χ^2 ($d; \nu$) distribution, with non-centrality parameter $\nu = (m - p) F_{X_2 \rightarrow X_1 | X_3}(u)$ equal to the scaled actual influence (which may, for the purpose of constructing confidence intervals, be replaced by its estimator). Similarly, it was demonstrated that the squared PDC estimator tends to a Gaussian distribution in the non-null case and to a χ^2 distribution in the null case. This assumption led to the development of a new approach, the asymptotic statistic, which allowed the derivation of the probability distribution of the null-case squared PDC estimator (the χ^2 distribution), by knowing its asymptotic variance [47], [49]. Note that these standard statistical tests are only capable to distinguish actually present GC/PDC effects from results obtained due to random signal fluctuations in the absence of GC/PDC. They are *not* capable of distinguishing actual GC/PDF effects that are due to genuine time delayed interaction from actual GC/PDC effects that are solely due to additive mixed noise in the absence of genuine time-delayed interaction. To test for the latter, the statistical significance of TRGC (or, time-reversed PDC) needs to be established. For difference-based TRGC, this can be achieved by testing whether (eq. 4.28) is significantly different from zero using non-parametric approaches like the bootstrap. In this work, we focus on conjunction-based TRGC and we used an alpha of 0.05, FDR corrected.

2.5 Simulation Framework

The simulation study developed for investigating the effects of the volume conduction on connectivity estimation accuracy and reliability is composed by the following main steps:

- Generation of brain signals with an imposed connectivity pattern
- Forward problem solution
- Inverse problem solution
- Connectivity estimation
- Performance evaluation

An overview of the simulation framework, with all the considered factors, is shown in *fig.4.1*.

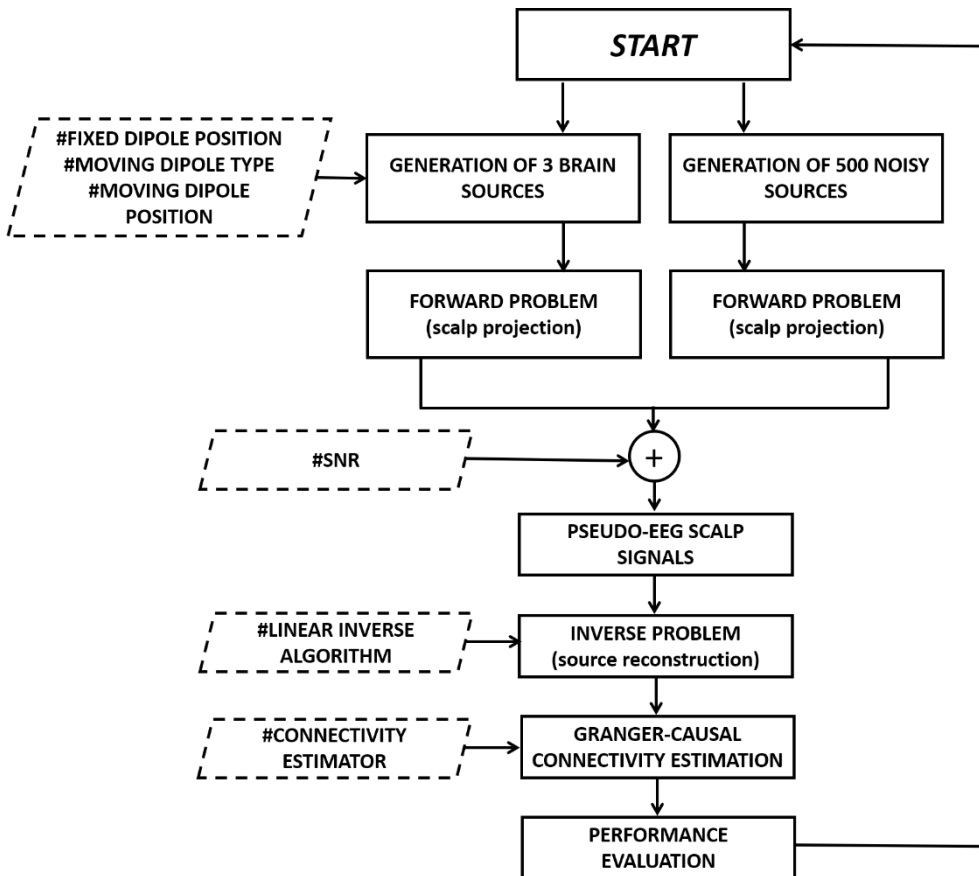


Figure 4.1 – Block diagram reporting the main steps of the simulation framework.

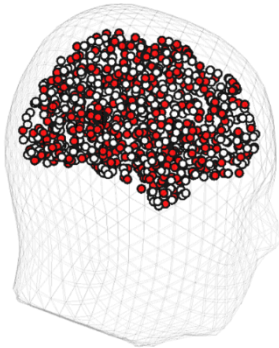
2.6 Simulated time series generation

Brain signals were generated using a multivariate autoregressive (MVAR) model with order 2 as generator filter. We simulated three time series and only one connection. Both, the autoregressive components and the off-diagonal elements of the coefficients matrix were randomly chosen within the range [0.3 1]. The three different time series will be called *Sender*, *Receiver* and *Non-Interacting dipole*, to indicate, respectively, the driving dipole, the receiving dipole, and the independent dipole. Each of them represents an active source contributing to the simulated EEG scalp potentials. In order to simulate an experimental condition as realistic as possible, we also generated 500 pink noise signals representing the background brain activity.

2.7 Simulated time series location

Brain activity was modelled with 1006 electric equivalent dipoles, equally distributed within the brain. Using the New York Head model, we obtained the dipole positions by subsampling the 75000 MNI coordinates available in the ICBM152 model. In the panel a of *fig. 4.2* we showed all the 1006 possible dipole locations.

a)



b)

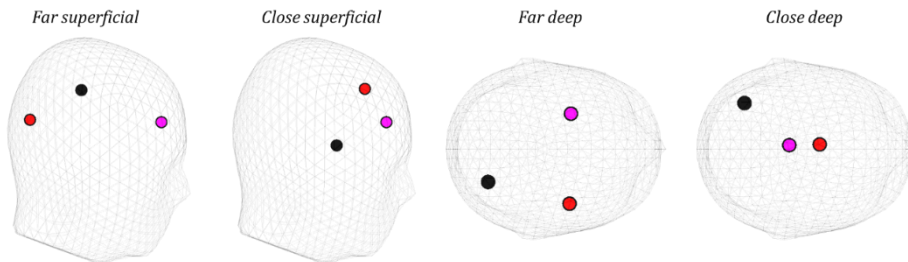


Figure 4.2 - Panel a) shows the 1006 locations in which activity was modelled. Red circle represents an example of the 500 locations associated with the brain noise activity. Panel b) presents the four conditions for the two fixed active dipoles, which are the red (Sender) and the purple (Receiver) one. The black circle represents the Non-Interacting dipole (noise).

For each simulation, we fixed the position of two active dipoles on four possible conditions (represented in *fig.4.2b*) defined from the combination of the following factors:

- Depth of the dipoles: “superficial” (distance from the origin >6.5 cm) or “deep” (distance from the origin <6 cm);
- Distance between the dipoles: “far” (relative distance >8 cm) or “close” (relative distance <5 cm).

The third dipole (*moving dipole*) instead, change its location on the 1004 possible remaining positions. Two different cases were analysed by changing the moving dipole. In the first case, it is the Non-Interacting dipole, thus the connection is fixed. In the second case, the moving dipole is the Receiver; thus, the relative

locations of Sender and Receiver varies across repetitions. The 500 additional noisy elements were randomly distributed within the brain.

2.8 Pseudo-EEG signal generation.

After the signals generation, the time series representing both the source activity and the noise, were projected onto 108 EEG electrodes defined by the New York Head model, and summed according to following equation:

$$x^{brain}(t) = \alpha * \frac{x^{act_s}(t)}{\|x^{act_s}(t)\|_F} + (\alpha - 1) * \frac{x^{noise_s}(t)}{\|x^{noise_s}(t)\|_F}, \quad (4.25)$$

where x^{act_s} and x^{noise_s} are the projections of the active sources signals and of the brain noise sources activity respectively, and where $\|x(t)\|_F$ is the Frobenius norm of the multivariate time series $x(t)$ (the square-root of the sum of the squared activity across time and space). The parameter α thereby defines the signal-to-noise ratio. Given α , the corresponding SNR in decibels (db_s) is:

$$db_s = 20 * \log_{10} \left(\frac{\alpha}{1-\alpha} \right). \quad (4.26)$$

Finally, in order to simulate the measurement noise, spatially and temporally uncorrelated signals are added to $x^{brain}(t)$ with an imposed α equal to 0.9. The overall pseudo-EEG data is defined from the following equation:

$$x(t) = 0.9 * \frac{x^{brain}(t)}{\|x^{brain}(t)\|_F} + 0.1 * \frac{x^{noise}(t)}{\|x^{noise}(t)\|_F}, \quad (4.27)$$

where x^{noise} is the white uncorrelated noise.

2.9 Source reconstruction and directed connectivity estimation

The simulated pseudo-EEG signal was projected onto the cortical surface using two different inverse problem solutions: LCMV and eLORETA. The regularization parameter to be set in the eLORETA algorithm was chosen by means of a cross-validation approach. In cortical source space, directed connectivity according to MVGC, TRGC and PDC was estimated at the locations of the three simulated active dipoles, and the statistical significance of the estimated connections was assessed.

2.10 Performance parameters

The quantitative evaluation of the accuracy in signals reconstruction and connectivity estimation was performed by means of three parameters: the False Positive Rate (FPR), the False Negative Rate (FNR) and the Area Under ROC Curve (AUC). Such parameters were computed by comparing the estimated connectivity pattern with the imposed ground-truth. A false positive (FP) is an estimated (statistically significant) connection that is not present in the simulated data, while a true negative (TN) is an absent simulated connection that is correctly estimated as being absent. The FPR (see *eq. 4.31*) is the number of false positives normalized by the number of absent connections. The FPR is thus defined as in the follows:

$$FPR = \frac{FP}{FP+TN}. \quad (4.28)$$

The FNR quantifies the percentage of missed (not statistically significant) connections (referred to as false negatives, FN) that are actually present in the simulated data relative to the total number of actually present simulated connections. The latter number is given as the sum of false negatives and true positives (TP, referring to actually present connections that are also estimated to be present). The FNR is thus defined as follows:

$$FNR = \frac{FN}{FN+TP}. \quad (4.29)$$

In this study, the total number of possible connections is six (2 possible directions for three distinct pairs of variables). As only one interaction was modelled, FN+TP equals one, while the number of absent connections (FP + TN) is equal to five.

The AUC is a measure of binary classification accuracy, which is applied here to the problem of distinguishing between interacting and Non-Interacting signals. It takes into account both the FPR and FNR across the entire range of all possible thresholds for the connectivity measure; therefore, it is independent of a specific significance level. The AUC is bounded between 0.5 (chance-level class separation) and 1 (perfect class separation) and was derived from the Wilcoxon-Mann-Whitney test [94].

2.11 Statistical Analysis

In order to statistically evaluate the accuracy of the employed algorithms in reconstructing the sources activity and estimating brain networks, a four-way ANalysis Of VAriance (ANOVA) was computed. The main within factors were:

- the fixed dipoles position (DIP_POS) with 4 levels: Close Deep, Close Superficial, Far Deep, Far Superficial;
- the adopted inverse methods (L_INV_METH) with 2 levels: eLORETA, LCMV;
- the connectivity estimator (EST_TYPE) with 3 levels: MVGC, PDC, TR_GC;
- the signal-to-noise ratio (SNR) defined by 3 levels of α : 0.5, 0.7, 0.9 (corresponding to SNR equal to 0, 7 and 19 dB respectively) that in the next will be identified as “low”, “medium” and “high” value of SNR.

The dependent variables were the three introduced performance parameters (FPR, FNR and AUC) averaged on the 1004 possible location of the moving dipole. The simulation was repeated 100 times for each experimental condition. Additionally, a post hoc analysis was performed in order to highlight the significant comparisons between the various level of the included factors and their interaction, using Tukey's range test.

2.12 Topographical visualization of the results

As described in the previous paragraph, the ANOVA investigates the performance parameters averaged for more than one thousand possible locations of the moving dipole. In order to obtain a detailed overview on the variations of the estimate accuracy as function of the position of the moving dipole, we averaged the parameters on the 100 iterations and reported the obtained results in 3D brain maps. The color of each one of the 1004 dipoles codes for the value of the FPR. We do not report the maps obtained for the false negatives because their amount is always very low (less than 5%). With the aim to summarize the complex information contained in the brain maps, we also calculated the FPR as function of the distance between Sender and Receiver as well as between Sender and Non-Interacting dipole for each SNR level, inverse approach, and connectivity estimator. The position of the fixed dipole (either Receiver or Non-Interacting dipole) in these analyses was *far* and *superficial*.

3. Results

3.1 Statistical analysis

The results of the four-way ANOVA computed separately for the three performance parameters are reported in Table 4.1. A four-way ANOVA consists of fifteen separate multiple tests (four main effects, six two-way interactions, four three-way interactions, and one four-way interaction). Therefore, a correction for multiple comparisons (Bonferroni-Holm for example) was performed.

<i>Factors</i>	<i>FPR</i>	<i>FNR</i>	<i>AUC</i>
L_INV METH (1,99)	86,25 $p=1*10^{-5}$	68,27 $p=1*10^{-5}$	41,43 $p=1*10^{-5}$
EST_TYPE (2,198)	1686,5 $p=1*10^{-5}$	8,45 $p=0,0003$	1652,6 $p=1*10^{-5}$
SNR (2,198)	357,14 $p=1*10^{-5}$	67,42 $p=1*10^{-5}$	570,29 $p=1*10^{-5}$
DIP_POS (3,297)	930,51 $p=1*10^{-5}$	62,13 $p=1*10^{-5}$	1292,1 $p=1*10^{-5}$
L_INV METH x EST_TYPE (2,198)	14,55 $p=1*10^{-5}$	15,16 $p=1*10^{-5}$	13,03 $p=1*10^{-5}$
L_INV METH x SNR (2,198)	23,68 $p=1*10^{-5}$	101,48 $p=1*10^{-5}$	2,5 $p=0,084$
EST_TYPE x SNR (4,396)	91,06 $p=1*10^{-5}$	45,73 $p=1*10^{-5}$	74,73 $p=1*10^{-5}$
DIP_POS x L_INV METH (3,297)	82 $p=1*10^{-5}$	86,54 $p=1*10^{-5}$	15,14 $p=1*10^{-5}$
EST_TYPE x DIP_POS (6,594)	225,55 $p=1*10^{-5}$	5,69 $p=1*10^{-5}$	181,71 $p=1*10^{-5}$
DIP_POS x SNR (6,594)	84,16 $p=1*10^{-5}$	90,47 $p=1*10^{-5}$	59,74 $p=1*10^{-5}$
L_INV METH*EST_TYPE*SNR (4,396)	34,76 $p=1*10^{-5}$	27,24 $p=1*10^{-5}$	18,96 $p=1*10^{-5}$
L_INV METH*EST_TYPE*DIP_POS (6,594)	23,43 $p=1*10^{-5}$	24,61 $p=1*10^{-5}$	29,39 $p=1*10^{-5}$
L_INV METH*SNR*DIP_POS (6,594)	14,54 $p=1*10^{-5}$	79,11 $p=1*10^{-5}$	54,39 $p=1*10^{-5}$
EST_TYPE*SNR*DIP_POS (12,1188)	3,42 $p=1*10^{-5}$	28,93 $p=1*10^{-5}$	3,98 $p=1*10^{-5}$
L_INV METH x EST_TYPE x SNR x DIP_POS (12,1188)	47,67 $p=1*10^{-5}$	17,3 $p=1*10^{-5}$	42,27 $p=1*10^{-5}$

Table 4.1 - Results of the four-way ANOVA (*F* values) computed considering as dependent variables FPR, FNR and AUC and as within main factors the type of inverse algorithm (L_INV METH), the connectivity estimator (EST_TYPE), the SNR and the position of the fixed dipoles (DIP_POS). In the column “Factors”, the degrees of freedom are also reported.

All factors and all interactions between factors have a significant effect on the FPR, FNR and AUC. In the following, we show a graphical depiction of the means of the four-way interaction factor (L_INV METH x EST_TYPE x SNR x DIP_POS) for each investigated performance measure.

False Positives Rate

Figure 4.3 shows means obtained for the FPR for different levels of SNR (α) and dipole positions when specific algorithms for the inverse solution and connectivity estimation are employed.

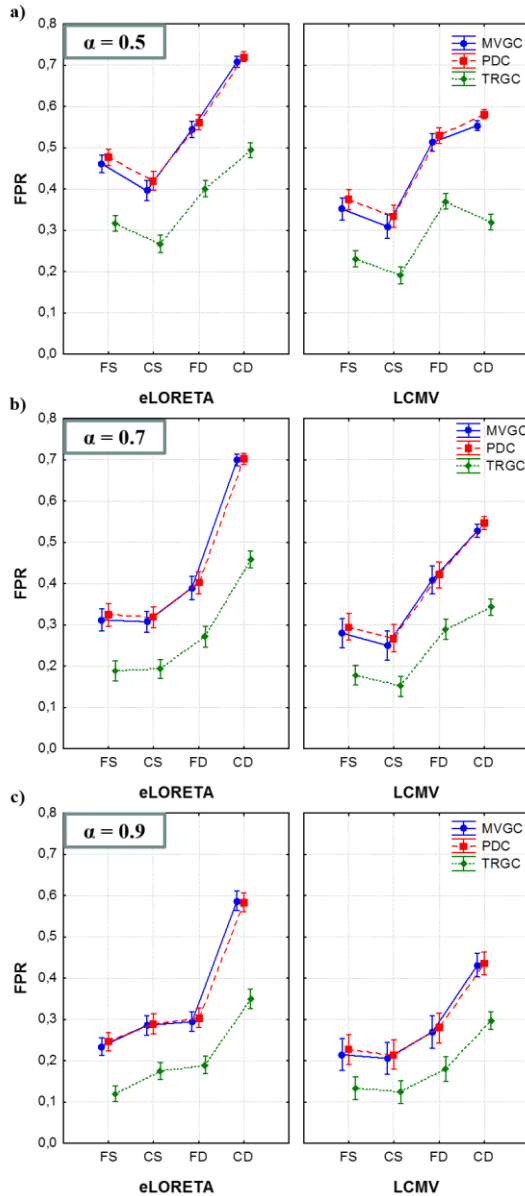


Figure 4.3 - Means associated with the four-way interaction factor (L_INV METH \times EST_TYPE \times SNR \times DIP_POS) of the ANOVA performed on the FPR. Each panel corresponds to a specific value of the SNR parameter α : 0.5 (panel a), 0.7 (panel b), 0.9 (panel c). For each panel, there are two graphs associated with the two different inverse solutions: eLORETA on the left and LCMV on the right. X-axes report the levels of the factor DIP_POS and the colours code for the three connectivity estimators. Whiskers represent 95% confidence intervals. Each panel depicts results obtained for one SNR level.

These graphs show how the two different inverse methods and the location of the fixed dipoles influence the amount of false positive connections when the estimation is performed with the three different connectivity estimation algorithms for different levels of SNR.

Connectivity Estimator: As expected, we found that the amount of false positive decreases when the connectivity pattern is extracted by means of TRGC. FPR associated with the TRGC is significantly lower (Tukey test) with respect to the other two methods independently of the dipoles position, the SNR level and to the inverse algorithm (see all the subplots). MVGC and PDC do not show significantly different results for each condition, and the number of estimated spurious connections is not significantly different.

Inverse Algorithm: For each panel, we can compare the performance associated with the different inverse solutions comparing the two subplots. Regardless of the SNR, the LCMV algorithm (on the right) for source reconstruction has globally better performance than eLORETA (on the left) for all the three SNR values. The post hoc analysis reveals a significant increase of the FPR for eLORETA, compared to LCMV, in all the considered conditions of SNR, dipoles position, and connectivity estimator. Only in the most advantageous configuration, when α equals 0.9, indicating high SNR, and the linked dipoles are in the *Far/Superficial* configuration, such difference is not significant. In the worst case, corresponding to the *Close/Deep* configuration, the FPR is considerably high, especially for the eLORETA reconstruction, where it exceeds 70%, and the difference between the performances of the two inverse methods appears to be emphasized.

Fixed dipoles position: It is worth to note how performance critically depends on the position of the fixed dipoles. Independently of the employed inverse algorithm and connectivity estimator, the ANOVA suggested that when they are located deep in the brain the amount of false positives significantly increases. When the fixed dipoles are superficial and α is equal 0.7, the relative distance (close/far) does not have a significant influence on the FPR. For the higher SNR levels, the ANOVA highlighted a significant increase of the FPR from 10% to 20%, suggesting that the optimal condition for the source reconstruction is given by far and superficial dipoles. For the very low SNR value of 0.5, for all the L_INV METH

and EST_TYPE levels, the statistical test revealed a significant decrease of FPR in the *Close/Superficial* case relative to the *Far/Superficial* case.

SNR: In all considered conditions, the test indicates a significant improvement of performance when the simulated SNR is higher. More in detail, when the SNR level is 0.9, the amount of false positives is less than 30% in all the cases except for the *Deep/Close* condition. The analysis of FPR suggests that the best combination of factors is given, for all the considered SNR levels, by: i) dipoles located superficial in the brain and not too close; ii) LCMV as algorithm for the inverse problem solution and iii) TRGC as connectivity estimator. Only in this case the percentage of false positives reached low values (around 10% for SNR equal to 0.9).

False Negative Rate

The graphs in *fig. 4.4* depict the means of the four-way interaction factor (L_INV METH x EST_TYPE x SNR x DIP_POS) obtained for the FNR index. The percentage of false negatives is less than 5% in all simulated cases, except for the lowest SNR level (α equal to 0.5) when LCMV is employed. In the easier condition with a higher signal to noise ratio and interacting dipoles that are not deep and close at the same time, the FNR is around 1% regardless of the chosen connectivity estimator.

Connectivity Estimator: The factor EST_TYPE does not have a significant effect on the FNR index independently of all the other factors (SNR value, type of algorithm chosen for the source reconstruction and connectivity estimation): its variations never exceed 1%. Also, the slight increase of false positives associated with the time reversed adaptation of GC is not statistically significant in this case.

Inverse Algorithm: The percentage of FN obtained with the two inverse methods is strictly linked to the dipoles' position. Results reported in panel a) show that for SNR equal to 0db, FNR significantly increases for LCMV only when the dipoles are located deep in the brain (accounting for an increase of 20% in the *Close/Deep* condition). Panel b) shows a similar but attenuated trend for α equal to 0.7 (increase of less than 5% in the *Close/Deep* condition). As shown in panel c), there are no significant differences between LCMV and eLORETA for the highest SNR value.

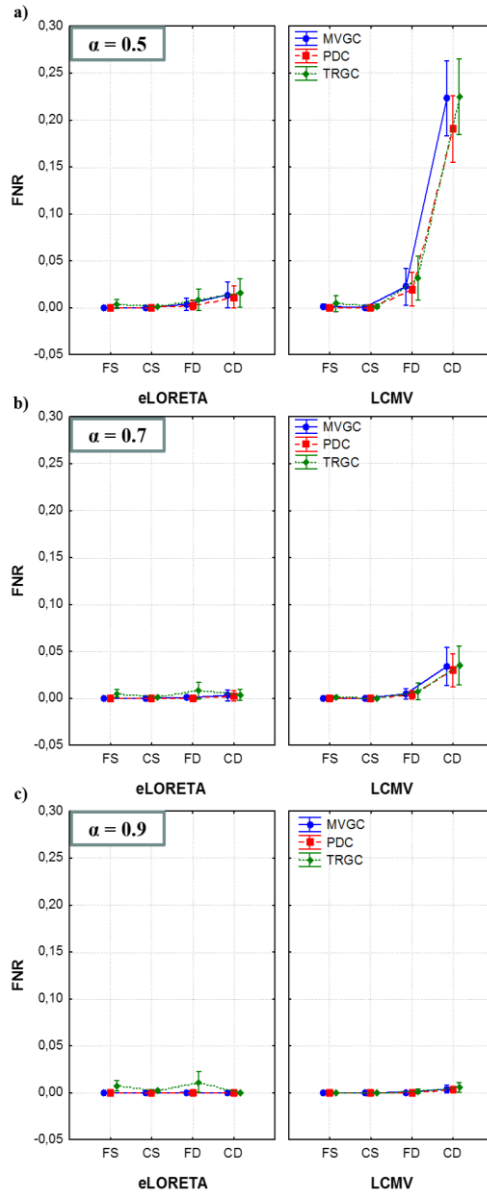


Figure 4.4 - Means associated with the four-way interaction factor ($L_INV\ METH \times EST_TYPE \times SNR \times DIP_POS$) of the ANOVA performed on the FNR. Each panel corresponds to a specific α level: 0.5 (panel a), 0.7 (panel b), 0.9 (panel c). For each panel, there are two graphs associated with the two different inverse solutions: eLORETA on the left and LCMV on the right. X-axes always show the levels of the factor DIP_POS and the colours code for the three connectivity estimators. Whiskers represent 95% confidence intervals. Each panel depicts results obtained for one SNR level.

Fixed dipoles position: The factor DIP_POS is significant for low and medium SNR values and L_INV METH corresponding to LCMV. In such conditions, for deep dipoles, the FNR is significantly higher, regardless the connectivity estimator. Moreover, focusing on the deep locations, there is a significant increase of the false negatives when the dipoles are close compared to when they are further away.

SNR: the signal-to-noise ratio associated to the three levels of the factor SNR significantly influences the presence of false negatives only when the inverse problem is solved by the LCMV algorithm. This is particularly the case for the condition *Close/Deep*, in which the FNR decreases from 20% when α is equal to 0.5 (panel a) to 4% when α is equal to 0.7 (panel b), and to 1% for the highest SNR level (panel c). This suggests that the amount of false negatives is independent of the algorithm employed for solving the inverse problem and for the connectivity estimation. In case of poor signal quality (low SNR), the FNR is considerable when the sources to be reconstructed are located deep in the brain. Algorithms that are more prone to missing connections are LCMV for source reconstruction and TRGC as connectivity estimation.

AUC

The graphs in *fig. 4.5* depict the means of the four-way interaction factor (L_INV METH x EST_TYPE x SNR x DIP_POS) obtained for the AUC parameter. The AUC index hereby summarizes the effect of the four considered factors on the accuracy of the estimation in term of false positives and false negatives, providing a unifying measure of the discriminability of actually present and non-existent connections.

Connectivity Estimator: As expected from the previous results concerning the FPR trend, the accuracy of the estimation considerably increases when performed by means of TRGC. The increase of the performances associated with TRGC is statistically significant and amounts to about 10%. Confirming what has already been demonstrated for FPR and FNR, the accuracy of MVGC and PDC is not significantly different in any condition.

Inverse Algorithm: On average, the difference between LCMV and eLORETA is not significant, but there are combinations of the factors for which either of the two performed better. The main discrimination is given by the linked dipoles position. When the sources are located deep in the brain (especially if they are

also close), the accuracy of the connectivity estimation appears significantly higher when LCMV is employed to reconstruct the brain activity. Once again, the only exception is the low SNR setting, in which this relationship is reversed because LCMV is more sensitive to the SNR level compared to the eLORETA algorithm, which shows more stable performance.

Fixed dipoles position: Independent of the employed inverse algorithm and connectivity estimator, the accuracy of the estimation significantly decreases when the linked dipoles are located deep in the brain. For higher SNR levels, the ANOVA highlights a performance degradation in terms of the AUC dropping from 90% (*Far/Superficial*) to 70% (*Close/Deep*).

SNR: As expected, the performance significantly improves in all considered conditions when the simulated SNR is high. More specifically, when the SNR level is 0.9, the accuracy is higher than 85% for eLORETA and higher than 90% for LCMV in all the cases except for the *Deep/Close* condition.

The analysis of the AUC index suggests that the optimal combination of factors is given by: i) dipoles located superficial in the brain and not too close; ii) LCMV algorithm when the SNR is not too low, otherwise eLORETA; iii) TRGC as connectivity estimator.

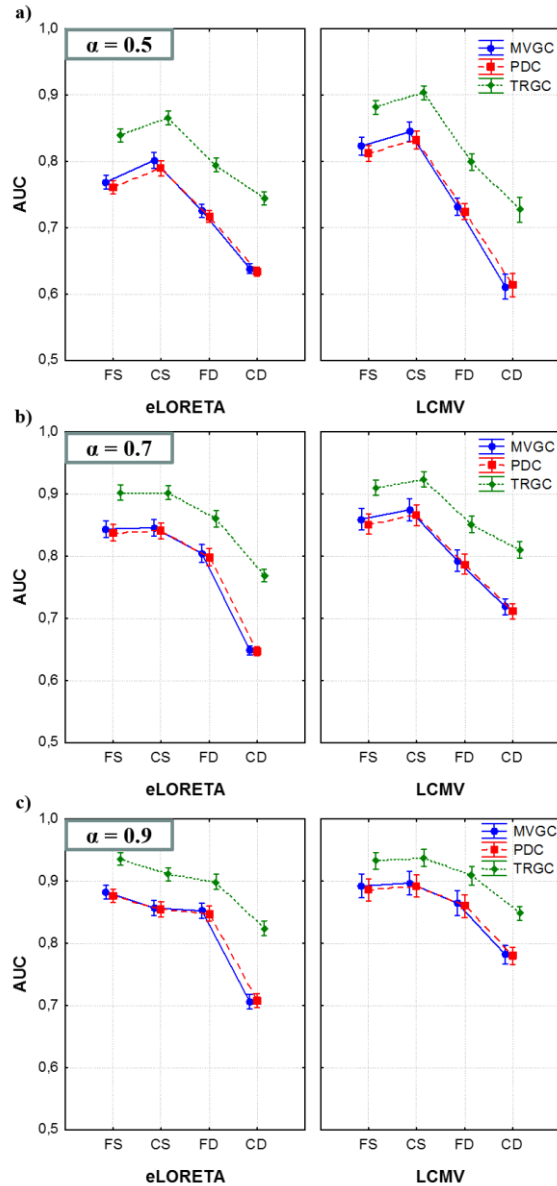


Figure 4.5 - Means associated with the four-way interaction factor (L_INV METH \times EST_TYPE \times SNR \times DIP_POS) of the ANOVA performed on the FNR. Each panel corresponds to a specific α level: 0.5 (panel a), 0.7 (panel b), 0.9 (panel c). In each panel, there are two graphs associated with the two different inverse solution: LCMV on the left and eLORETA on the right. X-axes report the levels of the factor DIP_POS and colours code for the three connectivity estimators. Whiskers represent 95% confidence intervals. Each panel depicts results obtained for one SNR level.

3.2 Brain maps

Non-Interacting dipole position

As mentioned before, in each simulated condition, the moving dipole changes its position over 1004 locations equally distributed in the brain. In order to map the performance of the three connectivity estimators for each investigated source reconstruction algorithm and each position of the fixed dipoles, MVGC, PDC and TRGC were computed considering all the 1004 possible configurations of the network. Since each simulation was iterated 100 times, we were able to obtain an average performance value. Only the maps depicting the FPR are reported because of the greater sensitivity of this indicator to the factors considered in the analysis. We report transparent axial views of the head for each choice of fixed dipoles position and inverse method. Only 2 out of 3 estimators are reported because the PDC performances are similar to those obtained using the MVGC algorithm in all the considered conditions. We report the value assumed by the FPR (coded by its color) in the position of the moving dipole associated with that measure. Figure 4.6 reports the results obtained for the lowest SNR level, when α is equal to 0.5.

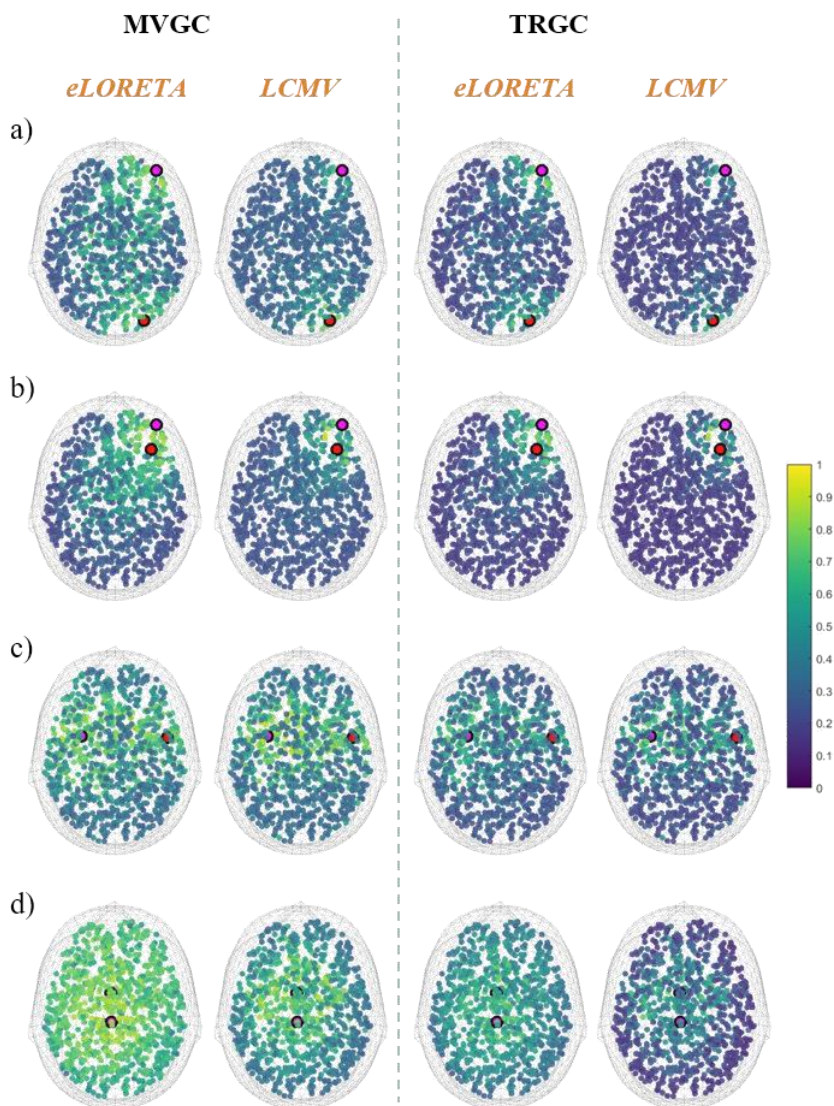


Figure 4.6 – Spatial distribution of the FPR in the Moving Non-Interacting Dipole condition for low SNR ($\alpha = 0.5$). Shown are the Sender (red circle) and Receiver (purple circle) of the interaction in the Far-Superficial (a), Far-Deep (b), Close-Superficial (c), and Close-Deep (d) conditions. The other points represent the mean value of the FPR across 100 iterations (coded by the colour bar on the right side) when the third active dipole (the Non-Interacting one) is moved across the brain. The first two columns refer to the classical GC (MVGC algorithm); the last two to the TRGC. For each column, results obtained with eLORETA and LCMV are reported next to each other.

The percentage of false positives depends on the distance of the Non-Interacting dipole from the two fixed ones. The most relevant result is that when the fixed dipoles are located deep in the brain and close to each other (panel d), high FPR values are spread across the whole brain, and reach 100% in the vicinity of the Sender and Receiver. Only TRGC combined with the LCMV algorithm mitigates this effect, which is then limited to the configurations in which the Non-Interacting dipole is close to the other two. Panels a), b) and c) clearly show a strong increase of the FPR when the Non-Interacting dipole is located in the areas close to the Receiver or to the Sender. Similar maps displaying the results obtained for α equal to 0.7 and 0.9 are reported in the supplementary material. These results confirm the trends commented for the previous maps but with globally better performances. The FPR considerably increases around the fixed dipoles. This phenomenon is focal when LCMV is employed and more spread-out if eLORETA combined with the MVGC estimator. Again, when the fixed dipoles are located deep in the brain and close each other, high FPR values are spread across the whole brain and reach 100% in the vicinity of Receiver and Sender. Maps associated with all the others fixed dipoles positions show that when the sources included in the model are far one from the other, the best performance is obtained with eLORETA. In order to summarize the information contained in these maps, *fig. 4.7* shows the value of the FPR as function of the distance of the moving dipole from the Sender of the interaction for all SNR values, inverse algorithms and connectivity estimators.

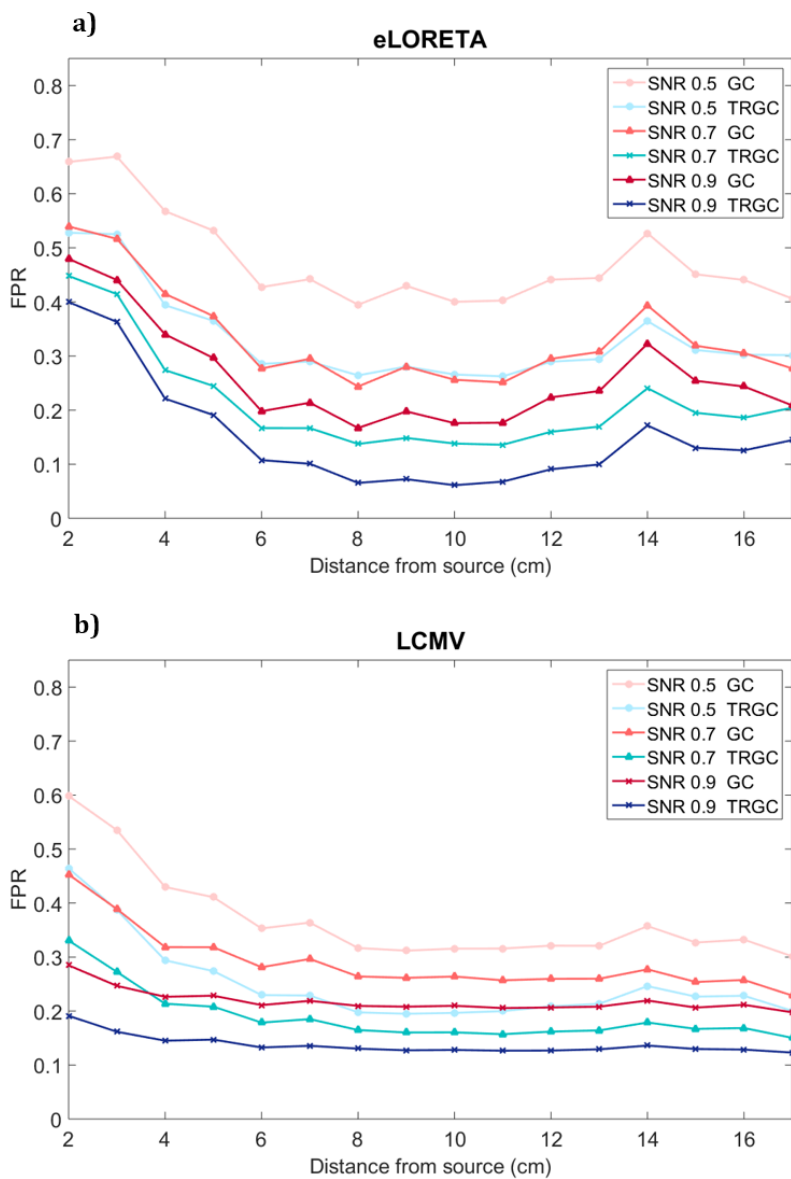


Figure 4.7 - FPR as function of the distance (in cm) of the Non-Interacting Moving Dipole from the Sender of the interaction for the two inverse reconstruction algorithms, eLORETA and LCMV. The MVGC and TRGC connectivity estimators are drawn in red and blue colours, respectively. The circle marker codes for low SNR, the triangle for medium SNR, and the cross for high SNR.

The results suggest that TRGC performs better than MVGC regardless of the distance of the moving dipole from the Sender. LCMV source reconstruction is less sensitive to the distance between dipoles. For example, in panel a), an increase of the FPR 14 cm away from the Sender is noticeable. This point corresponds to the position of the second interacting dipole. When the LCMV algorithm is employed the increase is much less evident. The trends are similar for all α levels, although higher FPRs are observed for lower SNRs. For high SNR, the best performance is achieved with eLORETA when the moving dipole is far from the other two.

Interactive dipole position

The last analysis was performed using a fixed location for the Non-Interacting and Sender dipoles, placing the Receiver dipole at different positions. The results are in line with the previous ones. Figure 4.8 depicts topographical maps for the low SNR level (in the supplementary material for medium and high SNR levels), while figure 4.9 depicts FPR as a function of the distance between Receiver and Sender.

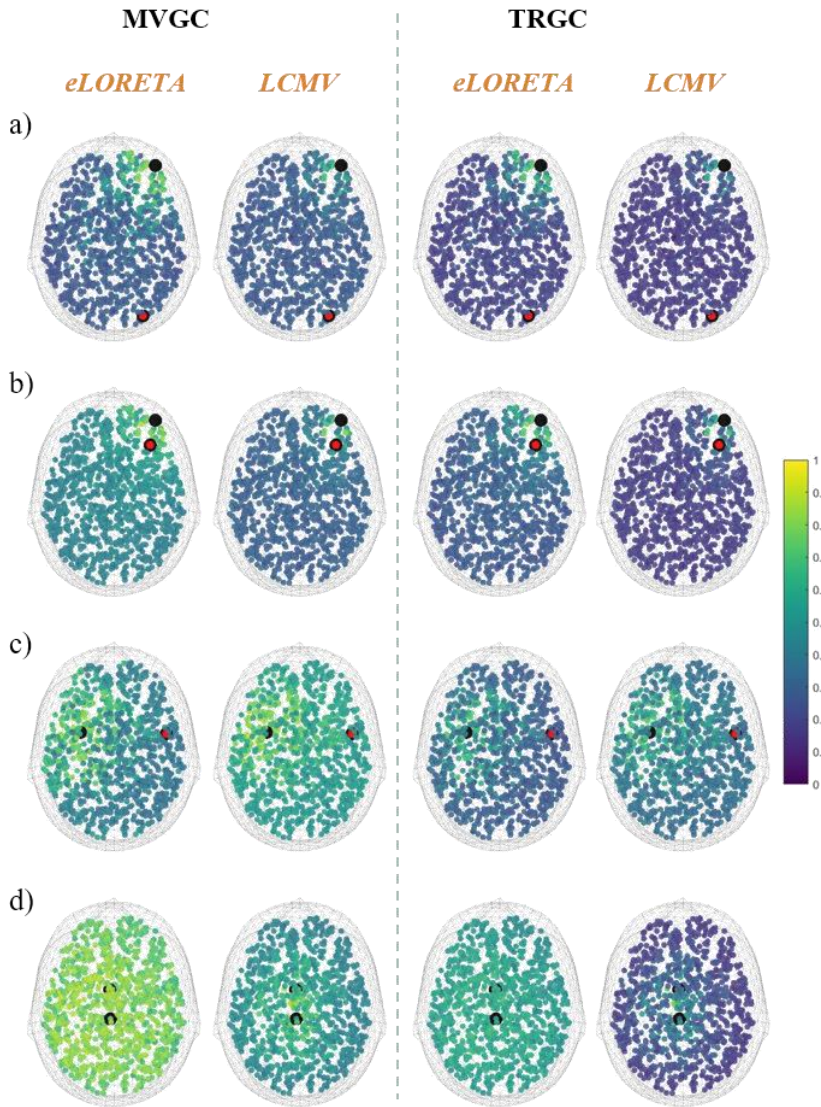


Figure 4.8 - Spatial distribution of the FPR in the Moving Receiver Dipole condition for low SNR ($\alpha = 0.5$). Shown are the Sender (red circle) and Receiver (purple circle) of the interaction in the Far-Superficial (a), Far-Deep (b), Close-Superficial (c), and Close-Deep (d) conditions. The other points represent the mean value of the FPR across 100 iterations (coded by the colour bar on the right side) when the third active dipole (the Non-Interacting one) is moved across the brain. The first two columns refer to the classical GC (MVGC algorithm); the last two to the TRGC. For each column, results obtained with eLORETA and LCMV are reported next to each other.

When the fixed dipoles are close (panels b and d), a high percentage of false positives appears throughout the brain, in particular for low and medium level of SNR. All others results are in line with the results reported above:

- the increase of the α value corresponds to a decrease in the number of false positives independently of all the other factors;
- on average, LCMV performed better than eLORETA. This advantage is predominantly due to an increased robustness w.r.t. the position of the nodes;
- TRGC provided more accurate connectivity estimates than MVGC and PDC;
- when the involved dipoles are far away from another, eLORETA leads to more accurate connectivity estimation, and the difference between the classical MVGC and TRGC is less pronounced than in the other conditions;
- with the dipoles in the *Far/Superficial* configuration, and α equal to 0.9, the percentage of false positives is less than 10% for all the inverse solutions and connectivity algorithms;
- with the dipoles in the *Close/Deep* configuration, the percentage of false positives reaches 100% regardless of the SNR value.

Fig. 4.9 shows the FPR as function of the distance between Sender and Receiver for all SNR values, inverse algorithms and connectivity estimators.

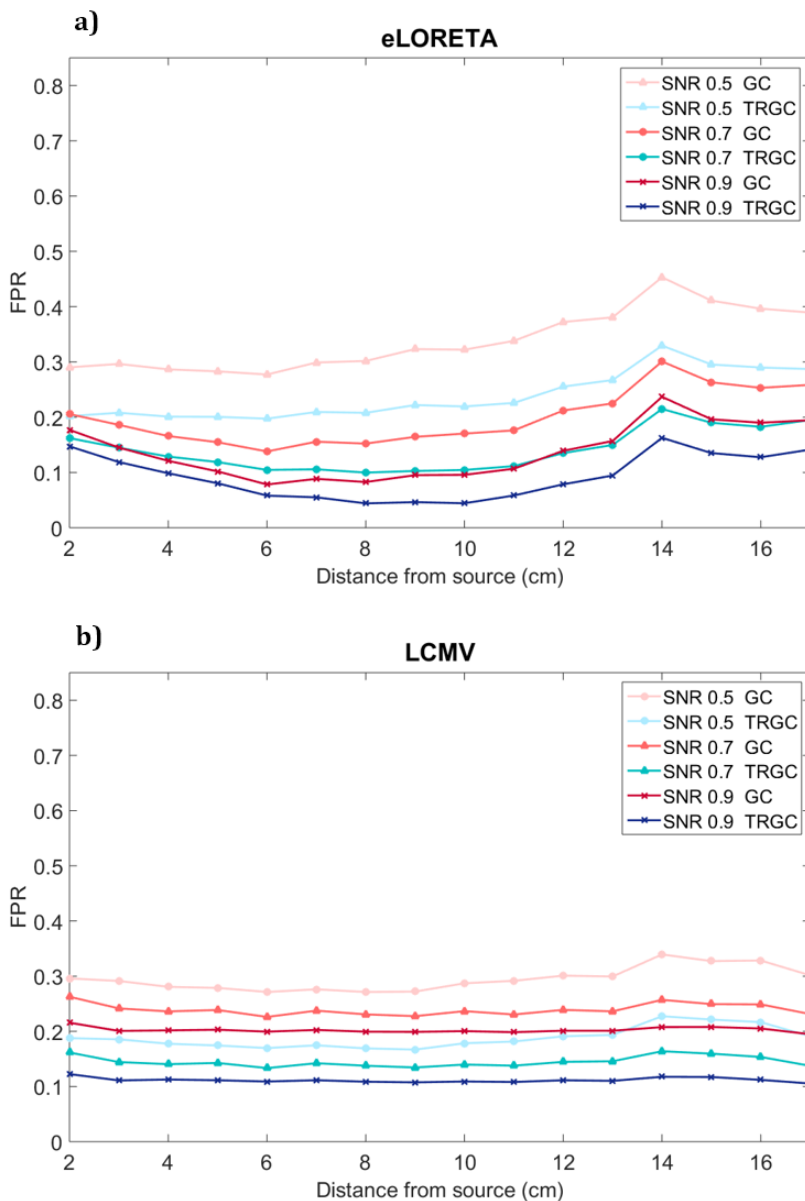


Figure 4.9. FPR as function of the distance (in cm) of the moving Receiver from the Sender for the two inverse reconstruction algorithms, eLORETA and LCMV. The MVGC and TRGC connectivity estimators are drawn in red and blue colours, respectively. The circle marker codes for low SNR, the triangle for medium SNR, and the cross for high SNR.

The first result is that the mean value of the FPR is lower than for the Non-Interacting moving dipole condition. Also, in this case, TRGC performed better than MVGC regardless of the distance of the moving Receiver dipole from the Sender. In panel a) it is possible to notice an increase of the FPR when the Receiver dipole is 14cm away from the Sender dipole (this being the position of the Non-Interacting dipole). Trends are similar for all the α levels, where, generally, decreases in SNR are associated with increases in FPR. For high SNR, the best performance is achieved using eLORETA when the moving dipole is far away from the other two (FPR around 5%).

4. Discussion and Conclusion

It is well established that neuroelectrical measures recorded on the scalp need to be projected back into the brain in order to be able to infer at least roughly where these signals have been generated. In the same way it is evident that measures of statistical dependencies between brain regions cannot be inferred by studying dependencies between scalp sensor signals [14], [15], [70]. Unfortunately, even with state-of-the-art localization of the brain sources underlying the measured signals, directed dynamical influences between these reconstructed sources do not always reflect the ground truth. This issue has been anticipated in [14], [15], [70] and thoroughly analysed by Palva and colleagues [95] for phase-based (undirected) connectivity measures. In the present comprehensive simulation study, we focused on directional connectivity measures and quantified the extent to which the estimation of influences between reconstructed sources is possible. We employed an analysis framework combining source localization approaches and brain connectivity estimators with the goal of identifying those analysis pipelines that are least affected by the presence of head volume conduction and, therefore, provide the most accurate and reliable connectivity estimates. Several realistic conditions of brain activity were simulated, where our goal was to simulate both advantageous and disadvantageous conditions for the following brain connectivity estimation. To this end, we modulated the depth of the sources, the distance between sources, and the SNR. Not surprisingly, a convenient condition we identified is the presence of far and superficial dipoles in

combination with a high SNR; in contrast, a disadvantageous condition is given by the presence of close and deep sources with a low SNR level. Our simulations suggest that all considered factors show a significant influence on the estimation quality and, consequently, their combination has a considerable impact on the connectivity estimation performance. LCMV source reconstruction appears to be more sensitive to the SNR value, while eLORETA achieves similar performance regardless of the SNR. In general, LCMV showed better performance than eLORETA. Only when the simulated sources were assigned to distant locations, the eLORETA performance is similar to or better than the performance of LCMV. In agreement with the theoretical hypothesis, we demonstrated that the TRGC algorithm provides a better estimation of the directed statistical dependencies between sources than classical MVGC and PDC. Indeed, the percentage of spurious connections decreased significantly and the overall detection of connectivity as measured by the AUC increased significantly in all considered experimental conditions when TRGC was used instead of MVGC or PDC. At the same time, the percentage of missed connections as measured by the FNR increased slightly, but still remained close to zero. GC and PDC showed similar performance independent of all other factors. As expected, we found that closer and deeper active sources decreased the obtained performance. Thus, a dependence between the dipoles position and the accuracy of the estimates was found. This is a clear effect of the volume conduction, since, when two sources are close to each other, they generate a highly mixed signal on the scalp, which compromises the correct estimation even after inverse source reconstruction. On the other hand, when the sources are far away from each other, they are less affected by volume conduction, leading to a better quality of the connectivity estimation. The insights obtained in this study may guide the choice of crucial parameters such as selection of regions-of-interest (ROI) as well as the selection of source reconstruction and connectivity estimation algorithms that promise to provide the most reliable and physiologically interpretable description of brain networks based on EEG data.

We agree with [95], advocating for the application of measures, for which promises and pitfalls are known, and which integrate knowledge of how neural activity in the whole brain as well as external (physiological or artifactual) activity

contribute to the signals that we record on the scalp. In this regard, it should be noted that connectivity estimates can only at most be as focal as the reconstructed source current densities they are derived from, and we know that common inverse methods lead to very blurry results. To distinguish correctly-identified connections from connections that are observed in the vicinity of the true interacting sources due to blurry inverse solutions, a data-driven clustering in the space of brain-wide pairwise connectivities, as recently proposed in [96], may a viable option, which may be preferable to a reduction of the source space to the level of static ROIs. It has to be kept in mind, however, that – although of importance – the main problem in EEG-based brain connectivity analysis is not the spatial blur of correctly identified connections but the emergence of spurious connectivity as a result of observing mixtures of signals even at the level of reconstructed sources. This problem can only be addressed by using appropriate connectivity measures that are robust to volume conduction effects by construction.

7. Supplementary material

Non-interactive dipole position

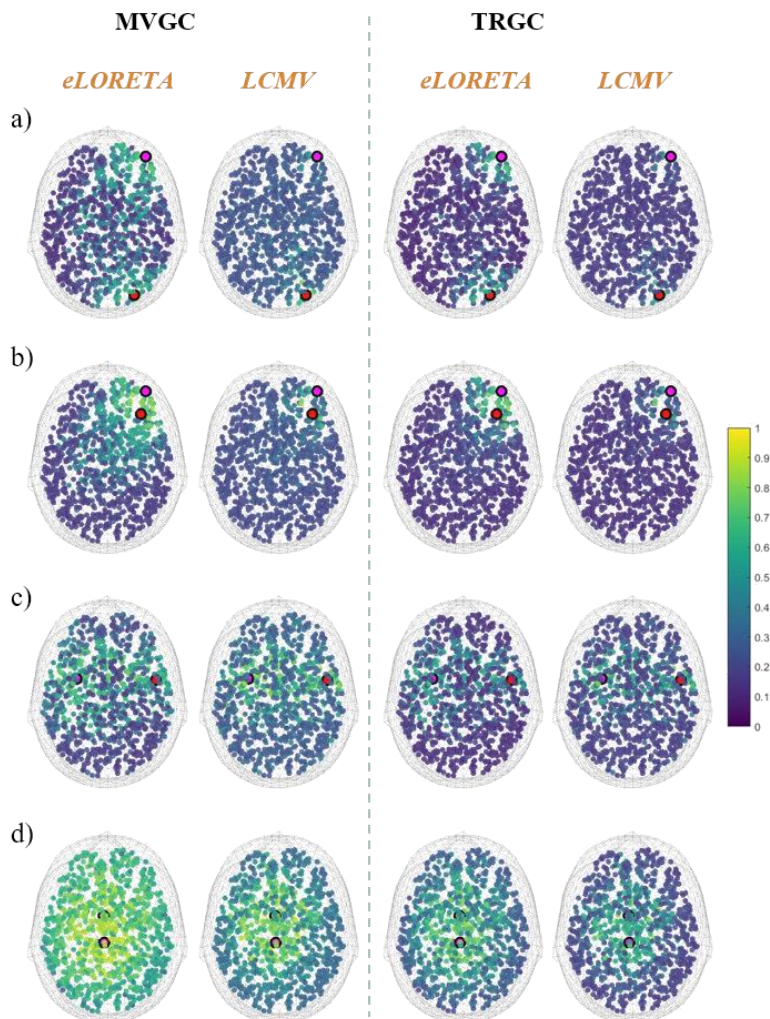


Figure 4.1s - Spatial distribution of the FPR in the Moving Non-Interacting Dipole condition for medium SNR ($\alpha = 0.7$). Shown are the Sender (red circle) and Receiver (purple circle) of the interaction in the Far-Superficial (a), Far-Deep (b), Close-Superficial (c), and Close-Deep (d) conditions. The other points represent the mean value of the FPR across 100 iterations (coded by the colour bar on the right side) when the third active dipole (the Non-Interacting one) is moved across the brain. The first two columns refer to the classical GC (MVGC algorithm); the last two to the TRGC. For each column, results obtained with eLORETA and LCMV are reported next to each other.

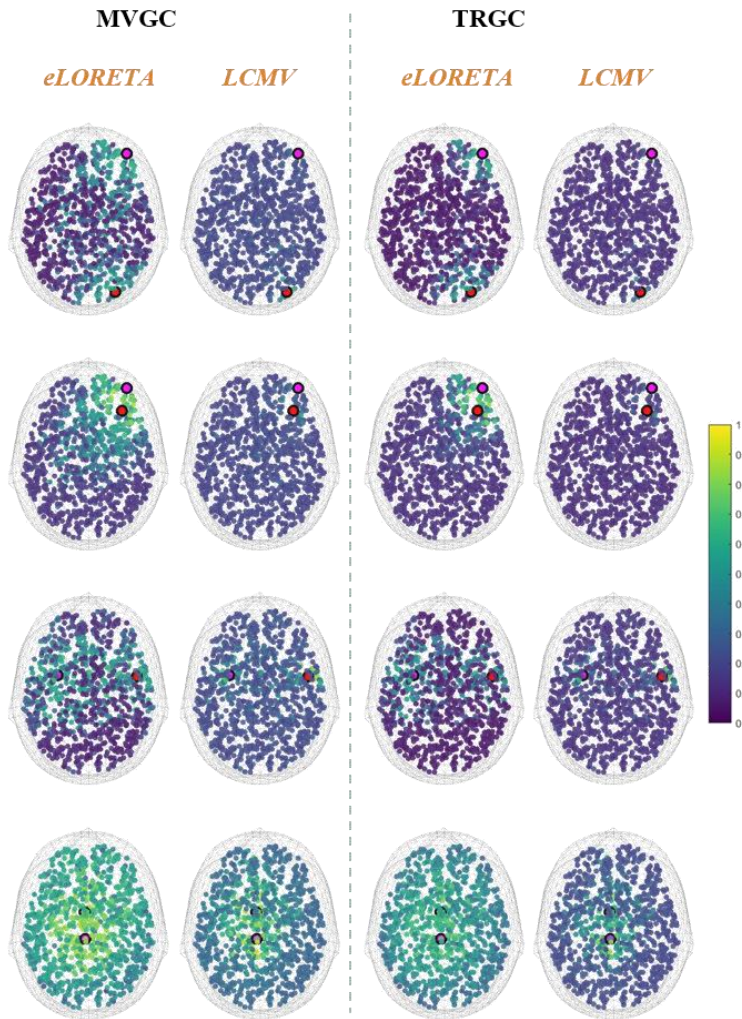


Figure 4.2s - Spatial distribution of the FPR in the Moving Non-Interacting Dipole condition for high SNR ($\alpha = 0.9$). Shown are the Sender (red circle) and Receiver (purple circle) of the interaction in the Far-Superficial (a), Far-Deep (b), Close-Superficial (c), and Close-Deep (d) conditions. The other points represent the mean value of the FPR across 100 iterations (coded by the colour bar on the right side) when the third active dipole (the Non-Interacting one) is moved across the brain. The first two columns refer to the classical GC (MVGC algorithm); the last two to the TRGC. For each column, results obtained with eLORETA and LCMV are reported next to each other.

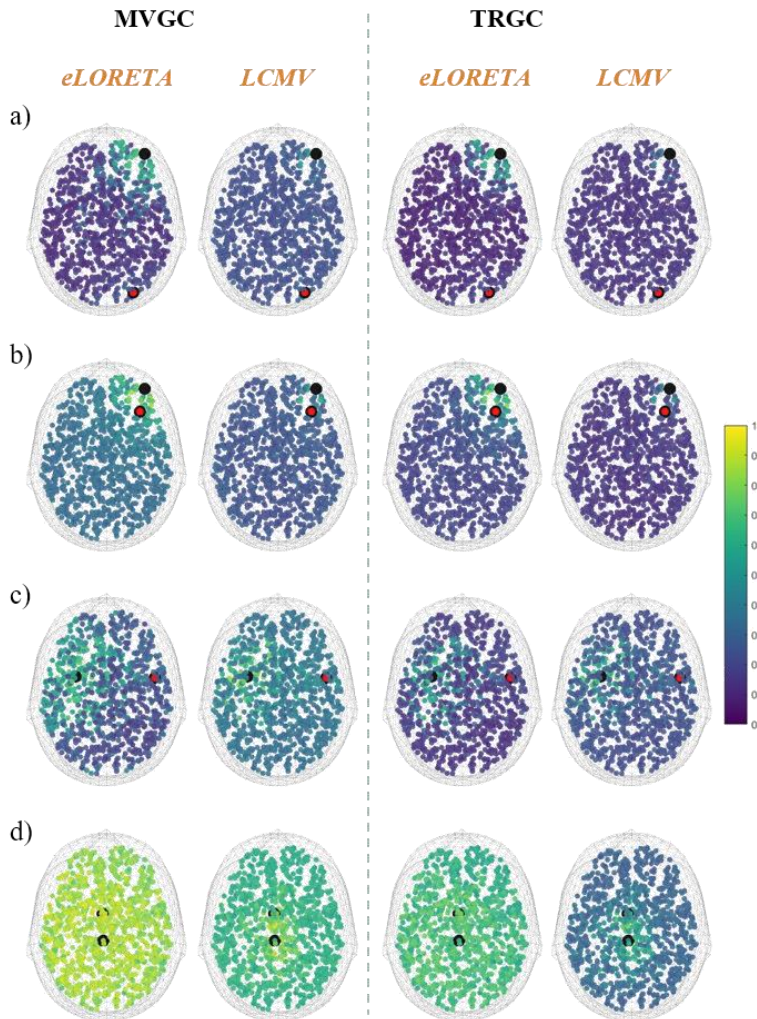
Interactive dipole position

Figure 4.3s - Spatial distribution of the FPR in the Moving Receiver Dipole condition for medium SNR ($\alpha = 0.7$). Shown are the Sender (red circle) and Receiver (purple circle) of the interaction in the Far-Superficial (a), Far-Deep (b), Close-Superficial (c), and Close-Deep (d) conditions. The other points represent the mean value of the FPR across 100 iterations (coded by the colour bar on the right side) when the third active dipole (the Non-Interacting one) is moved across the brain. The first two columns refer to the classical GC (MVGC algorithm); the last two to the TRGC. For each column, results obtained with eLORETA and LCMV are reported next to each other.

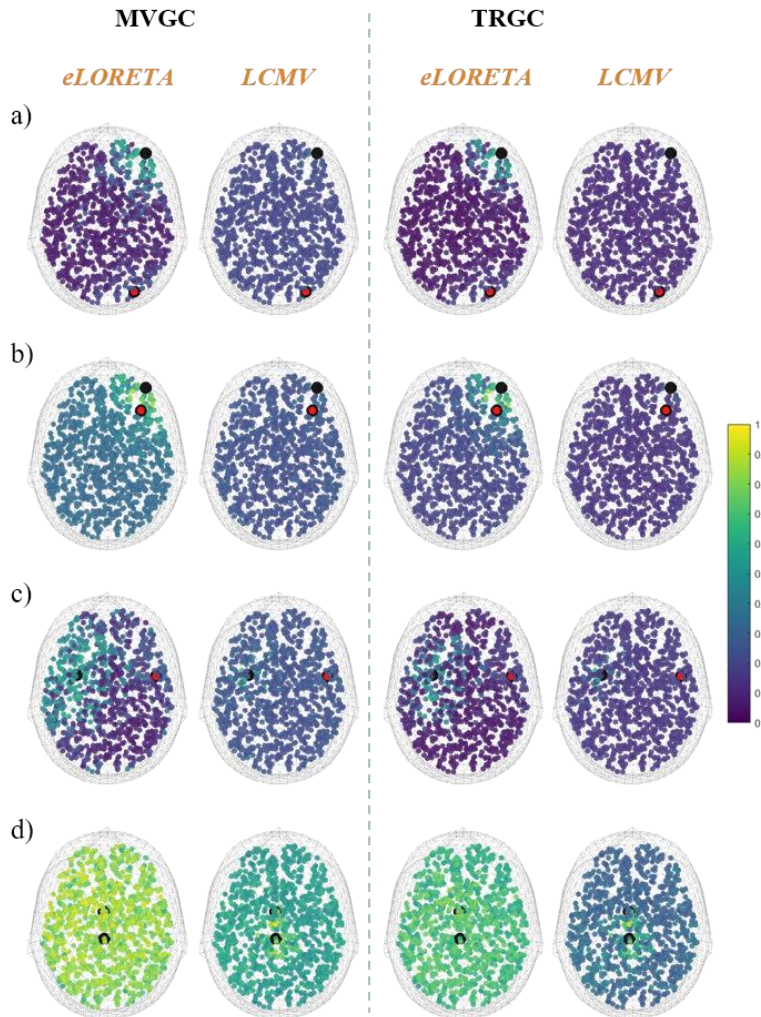


Figure 4.4s - Spatial distribution of the FPR in the Moving Receiver Dipole condition for high SNR ($\alpha = 0.7$). Shown are the Sender (red circle) and Receiver (purple circle) of the interaction in the Far-Superficial (a), Far-Deep (b), Close-Superficial (c), and Close-Deep (d) conditions. The other points represent the mean value of the FPR across 100 iterations (coded by the colour bar on the right side) when the third active dipole (the Non-Interacting one) is moved across the brain. The first two columns refer to the classical GC (MVGC algorithm); the last two to the TRGC. For each column, results obtained with eLORETA and LCMV are reported next to each other.

Code and data availability

The code necessary to reproduce these simulations is available at:

https://github.com/paolop21/simulation_source_connectivity.

The results of the simulations and the structures necessary to run the code are available at: <https://zenodo.org/record/1155857#.WmMVwqjiY2w>

Chapter 5

Connectivity in attention processes

Although extensively studied for decades, attention system remains an interesting challenge in neuroscience field. The Attention Network Task (ANT) has been developed to provide a measure of the efficiency for the three attention components identified in the Posner's theoretical model: alerting, orienting and executive control. Here we propose a study on 15 healthy subjects who performed the ANT. Several fMRI studies have already provided evidences on the anatomical separability and interdependency of these three networks, and EEG studies have also unveiled the related brain rhythms. What is still missing is a characterization of the brain circuits subtending the attentional components in terms of directed relationships between the brain areas and their frequency content. Here, we want to exploit the high temporal resolution of the EEG, improving its spatial resolution by means of advanced source localization methods, and to integrate the resulting information by a directed connectivity analysis. The results showed in the present study demonstrate the possibility to associate a specific directed brain circuit to each attention component and to identify synthetic indices able to selectively describe their neurophysiological, spatial and spectral properties. In the second part of the study, we focused on the scalp EEG signals in order to extract simple and reliable measures easily usable as neuro-physiological indices. Combining advanced methods for connectivity estimation on EEG signals and graph theory we identified some descriptors of the most important features of the three networks correlated with behavioral performances. Our results provided a set of band-specific connectivity indices able to follow the behavioral task performances among subjects for each attention component as defined in the ANT paradigm. Extracted EEG-based indices could be employed in future clinical applications to support the behavioral assessment or to evaluate the influence of specific attention deficits on Brain Computer Interface (BCI) performance and/or the effects of BCI training in cognitive rehabilitation applications.

1. Introduction

Attention is fundamental for human cognitive processing. As such, it includes a wide class of processes related with the ability of a subject to interact with the external environment. According to Posner's theoretical model [20], this is possible through a sustained state of alertness (alerting), the selection of the important information in a noisy context (orienting) and the ability to control a situation and solve conflicts (executive control). When the complex mechanism at the basis of attention is altered, e.g. following a stroke event, consequences may affect a wide range of behavioural and social aspects. Several neuroimaging and neurophysiological studies have employed the so-called Attention Network Task (ANT), a behavioural task which allows to disentangle the three components (alerting, orienting and executive control) as described by Fan et al. in [97]. The available evidences indicate that the three attention components are independent [98], involve different anatomical areas (functional magnetic resonance imaging - fMRI- studies) [99] and each of them has a distinct oscillatory activity and time course (EEG study) [100]. The available brain connectivity studies on attention are based on structural networks (anatomical connectivity) [101] or functional networks extracted from fMRI data [102]. EEG-based connectivity studies are still missing. Only for the executive functions a connectivity model was extracted employing an approach requiring strong a priori hypothesis [103]. In summary, despite the advancements in this field, a single approach including at the same time i) the spatial information about the involved areas, ii) the relationships between such areas and iii) the frequency content of their neuro-electrical activity is still missing. Here, we want to combine high density EEG recordings with techniques of brain sources localization to increase the spatial resolution of EEG and with a spectral, directed connectivity estimation to point out the communication between brain areas. In this study, we applied modern methodologies for sources reconstruction, effective connectivity estimation and graph theory approaches with two specific aims. The "source-level analysis" has the aim to integrate spatial and temporal information into a single neuro-functional model and to provide indices, based on the properties of the connectivity patterns, able to provide new evidences about the circuits at the basis

of the different attention processes. On the other side, the “scalp-level analysis” aims at the comprehension of the useful information contained in such data with an important impact in lots of the clinical applications, where simple but reliable measures are required. Thus, the main objective of this second study was to define stable descriptors of the dynamic brain circuits underpinning the attentional components in terms of directed relationships between the brain areas and their frequency content. We were interested in extracting markers of the brain circuits elicited by the ANT performed by healthy volunteers while recording high density EEG (hdEEG) and thus, exploiting its high temporal resolution, low invasiveness and cost-effective. To this purpose we explore whether connectivity-based indices would correlate with behavioural data in order to strengthen their relevance as measure of attention processing for future applications. [104], [41].

2. Materials and methods

2.1 Experimental Design

Neuro-electrical data (60 EEG channels + 4 EOG channels, reference at linked mastoids and ground at Fpz, Brain Products, sample frequency equal to 250 Hz) were recorded from 17 healthy volunteers (10 female, age 27.2 ± 2.5) during the execution of the ANT [100]. They had no history of neurological or psychiatric disorders. The experimental protocol was approved by the local Ethical Committee. Participants were seated in front of a computer screen; a row of 5 black arrows pointing left or right was presented in the middle part of the screen. Subjects were asked to indicate the direction of the central arrow (target stimulus) as quickly and accurately as possible with the left/right arrow keyboard buttons according to the direction of the target, using their right hand. Trials were defined as *Congruent* if the 4 lateral *flankers* and the central arrow had the same direction, *Incongruent* if the flankers pointed at the opposite direction. In addition there were three cue (an asterisk sign) conditions: *No cue*, *Center cue* (in the center of the screen for alerting), and *Spatial cue* (at the target location, above or below a fixation cross, for alerting plus orienting) [98]. The timeline of the paradigm is

showed in *fig.5.1*. The contrast between the different experimental conditions (72 trials each condition) allowed to extract the three attention components: i) *Center cue* and *No cue* conditions define the alerting, ii) *Spatial cue* and *Center cue* the orienting, iii) *Incongruent* and *Congruent* the executive control.

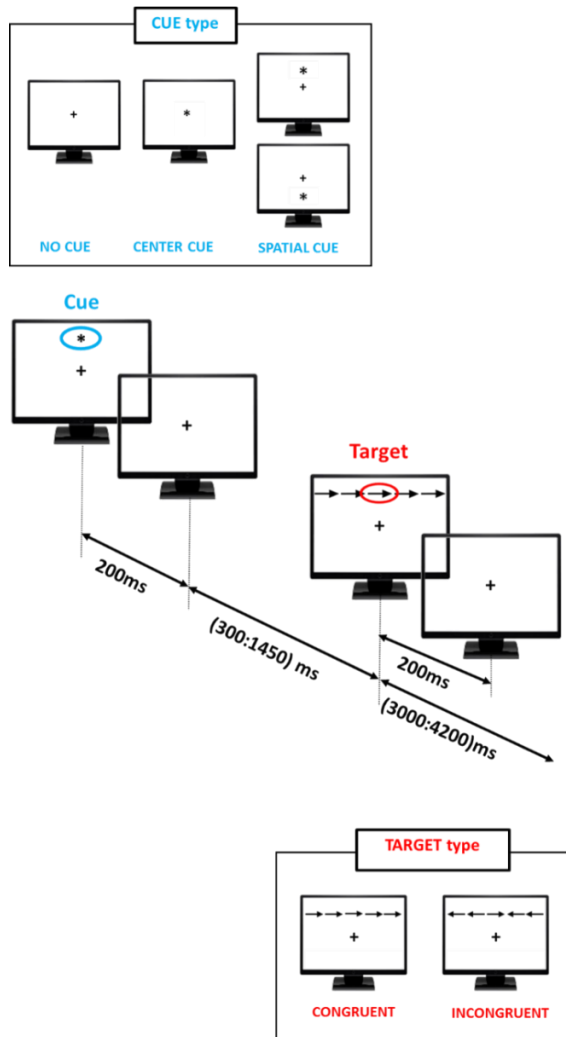


Figure 5.1 - Timeline of the ANT paradigm. In each trial, a cue (asterisk) may appear for 200 ms in the center of the screen (center cue condition) or in the semi-space in which the target will appear (spatial cue) or not appear (no cue). After a variable duration (300–1450ms), the target and the flankers (congruent or incongruent) are presented. The participant indicates the direction of the central arrow within a time window of 2000 ms. The target and flankers disappear after a response is given.

2.2 Behavioral data

As behavioral index for each attention component we used the efficiency measure introduced in [97]. Alerting efficiency (Eff_{Al}), orienting efficiency (Eff_{Or}) and executive control efficiency (Eff_{EC}) are defined as the difference between the mean reaction times (RT) in specific experimental conditions:

$$Eff_{Al} = RT_{No} - RT_{Center} \quad (5.1)$$

$$Eff_{Or} = RT_{Center} - RT_{Spatial} \quad (5.2)$$

$$Eff_{EC} = RT_{Incong} - RT_{Cong} \quad (5.3)$$

In order to confirm the correct implementation of the task and its correct execution by the experimental group, we collected their behavioural data in terms of efficiency (Eff) and correct answers. Such data were analysed qualitatively at single subject level and by means of a statistical group analysis. A two-way ANOVA was performed across the experimental group on the two acquired measures to repeat and confirm the results in [97]. The main within factors are:

- Cue Type with 3 levels: No, Center and Spatial;
- Target type with 2 levels: Congruent, Incongruent.

The dependent variables are the *Reaction Time* and the *Error Rate* (number of wrong answers expressed in percentage value). Tukey's post-hoc test was applied in order to investigate differences between the levels of the different considered factors.

2.3 EEG data pre-processing

EEG scalp data were band-pass filtered in the range [1-45] Hz and ocular artifacts were removed through Independent Component Analysis (fast-ICA algorithm). EOG channels were also included in the ICA decomposition. Signals were segmented in different time windows defined as [0 - 500] ms according to the *cue* onset and [0-400] ms according to the *target* onset. Residual artifacts were

removed by means of a semi-automatic procedure based on a threshold criterion ($\pm 80 \mu\text{V}$).

2.4 Study 1: Source data analysis

Source reconstruction and connectivity analysis

Cortical and subcortical brain signals were reconstructed on 5000 dipoles employing the eLORETA algorithm [19]. We selected such approach according to the results presented in *Chapter 4*: considering that all the brain areas involved in attention processes elicited by ANT are located in the cortex (thus “*Superficial*”), eLORETA represents the best choice as demixing procedure to be applied before the estimate. Then, a set of regions of interest (ROIs) was identified on the basis of previous fMRI studies after a spectral analysis performed on the acquired dataset in order to confirm the activation of the same areas. The 18 selected ROIs are: inferior\superior frontal gyrus, precentral gyrus, inferior\superior parietal lobule, fusiform gyrus, inferior fusiform gyrus in the left hemisphere; anterior cingulate gyrus, inferior\middle frontal gyrus, post-central gyrus, superior temporal gyrus, superior parietal lobule, fusiform gyrus, inferior fusiform gyrus in the right hemisphere. Their representation on fMRI slices is reported in *fig. 5.2*.

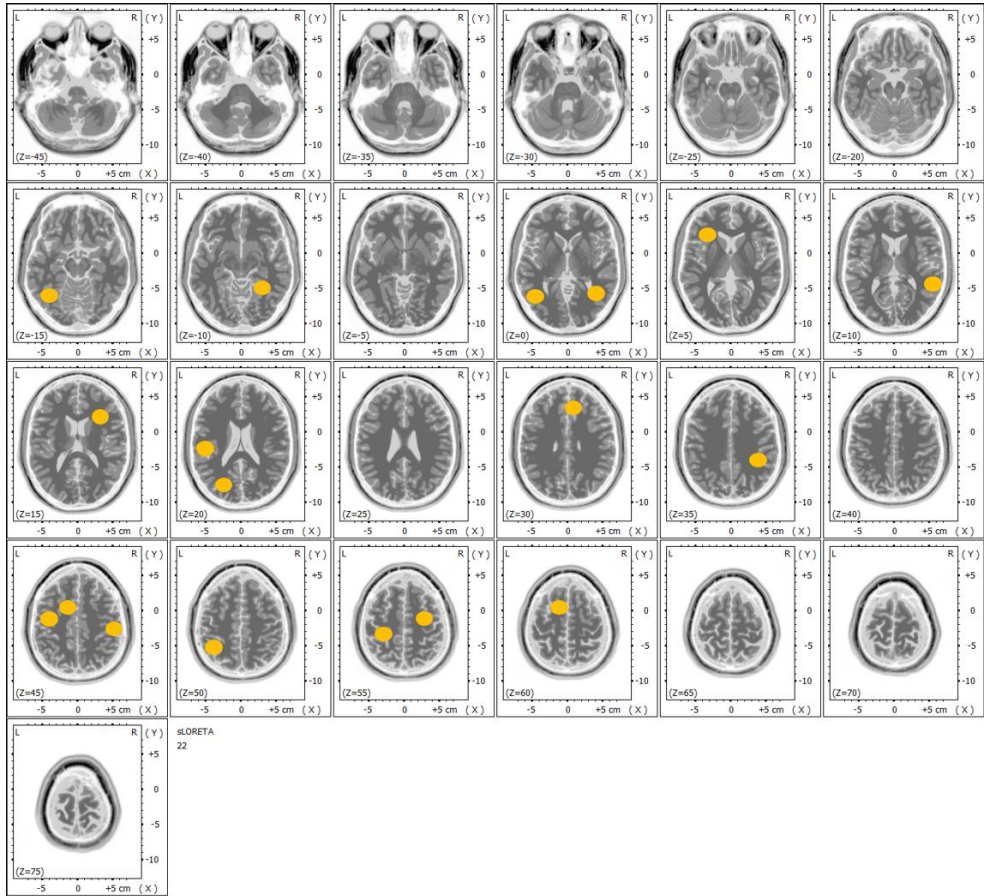


Figure 5.2 – Position of the 18 ROIs selected for the connectivity analysis. Brain surface is segmented in 5-mm slices that are reported from the bottom to the top of the head. Yellow point code for the position of the ROIs included in the study.

Causal connectivity was estimated on these ROIs by means of the time-varying Partial Directed Coherence (tvPDC) [78] for each samples and each experimental condition. Obtained matrices were averaged in in the typical four EEG frequency bands defined by means of the Individual Alpha Frequency (IAF) value [33]:

- Theta: [IAF-6; IAF-2] Hz;
- Alpha: [IAF-2; IAF+2] Hz;
- Beta [IAF+2; IAF+14] Hz;
- Gamma: [IAF+15; IAF+30] Hz.

The optimal order of the MVAR model used as predictor filter was estimated for each subject and experimental condition by means of the Akaike Information Criteria (AIC) [105]. In order to isolate the networks at single subject level associated with each of the three attention components (filtered PDC matrices), a statistical comparison (unpaired t-test, $p < 0.05$, False Discovery Rate, FDR, correction) was performed between appropriate experimental conditions (according to ANT theory). In particular, we compared: i) *center cue vs no cue* for alerting, ii) *spatial cue vs center cue* for orienting and iii) *incongruent vs congruent* for executive control. The same conditions were compared also to obtain the grand average maps (showed in figure 5.5). Firstly, the single subject PDC matrices were averaged in the two time intervals of interest: i) 500 ms after the *cue* stimulus and ii) 400 ms after *target* stimulus; then, a paired t-test ($p < 0.05$, FDR correction) was performed.

Graph theory

Graph theory indices were extracted from the networks underlying the five experimental conditions with the aim to synthesize and compare their main global and local properties. In this study, we adopted the following indices:

- *Density*: it is used to quantify the percentage of existing connections with respect to the totality of possible links. Here, it has been adapted to quantify the percentage of connections relative to a specific subnetwork.

$$sub_Density = \frac{n_{subnet}}{n_{TOT}} \quad (5.4)$$

Where n_{subnet} is the number of existing links connecting only the nodes (ROIs) belonging to the considered subnetwork and n_{TOT} is the number of all the existing connections of the entire circuit.

- *Influence*: measure of the difference in the number of inter-connections between two spatial regions [106].
- *Asymmetry*: measure of the difference between the number of intra-connections of two different subnetworks.

- *Global Efficiency (GE)*: global measure (considering all the connections in the whole-network) of how efficiently a network exchanges information internally. It is defined as the average of the inverse of the geodesic length (shortest path between two nodes in the network) and it represents the efficiency of the communication between all the nodes within the network [107]. It can be defined as follows:

$$E_g = \frac{1}{N(N-1)} \sum_{i \neq j} \frac{1}{d_{ij}} \quad (5.5)$$

where N represents the number of nodes in the graph and d_{ij} the geodesic distance between i and j .

- *Local Efficiency (LE)*: measure of the fault tolerance of a network. It verifies whether the communication between nodes is still efficient when a node is removed from the network. The higher the LE, the greater the robustness of the network at local scale. The LE is the average of the global efficiencies computed on each sub-graph S_i belonging to the network and it represents the efficiency of the communication between all the nodes around the node i in the network [107]. It can be defined as follows:

$$E_l = \frac{1}{N} \sum_{i=1}^N E_g(S_i) \quad (5.6)$$

where N represents the number of nodes in the graph and S_i the sub-graph obtained deleting the i^{th} row and the i^{th} column from the original adjacency matrix.

For the evaluation of the local indices (all but the global and local efficiencies) we considered three couples of subnetworks, derived from previous studies in literature: left and right hemispheres, frontal and parietal lobes, cerebral areas main involved in Bottom-Up (frontal gyrus and temporal parietal junction) and Top-Down processes (pre-frontal cortex, PFC, visual cortex, parietal lobule) [99].

Top-Down processes are characterized by flows of information from 'higher' to 'lower' centres, conveying knowledge derived from previous experience rather than sensory stimulation; Bottom-Up processes, instead, proceed in a single direction from sensory input, through perceptual analysis, towards motor output, and their flows move from 'higher' centres to 'lower' centres.

Statistical Analysis

To describe each attention component, statistical comparisons (paired t-test, $p < 0.05$) were performed between connectivity matrices in the appropriate conditions (according to ANT theory), obtaining a grand average connectivity pattern for each component (alerting, orienting and executive control). Graph indices variations were evaluated with the same procedure (paired t-test, $p < 0.05$). FDR correction was applied to mitigate the errors due to multiple comparisons. Such statistical analysis was performed for all the EEG typical frequency bands: theta, alpha, beta and gamma.

2.5 Study 2: Scalp data analysis

Connectivity analysis

After the pre-processing phase described in the previous paragraph, the causal connectivity was estimated on the signal recorded at scalp level. As in the previous analysis, we employed the Partial Directed Coherence (PDC) [78] for each experimental condition, and averaged in the following four frequency bands defined by means of the IAF value [33]. The optimal order of the MVAR model was estimated for each subject and each experimental condition. We obtained a network for each frequency band, each experimental condition and each subject. A statistical comparison (unpaired t-test, $p < 0.05$, False Discovery Rate, FDR, correction) was performed between appropriate conditions (according to ANT theory) in order to isolate the networks associated with each of the three attention components. In particular, we compared: i) *Center cue vs No cue* for alerting, ii) *Spatial cue vs Center cue* for orienting and iii) *Congruent vs Incongruent* for executive control.

Graph theory

Graph theory indices were extracted from the networks underlying the three attention components with the aim to synthesize their main global and local properties. The global indices considered to describe the general properties of the entire network [108] are:

- *Clustering*: to measure the tendency of the network to segregate the information in subnetworks;
- *Path Length*: to measure efficiency of the communication between the nodes on the basis of the shortest paths between them.

Similar to the previous analysis, the local indices were used to quantify the involvement of a specific sub-network and/or to investigate the relation between different sub-networks. In particular, as sub-networks we considered left (Fp1, AF7, AF3, F7, F5, F3, F1, FT7, FC5, FC3, FC1, T7, C5, C3, C1, TP7, CP5, CP3, CP1, P7, P5, P3, P1, PO7, PO3, O1) and right (Fp2, AF4, AF8, F2, F4, F6, F8, FC2, FC4, FC6, FT8, C2, C4, C6, T8, CP2, CP4, CP6, TP8, P2, P4, P6, P8, PO4, PO8, O2) hemispheres, anterior (Fp1, Fp2, AF7, AF3, AFz, AF4, AF8, F7, F5, F3, F1, Fz, F2, F4, F6, F8, FT7, FC5, FC3, FC1, FCz, FC2, FC4, FC6, FT8) and posterior (TP7, CP5, CP3, CP1, CPz, CP2, CP4, CP6, TP8, P7, P5, P3, P1, Pz, P2, P4, P6, P8, PO7, PO3, POz, PO4, PO8, O1, Oz, O2) areas [106]. In addition to the indices described for the previous analysis (*Density*, *Asymmetry* and *Influence*) we also computed *Divisibility and Modularity* to measure the level of interaction between subnetworks in terms of inter (divisibility) and intra (modularity) connections: strict interconnection or isolation [109].

Statistical Analysis

Connectivity indices extracted for each attention component were then correlated with the relative behavioral parameters (Eff_{AI} , Eff_{Or} , Eff_{EC}) by means of Pearson's correlation ($p < 0.05$). FDR correction was applied to take into account errors due to multiple correlations.

3. Results

3.1 Behavioral analysis

The behavioral data acquired for each subject during the execution of the ANT were subjected to statistical analysis to evaluate the effects of the cue (No cue, Center cue, Spatial cue) and the target type (Congruent, Incongruent) on participants' performance. Specifically, a two-way ANOVA was performed for the reaction time and the error rate. Table 5.1 and figure 5.3 report the obtained results.

<i>Factors</i>	<i>Reaction Time</i>	<i>Error Rate</i>
TARGET_TYPE (1,16)	9.67 $p=1*10^{-5}$	200.47 $p=0.0067$
CUE_TYPE (2,32)	154.88 $p=1*10^{-5}$	10.39 $p=3*10^{-4}$
TARGET_TYPE x CUE_TYPE (2,32)	26.124 $p=1*10^{-5}$	6.87 $p=3*10^{-3}$

Table 5.1 - Results of the two-way ANOVA (*F* values) computed considering as dependent variables Reaction Time (ms) and Error Rate (%) and as within main factors the type of Target (TARGET_TYPE, congruent or incongruent) and Cue (CUE_TYPE, No, Center or Spatial). In the column "Factors" are also reported the degrees of freedom.

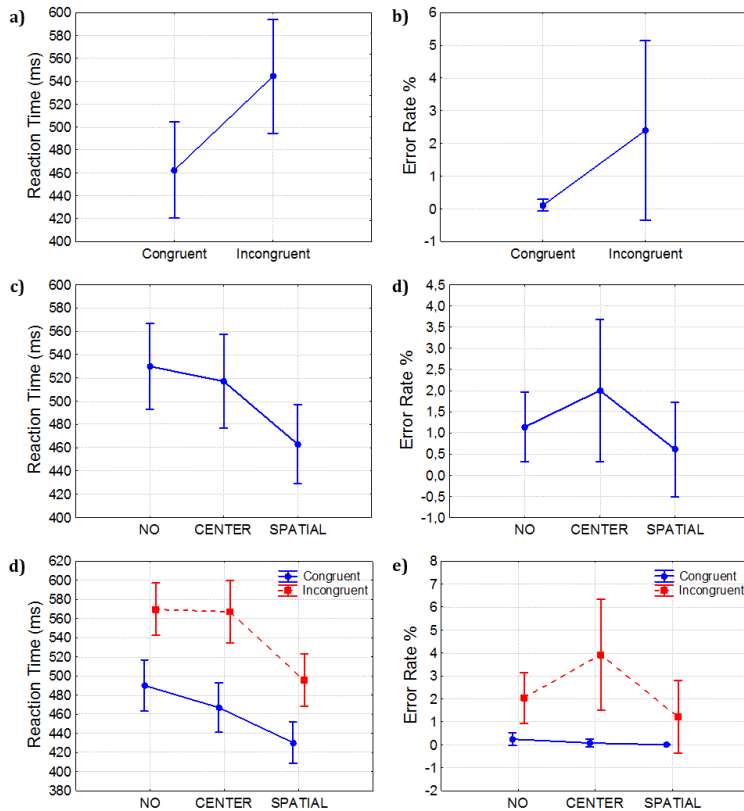


Figure 5.3 -Plot of means associated to the three-way ANOVA performed on the Reaction Time (left column) and the Error Rate (right column) acquired during the ANT execution on 17 healthy subjects. X-axes report the levels of the factor TARGET_TYPE (panel a and b) and CUE_TYPE (all the others). In the lowest row the interaction factor CUE_TYPE x TARGET_TYPE is reported.

Diagrams reported in panels a), b), e) and f) and the Tukey's test results revealed a statistically significant difference between Congruent and Incongruent conditions regardless of the cue type for both the performance parameters. As expected, subjects encounter greater difficulty in responding correctly and quickly when the target (central arrow) point out the opposite direction with respect to the other arrows (flankers). Also the CUE_TYPE factor has a significant effect on the error rate and on the reaction time as showed in panels c) and d), More in details, the observation of the interaction factor (panel e and f) highlighted that, for the Error Rate index, this is a specific effect of the Incongruent

condition. Tukey's test showed a significantly higher percentage of wrong answers in the Center cue condition with respect to the other cue conditions. If the target is congruent, the subjects report a very low percentage of error rate (close to zero regardless of the CUE_TYPE). The presented results are perfectly consistent with those found in literature [97]. In the following table we reported the values of efficiency computed for each subject and each attention component.

	<i>Efficiency (ms)</i>		
	<i>Alerting</i>	<i>Orienting</i>	<i>Ex.Control</i>
SUB01	26,12	48,28	50,84
SUB02	10,44	50,07	94,61
SUB03	23,92	67,58	101,47
SUB04	8,19	52,08	138,14
SUB05	11,64	66,78	82,02
SUB06	4,39	62,21	85,64
SUB07	38,8	9,97	62,81
SUB08	-4,09	73,31	100,5
SUB09	37,86	30,98	51,98
SUB10	4,09	72	75,71
SUB11	2,42	58,73	74,39
SUB12	21,84	45,28	52,52
SUB13	-7,83	89,39	68,26
SUB14	13,97	75,59	84,03
SUB15	6,13	23,82	67,64
SUB16	21,97	27,53	118,99
SUB17	7,54	52,02	78,3

Table 5.2 – *Efficiency values (in behavioural sense) for each attention component evaluated at single subject level. In the first column the ID of the involved participants have been reported.*

Because of the negative values of the Efficiency index in the alerting phase, 2 out of 17 subjects were considered outliers and not included in the following analysis.

3.2 Study 1: Source level analysis

Spectral Analysis

In this section we present the results obtained from the analysis of the significant activation at cortical level induced by the performed attention task. This study was conducted by using advanced source location techniques that allowed to identify the regions that are mainly involved in the cognitive functions under investigation. Firstly, we computed the Power Spectral Density (PSD) for each of the 5 experimental conditions. Then, to determine the significant features of each of the three attention components (alerting, orientating and executive control) within the frequency bands typical of the neuro-electrical activity a statistical comparison between the PSD values obtained for proper couples of experimental conditions was performed (t-test, $p < 0.05$, FDR correction). Such proper couples derive from the ANT theory mentioned in the previous paragraphs regarding the behavioral efficiency measure. In a similar way, No and Center cue conditions define the alerting, Center and Spatial Cue conditions define the orienting and Congruent and Incongruent conditions define the executive control. For the voxels in which such test resulted as significant, we reported on brain maps the corresponding t-value (t-Student's test). Figure 5.4 reported an example for each component of the obtained results. sLORETA software was employed for the visualization of the head volume. Because of the impossibility to report all the obtained maps and all the slices of the head volume, we synthesized the results of the spectral analysis in Table 5.3. In the first column, we reported for each attention component the brain regions identified by means of fMRI studies as proper of the specific function under investigation. After a screening of the single band results, the last column was coloured green only if at least in one frequency band a significant activation was found.

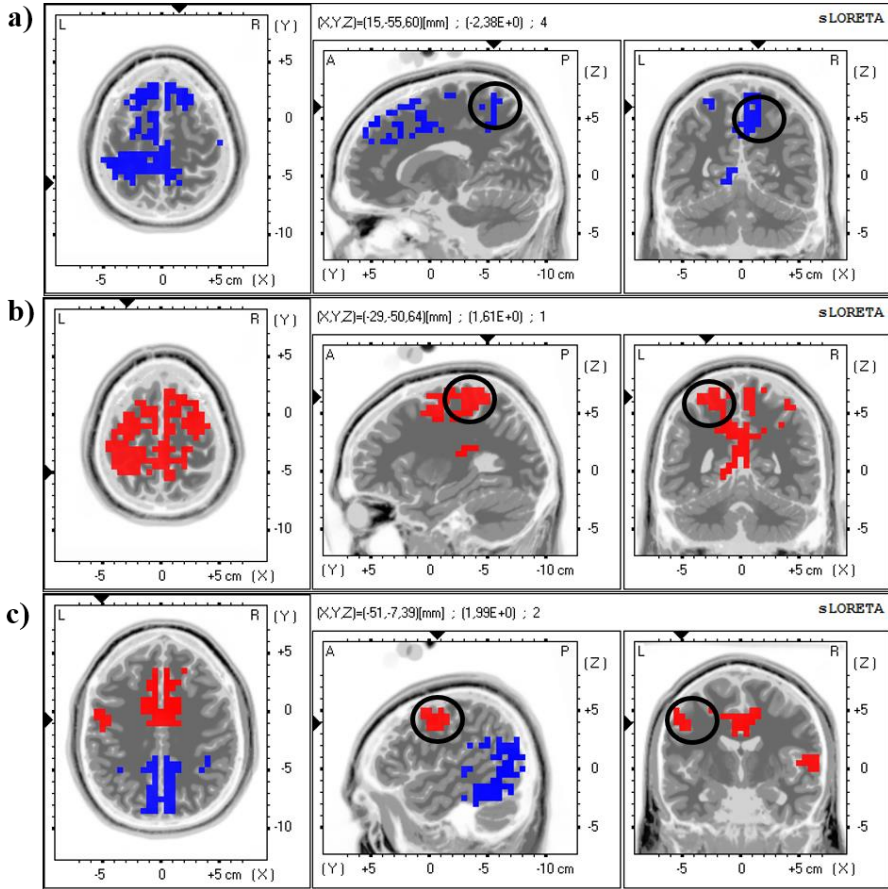


Figure 5.4 – Spectral statistical maps obtained with the LORETA software. As example, cortical and subcortical activations related with the alerting in alpha band (panel a), orienting in gamma band (panel b) and executive control in beta band (panel c) phases were reported. The maps derive from a *t*-test between proper couple of experimental conditions: No Cue and Center Cue in panel a); Center Cue and Spatial Cue in panel b); Congruent and Incongruent in panel c). Blue and red areas code for the *t* value associated to significant tests. Black circles highlight, as examples, one of the expected active brain area for each component: Right Superior Parietal Lobule for the alerting, Left Superior Parietal Lobule for the orienting, Left Precentral Gyrus.

		Theta	Alpha	Beta	Gamma	
Alerting	R Superior Temporal Gyrus	✓	✓	✓	✓	✓
	R Inferior Frontal Gyrus	✓	✓	✗	✓	✓
	R Anterior Cingulate Gyrus	✓	✓	✓	✓	✓
	R Superior Parietal Lobule	✓	✗	✗	✓	✓
	L Inferior Parietal Lobule	✓	✗	✓	✓	✓
	L Superior Parietal Lobule	✓	✗	✗	✓	✓
	L Precentral Gyrus	✓	✓	✓	✗	✓
L Superior Frontal Gyrus	✓	✓	✗	✓	✓	
Orienting	R Postcentral Gyrus	✓	✓	✗	✓	✓
	L Fusiform Gyrus	✓	✗	✗	✗	✓
	L Superior Frontal Gyrus	✓	✗	✗	✗	✓
	L Superior Parietal Lobule	✓	✗	✗	✗	✓
	L Precentral Gyrus (FEF)	✓	✗	✗	✗	✓
	L Inferior Parietal Lobule	✓	✗	✗	✓	✓
	L Inferior Frontal Gyrus	✓	✗	✗	✗	✓
Executive Control	R Inferior Frontal Gyrus	✗	✗	✗	✗	✗
	R Middle Frontal Gyrus	✓	✓	✗	✓	✓
	R Fusiform Gyrus	✗	✓	✓	✗	✓
	R Anterior Cingulate Gyrus	✓	✓	✓	✗	✓
	L Superior Frontal Gyrus	✓	✓	✗	✓	✓
	L Inferior Frontal Gyrus	✗	✓	✓	✓	✓
	L Precentral Gyrus (FEF)	✓	✓	✗	✗	✓
L Superior Frontal Gyrus (CL)	✓	✓	✗	✓	✓	

Table 5.3 – Spectral activations obtained by the source localization performed employing the sLORETA software. Green and red symbols in the first 4 columns code for the agreement or not with the previous fMRI studies. The last column is green when at least for one frequency band we found an agreement.

All the expected activations for each attention component have been found by means of the source localization approach. The only exception is represented by the Right Inferior Frontal Gyrus that was however selected as ROI in the following connectivity analysis because of its involvement in the alerting phase. The scientific contribution associated with this analysis is:

- To demonstrate the possibility of reconstructing the activities of the areas involved in the experimental task with good spatial resolution;

- In providing additional information about frequency bands that the fMRI cannot provide;
- In selecting the ROIs for the following connectivity analysis being sure that such areas had an important role for the isolated attention function.

Connectivity Analysis

In figure 5.5, we reported the statistical connectivity patterns obtained for the three attention components. Alerting networks show strong links mainly located in the frontal areas, especially in the lower frequency bands (theta and alpha bands). As regard the orienting network, the obtained maps highlight a prevalence of significant connection in Gamma band where Inferior and parietal areas appear involved in the network in both the hemispheres. The executive control network shows a more complex pattern in theta band, involving almost all the ROIs included in the model. It is worth of note the specific role of the right hemisphere as source of the information flow (*Right Superior Parietal Lobule*). Alpha and Beta bands showed few significant inter-connections linking the two hemispheres and directed predominantly from the right to the left one. The network obtained in gamma band appears characterized by a prevalent activity in the frontal-left regions. The analysis of these results allowed only qualitatively to understand the organization of the networks at the basis of the investigated cognitive functions. For this reason and to catch other important properties hidden by the strict group analysis we performed for extracting the showed maps, we decided to investigate the elicited pattern in an “indirect-way”. In other words, we evaluated the properties of the networks extracted for each experimental condition and we studied the attention components through the changes of the correspondent indices. A statistical test was performed between the graph measures evaluated in No/Center Cue, Center/Spatial Cue and Congruent/Incongruent conditions. In *tab. 5.4* we reported the results (p and t output of the paired t-test) only for the graph indices with a significance in at least one frequency band. All the other results are not statistically significant.

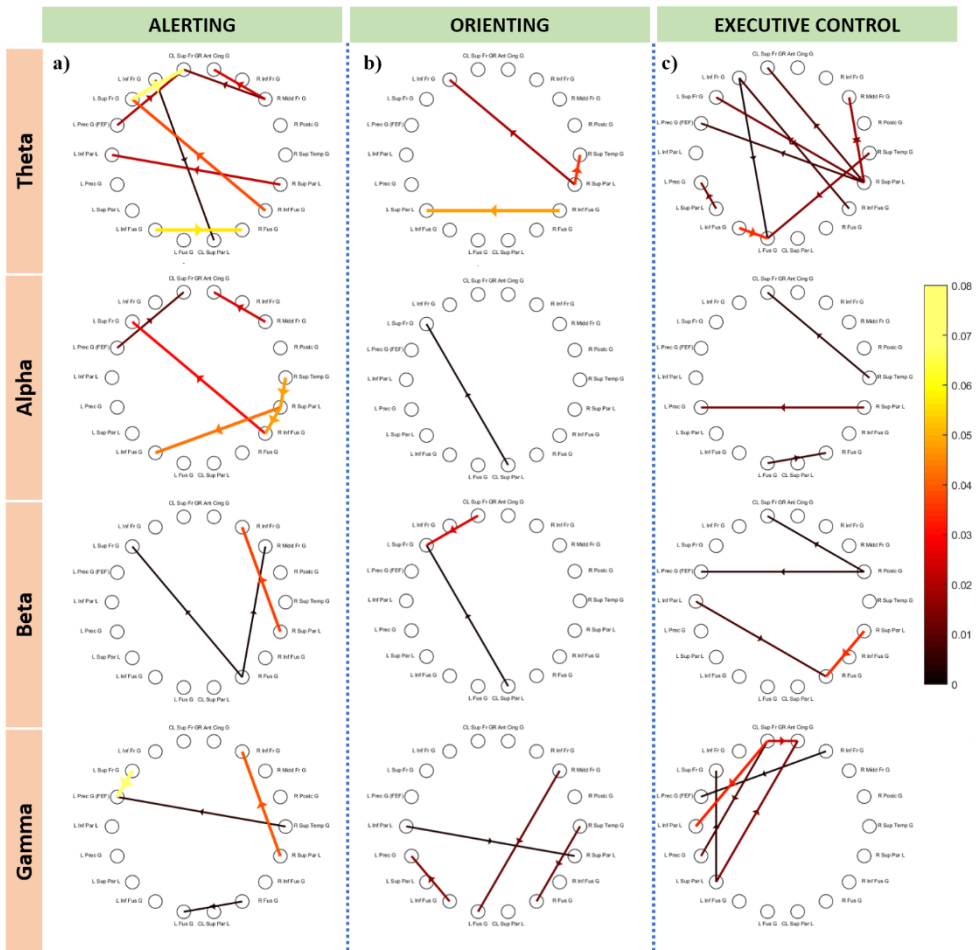


Figure 5.5 - Grand average statistical connectivity maps estimated for alerting (a), orienting (b) and executive control (c). Each network was reported for all the considered frequency bands: theta, alpha, beta and gamma. Nodes represent the 18 considered ROIs. The arrows represent the significant causal connections between them (paired t-test, $p < 0.05$ FDR corrected); their colour codes for the connection strength.

		<i>Theta</i>		<i>Alpha</i>		<i>Beta</i>		<i>Gamma</i>	
		<i>t</i>	<i>p</i>	<i>t</i>	<i>p</i>	<i>t</i>	<i>p</i>	<i>t</i>	<i>p</i>
<i>Al.</i>	<i>Density P</i>	0,153	1,51	0,162	1,48	0,019	2,64	0,598	0,54
	<i>Density BU</i>	0,148	1,53	0,628	0,50	0,012	-2,88	0,470	0,74
	<i>Density TD</i>	0,022	2,58	0,053	2,11	0,011	2,95	0,269	1,15
	<i>Asymmetry_BU/TD</i>	0,389	-0,89	0,670	-0,43	0,004	-3,47	0,757	-0,32
<i>Or.</i>	<i>Global Efficiency</i>	0,738	-0,34	0,262	1,17	0,615	0,52	0,015	2,77
<i>Ex. C.</i>	<i>Influence_L/R</i>	0,125	-1,63	0,001	-4,12	0,943	0,07	0,299	1,08
	<i>Influence_BU/TD</i>	0,016	-2,75	1,000	0,00	0,106	1,73	0,670	-0,43

Table 5.4 – Results of the statistical analysis (paired *t*-test, $\alpha = 0.05$, FDR correction) performed to compare the properties of the network associated to specific couple of experimental conditions: No/Center Cue for the alerting, Center/Spatial Cue for the orienting, Congruent/Incongruent for the executive control. For each frequency band the *p* value and the Student's *t* for the considered indices are reported.

To better render the obtained results, for each attention component we reported the boxplots of the compared distributions. Figure 5.6 shows the diagrams related with the alerting component. They showed a significant increase of the graph indices Parietal Density (panel a) and Top-Down Density (panel b) and a significant decrease of the Bottom-Up Density (panel c). The asymmetry between the Top-Down and Bottom-Up subnetwork, moves from a prevalence of the Bottom Up in the No Cue condition to a prevalence of the intra-connection of the Top-Down in the Center Cue condition (panel d). All the results were obtained in Beta band.

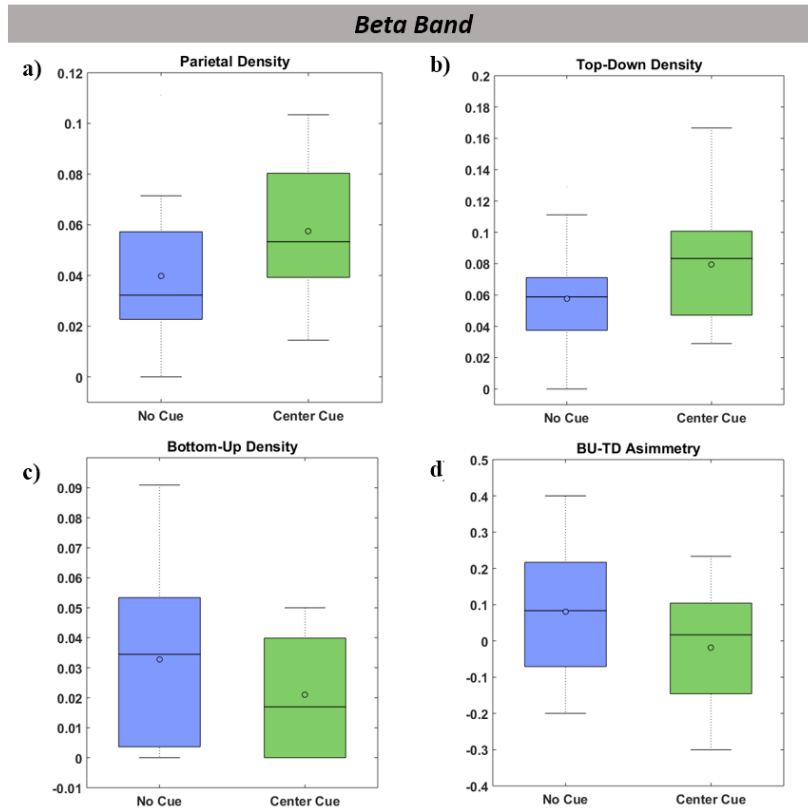


Figure 5.6 - Bar diagrams reporting the significant statistical comparisons (paired t -test, $\alpha=0.05$, FDR correction) between the experimental conditions No Cue, blue bar, and Center Cue, red bar, for the indices Parietal Density (panel a), Top-Down Density (panel b), Bottom-Up Density (panel c) and BU/TD Asymmetry (panel d). All the reported results are obtained for the beta band.

Results related with the orienting phase, reported in *fig. 5.7*, revealed a significant increase, in Gamma band, in terms of Global Efficiency. The orienting function, elicited by the spatial cue condition, is characterized by a different global organization of the network.

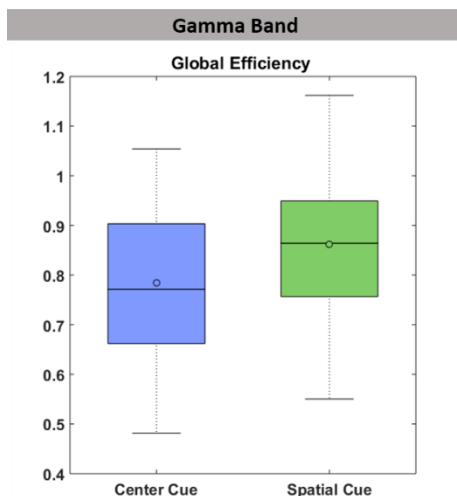


Figure 5.7 - Bar diagrams reporting the significant statistical comparisons (paired *t*-test, $\alpha=0.05$, FDR correction) between the experimental conditions Center Cue, blue bar, and Spatial Cue, red bar, for the Global Efficiency index in gamma band.

Analysis related with the executive control showed a significant variation of the indices BU/TD Influence in theta band and of the Left/Right Influence in alpha band (see *fig. 5.8*). Such result indicates that during the conflict resolution (Incongruent condition) the influence of the Bottom-Up network on the Top-Down one significantly decreases while the number of inter-connections from the left to the right hemisphere increases.

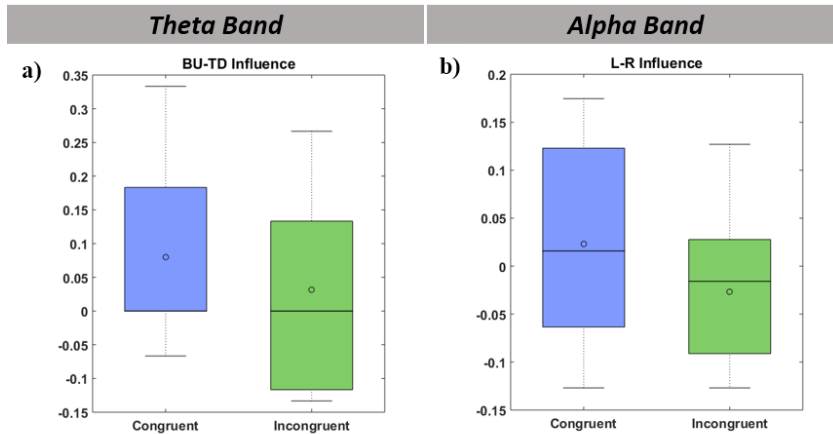


Figure 5.8 - Bar diagrams reporting the significant statistical comparisons (paired t -test, $\alpha=0.05$, FDR correction) between the experimental conditions Congruent, blue bar, and Incongruent, red bar, for the indices BU/TD Influence in theta band (panel a) and L/R Influence in alpha band (panel b).

3.3 Study 2: Sensors level analysis

Connectivity Analysis

In *fig. 5.9*, we reported the statistical connectivity patterns obtained for the three attention components. They are represented on a 2D model seen from above with the nose pointing to the top of the page in which nodes are the electrodes on the scalp and the edges are the causal significant connections. The high number of represented nodes and links does not allow to give a clear interpretation of the obtained results. It is evident how the executive control pattern shows the strongest connections in all the frequencies bands. To clarify the role of specific areas in the investigated attention function, we synthesize this huge amount of information by means of graph indices defined to catch the local and global properties of the networks.

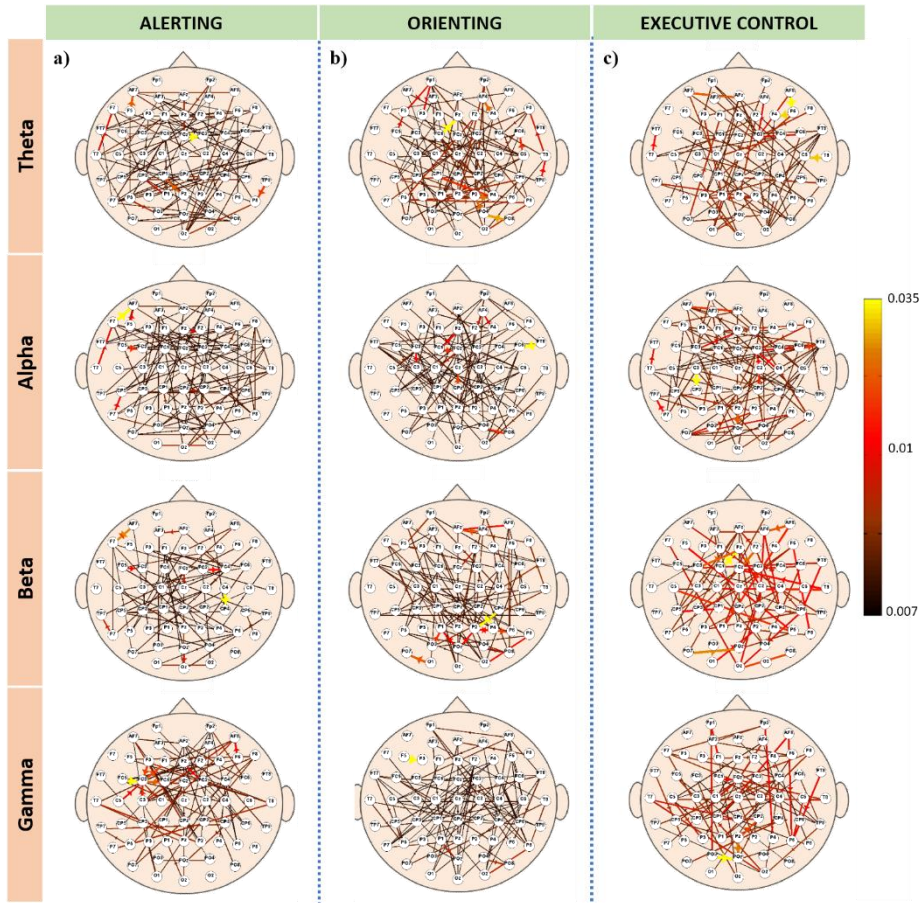


Figure 5.9 - Grand average statistical connectivity maps estimated for alerting (a), orienting (b) and executive control (c). Each network was reported for all the considered frequency bands: theta, alpha, beta and gamma. Nodes represent the 60 electrodes and the arrows represent the significant causal connections between them; their color codes for the connection strength.

Graph Indices

As in the previous section, results are reported separately for each component elicited by the ANT paradigm.

Alerting: as shown in *fig. 5.10*, we found significant negative correlations between the efficiency Eff_{Al} and i) the Path Length index in beta band (panel a) and ii) the Left/Right Influence index in theta band (panel b). Such correlations pointed out a relation between the behavioral performances and the speed in the exchange of

information between network nodes in the alerting phase (low path length) in beta band. Moreover, an efficient alerting is associated to a communication between the two hemispheres in theta band with a prevalence of the information flows directed from right to left (negative values for Left/Right Influence).

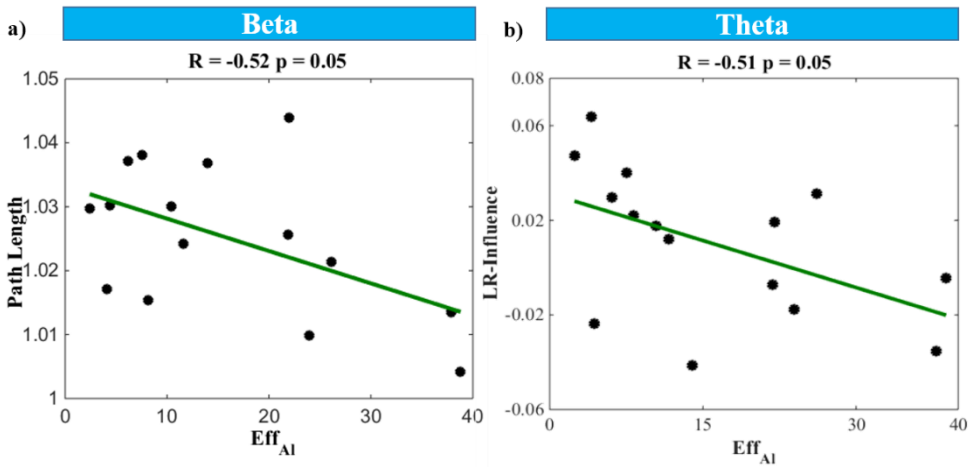


Figure 5.10 – Alerting: statistical correlations between the efficiency Eff_{Al} (y-axis) and the connectivity indices (x-axis): path length in beta band (panel a) and left/right influence in theta band (panel b). As in all figures, dots correspond to the values obtained for each of the 15 subjects involved in the study. The green line represents the linear fitting computed on the data. The associated values of correlation (R) and significance (p) are reported on the top of the figure.

Orienting: as shown in fig. 5.11, a positive correlation was found between the efficiency Eff_{or} and i) the Right Density (panel a) and ii) the Left/Right Divisibility (panel b) in the theta band. In particular, such results pointed out how an efficient orienting process is associated to a strong segregation of the information flows within the right hemispheres (high Right Density) and a low integration of the two hemispheres (high Left/Right Divisibility) in theta band. Furthermore, we found that the parameter Eff_{or} negatively correlated with the Posterior Density index (panel c) and the Anterior/Posterior Influence index (panel d) in the gamma band. This indicates that an efficient orienting process is associated to a low involvement of the posterior scalp regions (low Posterior Density) and to the establishment of a communication between anterior and posterior regions with a prevalent direction from posterior to anterior.

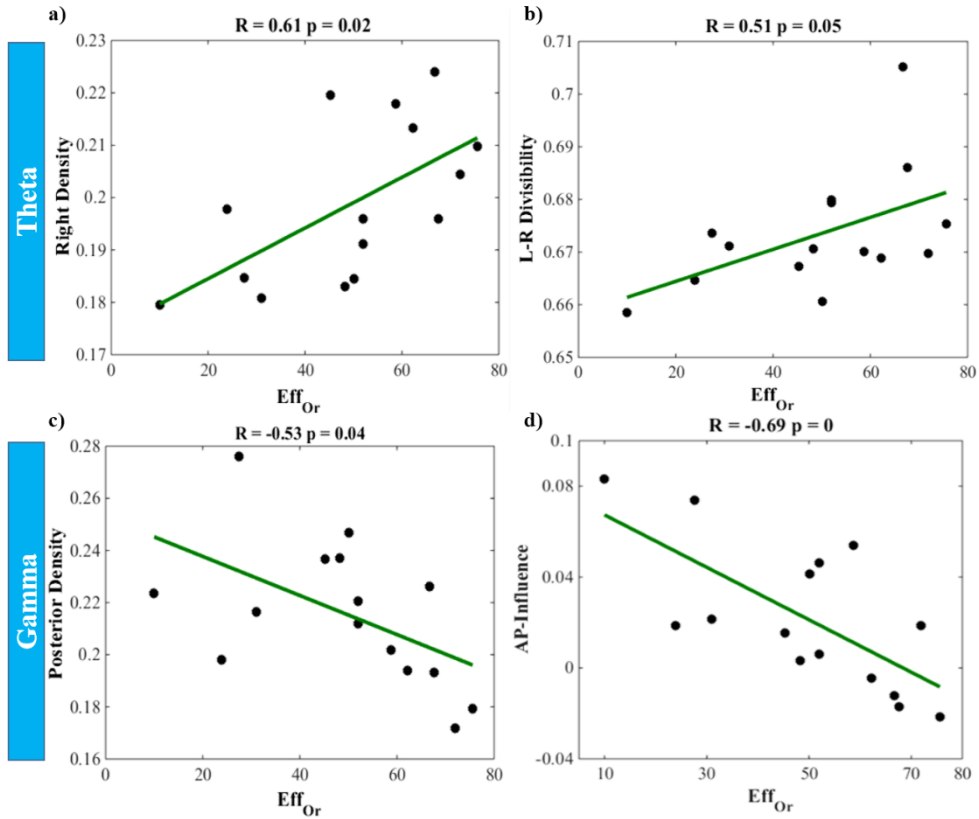


Figure 5.11 - Orienting: statistical correlations between the efficiency Eff_{Or} (y-axis) and the connectivity indices (x-axis) right density (panel a) and Left/Right Divisibility (panel b) in theta band, posterior density (panel c) and Anterior/Posterior Influence (panel d) in gamma band.

Executive Control: Figure 5.12 shows a significant positive correlation between executive control efficiency Eff_{EC} and both the Path Length (panel a) and the Clustering indices (panel b) in the gamma band. Significant correlations were also found between efficiency Eff_{EC} and Left/Right Divisibility (panel c), Left/Right Modularity (data not shown; $R=0.53$, $p=0.05$) and Left/Right influence indices (panel d) in the alpha band. In particular, such results indicated how a reduction in the time required for solving the conflict (low Eff_{EC}) is associated to a high communication speed between the electrodes (low Path Length) and to a less tendency of the network to create clusters (low Clustering). Moreover, an efficient (i.e. correlated with high behavioural performance) executive control is explained

by a high integration of the two hemispheres (low Left/Right Divisibility) with information flows directed from right to left (negative values of Left/Right Influence).

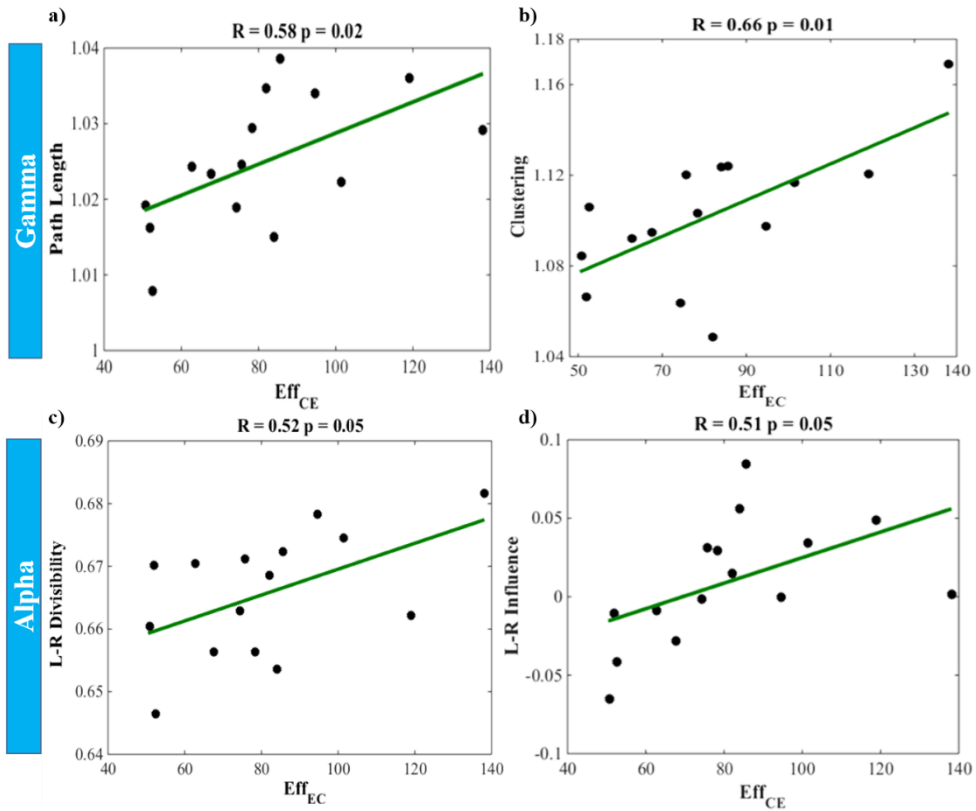


Figure 5.12 - Executive control: statistical correlations between the efficiency Eff_{EC} (y-axis) and the connectivity indices (x-axis) -Path Length (panel a) and Clustering (panel b) in gamma band -Left/Right Divisibility (panel c) and Left/Right Influence (panel d) in alpha band.

4. Discussion and Conclusion

4.1 Study 1: Source level analysis

The integration of source localization methods, connectivity estimation and GT indices allowed to provide spatial and temporal information and to extract synthetic neurophysiological indices directly related to the cerebral processes that underlie the three attentive components.

Alerting component: The results reported in *fig. 5.5a* and *fig. 5.6* suggest that the alerting component is characterized by: i) an important role played by the fronto-parietal network especially in the low bands theta and alpha and ii) a prevalence of the intra-connection of the parietal areas and of the regions involved in Top-Down processes. Such results are in agreement with the evidence that structures involved in Top-Down network are crucial in sensory processing of the stimulus [99]. Moreover, according to our findings, the alerting component is related to the fronto-parietal network activation that modulates the specific impact of a warning cue that precedes a target. The entire network appears to be characterized by a prevalence of information exchanged within parietal ROIs confirming that the area most consistently activated and modulate by attention to the stimulus include the dorsal parietal cortex [99].

Orienting component: The results reported in *fig. 5.5b* and *fig. 5.4* suggest that the orienting function is characterized by a high involvement of the right hemisphere in gamma band, in agreement with the evidence that activity in the right areas is associated with linking temporal and spatial information and with the specific presentation of a warning signals [110] when it is associated to the so-called “*covert-orienting*”. Such interesting results were obtained in gamma band, as expected in according with the Fan’s study of the brain oscillations related with the attention networks [100]. In addition, the graph theory approach allowed to identify in the Spatial Cue condition related with the orienting phase, an increase of the Global Efficiency of the whole network.

Executive Control: Conflict resolution is the most complex phase in the ANT and was described by indices referred to the cooperation between Bottom-Up and Top-Down networks and between the left and right hemispheres (*fig. 5.5c* and *fig.*

5.8). Results were obtained specifically for the theta and alpha bands in which a significant activity has been already demonstrated. In particular, theta activity has been associated with aspects of task monitoring, including error detection, that are often associated with executive attention [111] and changes in alpha activity have been related to the success of distracter suppression [112]. Altogether, these results reflect the highly integrative nature of the conflict processing, which requires more integration between existing sub-networks (Bottom-Up and Top-Down and the two hemisphere) of the information flows originated from several partially overlapping networks [113]. The performed connectivity analysis allowed to identify the prevalent directions of such flows. Inter-connections from the right to the left hemisphere and a symmetry exchange between Top-Down and Bottom-Up networks (BU/TD Influence index tends to zero) characterize the investigated attention component.

In conclusion, the results of this EEG connectivity study in the source domain allowed to integrate in a single model spatial, spectral and causal information about the brain areas involved in attention processes and to define synthetic indices able to give a contribution to the neuro-physiological description of the three processes. Future studies could confirm the selectivity of some of these indices. Our results showed the possibility to identify the specific cerebral areas involved in attention processes from EEG recording, analysed in the source space. Furthermore, the integration between source localization methods, connectivity estimation and GT indices allowed to provide spatial and temporal information and to extract synthetic neurophysiological indices directly related to the cerebral processes underlying the attentive functions.

4.2 Study 2: Sensor level analysis

In the present study, we used advanced techniques for EEG signals processing to extract the cortical connectivity patterns (causal relationship between scalp areas) associated with the 3 attention components as elicited by the ANT paradigm (i.e. alerting, orienting and executive control) performed by healthy subjects. Some indices, derived from the graph theory, allowed the quantitative description of the relevant local and global properties of the 3 different causal

connectivity networks in specific EEG frequency bands as they correlated with the behavioural performance (i.e. correlated with Eff_{Al} , Eff_{Or} , Eff_{EC}). According to our findings, the estimated *alerting* network was described mainly by a negative relationship between the behavioural efficiency (Eff_{Al}) and Path Length index in the beta band, (i.e., the higher efficiency the shorter Path Length) and the left/right Influence index in the theta band (i.e., the higher efficiency the higher interhemispheric connection from right-to-left; negative values for left-right influence index). The phasic *alerting* improves the speed of target response by changing the internal state of preparation for perceiving a (visual) stimulus [100]. Our results indicate that an efficient alerting function (higher speed to target response) is associated with a global network organization characterized by a shorter average Path Length which corresponds to a high efficiency information transfer [114]. As yet, the entire network appears to be characterized by a prevalent exchange of information directed from right to left hemisphere. Such prevalence might reflect the role of the right hemisphere to sustain alertness that was already stressed in previous studies in which lesions of the right frontal and parietal areas were associated to reduced ability in maintaining the alert state [115]. The above discussed index modulation occurred in beta and theta band, respectively. This finding is in line with previous EEG evidence of a relationship between these frequency oscillations and the alerting function [100]. The efficiency of the *orienting* function was in our study, described by a set of network indices which correlated with behavioural performance (Eff_{Or}). First, we found that the higher performance efficiency the higher right Density and left-right Divisibility in the theta band. In addition, higher orienting efficiency also correlated to both lower posterior Density and anterior/posterior Influence (prevalence for post-to-ant) in the gamma oscillations. Together, these results indicate a prevalent role of the right hemisphere versus the left (higher connectivity density) and poor communication between hemispheres (higher divisibility). About the frontal and parietal areas, results indicate a prevalence of connections from posterior to anterior areas (higher anterior/posterior influence and lower posterior density). This is in line with previous evidence of the (right) parietal and frontal areas involved in orienting function which enables for the

selection of specific information from a number of sensory inputs [3],[16][99]. The above discussed index modulation occurred in the theta and gamma frequency oscillations that may be in line with the evidence in favour of the contribution of the theta oscillation to long-range communications for cognitive processing by phase-locking to high gamma power [117]. Finally, an efficient *conflict* resolution (ie, *executive control*) was described mainly by a positive relationship between the behavioural efficiency (Eff_{EC}) and both the Clustering and Path Length indices in the gamma band, (i.e., the lower time to solve the conflict (low Eff_{EC}) the lower tendency to clustering and shorter Path Length) and both the left/right Divisibility and Influence indices in the alpha band (i.e., the higher efficiency the higher interhemispheric connection with a prevalent right-to-left direction flow; negative values for left-right influence index). Altogether these results reflect the highly integrative nature of the conflict processing which requires more integration than segregation of information flow which are originated from several partially overlapping networks [113].

In order to understand the relation existing between source and scalp measure, other specific analysis should be performed. The role of the single ROIs, for example, could provide a direct explanation of networks obtained from the mixed scalp signals. The results obtained in the present work indicate that:

- the alerting network is characterized by a high involvement of the parietal areas and top-down processes at source level, but such local properties are not visible in the sensors domain where global properties, like the Path Length, showed a correlation with the behavioral responses.
- The orienting network, is characterized by a high Global Efficiency in gamma band; in the same frequency band we found significant correlations at scalp level involving local properties regarding the greater involvement of the anterior areas;
- The executive control was described by the index Left/Right Influence in alpha band that highlight a prevalence of the flows from the right to the left hemisphere. The same index in the same band correlate at scalp level with the behavioral measure *Efficiency* with other global indices like the Clustering and the Path Length in gamma band.

Advanced EEG signals elaboration based on time-varying connectivity estimation and graph theory were applied to extract direct and weighted connectivity patterns elicited by the ANT paradigm at scalp level. Correlation results pointed out a set of EEG-based indices able to synthetically describe each of the three attention components in the different frequency bands and to follow the variations in the corresponding behavioural measures. Such preliminary results could be used in the near future to: i) support the neuropsychological assessment in healthy subject and people with attention impairments; ii) clarify the role of specific attention components in BCI contexts (P300- and SMR-based BCI) and eventually improve the design of BCIs targeting attention rehabilitation; iii) increase the knowledge on attention brain networks elicited by the ANT paradigm. Altogether, our findings at the scalp level might have a strong impact on several clinical/non-clinical applications related to the BCI field.

Chapter 6

Connectivity in memory functions

Several non-invasive imaging methods have contributed to shed light on the brain mechanisms underlying working memory (WM) in normal aging humans. The aim of the present study was to depict the topology of the relevant EEG derived brain networks for distinct operations of WM function elicited by the Sternberg Item Recognition Task (SIRT) such as encoding, storage and retrieval in healthy, middle age (46 ± 5 yrs) adults. Seventeen participants underwent an EEG recording whilst performing the visual SIRT. Neural correlates of WM were assessed by means of a combination of EEG signal processing methods (i.e., time-varying connectivity estimation and graph theory), with the aim to extract synthetic descriptors of the encoding, storage and retrieval phases of WM construct as elicited by SIRT, and sensitive to different memory workload¹. Overall network findings illustrated in this study indicate that the use of EEG-derived connectivity measures and their related topological indices might offer a valuable approach to support the clinical assessment of cognitive functions in presence of WM decline/impairment, as it occurs after stroke. A brief preliminary study on a stroke population will be also illustrated.

1. Introduction

The working memory (WM) is a non-unitary construct that involves the temporary maintenance and manipulation of information either recently acquired or retrieved from long-term storage [118]. The Baddeley's model is one of the most recognized among the several current models describing the operating principles of WM [119]. It encompasses diverse separable but interacting subsystems such as: 2 unimodal storage sub-systems (phonological loop for verbal material and visuo-spatial sketchpad for visuo-spatial material), a flexible system (central executive) which is responsible for the control and regulation of the storage sub-systems and a multimodal system with limited capacity storage

¹The study reported in the chapter has been accepted as research article to the journal *Frontiers in Human Neuroscience* (DOI: 10.3389/fnhum.2017.00637).

(episodic buffer) that allows the interaction between the various components of WM and the interface with long-term memory [120], [121]. The Sternberg Item Recognition Task (SIRT; Sternberg, 1966) has been largely used in cognitive neuroscience to assess WM capacity in terms of storage and data retrieval [122], [123]. It allows for a segregation of encoding, executive maintenance and retrieval processes (not manipulation) regarded as central within the multi-component model of WM. The SIRT is also relatively free from practice effects [124]. The SIRT was initially introduced to investigate the neurophysiological processes at the basis of WM by means of indirect behavioural measures [125], [126]. Its application was extended later into the field of neuroimaging techniques, functional magnetic resonance imaging (fMRI), electroencephalography (EEG) and magnetoencephalography (MEG) aiming at directly measuring the neural correlates underpinning WM processes [127]–[130]. Several fMRI studies have shown that verbal WM processing in adult humans requires the involvement of a large network which includes bilateral dorso-lateral prefrontal, left inferior frontal, middle and superior frontal areas, premotor and supplementary motor areas as well as inferior parietal and superior temporal areas, the insula and parts of the cerebellum [131]–[133]. Further studies using SIRT found specific patterns of activation for each of the three phases of WM (encoding, storage and retrieval). A modulation of the hemodynamic response as function of different WM load levels was also reported [134], [135], [132], [136], [129], [137]. Evidence for specific brain oscillatory responses elicited during the different phases of WM emerged from EEG and MEG studies using the SIRT. In particular, the maintenance (storage) phase of verbal SIRT was associated with oscillatory power in theta (4–8 Hz) predominantly over the frontal midline and left temporal-parietal sites [138], [139], [128] as well as in alpha (8–13 Hz) power over the parietal midline, the parieto-occipital and left tempo-parietal regions [140]–[143]. The involvement of such frequency bands/areas was also modulated by the changes in memory load [144], [145], [139], [128], [146]. In particular, an increase of frontal-midline theta and temporo-parietal alpha and a decrease of beta and gamma activities in frontal areas were observed as function of WM load. An involvement of frontal and occipital regions was also found in beta and gamma

frequency bands [139], [147]–[149]. To fully understand brain functions involving distributed neural networks, it has recently become attractive to apply functional neuroimaging methods that allow to describe the dynamics within a network of areas sustaining a specific cognitive process (such as WM), and how the brain damage-induced disruption of circuits can account for the behavioural impairment [150]–[153]. A functional-connectivity based approach has been recently applied to track age-related changes in brain connectivity in a group of children and adolescents performing a modified version of the SIRT [154]. Task related networks were identified for encoding and recognition phases and their load-induced modulation was also correlated with age [154], [155]. In this study, we applied a combined approach based on EEG-derived connectivity patterns and graph theory [156], [104], [41] to isolate synthetic descriptors of the encoding, storage and retrieval phases of WM construct as elicited by SIRT, in healthy condition. We expected such combined approach to return quantitative measurements specific for the 3 different WM phases and sensitive to different memory workload. The relationship between extracted neurophysiological indices and subject memory performance was also assessed to explore to what extent the estimated EEG networks topology would account for memory behaviour. A preliminary study proved the feasibility of this approach to capture the WM processes in different phases of the SIRT [157]. Life span studies have indicated that changes in memory task-related neural activity may emerge from middle age onward [158]–[160]. Moreover, Aine and colleagues (2006-2011) have recently suggested that a middle age group could be another critical comparison group with respect to young and old adult, since there is evidence that brain maturation continues into the fourth decade of life [161], [162]. Hence, we targeted middle-age population (i.e. between 40 and 50 years) to limit possible confounding effects on the stability of measures as due to age-related differences occurring in young and old population sample.

2. Materials and methods

2.1 Experimental group

Seventeen healthy subjects (age: 46 ± 5 years old; 8 males; education: 14.8 ± 3 years) were enrolled in the study. All participants except one were right-handed with normal or corrected-to-normal vision. No participant reported a history of neurological or psychiatric diseases; in addition, they were all screened for intake medications and none was receiving any pharmacological treatment affecting cognitive functions. Participants underwent some subtests (Similarities, Information, Coding, Picture Completion, Mosaic Test) from the German adaptation of the Wechsler Adult Intelligence Scale (WAIS III, von Aster, Neubauer & Horn, 2006), for a general screening of the cognitive function and also a deep evaluation of the memory functions. In particular, for the evaluation of the verbal and visuo-spatial memory, subjects performed the Corsi Block Tapping Test (CBTT) [163], the Visual and Verbal Memory Test (VVM 2) [164], the Digit Span [165], the Verbal Learning Memory Test (VLMT), the Nonverbal Learning Test (NVLMT), the Verbal Learning Test (VLT) [166]. All the subjects achieved normal scores in all the investigated cognitive domains. All participants provided written informed consent according to the convention of Helsinki. The ethics committee of the University of Graz approved the study. All participants received monetary reward for their participation to the study.

2.2 Experimental Design

The EEG potentials were recorded from 60 scalp electrodes embedded in a lycra cap, with a left mastoid reference and ground at Fpz. Horizontal and vertical electro-oculogram (EOG) signals were recorded from 3 electrodes in total, two placed on the outer canthi of the eyes and one below the right eye, respectively. EEG signals were amplified (BrainAmp; Brain Products GmbH, Munich, Germany) and filtered by means of a [0.01 – 100] Hz band-pass filter prior to digitization at 500 Hz. Electrode impedances were kept below 5 kOhms and 10 kOhms for the EEG and EOG recording, respectively. After 2 minutes of resting EEG acquisition

(of eyes open and close), each subject performed the Sternberg task [126]. Accordingly, the experimental procedure to deliver the paradigm was as follows: first, a series of numeric digits was visually presented to the participants who had to memorize it (encoding phase); then, the participants had to retain the memorized information for a fixed period (storage phase) and finally, participants had to retrieve such memorized content in a brief time interval (retrieval phase). In particular, participants were asked to remember a set of unique digits (between 1 and 9), and then a probe stimulus in the form of a digit was presented. Subjects were instructed to answer, as quickly as possible, whether the probe was in the previously presented set of digits or not. The size of the initial set of digits determined the WM load required to the subject to execute the task (4 digits → easy, low workload; 6 digits → difficult, high workload). Details about the timeline of the experiment can be found in figure 5.1.

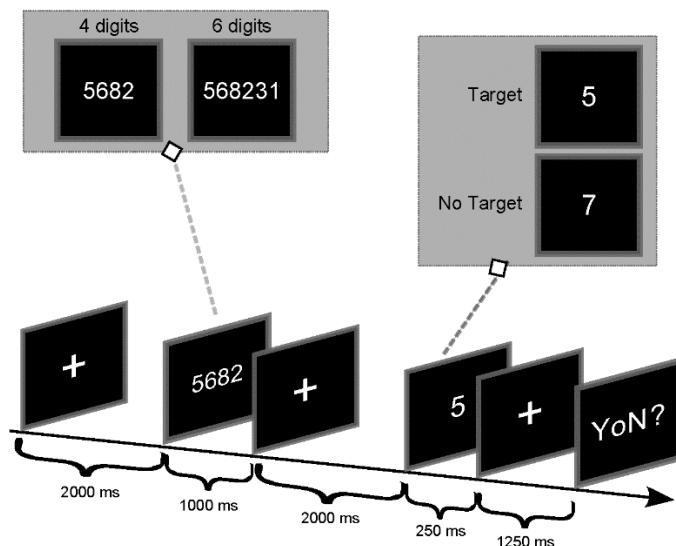


Figure 5.1 - Timing of the Sternberg experiment. Each trial started with a 2 sec presentation of a fixation cross in the middle of the screen. Afterwards, a “memory set” of 4 (e.g. 5682) or 6 digits (e.g. 146372) was presented (1 sec) to allow for memorization (encoding phase). The presentation of the digit series was then followed by a fixation cross, displayed for 2 sec (storage period). A single probe digit was then presented for 250 ms (retrieval phase) followed by a fixation cross presented for 1250 ms. Afterwards, the question “yes or no?” appeared on the screen (maximum duration of 1500 ms) and the participant had to answer

2.3 Behavioral data

We collected reaction times (RT) and the percentage of correct answers for each subject and each condition (Target/no-Target and 4-6 digits). To examine any effect of task-related complexity and task-related trials on the subject behavioural performances, two separate two-way repeated measures ANOVAs with digits number (DIGITS; 4 or 6) and target type (TYPE; Target/No Target) as within main factors were performed considering the percentage of correct answers and reaction times (RTs) parameters as dependent variables.

2.4 EEG data pre-processing

EEG signals were down sampled to 100 Hz (with anti-aliasing low-pass filter) to optimize the following connectivity analysis and then band-pass filtered in the range [1 45] Hz. in order to isolate the EEG spectral content of interest. Independent Component Analysis (ICA) was used to remove ocular artifacts. EEG traces were segmented in relation with the specific timing of the paradigm, [0 4500] ms (period of interest) according to the onset of the first screen containing the digits series and classified according to different conditions (Target_4digits, No Target_4digits, Target_6digits, No Target_6digits). Only trials correctly executed were included in the analysis. Residual artifacts were then removed by means of a semi-automatic procedure based on a threshold criterion ($\pm 80 \mu\text{V}$). Only the artifacts-free trials were used for further analysis.

2.5 Time-varying Connectivity estimation

Pre-processed EEG signals were subjected to a time-varying connectivity estimation process for each subject and each experimental condition (4/6 digits, target/no-target). Here, we employed the time-varying adaptation of Partial Directed Coherence (PDC) based on the General Linear Kalman Filter (GLKF) which is able to follow temporal dynamics of brain networks with high temporal resolution in high density EEG data (see results of the *Chapter 3*). We used it to estimate the relationships between signals for all frequency samples in the range [1 45] Hz and for all the samples in the time interval [0 4500] ms. Any relevant

changes in the time-varying connectivity matrices related to the different experimental conditions were evaluated by means of statistical comparison (independent samples t-test) performed between each experimental condition (Encoding, Storage, Retrieval phases, 4/6 digits; correct answer trials) and the corresponding baseline. The baseline period was the time interval [-1000-0] ms preceding the appearance of the digits series (subjects fixing a cross on the screen). Time samples were used as observations for statistical test. The test was repeated for each frequency band and each subject. The significance level was set at 5%. A False Discovery Rate (FDR) was conducted for multiple comparison correction [167]. The PDC values contrasted with the baseline period were estimated for each time sample and averaged in the 4 frequency bands-of-interest and in 3-time intervals (periods-of-interest). As in the previous chapter, the frequency bands were individually defined according to the IAF. The three periods-of-interest correspond to: [0 1000] ms (encoding phase); [1000 3000] ms (storage phase) and [3000 4500] ms (retrieval phase). The analysis was conducted only on Target condition.

2.6 Graph indices

General properties of the network: the human brain can be viewed as a large-scale complex network that is simultaneously segregated and integrated via specific connectivity patterns [168]. We selected the 3 indices - local and global efficiency and small-worldness - that are widely utilized to describe the general topological properties of a network, thus reflecting the integration and segregation of the information flow between areas [169].

Global Efficiency (GE) and *Local Efficiency (LE)* were described in *Chapter 5*.

Small-Worldness (SW). It has been suggested that the human networks are organized to optimize efficiency, due to a small-world topology allowing simultaneous global and local parallel information processing [170]. SW is a measure of a network global organization in terms of its integration and segregation properties. Small-world topology is typical of networks highly segregated (nodes organized according to clusters) and highly integrated (high communication speed between electrodes). A network G is defined as small-world

network if $L_G \geq L_{rand}$ and $C_G \gg C_{rand}$ where L_G and C_G represent the characteristic path length [171] and the clustering coefficient of a generic graph and L_{rand} and C_{rand} represent the correspondent quantities for a random graph [172]. On the basis of this definition, a measure of small-worldness of a network can be introduced as follows:

$$SW = \frac{C_G / C_{rand}}{L_G / L_{rand}} \quad (5.1)$$

being a *small-world* network if $S > 1$ [173].

Local properties of the network: the topology of the networks was further investigated by computing the degree index for each scalp electrode to characterize the (local) level of in- and out- information flows exchanged within the network.

Degree. The degree of a node is the number of connections directly to it. As such the degree is the simplest index identifying hubs in graphs. In directed networks, the indegree is the number of inward links and the outdegree is the number of outward links [171]. It can be defined as follows:

$$k_f = \sum_{j \in N, j \neq f} g_{fj} + \sum_{i \in N, i \neq f} g_{if} \quad (5.2)$$

where k_f is the degree of node f and g_{ij} represents the entry ij of the adjacency matrix G . The degree of a specific electrode was normalized with respect to the network density, in order to capture local changes and not a general increase/decrease of the network density.

2.7 Statistical Analysis

All the extracted global and local indices were subjected to a two-way ANOVA with memory phases (PHASES: Encoding, Storage, Retrieval) and digits number (DIGITS: 4, 6) as main *within-subject* factors. Duncan's post-hoc test was used to verify differences between the ANOVA levels. FDR was further applied to correct

for multiple ANOVAs. Furthermore, to explore the relationship between the indices extracted for each memory phase and the relative behavioural data (correct answers rate, reaction time) a Pearson correlation analysis was performed. FDR was applied to reduce type I errors due to multiple correlations.

2.8 Preliminary study on stroke patients

Several times in the context of this thesis, we mentioned the possibility to employ the introduced connectivity-base indices as clinical measure. In the follows we present a first preliminary study in which they were used in the description of cortical re-organization induced by neurofeedback training in a population of 16 stroke patients with memory deficits (age: 41.1 ± 14.1 years; 7 males). To this purpose, the proposed indices quantifying the properties of brain connectivity networks were estimated during a high-density EEG preceding (PRE) and following (POST) one month of cognitive rehabilitation treatment, as possible indicators of the changes in cortical organization induced by the intervention. These indices were defined on the basis of a thorough revision of the literature about connectivity in cognitive functions and of the results obtained in the study performed on the healthy elderly volunteers. The task, the experimental design of the EEG sessions and the pre-processing of the acquired signals were described in detail in the previous paragraph of the chapter, being the same employed for the healthy group. Also in this case, brain networks associated to each of the targeted cognitive functions (Encoding, Storage and Retrieval) were obtained by means the time-varying adaptation of the PDC based on the Kalman filter (see Chapter 3). The global indices introduced in the previous section were computed. As local measure, we used the Density index evaluated for macro-areas (right and left hemispheres, anterior and parietal electrodes) instead of the degree of the single sensors because of the lesions presence. The following step was to test whether specific brain indices could be suitable to quantify the effects induced by a cognitive training in terms of changes in the brain organization. To overcome the limitations due to patients' different conditions and outcome, we evaluated the significant changes in the connectivity networks and indices at the single subject level. The main steps of the data analysis are summarized in the follows:

1. PRE and POST EEG data pre-processing;
2. Time-varying effective connectivity networks estimation for each memory phase and frequency band and graph theory indices evaluation;
3. Statistical comparisons between PRE and POST measurements (clinical data, graph indices) in order to describe modifies in memory processes induced by the rehabilitative treatment: single subject analysis (independent samples t-test, $p < 0.05$, FDR correction);
4. Statistical correlations (Pearson, $p < 0.05$, FDR correction) between the relative increase of neuro-physiological indices and behavioral scores;
5. Logistic binary regression to validate the connectivity indices as outcome measures for the memory training. i) internal validation: agreement between neuro-physiological indices and behavioral improvements; ii) external validation: agreement between neuro-physiological indices and clinical scales.

3. Results

3.1 Behavioral analysis

The overall behavioural data obtained from each subject is reported in table 6.1. All the participants showed a percentage of correct answers above 80% (except for subject 5 in 6 Digits who was removed from the analysis) and reaction times (RTs) comprised between 250 and 700 ms for the 4 SIRT conditions. The variability ranges observed for the 2 behavioural parameters are in agreement with literature and comparable with those reported in other studies [174], [175], [126].

Subj #	Correct Answers (%)				Reaction Time (ms)			
	Target		No Target		Target		No Target	
	4 digits	6 digits	4 digits	6 digits	4 digits	6 digits	4 digits	6 digits
1	94	81	94	94	356.91	346.97	422.76	469.35
2	94	78	97	92	373.97	386.68	382.66	444.73
3	100	81	97	86	548.39	468.03	502.80	521.00
4	97	100	94	89	306.37	321.53	305.26	382.34
5	92	72	97	97	411.48	498.77	405.94	511.97
6	94	81	97	89	619.24	632.31	597.43	620.78
7	86	86	94	83	425.81	458.03	483.50	499.70
8	94	86	89	83	473.76	460.26	607.34	554.80
9	83	89	86	78	430.63	509.16	433.10	504.71
10	97	81	92	89	778.11	785.28	704.91	722.66
11	97	97	97	97	319.51	331.20	295.80	371.71
12	97	92	86	94	413.97	347.45	381.87	398.74
13	94	94	92	94	282.38	250.29	265.58	285.88
14	92	81	92	81	444.70	573.41	608.03	595.31
15	97	94	97	89	460.71	474.68	559.97	516.81
16	92	83	94	89	616.64	626.97	580.24	705.78
17	92	83	94	89	616.64	626.97	580.24	705.78
MEAN	94	86	94	89	463.48	476.35	477.50	518.36
STD	4,2	7,6	3,8	5,6	133.01	140.16	128.55	124.12

Table 6.1 – Mean values of the percentage of correct answers and relative reaction time (RTs) obtained from each participant. Missing answers (RT=0) were excluded.

The two-way ANOVA revealed a significant influence of the main factor DIGITS ($p=0.00007$, $F(1,15) = 28.15$, $MSE = 672.8$) on the percentage of correct answers and of the main factors TYPE ($p = 0.013$, $F(1, 15) = 7.83$, $MSE = 12269$) and DIGITS ($p = 0.021$, $F(1, 15) = 6.54$, $MSE = 13336$) on the RTs. In particular, the percentages of correct answers significantly decreased ($94\pm 3\%$ to $87\pm 5\%$) when the subjects were challenged with the condition of 6 digits with respect to 4. The RTs were also significantly longer in the condition 6 digits with respect to 4. Furthermore, the No Target condition was associated to significantly longer RTs

as compared to those obtained during the Target condition (470 ± 126 vs 500 ± 130 ms) in the 6 digits case. Subject 5 was excluded from the EEG analysis for his/her low accuracy in the task execution (30% error rate).

3.2 Healthy subjects

Global properties of the networks

The results of the two-way ANOVA for the Local Efficiency (LE), Global efficiency (GE) and Small-Worldness (SW) indices with respect to memory phases and WM load are reported in table 6.2 for the four frequency bands.

GLOBAL INDEX	BAND	PHASES (d.f.=2,30)	DIGITS (d.f.=1,15)	PHASES x DIGITS (d.f.=2,30)
Local Efficiency	θ	27,58**	0,02	0,01
	α	30,38**	4,66*	3,4*
	β	79,55**	0,11	0,3
	γ	177,77**	9,62*	8,75*
Global Efficiency	θ	21,51**	1,2	0,21
	α	39,31**	0,03	0,58
	β	10,64**	2,98	0,51
	γ	9,19**	0,95	1,81
Small-Worldness	θ	65,32**	0,71	1,1
	α	48,84**	4,56*	4,07*
	β	148,16**	0,07	0,002
	γ	122,52**	0,61	0,51

Table 6.2 – Results of two-way repeated measures ANOVA on global indices (F values, ** $p < 0.001$, * $p < 0.05$). FDR correction for multiple ANOVAs was applied

We found a significant effect of the main factor PHASES on LE index in all frequency bands and of the main factor DIGITS in alpha and gamma bands. The interaction factor DIGITS x PHASES had a significant effect in both alpha and gamma bands. Similarly, a significant effect of the main factor PHASES was found on the SW index in all bands of frequency; the main factor DIGITS and the interaction factor DIGITS x PHASES were also significant for SW in alpha band. Finally, the main factor PHASES has a significant effect on GE index in all frequency bands. As shown in *fig. 6.2*, the LE index mean value ($n = 16$) relative to alpha band was significantly higher in the *Encoding* with respect to both *Storage* and *Retrieval* phases (*fig. 6.2*, panel a). An opposite trend was observed for the GE index (*fig. 6.2*,

panel b) that was significantly higher in the *Retrieval* as compared to both *Encoding* and *Storage* (fig. 6.2, panel b). Finally, the SW index (fig. 6.2, panel c) was significantly higher in the *Encoding* as compare with *Storage* and *Retrieval*. Similar significant results were found for the three indices in the other frequency bands.

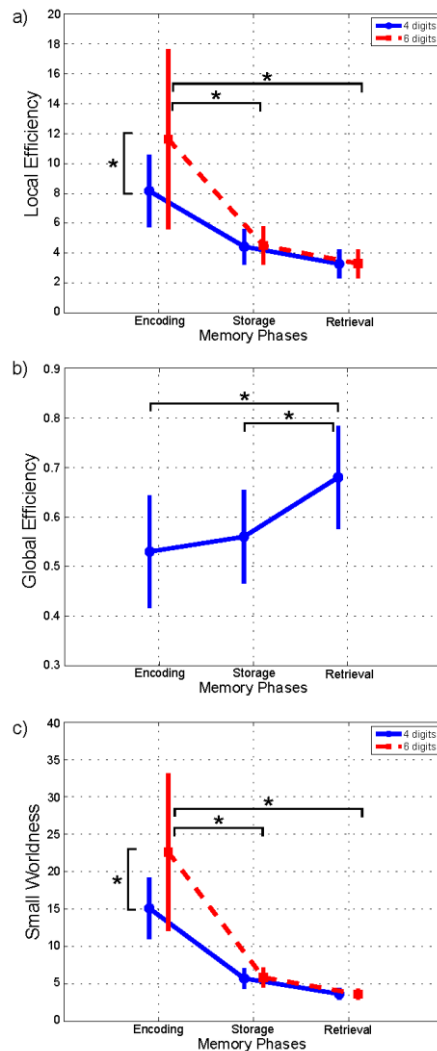


Figure 6.2 – Plot of means (\pm SD) values of Local Efficiency (panel a), Global Efficiency (panel b) and Small-Worldness (panel c) indices estimated in alpha band, and relative to Encoding, Storage and Retrieval phases. The asterisks indicate significant differences (Duncan's post-hoc; $p < 0.05$).

We found significant differences between 4 and 6 digits conditions for the LE and the SW indices (*fig. 6.2a* and *fig. 6.2c*). In particular, the LE and SW showed significantly higher values for the 6 with respect to 4 digits only during *Encoding* in alpha (*fig. 6.2*, panels a and c). Similar results were found in gamma band. No significant differences between 4 and 6 digits were found for the GE. Furthermore, the LE index computed for alpha band and relative to the *Encoding* phase negatively correlated with RTs obtained from both 4 ($r=-0.7026$, $p=0.0024$) and 6 ($r=-0.7048$, $p=0.0023$) digits cases.

Local properties of the networks

The degree index was computed for each electrode and each subject and then averaged within the experimental group for the three PHASES and the two DIGIT conditions (Grand Average (GA) Degree Maps). A spatial representation of such index is reported in the topographical maps of *fig. 6.3* for 4 digits (panel a) and 6 digits (panel b) cases.

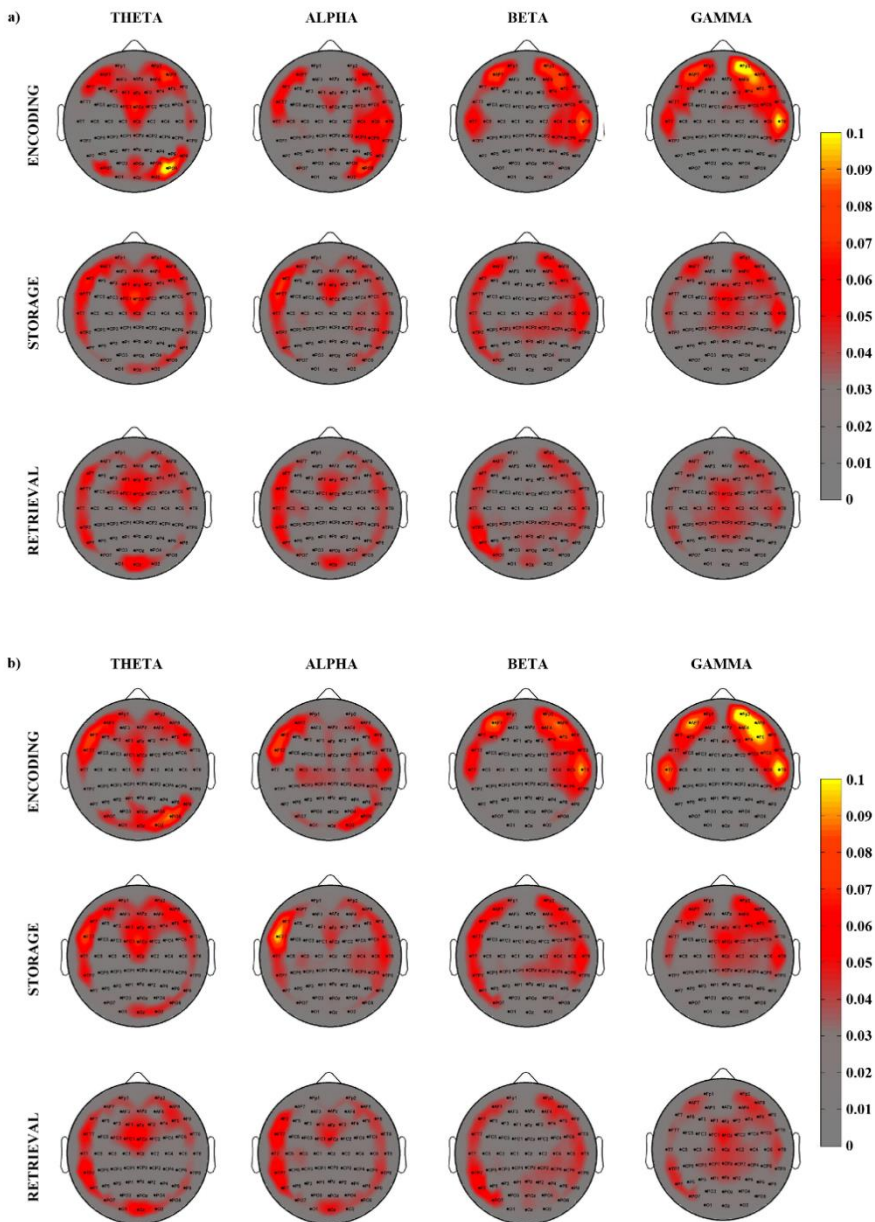


Figure 6.3 –Grand Average Degree –inward and outward- maps relative to the 3 different phases of WM process as elicited by the SIRT (Encoding, Storage, an Retrieval) for 4 digits (panel a) and 6 digits (panel b) condition and for 4 EEG frequency bands. Degree maps are represented on a 2D scalp model and seen from above. The color of each pixel codes for the corresponding degree magnitude.

The visual inspection of the GA Degree Maps relative to the 4 digits condition revealed that the 3 WM phases were associated with distinct connectivity networks for each frequency band oscillation (*fig. 6.3a*). During the *Encoding*, we observed a connectivity pattern which mainly included (high degree index) the central midline, the bilateral frontal areas and the bilateral posterior areas in the theta frequency band. In the alpha band, such patterns were mainly represented over the frontal midline, the left frontal areas and the right hemisphere from frontal to parietal areas. In beta and gamma oscillation ranges, the patterns were prevalent over the bilateral fronto-temporal areas. *Storage* was consistently associated with a high involvement (high degree) of the bilateral fronto-temporal areas, the frontal midline and the right posterior areas in the theta and alpha bands. Bilateral fronto-temporal areas, left tempo-parietal areas and right central areas have an important role in the beta band. In gamma band, we found an involvement of bilateral fronto-temporal areas and frontal midline. The *Retrieval* of digits showed a connectivity pattern mainly involving (high degree) frontal-central midline, left fronto-tempo-parietal areas, right frontal areas and occipital areas in the theta and alpha band. In beta band, we found a high involvement of bilateral fronto-tempo-parietal areas and parieto-occipital midline. An important role of bilateral fronto-temporal areas and central areas resulted in gamma band. The averaged patterns obtained for the 6 digits condition are illustrated in figure 6.3b. The qualitative (visual inspection) analysis of 6 digits condition revealed a general superimposition with the areas mainly involved in the 4 digits condition. On the basis of these findings (*fig. 6.3*), we selected eight scalp areas (macro-areas) symmetrically distributed over the left and right sides and computed the respective average degree index. The following macro-areas were considered: Left Frontal (Fp1, AF7, F7), Frontal Midline (AFz, Fz, FCz), Right Frontal (Fp2, AF8, F8), Left Temporal (FT7, T7, TP7), Right Temporal (FT8, T8, TP8), Left Parietal (PO7, O1), Right Parietal (PO8, O2), Occipital (Oz). The results of the two-way ANOVA on degree index with respect to the memory phases and WM load are reported in table 6.3 for each macro-area and frequency band. The ANOVA revealed a significant effect of the main factor PHASES on Left Frontal Degree, Right Temporal Degree, Left Parietal Degree in beta and gamma bands, on Frontal

Midline Degree in gamma band, on Right Frontal Degree in theta, beta and gamma bands, on Occipital Degree in alpha, beta and gamma bands and on Right Parietal Degree in theta and alpha bands. The main factor DIGITS has a significant effect only in alpha band for Left Temporal Degree and in gamma band for Right Frontal and Left Parietal Degree. No significant effect was found for the interaction PHASESxDIGITS except for Occipital Degree in gamma band.

LOCAL INDEX	BAND	PHASES (d.f.=2,30)	DIGITS (d.f.=1,15)	PHASES x DIGITS (d.f.=2,30)
Left Frontal Degree	θ	2.67	0.37	2.89
	α	2.12	1.31	1.65
	β	4,11*	0.38	0.14
	γ	26,16**	4.77	1.48
Frontal Midline Degree	θ	1.42	0.72	0.38
	α	0.11	0.65	0.65
	β	2.31	0.49	0.05
	γ	6,39*	0.01	0.83
Right Frontal Degree	θ	4,98*	0.12	1.05
	α	0.58	0.13	0.08
	β	12,16**	2.23	0.74
	γ	20,56**	6,51*	3.22
Left Temporal Degree	θ	3.01	2.33	0.46
	α	1.39	7,62*	2.84
	β	0.78	2.02	0.57
	γ	0.53	0.001	0.75
Right Temporal Degree	θ	1.5	0.19	0.73
	α	1.53	0.34	0.93
	β	9,14**	0.38	2.52
	γ	15,35**	0.09	0.27
Left Parietal Degree	θ	1.11	0.12	1.55
	α	0.46	0.93	0.42
	β	7,55*	1.15	0.79
	γ	26,74**	4,89*	2.08
Occipital Degree	θ	1.22	0.22	1.55
	α	5,63*	1.16	1.04
	β	8,95**	0.43	2.49
	γ	6,42*	0.49	5,04*
Right Parietal Degree	θ	11,19**	0.09	0.09
	α	5,75*	0.009	0.14
	β	0.17	0.01	0.2
	γ	0.14	0.001	0.17

Table 6.3 – Results of two-way repeated measures ANOVA on local indices (*F* values, ** $p < 0.001$, * $p < 0.01$). FDR correction for multiple ANOVAs was applied.

The schematic representation of *fig. 6.4* summarizes the trends obtained for the macro-areas degree across the 3 memory phases in the 4 frequency bands. In particular, the areas distinctive for the Encoding were the right frontal and right parietal areas in theta band, right parietal area in alpha band, left and right frontal

and right temporal areas in beta and gamma bands. The Storage was instead characterized by right frontal area in theta band and frontal midline in gamma band. The retrieval involved occipital area in alpha, left parietal and occipital areas in beta band and frontal midline, left parietal and occipital areas in gamma band.

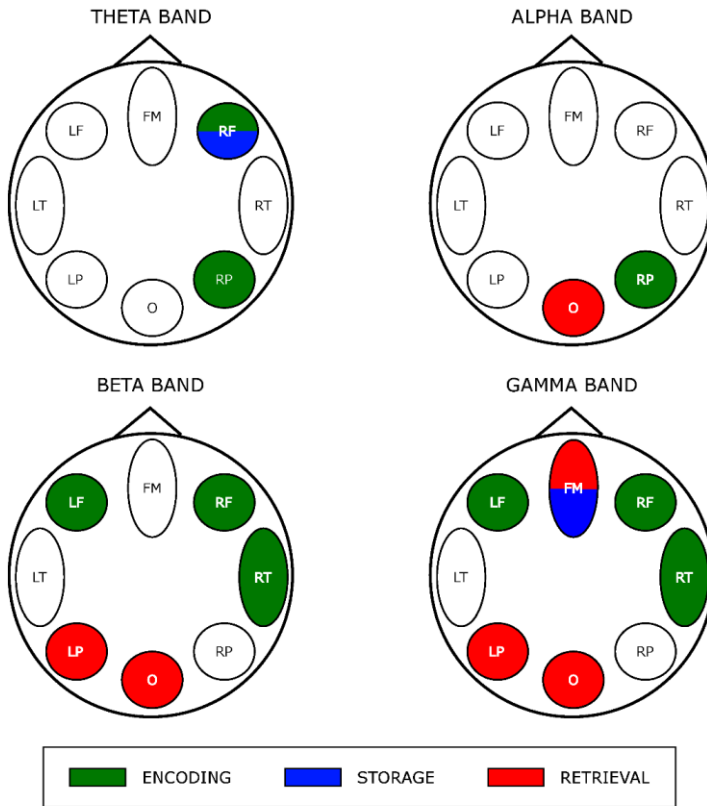


Figure 6.4 - Prevalent network involvement in each WM phase as schematically represented by 8 scalp macro-areas for each frequency band. Such schematic representation was derived by the results of the ANOVA obtained for the factor PHASES on macro-areas Degree index (see tab. 6.3). We assigned an area to a specific phase if its Degree was significantly higher with respect to the other macro-areas.

3.3 Stroke patients

Figures 6.5 and 6.6 report the results obtained at single subject level for two stroke patients. Patient A (fig. 6.5) showed a positive outcome and Patient B (fig. 6.6) a negative outcome (no improvement).

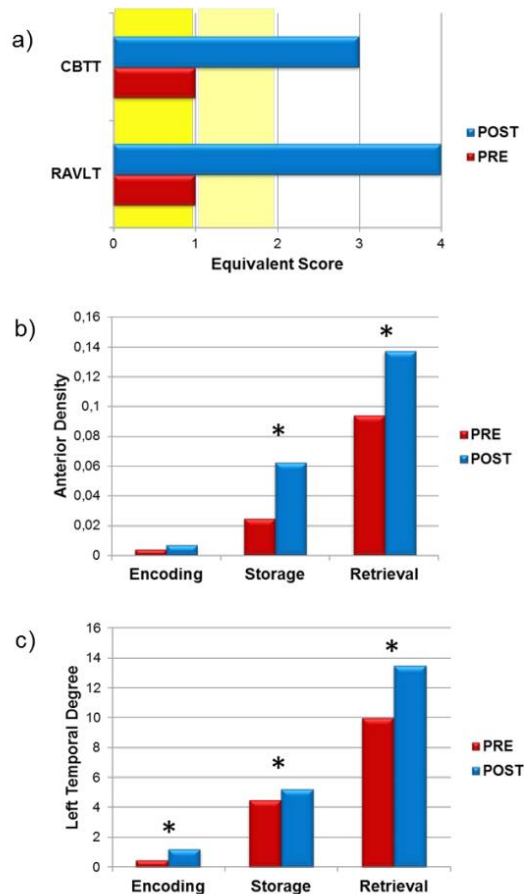


Figure 6.5 - a) Bar diagrams reporting the equivalent scores achieved for RAVLT and CBTT neuropsychological tests administered to patient A before (PRE, red bars) and after (POST, blue bars) the rehabilitation period. Equivalent scores below 2 (in yellow) highlight a pathological condition for the specific cognitive function investigated by the test. b,c) Anterior Density and Left Temporal Degree indexes achieved in Alpha band during Sternberg task in PRE (red bars) and POST (blue bars) sessions for the representative stroke patient A. The symbol (*) reported above the bars highlights a statistical significance between PRE and POST sessions (paired t-test; $p < 0.05$, FDR correction).

Results for Patient A

Memory Assessment: as reported in fig. 6.5a, the neuropsychological tests revealed a significant improvement of the tested memory function after the rehabilitation period. Equivalent scores for both CBTT and RAVLT tests increased from 1 to 3 and 4 respectively, thus indicating a transition from a pathological (PRE) to a physiological (POST) condition.

Behavioural Data: analysis of the behavioural performance obtained at the Sternberg task revealed a significant increase of correct answers and a significant decrease of the reaction time after training.

EEG derived Brain Network: analysis of the connectivity patterns revealed a significant POST training increase of the Anterior Density index (fig. 6.5b) estimated in the alpha band only for Storage and Retrieval phases of the Sternberg task associated with an increase of Left Temporal Degree index (fig. 6.5c) in alpha band for all the three memory phases (Encoding, Storage and Retrieval).

Results for Patient B

Memory Assessment: in this patient we did not find significant changes in the memory functions as evaluated by means of neuropsychological assessment (fig. 6.6a). Equivalent scores for both RAVLT and CBTT tests remained around 1 and 2 respectively, indicating a persistency of the pathological profile.

Behavioural Data: similar negative outcome was found for the behavioural assessment. Data analysis revealed a decrease of the percentage of correct answers and no significant difference in reaction time between PRE and POST sessions of Sternberg task.

EEG derived Brain Network: connectivity pattern analysis revealed in Patient B an opposite profile of changes in the POST training analysis with respect to what observed in Patient A. In fact, a significant decrease in the Anterior Density index (fig. 6.2b) for Storage and Retrieval phases and of Left Temporal Degree index (fig. 6.2c) for the Retrieval memory phase both estimated in the alpha band, were observed.

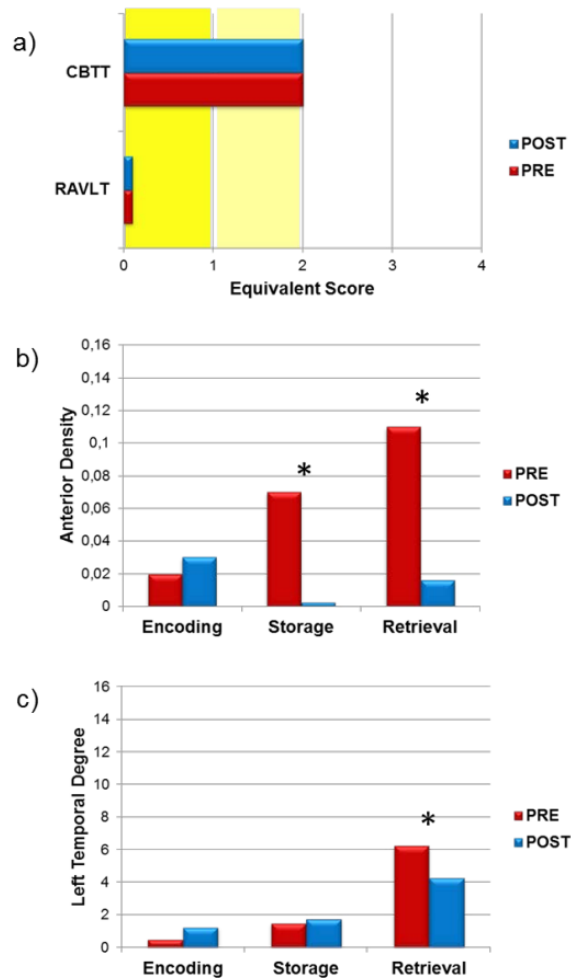


Figure 6.6 - a) Bar diagrams reporting the equivalent scores achieved for RAVLT and CBTT neuropsychological tests administered to patient B before (PRE, red bars) and after (POST, blue bars) the rehabilitation period. Equivalent scores below 2 (in yellow) highlight a pathological condition for the specific cognitive function investigated by the test. b,c) Anterior Density and Left Temporal Degree indexes achieved in Alpha band during Sternberg task in PRE (red bars) and POST (blue bars) sessions for the representative stroke patient A. The symbol (*) reported above the bars highlights a statistical significance between PRE and POST sessions (paired t-test; $p < 0.05$)

Correlation Study

After the first evaluation of the single patient conditions, we selected three measure that mainly change their value in the positive outcomes: Anterior Density, Left Temporal Degree (showed also in *Patient A*) and the Local Efficiency. The correlation study (Pearson correlation, $p < 0.05$, FDR correction) performed between the variation of such three indices in theta and alpha bands and the variation of the behavioural measure provided the results showed in *tab 6.4*. Such correlation was performed separately for the indices computed during each memory phase.

			Behavioral Data					
			Correct Answers			Reaction Time		
			ENC	STO	RET	ENC	STO	RET
Neuro-Physiological Indexes	Theta Band	Anterior Density	0,44	0,29	0,15	-0,41(*)	-0,61(**)	-0,51(*)
		Left Temporal Degree	0,54(**)	0,34	0,3	-0,72(**)	0,35	0,04
		Local Efficiency Norm	0,13	-0,08	-0,01	-0,14	-0,09	-0,2
	Alpha Band	Anterior Density	0,31	0,36	0,07	-0,35	-0,51(*)	-0,39
		Left Temporal Degree	0,13	0,14	0,32	-0,31	0,1	0,01
		Local Efficiency Norm	0,11	0,1	0,13	0,14	-0,22	-0,59(**)

Table 6.4 - Correlation coefficients between the PRE-POST variation of connectivity indices in theta and alpha bands and behavioural scores. The indices were computed for each of the three memory phases. The symbol (**) was used to indicate significant correlations, while the symbol (*) indicates correlations associated to a p value between 0.1 and 0.05.

In theta, the Anterior density showed a strong negative correlation with the reaction time (correlation significant in the storage phase, and close to the significance in the other two phases), while the Left temporal degree showed a significant positive correlation with the number of correct answers and a negative correlation with reaction time, during the encoding phase. In alpha, the Local Efficiency showed a significant negative correlation with reaction time during the retrieval phase while the negative correlation of Anterior density with the same behavioural data was close to significance in the storage phase.

Internal Validation

To prove the capability of the connectivity indices to be a measure of the function elicited by the task, we performed a binary logistic regression considering each of the selected index in the three different memory phases of the Sternberg paradigm (encoding, storage, retrieval) as independent variables, and the behavioural outcome (1= improvement in behavioural performances, 0 = no improvement) as a dichotomous dependent variable. The logistic regression was repeated for each of the three indices and separately for the two frequency bands of interest (theta and alpha). It describes how we can correctly classify patients who showed behavioural improvements in the task from those who didn't on the basis of variations in their connectivity indices. In *tab. 6.5* we reported the results of the regression performed separately for the three indices and the two frequency bands.

LOGISTIC BINARY REGRESSION		BEHAVIORAL OUTCOME	
		R-square	Accuracy
THETA	Anterior Density	0,68	92,9
	Left Temporal Degree	0,78	92,9
	Local Efficiency	0,12	57,1
ALPHA	Anterior Density	0,15	64,3
	Left Temporal Degree	0,63	85,7
	Local Efficiency	0,32	78,6

Table 6.5 – Results of the binary logistic regression computed considering the values of the index in the three different memory phases of Sternberg paradigm (encoding, storage, retrieval) as independent variables, and the behavioural outcome (1 → improvement in behavioural performances, 0 → no improvement) as dichotomous dependent variable. The results were reported separately for the three indices and the two frequency bands. In red, the significant regressions.

The results show that we can correctly classify the patients who improved their behavioural performances after the training on the basis of the Anterior Density and the Left Temporal degree in theta band. The classification accuracies were 92.9% (Anterior Density \square Nagelkerke R-square = 0.68, $p < 0.05$; Left Temporal Degree \square Nagelkerke R-square = 0.78, $p < 0.05$) for both indices. Similar results,

with a significant (even if smaller) accuracy were found for the Left Temporal Degree in alpha band (85.7%, Nagelkerke R-square = 0.63, $p < 0.05$).

4. Conclusion and discussion

This study applied a graph theory- driven approach to complex causality patterns derived from EEG recordings, with the aim to identify network topological properties, which describe the encoding, storage, retrieval phases of WM as elicited during visual SIRT performed by healthy, middle age adults. During the encoding phase, the global network exhibited a small-world topology (in all frequency bands), a network configuration known as optimal for global information transfer and local processing (see below). The requirement of such optimal configuration during item encoding appears further corroborated by the negative correlation between local efficiency and behavioural task performance. The small-world configuration of the whole network persisted across maintenance and rehearsal of encoded items, but it showed a descendent trend. At the local scale, the degree of information flow between scalp regions was specific to each one of the 3 different WM phases, according to the different role of regions in different WM phases.

Behavioural Results

The behavioural results obtained from our sample of healthy, middle age adults are in line with what was reported by previous studies conducted in healthy adults and wherein, the SIRT was applied to investigate working memory (WM) processes [174], [175], [126]. As expected, WM loads (4, 6 digits condition) had a significant effect on the response time and accuracy for both target and no-target probe, in our sampled population. These WM load-related behavioral changes have been previously ascribed to a serial scanning of memorized elements required in order to recall the memorized material [176].

Global organization of the WM network

The complex human brain networks have been found to have a “small-world” topology (*fig. 6.2c*) which is characterized by a high local specialization and a high global integration, to sustain a high efficiency at a low wiring cost [177]. As

pointed out by Toppi and colleagues in 2012, SW properties (SW index above 1) of real EEG-derived networks could be induced by the spatial localization of EEG electrodes and by the position of the reference [178]. Thus, only significant variations in SW index between one experimental condition and another one are worth of note and representative of a modification in the network configuration. For this reason, in the present work, we statistically compared SW values of EEG-derived networks across the three different WM phases. Only variations in SW index have been described.

The significant effect of phase factor on global indices (global and local efficiency, small-worldness; *tab. 6.2*) indicated that a small-world topology of the networks was present in all 3 WM phases (small-worldness >1 for the three phases). We found however, that such topological organization was not equally represented across the 3 WM phases. Accordingly, the highest small-worldness values were associated with encoding (between 10 and 20 in alpha band; *fig. 6.2*) whereas storage and retrieval showed a trend toward a small-worldness decrease (*fig. 6.2*). This trend was also paralleled by that observed for the local and global efficiency indices: the highest values of local efficiency together with the lowest values of global efficiency were observed for encoding with respect to storage and retrieval phases. Such descendent trend was evident in lower to higher frequency oscillations (*tab. 6.2*). Our findings indicate that such descendent trend in the network small-worldness topology may reflect a general network tendency to reduce local segregation in favor of global integration of the information exchange between/within the different brain regions as cognitive processing evolve from encoding to retrieval. Such topological re-arrangement, underscored by the modulation of global indices across the 3 WM phases, is in line with the recently released global workspace theory [179], [180] postulating that the networks' structure reorganizes across the temporal evolution of WM cognitive processing [181]. As such, this dynamics observed for the topology networks might reflect the operational mode of the “episodic buffer” component of the Baddeley model (Baddeley 2010). This “buffer” serves as an intermediary between the storage subsystems with different codes (i.e., phonological loop and visuo-spatial sketchpad) whose content is bounded by the buffer into unitary multi-

dimensional representations. Thus, one can speculate that a tendency towards a more global versus local integration network topology (ie, the decrease of small-worldness across WM phases) would “*optimally*” serve the function of the episodic buffer by favoring the information flow between WM networks (ie, 2 storage subsystems, central executive).

The encoding process directly influences the precision and accuracy of subsequent WM representations [182], [183]. The well-known limitation in the capacity to simultaneously encode objects requires efficient mechanisms in the encoding phase to select only the most relevant objects from the immediate environment to be represented in memory and to restrict irrelevant items from consuming capacity [184]. Several studies have shown how the encoding phase is characterized by a strong interplay between brain circuits underlying WM and selective attention [185]–[187]. Successful working memory performance is, in fact, associated to selective attention mechanisms allowing to focus on a limited number of visual objects and events important for the ongoing cognition and action [188]. A small-world topology, which supports both specialized and integrated information processing in the brain, could well account for complex network interplay. It comprises both high segregated or modular processing (high clustering) and distributed or integrated processing (short path length) [189], [170]. Small-world properties allow networks to operate dynamically in a critical state, facilitating rapid adaptive reconfiguration of neuronal assemblies in support of changing cognitive states. The small-world behavior of encoding networks might be associated to the necessity of the brain to combine the functioning of specialized (segregated) modules with a number of inter-modular links integrating those modules. In line with this interpretation, several evidence indicate a topological disruption of an optimal small-world network in schizophrenic patients [190] who exhibit WM performance deficits that have been related to a decreased efficiency in item encoding [191], [192]. In addition, altered oscillatory dynamics during encoding of information have been reported in normal and pathological aging associated with cognitive decline conditions [161], [193], [194]. We found that the encoding-related network displayed a higher *optimal* topology (higher local efficiency and small-worldness) with WM load

increase (4 vs 6 digits), both in alpha and gamma frequency band. This WM load-induced modulation of network topology reinforce the above interpretation of an high network modularity required during encoding, since a correct memorization of increasing number of items would be best achieved by enhanced selective attention to focus exclusively on target objects [195]. From a behavioral viewpoint, this in line with the *set size effect* theory according to which the ability to successfully report items in WM is inversely proportional to the number of items to be memorize [196]. Recent neurophysiological evidence support the idea that visual WM capacity limitation (i.e., the set size effect) begins with neural resource allocation at encoding [197]. The observed WM load-induced modulation of network topology was prominent in alpha and gamma bands. Alpha oscillations have been hypothesized to play an active role in protecting WM items from non-relevant information [198] for instance, by suppressing distracting sensory information [199]. The increase of WM load is also associated to an increase of alpha-band coherence between midline parietal and left temporal/parietal sites during encoding [128]. Moreover, amplitude of gamma bands directly correlates with the number of items to be memorized (WM load) [149], [200], [201]. In line with the aforementioned reasoning, the network local efficiency estimated in alpha band and relative to encoding varied as function of the RTs (negative correlation; *fig. 6.3*). Similarly, [202] reported a significant correlation between small-worldness index and memory performances [202]. We further elucidated the relationship between network topology dynamics and WM performance unveiling the role of encoding in determining the WM behavioural performance. The existence of such correlation exclusively in alpha band is in accordance with previous evidence of a correlation between changes in α -power and behavioural performance during encoding [203], [204].

Local organization of the Working Memory networks

As illustrated in figure 6.4, the GA degree maps allowed the isolation of scalp areas common to the 3 WM phases. The encoding, storage and retrieval WM phases elicited by the visual SIRT were consistently characterized by an involvement of bilateral fronto-temporal regions in all frequency oscillations while an anterior-

to-posterior midline pattern was prevalent in theta/alpha oscillations. In addition, a bilateral *parieto-occipital connectivity pattern* was observed mainly in theta oscillations during the encoding, while storage/retrieval phase were characterized by a prevalent *left temporo-parietal and right fronto-parietal connectivity patterns* in alpha/beta bands. These patterns were sensitive to WM load increase. The observed common engagement of bilateral dorsolateral frontal, temporal cortices and midline reflects the typical pattern of activity during WM tasks that includes prefrontal cortex, bilateral premotor areas, supplementary motor areas and the dorsal anterior cingulate cortex [205]. All these areas are frequently associated with the “central executive” system [128], [206], which is active during all the phases of the memory process. In fact, the pre-frontal cortex is associated to the capacity to continuously modify the content of working memory according to newer external sensory input, to allocate resources during the simultaneous execution of different tasks and to switch relevant strategies of retrieval [207]. The supplementary motor area is engaged in the repetition of the stimuli to be maintained in memory and in the planning of the motor actions for the inner speech [208], one of the most used memorization strategies. The interplay between rhythmic activity at low (alpha/theta) and high (beta/gamma) frequency has been suggested to enable WM item encoding and maintenance in humans. Particularly, the gamma band would be relevant for active maintenance of WM information, whereas theta band would be involved in the temporal organization of WM items. The relevance of alpha oscillation would reside in filtering task non-relevant information [149]. As expected, the local network organization expressed as (local) degree index was differently modulated across the 3 WM phases, and thus it well describes the distinct processing related to encoding, maintenance and rehearsal of memory information (see *tab. 6.3*). As schematically illustrated in figure 6.5, *Encoding* is mainly described by a bilateral involvement of frontal scalp areas (encoding –related degree contrasted against that related to storage and retrieval time series) and right fronto-temporal scalp area in the high frequency oscillation range (beta/gamma). At lower range of frequency, encoding was described by a right frontal and parietal area involvement. As mentioned above, gamma band activity plays a role in

maintenance of visual (and others sensory) WM items [209], [210]. In addition, EEG/MEG source localization studies pointed out that gamma oscillatory activity changes (increased power) is mainly localized over frontal (and parietal) regions [211]. We hypothesized that our findings in encoding phase likely reflect the correspondence in neural activity between encoding and maintenance of WM information - that would be the active role of the episodic buffer component of WM construct (Baddeley 2010). Although the functional relevance of correspondence in neural activity between encoding and maintenance still remains matter of debate [212]–[214], recent work by Cohen and colleagues [215] provides empirical evidence for an overlap between encoding and maintenance processes as a critical element of WM [216], [217]. The observed theta/alpha-related higher magnitude of local degree indices during encoding (with respect to storage and retrieval) over right fronto-parietal regions may be ascribed to spatial attentional demand needed to cope with the sensory processing during WM item encoding. These areas has been previously reported as fundamental for the recruitment of sustained, and selective component of attention during a visual working memory task in theta and alpha band [204], [218], [219]. The *storage* phase was characterized by a partial overlap with *encoding* as it involved right frontal area in theta band. The interplay between theta/gamma oscillatory activities had been previously mentioned as pivotal in tasks that require sequential coding and maintenance of multiple WM items such as during Sternberg paradigm ([126] *fig.* 6.2). Storage was also described by a gamma-related frontal midline degree index that also well reflects the high oscillations modulation localized over the core nodes of WM maintenance processing [95][114]. Finally, during *retrieval* we observed a selective involvement of occipital area in alpha, beta and gamma bands as well as left parietal region in high frequency oscillations (beta/gamma band). Such parieto-occipital engagement could account for visual stimulus presentation and visual information processing during retrieval [221]. Moreover, neuronal synchronization in the gamma band over occipital areas has been associated to subject ability during encoding and retrieval memory phases [222]. As for the WM load modulation, we found that right frontal degree was sensitive to WM load as well as the left parietal degree in

gamma oscillations. The left temporal degree was also modulated in alpha band as function of WM load (*tab. 6.3*). WM load-related gamma activity has been found to spatially localize to core nodes of WM network which includes parietal and pre-frontal cortices [223], [224]. Moreover, evidence from ECoG data further support the modulation of gamma band activity occurring in frontal and hippocampal regions as function of WM load [225], [226]. The alpha- related left temporal degree is consistent with a role of (left) temporal region in sub-lexical phonological processing of visual material [227], [228]. During Sternberg tasks sequential encoding would activate the phonological loop to support the maintenance of sequenced WM items by means of subvocal rehearsal (silent speech) [206], [229]. Overall network findings illustrated in this study well describe the multi-faceted nature of the WM processing as elicited by the SIRT, which is without manipulation of memory traces. As such, the use of connectivity measures as derived from EEG might offer a valuable approach to support the clinical assessment of cognitive function, providing that the accuracy of EEG-derived connectivity networks and their related topological indices is demonstrated in presence of WM decline/impairment, as it occurs after stroke.

Application to stroke patients

In this application to the clinical environment, we proposed a single subject approach based on the use of advanced methodologies for time varying connectivity estimation and graph theory for defining a set of neurophysiological indexes able to describe the modifies related to the plasticity induced by rehabilitative interventions. In particular, we selected as descriptors of memory processes at the basis of Sternberg task, the Anterior Density, the Left Temporal Degree and the Local Efficiency indices in theta and alpha band. The importance of fronto-central and left frontotemporal areas in Sternberg task has been already demonstrated in a preliminary study conducted on healthy subjects performing the task [157]. The central executive, located in frontal areas of the brain, is in fact responsible for coordinating the other working memory subsystems, for recruiting and allocating attentive resources to inhibit the irrelevant processes and for decoding the information associated with the material to keep in memory [121]. The left temporal areas are instead responsible for the strategy planning,

the recoding of the visual material into phonological code, the rehearsal of the stimuli by inner speech and the provisional storage of the material [137]. The results showed in this paper confirmed the role of such indexes as valid descriptors of modifies in networks elicited during Sternberg task. In particular for two representative subjects the variations of such indexes between PRE and POST sessions were in agreement with behavioural results and above all with the outcome of neuropsychological tests on memory functions. Finally, the subsequent correlation study and validation phase allowed to confirm the ability of the selected indices to describe some of the neurophysiological phenomena elicited by the Sternberg task at the basis of the memory recovery. Other important analysis and validation tests will be performed in future studies before the employment of such indices in the clinical environment, but such promising result could open the way to a wide range of important applications.

General conclusion

Understanding brain functions requires not only information about the spatial localization of neural activity, but also about the dynamic functional links between the involved groups of neurons, which do not work in an isolated way, but rather interact together through ingoing and outgoing connections. The work carried on during the three years of PhD course returns a methodological framework for the estimation of the causal brain connectivity and its validation on simulated and real datasets at scalp and source level. Important open issues like the selection of the best algorithms for the source reconstruction and for time-varying estimates were addressed. Moreover, after the application of such approaches on real dataset recorded from healthy subjects and post-stroke patients, we extracted neurophysiological indices describing in a stable and reliable way the properties of the brain circuits underlying different cognitive states in humans (attention, memory). More in detail:

- I defined and implemented the SEED-G toolbox able to provide a useful validation instrument addressed to researchers that conduct their activity in the field of brain connectivity estimation. It allows to test the ability of different estimators in increasingly less ideal conditions: low number of available samples and trials, high inter-trial variability (very realistic situations when patients are involved in protocols) or, again, time varying connectivity patterns to be estimate (where stationary hypothesis in wide sense failed). Such tool will be available online for all the scientific community interested in this topic.
- A first simulation study demonstrated the robustness and the accuracy of the PDC with respect to the inter-trials variability under a large range of conditions usually encountered in practice.
- I identified a tool combining source localization approaches and brain connectivity estimation able to provide accurate and reliable estimates as less as possible affected to the presence of spurious links due to the head volume conduction.

- The simulations carried on the time-varying algorithms allowed to highlight the performance of the existing methodologies in different conditions of signals amount and number of available trials. Moreover, the adaptation of the GLKF based algorithm I implemented, with the introduction of the preliminary estimation of the initial conditions for the algorithm, lead to significantly better performance.
- The developed and tested methodologies were successfully applied on three real datasets. The first one was recorded from a group of healthy subjects performing an attention task that allowed to describe the brain circuit at scalp and source level related with three important attention functions: alerting, orienting and executive control. The second EEG dataset come from a group of healthy subjects performing a memory task. Also in this case, the approaches under investigation allowed to identify synthetic connectivity-based descriptors able to characterize the three main memory phases (encoding, storage and retrieval). For the last analysis I recorded EEG data from a group of stroke patients performing the same memory task before and after one month of cognitive rehabilitation. The promising results of this preliminary study showed the possibility to follow the changes observed at behavioural level by means of the introduced neurophysiological indices.

References

- [1] L. Lee, L. M. Harrison, and A. Mechelli, “The Functional Brain Connectivity Workshop: report and commentary,” *Netw. Bristol Engl.*, vol. 14, no. 2, pp. R1-15, May 2003.
- [2] R. Kuś, M. Kamiński, and K. J. Blinowska, “Determination of EEG activity propagation: pair-wise versus multichannel estimate,” *IEEE Trans. Biomed. Eng.*, vol. 51, no. 9, pp. 1501–1510, Sep. 2004.
- [3] A. Brovelli, M. Ding, A. Ledberg, Y. Chen, R. Nakamura, and S. L. Bressler, “Beta oscillations in a large-scale sensorimotor cortical network: directional influences revealed by Granger causality,” *Proc. Natl. Acad. Sci. U. S. A.*, vol. 101, no. 26, pp. 9849–9854, Jun. 2004.
- [4] A. Brovelli, J.-P. Lachaux, P. Kahane, and D. Boussaoud, “High gamma frequency oscillatory activity dissociates attention from intention in the human premotor cortex,” *NeuroImage*, vol. 28, no. 1, pp. 154–164, Oct. 2005.
- [5] L. Astolfi *et al.*, “Comparison of different cortical connectivity estimators for high-resolution EEG recordings,” *Hum. Brain Mapp.*, vol. 28, no. 2, pp. 143–157, Feb. 2007.
- [6] R. E. Greenblatt, M. E. Pflieger, and A. E. Ossadtchi, “Connectivity measures applied to human brain electrophysiological data,” *J. Neurosci. Methods*, vol. 207, no. 1, pp. 1–16, May 2012.
- [7] S. M. Bowyer, “Coherence a measure of the brain networks: past and present,” *Neuropsychiatr. Electrophysiol.*, vol. 2, p. 1, 2016.
- [8] C. W. J. Granger, “Investigating Causal Relations by Econometric Models and Cross-spectral Methods,” *Econometrica*, vol. 37, no. 3, pp. 424–438, 1969.
- [9] S. L. Bressler and A. K. Seth, “Wiener–Granger Causality: A well established methodology,” *NeuroImage*, vol. 58, no. 2, pp. 323–329, Sep. 2011.
- [10] A. B. Barrett, L. Barnett, and A. K. Seth, “Multivariate Granger Causality and Generalized Variance,” *Phys. Rev. E*, vol. 81, no. 4, Apr. 2010.
- [11] K. J. Blinowska, “Review of the methods of determination of directed connectivity from multichannel data,” *Med. Biol. Eng. Comput.*, vol. 49, no. 5, pp. 521–529, May 2011.
- [12] F. van de Steen, L. Faes, E. Karahan, J. Songsiri, P. A. V. Sosa, and D. Marinazzo, “Critical comments on EEG sensor space dynamical connectivity analysis,” *ArXiv160703687 Q-Bio Stat*, Jul. 2016.

- [13] P. L. Nunez and R. Srinivasan, *Electric Fields of the Brain: The Neurophysics of EEG*. Oxford University Press, 2006.
- [14] S. Haufe, V. V. Nikulin, K.-R. Müller, and G. Nolte, “A critical assessment of connectivity measures for EEG data: A simulation study,” *NeuroImage*, vol. 64, pp. 120–133, Jan. 2013.
- [15] C. Brunner, M. Billinger, M. Seeber, T. R. Mullen, and S. Makeig, “Volume Conduction Influences Scalp-Based Connectivity Estimates,” *Front. Comput. Neurosci.*, vol. 10, Nov. 2016.
- [16] F. Babiloni *et al.*, “Estimation of the cortical functional connectivity with the multimodal integration of high-resolution EEG and fMRI data by directed transfer function,” *NeuroImage*, vol. 24, no. 1, pp. 118–131, Jan. 2005.
- [17] L. A. Baccalá and K. Sameshima, “Overcoming the limitations of correlation analysis for many simultaneously processed neural structures,” *Prog. Brain Res.*, vol. 130, pp. 33–47, 2001.
- [18] B. D. Van Veen, W. van Drongelen, M. Yuchtman, and A. Suzuki, “Localization of brain electrical activity via linearly constrained minimum variance spatial filtering,” *IEEE Trans. Biomed. Eng.*, vol. 44, no. 9, pp. 867–880, Sep. 1997.
- [19] R. D. Pascual-Marqui *et al.*, “Assessing interactions in the brain with exact low-resolution electromagnetic tomography,” *Philos. Transact. A Math. Phys. Eng. Sci.*, vol. 369, no. 1952, pp. 3768–3784, Oct. 2011.
- [20] M. I. Posner and S. E. Petersen, “The attention system of the human brain,” *Annu. Rev. Neurosci.*, vol. 13, pp. 25–42, 1990.
- [21] R. T. Pivik, R. J. Broughton, R. Coppola, R. J. Davidson, N. Fox, and M. R. Nuwer, “Guidelines for the recording and quantitative analysis of electroencephalographic activity in research contexts,” *Psychophysiology*, vol. 30, no. 6, pp. 547–558, Nov. 1993.
- [22] R. J. Croft and R. J. Barry, “Removal of ocular artifact from the EEG: a review,” *Neurophysiol. Clin. Neurophysiol.*, vol. 30, no. 1, pp. 5–19, Feb. 2000.
- [23] T. Gasser, P. Ziegler, and W. F. Gattaz, “The deleterious effect of ocular artefacts on the quantitative EEG, and a remedy,” *Eur. Arch. Psychiatry Clin. Neurosci.*, vol. 241, no. 6, pp. 352–356, 1992.
- [24] G. Buzsáki, “Theta Oscillations in the Hippocampus,” *Neuron*, vol. 33, no. 3, pp. 325–340, Jan. 2002.
- [25] J. L. Cantero, M. Atienza, R. Stickgold, M. J. Kahana, J. R. Madsen, and B. Kocsis, “Sleep-dependent theta oscillations in the human

- hippocampus and neocortex,” *J. Neurosci. Off. J. Soc. Neurosci.*, vol. 23, no. 34, pp. 10897–10903, Nov. 2003.
- [26] Y. Kubota *et al.*, “Frontal midline theta rhythm is correlated with cardiac autonomic activities during the performance of an attention demanding meditation procedure,” *Brain Res. Cogn. Brain Res.*, vol. 11, no. 2, pp. 281–287, Apr. 2001.
- [27] K. Hagemann, “The alpha band as an electrophysiological indicator for internalized attention and high mental workload in real traffic driving,” Jan. 2018.
- [28] G. Sammer *et al.*, “Relationship between regional hemodynamic activity and simultaneously recorded EEG-theta associated with mental arithmetic-induced workload,” *Hum. Brain Mapp.*, vol. 28, no. 8, pp. 793–803, Aug. 2007.
- [29] M. E. Smith, A. Gevins, H. Brown, A. Karnik, and R. Du, “Monitoring task loading with multivariate EEG measures during complex forms of human-computer interaction,” *Hum. Factors*, vol. 43, no. 3, pp. 366–380, 2001.
- [30] A. Gundel and G. F. Wilson, “Topographical changes in the ongoing EEG related to the difficulty of mental tasks,” *Brain Topogr.*, vol. 5, no. 1, pp. 17–25, 1992.
- [31] A. Gevins *et al.*, “Monitoring working memory load during computer-based tasks with EEG pattern recognition methods,” *Hum. Factors*, vol. 40, no. 1, pp. 79–91, Mar. 1998.
- [32] W. Klimesch, P. Sauseng, and S. Hanslmayr, “EEG alpha oscillations: the inhibition-timing hypothesis,” *Brain Res. Rev.*, vol. 53, no. 1, pp. 63–88, Jan. 2007.
- [33] W. Klimesch, “EEG alpha and theta oscillations reflect cognitive and memory performance: a review and analysis,” *Brain Res. Rev.*, vol. 29, no. 2, pp. 169–195, Apr. 1999.
- [34] C. Dooley, “The Impact of Meditative Practices on Physiology and Neurology: A Review of the Literature,” Jan. 2009.
- [35] O. Jensen, J. Kaiser, and J.-P. Lachaux, “Human gamma-frequency oscillations associated with attention and memory,” *Trends Neurosci.*, vol. 30, no. 7, pp. 317–324, Jul. 2007.
- [36] K. Sameshima, D. Y. Takahashi, and L. A. Baccalá, “Partial directed coherence statistical performance characteristics in frequency domain,” *Conf. Proc. Annu. Int. Conf. IEEE Eng. Med. Biol. Soc. IEEE Eng. Med. Biol. Soc. Annu. Conf.*, vol. 2015, pp. 5388–5391, 2015.

- [37] B. Schelter, M. Winterhalder, B. Hellwig, B. Guschlbauer, C. H. Lücking, and J. Timmer, “Direct or indirect? Graphical models for neural oscillators,” *J. Physiol.-Paris*, vol. 99, no. 1, pp. 37–46, Jan. 2006.
- [38] L. Faes and G. Nollo, “Multivariate Frequency Domain Analysis of Causal Interactions in Physiological Time Series,” 2011.
- [39] L. Barnett and A. K. Seth, “The MVGC multivariate Granger causality toolbox: a new approach to Granger-causal inference,” *J. Neurosci. Methods*, vol. 223, pp. 50–68, Feb. 2014.
- [40] S. Haufe and A. Ewald, “A Simulation Framework for Benchmarking EEG-Based Brain Connectivity Estimation Methodologies,” *Brain Topogr.*, pp. 1–18, Jun. 2016.
- [41] L. A. Baccalá and K. Sameshima, “Partial directed coherence: a new concept in neural structure determination,” *Biol. Cybern.*, vol. 84, pp. 463–474, May 2001.
- [42] C. W. J. Granger, “Investigating Causal Relations by Econometric Models and Cross-spectral Methods,” *Econometrica*, vol. 37, no. 3, pp. 424–438, Aug. 1969.
- [43] J. Toppi *et al.*, “The effect of normalization of Partial Directed Coherence on the statistical assessment of connectivity patterns: A simulation study,” *Conf. Proc. Annu. Int. Conf. IEEE Eng. Med. Biol. Soc. IEEE Eng. Med. Biol. Soc. Conf.*, vol. 2013, pp. 4346–4349, 2013.
- [44] C. J. Holmes, R. Hoge, L. Collins, R. Woods, A. W. Toga, and A. C. Evans, “Enhancement of MR images using registration for signal averaging,” *J. Comput. Assist. Tomogr.*, vol. 22, no. 2, pp. 324–333, Apr. 1998.
- [45] M. S. Hämäläinen and R. J. Ilmoniemi, “Interpreting magnetic fields of the brain: minimum norm estimates,” *Med. Biol. Eng. Comput.*, vol. 32, no. 1, pp. 35–42, Jan. 1994.
- [46] M. Petti *et al.*, “Effect of inter-trials variability on the estimation of cortical connectivity by Partial Directed Coherence,” *Conf. Proc. Annu. Int. Conf. IEEE Eng. Med. Biol. Soc. IEEE Eng. Med. Biol. Soc. Annu. Conf.*, vol. 2015, pp. 3791–3794, Aug. 2015.
- [47] D. Y. Takahashi, L. A. Baccalá, and K. Sameshima, “Connectivity Inference between Neural Structures via Partial Directed Coherence,” *J. Appl. Stat.*, vol. 34, no. 10, pp. 1259–1273, Dec. 2007.
- [48] K. Sameshima, D. Y. Takahashi, and L. A. Baccalá, “On the Statistical Performance of Connectivity Estimators in the Frequency Domain,” in *Brain Informatics and Health*, 2014, pp. 412–423.

-
- [49] J. Toppi, D. Mattia, M. Riseti, R. Formisano, F. Babiloni, and L. Astolfi, "Testing the Significance of Connectivity Networks: Comparison of Different Assessing Procedures," *IEEE Trans. Biomed. Eng.*, vol. 63, no. 12, pp. 2461–2473, Dec. 2016.
- [50] L. Astolfi *et al.*, "Estimation of the effective and functional human cortical connectivity with structural equation modeling and directed transfer function applied to high-resolution EEG," *Magn. Reson. Imaging*, vol. 22, no. 10, pp. 1457–1470, Dec. 2004.
- [51] L. Faes, D. Marinazzo, G. Nollo, and A. Porta, "An information-theoretic framework to map the spatiotemporal dynamics of the scalp electroencephalogram," *IEEE Trans. Biomed. Eng.*, vol. 63, no. 12, pp. 2488–2496, 2016.
- [52] A. Khadem and G.-A. Hossein-Zadeh, "Quantification of the effects of volume conduction on the EEG/MEG connectivity estimates: an index of sensitivity to brain interactions," *Physiol. Meas.*, vol. 35, no. 10, p. 2149, 2014.
- [53] L. A. Baccalá, C. S. N. de Brito, D. Y. Takahashi, and K. Sameshima, "Unified asymptotic theory for all partial directed coherence forms," *Philos. Transact. A Math. Phys. Eng. Sci.*, vol. 371, no. 1997, p. 20120158, Aug. 2013.
- [54] M. Ding, S. L. Bressler, W. Yang, and H. Liang, "Short-window spectral analysis of cortical event-related potentials by adaptive multivariate autoregressive modeling: data preprocessing, model validation, and variability assessment," *Biol. Cybern.*, vol. 83, no. 1, pp. 35–45, Jul. 2000.
- [55] E. Möller, B. Schack, M. Arnold, and H. Witte, "Instantaneous multivariate EEG coherence analysis by means of adaptive high-dimensional autoregressive models," *J. Neurosci. Methods*, vol. 105, no. 2, pp. 143–158, Feb. 2001.
- [56] W. Hesse, E. Möller, M. Arnold, and B. Schack, "The use of time-variant EEG Granger causality for inspecting directed interdependencies of neural assemblies," *J. Neurosci. Methods*, vol. 124, no. 1, pp. 27–44, Mar. 2003.
- [57] T. Milde *et al.*, "A new Kalman filter approach for the estimation of high-dimensional time-variant multivariate AR models and its application in analysis of laser-evoked brain potentials," *NeuroImage*, vol. 50, no. 3, pp. 960–969, Apr. 2010.

- [58] R. Kus, M. Kaminski, and K. J. Blinowska, “Determination of EEG activity propagation: pair-wise versus multichannel estimate,” *IEEE Trans. Biomed. Eng.*, vol. 51, no. 9, pp. 1501–1510, Sep. 2004.
- [59] E. Möller, B. Schack, M. Arnold, and H. Witte, “Instantaneous multivariate EEG coherence analysis by means of adaptive high-dimensional autoregressive models,” *J. Neurosci. Methods*, vol. 105, no. 2, pp. 143–158, Feb. 2001.
- [60] L. Astolfi *et al.*, “Tracking the time-varying cortical connectivity patterns by adaptive multivariate estimators,” *IEEE Trans. Biomed. Eng.*, vol. 55, no. 3, pp. 902–913, Mar. 2008.
- [61] T. Weiss *et al.*, “How do brain areas communicate during the processing of noxious stimuli? An analysis of laser-evoked event-related potentials using the Granger causality index,” *J. Neurophysiol.*, vol. 99, no. 5, pp. 2220–2231, May 2008.
- [62] T. Milde, P. Putsche, K. Schwab, M. Wacker, M. Eiselt, and H. Witte, “Dynamics of directed interactions between brain regions during interburst–burst EEG patterns in quiet sleep of full-term neonates,” *Neurosci. Lett.*, vol. 488, no. 2, pp. 148–153, Jan. 2011.
- [63] C. Zhu *et al.*, “Influences of brain development and ageing on cortical interactive networks,” *Clin. Neurophysiol.*, vol. 122, no. 2, pp. 278–283, Feb. 2011.
- [64] H. Akaike, “A new look at statistical model identification,” *IEEE Trans Autom. Control*, vol. 19, pp. 716–723, 1974.
- [65] S. Haykin, *Adaptive Filter Theory*, 2nd edition. Englewood Cliffs, NJ: Prentice-Hall, 1991.
- [66] K. J. Friston, “Functional and effective connectivity in neuroimaging: A synthesis,” *Hum. Brain Mapp.*, vol. 2, no. 1–2, pp. 56–78, Jan. 1994.
- [67] B. Horwitz, “The elusive concept of brain connectivity,” *NeuroImage*, vol. 19, no. 2, pp. 466–470, Jun. 2003.
- [68] K. J. Blinowska, “Review of the methods of determination of directed connectivity from multichannel data,” *Med. Biol. Eng. Comput.*, vol. 49, no. 5, pp. 521–529, May 2011.
- [69] P. L. Nunez *et al.*, “EEG coherency: I: statistics, reference electrode, volume conduction, Laplacians, cortical imaging, and interpretation at multiple scales,” *Electroencephalogr. Clin. Neurophysiol.*, vol. 103, no. 5, pp. 499–515, Nov. 1997.
- [70] F. V. de Steen, L. Faes, E. Karahan, J. Songsiri, P. A. Valdes-Sosa, and D. Marinazzo, “Critical Comments on EEG Sensor Space Dynamical Connectivity Analysis,” *Brain Topogr.*, pp. 1–12, Nov. 2016.

- [71] G. Gómez-Herrero, M. Atienza, K. Egiazarian, and J. L. Cantero, "Measuring directional coupling between EEG sources," *NeuroImage*, vol. 43, no. 3, pp. 497–508, Nov. 2008.
- [72] S. Haufe, R. Tomioka, G. Nolte, K. R. Müller, and M. Kawanabe, "Modeling Sparse Connectivity Between Underlying Brain Sources for EEG/MEG," *IEEE Trans. Biomed. Eng.*, vol. 57, no. 8, pp. 1954–1963, Aug. 2010.
- [73] G. Nolte *et al.*, "Robustly Estimating the Flow Direction of Information in Complex Physical Systems," *Phys. Rev. Lett.*, vol. 100, no. 23, p. 234101, Jun. 2008.
- [74] G. Nolte, O. Bai, L. Wheaton, Z. Mari, S. Vorbach, and M. Hallett, "Identifying true brain interaction from EEG data using the imaginary part of coherency," *Clin. Neurophysiol.*, vol. 115, no. 10, pp. 2292–2307, Oct. 2004.
- [75] K. J. Blinowska, R. Kuś, and M. Kamiński, "Granger causality and information flow in multivariate processes," *Phys. Rev. E Stat. Nonlin. Soft Matter Phys.*, vol. 70, no. 5 Pt 1, p. 050902, Nov. 2004.
- [76] C. W. J. Granger, "Investigating Causal Relations by Econometric Models and Cross-spectral Methods," *Econometrica*, vol. 37, no. 3, pp. 424–438, 1969.
- [77] I. Winkler, D. Panknin, D. Bartz, K. R. Müller, and S. Haufe, "Validity of Time Reversal for Testing Granger Causality," *IEEE Trans. Signal Process.*, vol. 64, no. 11, pp. 2746–2760, Jun. 2016.
- [78] L. A. Baccalá and K. Sameshima, "Partial directed coherence: a new concept in neural structure determination," *Biol. Cybern.*, vol. 84, no. 6, pp. 463–474, Jun. 2001.
- [79] K. Mahjoory, V. V. Nikulin, L. Botrel, K. Linkenkaer-Hansen, M. M. Fato, and S. Haufe, "Consistency of EEG source localization and connectivity estimates," *NeuroImage*, vol. 152, pp. 590–601, May 2017.
- [80] Y. Huang, L. C. Parra, and S. Haufe, "The New York Head—A precise standardized volume conductor model for EEG source localization and tES targeting," *NeuroImage*, vol. 140, pp. 150–162, Oct. 2016.
- [81] R. Grech *et al.*, "Review on solving the inverse problem in EEG source analysis," *J. Neuroengineering Rehabil.*, vol. 5, p. 25, Nov. 2008.
- [82] V. Fonov *et al.*, "Unbiased average age-appropriate atlases for pediatric studies," *NeuroImage*, vol. 54, no. 1, pp. 313–327, Jan. 2011.
- [83] K. Whittingstall, G. Stroink, L. Gates, J. Connolly, and A. Finley, "Effects of dipole position, orientation and noise on the accuracy of EEG source localization," *Biomed. Eng. OnLine*, vol. 2, p. 14, 2003.

- [84] R. D. Pascual-Marqui, “Discrete, 3D distributed, linear imaging methods of electric neuronal activity. Part 1: exact, zero error localization,” *ArXiv07103341 Math-Ph Physicsphysics Q-Bio*, Oct. 2007.
- [85] A. N. Tikhonov and V. I. Arsenin, *Solutions of ill-posed problems*. Winston, 1977.
- [86] R. D. Pascual-Marqui *et al.*, “Assessing interactions in the brain with exact low-resolution electromagnetic tomography,” *Philos. Trans. R. Soc. Lond. Math. Phys. Eng. Sci.*, vol. 369, no. 1952, pp. 3768–3784, Oct. 2011.
- [87] J. F. Geweke, “Measures of Conditional Linear Dependence and Feedback Between Time Series,” *J. Am. Stat. Assoc.*, vol. 79, no. 388, pp. 907–915, 1984.
- [88] L. Barnett and A. K. Seth, “The MVGC multivariate Granger causality toolbox: a new approach to Granger-causal inference,” *J. Neurosci. Methods*, vol. 223, pp. 50–68, Feb. 2014.
- [89] L. Faes, S. Stramaglia, and D. Marinazzo, “On the interpretability and computational reliability of frequency-domain Granger causality,” *F1000Research*, vol. 6, p. 1710, Sep. 2017.
- [90] S. Haufe, V. V. Nikulin, and G. Nolte, “Alleviating the Influence of Weak Data Asymmetries on Granger-Causal Analyses,” in *Latent Variable Analysis and Signal Separation*, 2012, pp. 25–33.
- [91] M. Vinck *et al.*, “How to detect the Granger-causal flow direction in the presence of additive noise?,” *NeuroImage*, vol. 108, no. Supplement C, pp. 301–318, Mar. 2015.
- [92] A. M. Bastos and J.-M. Schoffelen, “A Tutorial Review of Functional Connectivity Analysis Methods and Their Interpretational Pitfalls,” *Front. Syst. Neurosci.*, vol. 9, p. 175, 2015.
- [93] S. S. Wilks, “The Large-Sample Distribution of the Likelihood Ratio for Testing Composite Hypotheses,” *Ann. Math. Stat.*, vol. 9, no. 1, pp. 60–62, Mar. 1938.
- [94] J. A. Hanley and B. J. McNeil, “The meaning and use of the area under a receiver operating characteristic (ROC) curve.,” *Radiology*, vol. 143, no. 1, pp. 29–36, Apr. 1982.
- [95] J. M. Palva *et al.*, “Ghost interactions in MEG/EEG source space: A note of caution on inter-areal coupling measures,” *bioRxiv*, p. 220459, Nov. 2017.
- [96] S. H. Wang, M. Lobier, F. Siebenhühner, T. Puolivali, S. Palva, and J. M. Palva, “Hyperedge bundling: A practical solution to spurious

- interactions in MEG/EEG source connectivity analyses,” *bioRxiv*, p. 219311, Nov. 2017.
- [97] J. Fan, B. D. McCandliss, T. Sommer, A. Raz, and M. I. Posner, “Testing the efficiency and independence of attentional networks,” *J. Cogn. Neurosci.*, vol. 14, no. 3, pp. 340–347, Apr. 2002.
- [98] J. Fan, B. D. McCandliss, J. Fossella, J. I. Flombaum, and M. I. Posner, “The activation of attentional networks,” *NeuroImage*, vol. 26, no. 2, pp. 471–479, Jun. 2005.
- [99] M. Corbetta and G. L. Shulman, “Control of goal-directed and stimulus-driven attention in the brain,” *Nat. Rev. Neurosci.*, vol. 3, no. 3, pp. 201–215, Mar. 2002.
- [100] J. Fan *et al.*, “The Relation of Brain Oscillations to Attentional Networks,” *J. Neurosci.*, vol. 27, no. 23, pp. 6197–6206, Jun. 2007.
- [101] M. Xiao *et al.*, “Attention Performance Measured by Attention Network Test Is Correlated with Global and Regional Efficiency of Structural Brain Networks,” *Front. Behav. Neurosci.*, vol. 10, Oct. 2016.
- [102] S. Markett *et al.*, “Assessing the function of the fronto-parietal attention network: insights from resting-state fMRI and the attentional network test,” *Hum. Brain Mapp.*, vol. 35, no. 4, pp. 1700–1709, Apr. 2014.
- [103] J. Fan, P. R. Hof, K. G. Guise, J. A. Fossella, and M. I. Posner, “The functional integration of the anterior cingulate cortex during conflict processing,” *Cereb. Cortex N. Y. N 1991*, vol. 18, no. 4, pp. 796–805, Apr. 2008.
- [104] M. Rubinov and O. Sporns, “Complex network measures of brain connectivity: uses and interpretations,” *Neuroimage*, vol. 52, no. 3, pp. 1059–1069, Sep. 2010.
- [105] H. Akaike, “A new look at statistical model identification,” vol. 19, pp. 716–723, 1974.
- [106] J. Toppi *et al.*, “Describing relevant indices from the resting state electrophysiological networks,” *Conf. Proc. Annu. Int. Conf. IEEE Eng. Med. Biol. Soc. IEEE Eng. Med. Biol. Soc. Annu. Conf.*, vol. 2012, pp. 2547–2550, 2012.
- [107] V. Latora and M. Marchiori, “Efficient behavior of small-world networks,” *Phys Rev Lett*, vol. 87, no. 19, p. 198701, Nov. 2001.
- [108] M. Rubinov and O. Sporns, “Complex network measures of brain connectivity: Uses and interpretations,” *NeuroImage*, vol. 52, no. 3, pp. 1059–1069, Sep. 2010.
- [109] M. E. J. Newman, “Finding community structure in networks using the eigenvectors of matrices,” *Phys. Rev. E*, vol. 74, no. 3, Sep. 2006.

- [110] A. Raz and J. Buhle, “Typologies of attentional networks,” *Nat. Rev. Neurosci.*, vol. 7, no. 5, pp. 367–379, May 2006.
- [111] P. Luu, D. M. Tucker, and S. Makeig, “Frontal midline theta and the error-related negativity: neurophysiological mechanisms of action regulation,” *Clin. Neurophysiol. Off. J. Int. Fed. Clin. Neurophysiol.*, vol. 115, no. 8, pp. 1821–1835, Aug. 2004.
- [112] M. S. Worden, J. J. Foxe, N. Wang, and G. V. Simpson, “Anticipatory biasing of visuospatial attention indexed by retinotopically specific alpha-band electroencephalography increases over occipital cortex,” *J. Neurosci. Off. J. Soc. Neurosci.*, vol. 20, no. 6, p. RC63, Mar. 2000.
- [113] J. Fan *et al.*, “Testing the behavioral interaction and integration of attentional networks,” *Brain Cogn.*, vol. 70, no. 2, pp. 209–220, Jul. 2009.
- [114] V. Latora and M. Marchiori, “Efficient Behavior of Small-World Networks,” *Phys. Rev. Lett.*, vol. 87, no. 19, Oct. 2001.
- [115] W. Sturm and K. Willmes, “On the functional neuroanatomy of intrinsic and phasic alertness,” *NeuroImage*, vol. 14, no. 1 Pt 2, pp. S76-84, Jul. 2001.
- [116] M. Corbetta, “Frontoparietal cortical networks for directing attention and the eye to visual locations: Identical, independent, or overlapping neural systems?,” *Proc. Natl. Acad. Sci. U. S. A.*, vol. 95, no. 3, pp. 831–838, Feb. 1998.
- [117] P. Fries, “Rhythms For Cognition: Communication Through Coherence,” *Neuron*, vol. 88, no. 1, pp. 220–235, Oct. 2015.
- [118] A. Baddeley, “The fractionation of working memory,” *Proc Natl Acad Sci USA*, vol. 93, no. 24, pp. 13468–13472, Nov. 1996.
- [119] M. D’Esposito and B. R. Postle, “The cognitive neuroscience of working memory,” *Annu. Rev. Psychol.*, vol. 66, pp. 115–142, Jan. 2015.
- [120] null Baddeley, “The episodic buffer: a new component of working memory?,” *Trends Cogn. Sci.*, vol. 4, no. 11, pp. 417–423, Nov. 2000.
- [121] A. Baddeley, “Working memory,” *Curr. Biol. CB*, vol. 20, no. 4, pp. R136-140, Feb. 2010.
- [122] R. M. Nosofsky, D. R. Little, C. Donkin, and M. Fific, “Short-term memory scanning viewed as exemplar-based categorization,” *Psychol. Rev.*, vol. 118, no. 2, pp. 280–315, Apr. 2011.
- [123] L. Corbin and J. Marquer, “Is Sternberg’s Memory Scanning Task Really a Short-Term Memory Task?,” *Swiss J. Psychol.*, vol. 72, no. 4, pp. 181–196, Jan. 2013.

- [124] M. W. Kristofferson, “Effects of practice on character-classification performance,” *Can. J. Psychol. Can. Psychol.*, vol. 26, no. 1, pp. 54–60, 1972.
- [125] S. Sternberg, “Memory-scanning: mental processes revealed by reaction-time experiments,” *Am Sci*, vol. 57, no. 4, pp. 421–457, 1969.
- [126] Sternberg, “High-speed scanning in human memory,” *Science*, vol. 153, pp. 652–654, 1966.
- [127] E. Keren-Happuch, S.-H. A. Chen, M.-H. R. Ho, and J. E. Desmond, “A meta-analysis of cerebellar contributions to higher cognition from PET and fMRI studies,” *Hum Brain Mapp*, Nov. 2012.
- [128] L. Payne and J. Kounios, “Coherent oscillatory networks supporting short-term memory retention,” *Brain Res*, vol. 1247, pp. 126–132, Jan. 2009.
- [129] T. A. Cairo, P. F. Liddle, T. S. Woodward, and E. T. C. Ngan, “The influence of working memory load on phase specific patterns of cortical activity,” *Brain Res Cogn Brain Res*, vol. 21, no. 3, pp. 377–387, Nov. 2004.
- [130] B. Rypma, V. Prabhakaran, J. E. Desmond, G. H. Glover, and J. D. Gabrieli, “Load-dependent roles of frontal brain regions in the maintenance of working memory,” *Neuroimage*, vol. 9, no. 2, pp. 216–226, Feb. 1999.
- [131] E. O. Luis *et al.*, “Successful Working Memory Processes and Cerebellum in an Elderly Sample: A Neuropsychological and fMRI Study,” *PLOS ONE*, vol. 10, no. 7, p. e0131536, lug 2015.
- [132] C. L. Marvel and J. E. Desmond, “Functional Topography of the Cerebellum in Verbal Working Memory,” *Neuropsychol Rev*, vol. 20, no. 3, pp. 271–279, Sep. 2010.
- [133] E. E. Smith and J. Jonides, “Neuroimaging analyses of human working memory,” *Proc. Natl. Acad. Sci.*, vol. 95, no. 20, pp. 12061–12068, Sep. 1998.
- [134] E. Vergauwe, E. Hartstra, P. Barrouillet, and M. Brass, “Domain-general involvement of the posterior frontolateral cortex in time-based resource-sharing in working memory: An fMRI study,” *NeuroImage*, vol. 115, pp. 104–116, Jul. 2015.
- [135] M. Thürling *et al.*, “Involvement of the cerebellar cortex and nuclei in verbal and visuospatial working memory: a 7 T fMRI study,” *Neuroimage*, vol. 62, no. 3, pp. 1537–1550, Sep. 2012.

- [136] S. H. A. Chen and J. E. Desmond, “Cerebrocerebellar networks during articulatory rehearsal and verbal working memory tasks,” *Neuroimage*, vol. 24, no. 2, pp. 332–338, Jan. 2005.
- [137] B. Rypma and M. D’Esposito, “The roles of prefrontal brain regions in components of working memory: effects of memory load and individual differences,” *Proc Natl Acad Sci USA*, vol. 96, no. 11, pp. 6558–6563, May 1999.
- [138] M. Kottlow, A. Schlaepfer, A. Baenninger, L. Michels, D. Brandeis, and T. Koenig, “Pre-stimulus BOLD-network activation modulates EEG spectral activity during working memory retention,” *Front. Behav. Neurosci.*, vol. 9, p. 111, 2015.
- [139] M. J. Brookes *et al.*, “Changes in brain network activity during working memory tasks: a magnetoencephalography study,” *Neuroimage*, vol. 55, no. 4, pp. 1804–1815, Apr. 2011.
- [140] Y. Xie, Z. Feng, Y. Xu, C. Bian, and M. Li, “The different oscillation patterns of alpha band in the early and later stages of working memory maintenance,” *Neurosci. Lett.*, vol. 633, pp. 220–226, Oct. 2016.
- [141] E. Heinrichs-Graham and T. W. Wilson, “Spatiotemporal oscillatory dynamics during the encoding and maintenance phases of a visual working memory task,” *Cortex J. Devoted Study Nerv. Syst. Behav.*, vol. 69, pp. 121–130, Aug. 2015.
- [142] R. Scheeringa, K. M. Petersson, R. Oostenveld, D. G. Norris, P. Hagoort, and M. C. M. Bastiaansen, “Trial-by-trial coupling between EEG and BOLD identifies networks related to alpha and theta EEG power increases during working memory maintenance,” *Neuroimage*, vol. 44, no. 3, pp. 1224–1238, Feb. 2009.
- [143] O. Jensen, J. Gelfand, J. Kounios, and J. E. Lisman, “Oscillations in the Alpha Band (9–12 Hz) Increase with Memory Load during Retention in a Short-term Memory Task,” *Cereb Cortex*, vol. 12, no. 8, pp. 877–882, Aug. 2002.
- [144] U. Maurer, S. Brem, M. Liechti, S. Maurizio, L. Michels, and D. Brandeis, “Frontal midline theta reflects individual task performance in a working memory task,” *Brain Topogr.*, vol. 28, no. 1, pp. 127–134, Jan. 2015.
- [145] M. Z. Zakrzewska and A. Brzezicka, “Working memory capacity as a moderator of load-related frontal midline theta variability in Sternberg task,” *Front. Hum. Neurosci.*, vol. 8, p. 399, 2014.

- [146] O. Jensen and C. D. Tesche, "Frontal theta activity in humans increases with memory load in a working memory task," *Eur. J. Neurosci.*, vol. 15, no. 8, pp. 1395–1399, Apr. 2002.
- [147] N. Axmacher, F. Mormann, G. Fernández, M. X. Cohen, C. E. Elger, and J. Fell, "Sustained Neural Activity Patterns during Working Memory in the Human Medial Temporal Lobe," *J Neurosci*, vol. 27, no. 29, pp. 7807–7816, Jul. 2007.
- [148] G. Hwang, J. Jacobs, A. Geller, J. Danker, R. Sekuler, and M. J. Kahana, "EEG correlates of verbal and nonverbal working memory," *Behav. Brain Funct. BBF*, vol. 1, p. 20, Nov. 2005.
- [149] F. Roux and P. J. Uhlhaas, "Working memory and neural oscillations: α - γ versus θ - γ codes for distinct WM information?," *Trends Cogn. Sci.*, vol. 18, no. 1, pp. 16–25, Jan. 2014.
- [150] C. Grefkes and G. R. Fink, "Connectivity-based approaches in stroke and recovery of function," *Lancet Neurol.*, vol. 13, no. 2, pp. 206–216, Feb. 2014.
- [151] C. Grefkes and G. R. Fink, "Reorganization of cerebral networks after stroke: new insights from neuroimaging with connectivity approaches," *Brain*, vol. 134, no. Pt 5, pp. 1264–1276, May 2011.
- [152] S. C. Cramer *et al.*, "Harnessing neuroplasticity for clinical applications," *Brain J. Neurol.*, vol. 134, no. Pt 6, pp. 1591–1609, Jun. 2011.
- [153] C. J. Honey and O. Sporns, "Dynamical consequences of lesions in cortical networks," *Hum. Brain Mapp.*, vol. 29, no. 7, pp. 802–809, Jul. 2008.
- [154] G. E. van den Bosch *et al.*, "Brain connectivity during verbal working memory in children and adolescents," *Hum. Brain Mapp.*, vol. 35, no. 2, pp. 698–711, Feb. 2014.
- [155] T. S. Woodward, E. Feredoes, P. D. Metzak, Y. Takane, and D. S. Manoach, "Epoch-specific functional networks involved in working memory," *NeuroImage*, vol. 65, pp. 529–539, Jan. 2013.
- [156] T. Milde *et al.*, "A new Kalman filter approach for the estimation of high-dimensional time-variant multivariate AR models and its application in analysis of laser-evoked brain potentials," *Neuroimage*, vol. 50, no. 3, pp. 960–969, Apr. 2010.
- [157] L. Astolfi *et al.*, "Advanced methods for time-varying effective connectivity estimation in memory processes," *Conf. Proc. Annu. Int. Conf. IEEE Eng. Med. Biol. Soc. IEEE Eng. Med. Biol. Soc. Annu. Conf.*, vol. 2013, pp. 2936–2939, 2013.

- [158] S. E. MacPherson, G. P. Wagner, P. Murphy, M. Bozzali, L. Cipolotti, and T. Shallice, “Bringing the Cognitive Estimation Task into the 21st Century: Normative Data on Two New Parallel Forms,” *PLoS ONE*, vol. 9, no. 3, p. e92554, Mar. 2014.
- [159] C. Grady, M. Springer, D. Hongwanishkul, A. McIntosh, and G. Winocur, “Age-related Changes in Brain Activity across the Adult Lifespan,” *J. Cogn. Neurosci.*, vol. 18, no. 2, pp. 227–241, Feb. 2006.
- [160] V. S. Mattay *et al.*, “Neurophysiological correlates of age-related changes in working memory capacity,” *Neurosci. Lett.*, vol. 392, no. 1–2, pp. 32–37, Jan. 2006.
- [161] C. J. Aine, L. Sanfratello, J. C. Adair, J. E. Knoefel, A. Caprihan, and J. M. Stephen, “Development and decline of memory functions in normal, pathological and healthy successful aging,” *Brain Topogr.*, vol. 24, no. 3–4, pp. 323–339, Oct. 2011.
- [162] C. J. Aine *et al.*, “Aging: Compensation or maturation?,” *NeuroImage*, vol. 32, no. 4, pp. 1891–1904, Oct. 2006.
- [163] P. M. Corsi and P. Michael, *Human memory and the medial temporal region of the brain*, vol. 34. McGill University Montreal, 1972.
- [164] D. Schellig and B. Schächtele, *Visueller und verbaler Merkfähigkeitstest: VVM ; Manual*. Pearson, 2009.
- [165] C. Härting, *Wechsler-Gedächtnistest - revidierte Fassung : WMS-R ; deutsche Adaptation der revidierten Fassung der Wechsler Memory scale von David Wechsler*. Huber, 2000.
- [166] W. Sturm and K. Willmes, *Verbaler Lerntest (VLT): Nonverbaler Lerntest (NVL) : Handanweisung*. Hogrefe, Verlag für Psychologie, 1999.
- [167] Y. Benjamini and D. Yekutieli, “The Control of the False Discovery Rate in Multiple Testing under Dependency,” *Ann. Stat.*, vol. 29, no. 4, pp. 1165–1188, Aug. 2001.
- [168] E. Bullmore and O. Sporns, “Complex brain networks: graph theoretical analysis of structural and functional systems,” *Nat. Rev. Neurosci.*, vol. 10, no. 3, pp. 186–198, Mar. 2009.
- [169] O. Sporns, “Structure and function of complex brain networks,” *Dialogues Clin. Neurosci.*, vol. 15, no. 3, pp. 247–262, Sep. 2013.
- [170] D. S. Bassett and E. Bullmore, “Small-World Brain Networks,” *The Neuroscientist*, vol. 12, no. 6, pp. 512–523, Dec. 2006.
- [171] Sporns, D. R. Chialvo, M. Kaiser, and C. C. Hilgetag, “Organization, development and function of complex brain networks,” *Trends Cogn Sci*, vol. 8, no. 9, pp. 418–425, 2004.

- [172] D. J. Watts and S. H. Strogatz, “Collective dynamics of ‘small-world’ networks,” *Nature*, vol. 393, no. 6684, pp. 440–442, Jun. 1998.
- [173] M. D. Humphries and K. Gurney, “Network ‘small-world-ness’: a quantitative method for determining canonical network equivalence,” *PloS One*, vol. 3, no. 4, p. e0002051, 2008.
- [174] T. D. R. Cummins and S. Finnigan, “Theta power is reduced in healthy cognitive aging,” *Int. J. Psychophysiol. Off. J. Int. Organ. Psychophysiol.*, vol. 66, no. 1, pp. 10–17, Oct. 2007.
- [175] A. M. Tuladhar, N. ter Huurne, J.-M. Schoffelen, E. Maris, R. Oostenveld, and O. Jensen, “Parieto-occipital sources account for the increase in alpha activity with working memory load,” *Hum. Brain Mapp.*, vol. 28, no. 8, pp. 785–792, Aug. 2007.
- [176] S. Majerus *et al.*, “The left intraparietal sulcus and verbal short-term memory: focus of attention or serial order?,” *NeuroImage*, vol. 32, no. 2, pp. 880–891, Aug. 2006.
- [177] O. Sporns, “Network attributes for segregation and integration in the human brain,” *Curr. Opin. Neurobiol.*, vol. 23, no. 2, pp. 162–171, Apr. 2013.
- [178] J. Toppi *et al.*, “How the statistical validation of functional connectivity patterns can prevent erroneous definition of small-world properties of a brain connectivity network,” *Comput. Math. Methods Med.*, vol. 2012, p. 130985, 2012.
- [179] B. J. Baars, S. Franklin, and T. Z. Ramsøy, “Global Workspace Dynamics: Cortical ‘Binding and Propagation’ Enables Conscious Contents,” *Front. Psychol.*, vol. 4, 2013.
- [180] B. J. Baars and S. Franklin, “How conscious experience and working memory interact,” *Trends Cogn. Sci.*, vol. 7, no. 4, pp. 166–172, Apr. 2003.
- [181] M. Bola and B. A. Sabel, “Dynamic reorganization of brain functional networks during cognition,” *NeuroImage*, vol. 114, pp. 398–413, Jul. 2015.
- [182] E. Awh and E. K. Vogel, “The bouncer in the brain,” *Nat. Neurosci.*, vol. 11, no. 1, pp. 5–6, Jan. 2008.
- [183] A. M. Rutman, W. C. Clapp, J. Z. Chadick, and A. Gazzaley, “Early top-down control of visual processing predicts working memory performance,” *J. Cogn. Neurosci.*, vol. 22, no. 6, pp. 1224–1234, Jun. 2010.

- [184] E. K. Vogel, A. W. McCollough, and M. G. Machizawa, “Neural measures reveal individual differences in controlling access to working memory,” *Nature*, vol. 438, no. 7067, pp. 500–503, Nov. 2005.
- [185] E. Awh, E. K. Vogel, and S.-H. Oh, “Interactions between attention and working memory,” *Neuroscience*, vol. 139, no. 1, pp. 201–208, Apr. 2006.
- [186] C. N. L. Olivers, J. Peters, R. Houtkamp, and P. R. Roelfsema, “Different states in visual working memory: when it guides attention and when it does not,” *Trends Cogn. Sci.*, vol. 15, no. 7, pp. 327–334, Jul. 2011.
- [187] A. Gazzaley and A. C. Nobre, “Top-down modulation: bridging selective attention and working memory,” *Trends Cogn. Sci.*, vol. 16, no. 2, pp. 129–135, Feb. 2012.
- [188] M. M. Chun, “Visual working memory as visual attention sustained internally over time,” *Neuropsychologia*, vol. 49, no. 6, pp. 1407–1409, May 2011.
- [189] F. Vecchio, F. Miraglia, A. Romano, P. Bramanti, and P. M. Rossini, “Small world brain network characteristics during EEG Holter recording of a stroke event,” *Clin. Neurophysiol.*, vol. 128, no. 1, pp. 1–3, Jan. 2017.
- [190] A. Fornito, A. Zalesky, C. Pantelis, and E. T. Bullmore, “Schizophrenia, neuroimaging and connectomics,” *NeuroImage*, vol. 62, no. 4, pp. 2296–2314, Oct. 2012.
- [191] K. Koch *et al.*, “Altered error-related activity in patients with schizophrenia,” *Neuropsychologia*, vol. 47, no. 13, pp. 2843–2849, Nov. 2009.
- [192] T. A. Cairo, T. S. Woodward, and E. T. C. Ngan, “Decreased Encoding Efficiency in Schizophrenia,” *Biol. Psychiatry*, vol. 59, no. 8, pp. 740–746, Apr. 2006.
- [193] A.-M. Kirova, R. B. Bays, and S. Lagalwar, “Working memory and executive function decline across normal aging, mild cognitive impairment, and Alzheimer’s disease,” *BioMed Res. Int.*, vol. 2015, p. 748212, 2015.
- [194] A. L. Proskovec, E. Heinrichs-Graham, and T. W. Wilson, “Aging modulates the oscillatory dynamics underlying successful working memory encoding and maintenance,” *Hum. Brain Mapp.*, vol. 37, no. 6, pp. 2348–2361, Jun. 2016.
- [195] A. Gazzaley, “Influence of early attentional modulation on working memory,” *Neuropsychologia*, vol. 49, no. 6, pp. 1410–1424, 2011.

- [196] S. J. Luck and E. K. Vogel, “The capacity of visual working memory for features and conjunctions,” *Nature*, vol. 390, no. 6657, pp. 279–281, Nov. 1997.
- [197] G. Gurariy, K. W. Killebrew, M. E. Berryhill, and G. P. Caplovitz, “Induced and Evoked Human Electrophysiological Correlates of Visual Working Memory Set-Size Effects at Encoding,” *PloS One*, vol. 11, no. 11, p. e0167022, 2016.
- [198] O. Jensen and A. Mazaheri, “Shaping Functional Architecture by Oscillatory Alpha Activity: Gating by Inhibition,” *Front. Hum. Neurosci.*, vol. 4, Nov. 2010.
- [199] V. Romei, J. Gross, and G. Thut, “On the role of prestimulus alpha rhythms over occipito-parietal areas in visual input regulation: correlation or causation?,” *J. Neurosci. Off. J. Soc. Neurosci.*, vol. 30, no. 25, pp. 8692–8697, Jun. 2010.
- [200] M. W. Howard *et al.*, “Gamma Oscillations Correlate with Working Memory Load in Humans,” *Cereb. Cortex*, vol. 13, no. 12, pp. 1369–1374, Dec. 2003.
- [201] F. Roux, M. Wibrals, H. M. Mohr, W. Singer, and P. J. Uhlhaas, “Gamma-Band Activity in Human Prefrontal Cortex Codes for the Number of Relevant Items Maintained in Working Memory,” *J. Neurosci.*, vol. 32, no. 36, pp. 12411–12420, Sep. 2012.
- [202] F. Vecchio *et al.*, “Cortical connectivity and memory performance in cognitive decline: A study via graph theory from EEG data,” *Neuroscience*, vol. 316, pp. 143–150, 2016.
- [203] P. Bashivan, G. M. Bidelman, and M. Yeasin, “Spectrotemporal dynamics of the EEG during working memory encoding and maintenance predicts individual behavioral capacity,” *Eur. J. Neurosci.*, vol. 40, no. 12, pp. 3774–3784, Dec. 2014.
- [204] W. Klimesch, “EEG alpha and theta oscillations reflect cognitive and memory performance: a review and analysis,” *Brain Res. Brain Res. Rev.*, vol. 29, no. 2–3, pp. 169–195, Apr. 1999.
- [205] T. D. Wager and E. E. Smith, “Neuroimaging studies of working memory: a meta-analysis,” *Cogn. Affect. Behav. Neurosci.*, vol. 3, no. 4, pp. 255–274, Dec. 2003.
- [206] J. G. Barry, B. Sabisch, A. D. Friederici, and J. Brauer, “Encoding: the keystone to efficient functioning of verbal short-term memory,” *Neuropsychologia*, vol. 49, no. 13, pp. 3636–3647, Nov. 2011.

- [207] F. Collette and M. Van der Linden, “Brain imaging of the central executive component of working memory,” *Neurosci. Biobehav. Rev.*, vol. 26, no. 2, pp. 105–125, Mar. 2002.
- [208] J. M. Chein and J. A. Fiez, “Dissociation of verbal working memory system components using a delayed serial recall task,” *Cereb. Cortex N. Y. N 1991*, vol. 11, no. 11, pp. 1003–1014, Nov. 2001.
- [209] J. Kaiser, T. Heidegger, M. Wibrall, C. F. Altmann, and W. Lutzenberger, “Distinct gamma-band components reflect the short-term memory maintenance of different sound lateralization angles,” *Cereb. Cortex N. Y. N 1991*, vol. 18, no. 10, pp. 2286–2295, Oct. 2008.
- [210] C. Tallon-Baudry, O. Bertrand, F. Peronnet, and J. Pernier, “Induced gamma-band activity during the delay of a visual short-term memory task in humans,” *J. Neurosci. Off. J. Soc. Neurosci.*, vol. 18, no. 11, pp. 4244–4254, Jun. 1998.
- [211] S. Palva and J. M. Palva, “Discovering oscillatory interaction networks with M/EEG: challenges and breakthroughs,” *Trends Cogn. Sci.*, vol. 16, no. 4, pp. 219–230, Apr. 2012.
- [212] A. Gazzaley, J. Rissman, and M. D’Esposito, “Functional connectivity during working memory maintenance,” *Cogn. Affect. Behav. Neurosci.*, vol. 4, no. 4, pp. 580–599, Dec. 2004.
- [213] T. S. Woodward, T. A. Cairo, C. C. Ruff, Y. Takane, M. A. Hunter, and E. T. C. Ngan, “Functional connectivity reveals load dependent neural systems underlying encoding and maintenance in verbal working memory,” *Neuroscience*, vol. 139, no. 1, pp. 317–325, Apr. 2006.
- [214] C. Chang, S. Crottaz-Herbette, and V. Menon, “Temporal dynamics of basal ganglia response and connectivity during verbal working memory,” *NeuroImage*, vol. 34, no. 3, pp. 1253–1269, Feb. 2007.
- [215] J. R. Cohen, K. K. Sreenivasan, and M. D’Esposito, “Correspondence between stimulus encoding- and maintenance-related neural processes underlies successful working memory,” *Cereb. Cortex N. Y. N 1991*, vol. 24, no. 3, pp. 593–599, Mar. 2014.
- [216] M. D’Esposito, “From cognitive to neural models of working memory,” *Philos. Trans. R. Soc. B Biol. Sci.*, vol. 362, no. 1481, pp. 761–772, May 2007.
- [217] B. R. Postle, “Working Memory as an Emergent Property of the Mind and Brain,” *Neuroscience*, vol. 139, no. 1, pp. 23–38, Apr. 2006.
- [218] C. L. Asplund, J. J. Todd, A. P. Snyder, and R. Marois, “A central role for the lateral prefrontal cortex in goal-directed and stimulus-driven attention,” *Nat Neurosci*, vol. 13, no. 4, pp. 507–512, Apr. 2010.

- [219] M. Corbetta and G. L. Shulman, “Control of goal-directed and stimulus-driven attention in the brain,” *Nat Rev Neurosci*, vol. 3, no. 3, pp. 201–215, Mar. 2002.
- [220] J. Kaiser, W. Lutzenberger, C. Decker, M. Wibral, and B. Rahm, “Task- and performance-related modulation of domain-specific auditory short-term memory representations in the gamma-band,” *NeuroImage*, vol. 46, no. 4, pp. 1127–1136, Jul. 2009.
- [221] B. Voytek, R. T. Canolty, A. Shestiyuk, N. E. Crone, J. Parvizi, and R. T. Knight, “Shifts in Gamma Phase–Amplitude Coupling Frequency from Theta to Alpha Over Posterior Cortex During Visual Tasks,” *Front. Hum. Neurosci.*, vol. 4, Oct. 2010.
- [222] D. Osipova, A. Takashima, R. Oostenveld, G. Fernández, E. Maris, and O. Jensen, “Theta and Gamma Oscillations Predict Encoding and Retrieval of Declarative Memory,” *J. Neurosci.*, vol. 26, no. 28, pp. 7523–7531, Jul. 2006.
- [223] D. E. J. Linden, N. N. Oosterhof, C. Klein, and P. E. Downing, “Mapping brain activation and information during category-specific visual working memory,” *J. Neurophysiol.*, vol. 107, no. 2, pp. 628–639, Jan. 2012.
- [224] J. M. Palva, S. Monto, S. Kulashekhar, and S. Palva, “Neuronal synchrony reveals working memory networks and predicts individual memory capacity,” *Proc Natl Acad Sci USA*, vol. 107, no. 16, pp. 7580–7585, Apr. 2010.
- [225] N. Axmacher, M. M. Henseler, O. Jensen, I. Weinreich, C. E. Elger, and J. Fell, “Cross-frequency coupling supports multi-item working memory in the human hippocampus,” *Proc. Natl. Acad. Sci.*, vol. 107, no. 7, pp. 3228–3233, Feb. 2010.
- [226] M. K. van Vugt, A. Schulze-Bonhage, B. Litt, A. Brandt, and M. J. Kahana, “Hippocampal gamma oscillations increase with memory load,” *J. Neurosci. Off. J. Soc. Neurosci.*, vol. 30, no. 7, pp. 2694–2699, Feb. 2010.
- [227] C. J. Price, “The functional anatomy of word comprehension and production,” *Trends Cogn. Sci.*, vol. 2, no. 8, pp. 281–288, Aug. 1998.
- [228] D. Howard *et al.*, “The cortical localization of the lexicons. Positron emission tomography evidence,” *Brain J. Neurol.*, vol. 115 (Pt 6), pp. 1769–1782, Dec. 1992.
- [229] R. N. Henson, N. Burgess, and C. D. Frith, “Recoding, storage, rehearsal and grouping in verbal short-term memory: an fMRI study,” *Neuropsychologia*, vol. 38, no. 4, pp. 426–440, 2000.

Acknowledgement

The research presented in this thesis was supported by:

- The project FIRB 2013 (Fondo per gli investimenti della Ricerca di Base – Futuro in Ricerca) – RBFR136E24: HYPERBRAIN (Brain-to-brain connectivity from simultaneous neuroelectric and autonomic multi-subjects recordings as a new tool to study human social interaction).
- The European ICT Program FP7-ICT-2009-4 Grant Agreement 287320 CONTRAST (“Cognitive Enhancement Training for Successful Rehabilitation After Stroke”).
- The project SWDISCOVERY (“Small World Discovery”) founded by Regione Lazio.
- Sapienza University of Rome (Progetti di Ateneo 2015 and 2016).
- Progetti di Avvio alla Ricerca 2016 founded by Sapienza, University of Rome (NeMAT - From a theoretical to a Neuro-functional Model of ATtention: integration of high resolution EEG and effective connectivity)
- Progetti di Avvio alla Ricerca 2017 founded by Sapienza, University of Rome (Head volume conduction and functional connectivity estimates: main effects and possible solutions)
- Progetti di Mobilità 2016/2017 founded by Sapienza, University of Rome (NeuroNet - Realistic Modeling of Anatomico-Functional Conditions in EEG-based Brain Functional Connectivity)

RESEARCH PRODUCTS

Toppi J., Mattia D., **Anzolin A.**, Risetti M., Petti M., Cincotti F., Babiloni F., Astolfi L. (2014). **“Time varying effective connectivity for describing brain network changes induced by a memory rehabilitation treatment”**. In: IEEE ENGINEERING IN MEDICINE AND BIOLOGY - ANNUAL CONFERENCE. IEEE ENGINEERING IN MEDICINE AND BIOLOGY ANNUAL CONFERENCE PROCEEDINGS, vol. 2014, p. 6786-6789, ISSN: 1557-170X, 2014-Aug, doi: 10.1109/EMBC.2014.6945186

Toppi J., Astolfi L., Risetti M., Kober S. E., **Anzolin A.**, Cincotti F., Wood and D Mattia G. Wood and D. Mattia (2014). **“Detecting brain network changes induced by a neurofeedback-based training for memory function rehabilitation after stroke”**. In: 6th International Brain-Computer Interface Conference. p. 300-303, Graz, September 15, 2014 doi: 10.3217/978-3-85125-378-8-75

Toppi J., **Anzolin A.**, Petti M., Cincotti F., Mattia D., Salinari S., Babiloni F., Astolfi L. (2014). **“Investigating statistical differences in connectivity patterns properties at single subject level: A new resampling approach”**. In: IEEE ENGINEERING IN MEDICINE AND BIOLOGY ANNUAL CONFERENCE. IEEE ENGINEERING IN MEDICINE AND BIOLOGY ANNUAL CONFERENCE PROCEEDINGS, vol. 2014, p. 6357-6360, ISSN: 1557-170X, 2014-Aug, doi: 10.1109/EMBC.2014.6945082

Petti M, Caschera S., **Anzolin A.**, Toppi J., Pichiorri F., Babiloni F., Cincotti F., Mattia D., Astolfi L. (2015). **“Effect of inter-trials variability on the estimation of cortical connectivity by Partial Directed Coherence”**. In: Proceedings of the Annual International Conference of the IEEE Engineering in Medicine and Biology Society, EMBS. vol. 2015-, p. 3791-3794, Institute of Electrical and Electronics Engineers Inc., ISBN: 9781424492718, MiCo Center, Milano Congressi Center, ita, 2015. doi:10.1109/EMBC.2015.7319219

Toppi J., Sciaraffa N., Antonacci Y., **Anzolin A.**, Caschera, S., Petti M., Mattia D., Astolfi L. (2016). **“Measuring the agreement between brain connectivity networks”**. In: Proceedings of the Annual International Conference of the IEEE Engineering in Medicine and Biology Society, EMBS. vol. 2016-October, p. 68-71, Institute of Electrical and Electronics Engineers Inc., ISBN: 9781457702204, Orlando; USA, 16-20 August 2016. doi: 10.1109/EMBC.2016.7590642. Congresso del Gruppo Nazionale di Bioingegneria, Pavia (Italy), Jun. 25-27, 2014

J. Toppi, L. Astolfi, M. Risetti, S. E. Kober, **A. Anzolin**, F. Cincotti, G. Wood, D. Mattia. **“Detecting Brain Network Changes Induced by a Neurofeedback-based Training for Memory Function Rehabilitation After Stroke”**. Proceedings of the 6th International Brain-Computer Interface Conference, Graz (Austria), Sept. 16-19, 2014

J. Toppi, L. Astolfi, M. Risetti, **A. Anzolin**, F. Cincotti, D. Mattia. **“Electroencephalographic descriptors of Working Memory Processes: A Graph Theory Study”**. Proceeding of the Società Italiana Neurologia National Congress, Cagliari (Italy), 11-14 Oct. 2014.

A. Anzolin, D. Mattia, J. Toppi, A. Riccio, F. Pichiorri, F. Cincotti, L. Astolfi **“Neuroelectrical Signatures of Attentional Network Task”**. Proceeding of the V Congresso Gruppo Nazionale di Bioingegneria, Napoli (Italy) 20-22 June. 2016

A. Anzolin, D. Mattia, J. Toppi, F. Pichiorri, A. Riccio, L. Astolfi **“Brain connectivity networks at the basis of human attention components: An EEG study”**. 39th Annual International Conference of IEEE Engineering in Medicine and Biology Society, Jeju Island (Korea) 11-15 In: Proceedings of the Annual International Conference of the IEEE Engineering in Medicine and Biology Society, EMBS. vol. 2017-September, doi: 10.1109/EMBC.2017.8037721

Y. Antonacci, J. Toppi, S. Caschera, **A. Anzolin**, D. Mattia, L. Astolfi **“Estimating brain connectivity when few data points are available: Perspectives and limitations”**. 39th Annual International Conference of IEEE Engineering in Medicine and Biology Society, Jeju Island (Korea) 11-15 In: Proceedings of the Annual International

Conference of the IEEE Engineering in Medicine and Biology Society, EMBS. vol. 2017-September, doi: 10.1109/EMBC.2017.8037819

A. Anzolin, L. Astolfi, J. Toppi, A. Riccio, F. Pichiorri, F. Cincotti, D. Mattia **“Electroencephalography (EEG)-derived markers to measure components of attention processing”**. Proceedings of the 7th Graz Brain-Computer Interface Conference (GBCIC 2017), Graz (Austria) 18-22 September 2017

K. Bombeke, A. Van Dongen, **A. Anzolin**, H. Almgren, A. All, J. Van Looy, L. De Marez¹, D. Marinazzo & E. P. Núñez Castellar **“Do Not Disturb: Psychophysiological Correlates of Flow Experience in VR”** Proceeding of the 20th International Conference on Human-Computer Interaction, Las Vegas (Nevada) 15-20 June 2018

J. Toppi, L. Astolfi, M. Riseti, **A. Anzolin**, S.E. Kober, G. Wood, D. Mattia **“Different Topological Properties of EEG-derived Networks Describe Working Memory Phases as revealed by Graph Theoretical Analysis”**. Frontiers in Human Neuroscience, 12 January 2018.